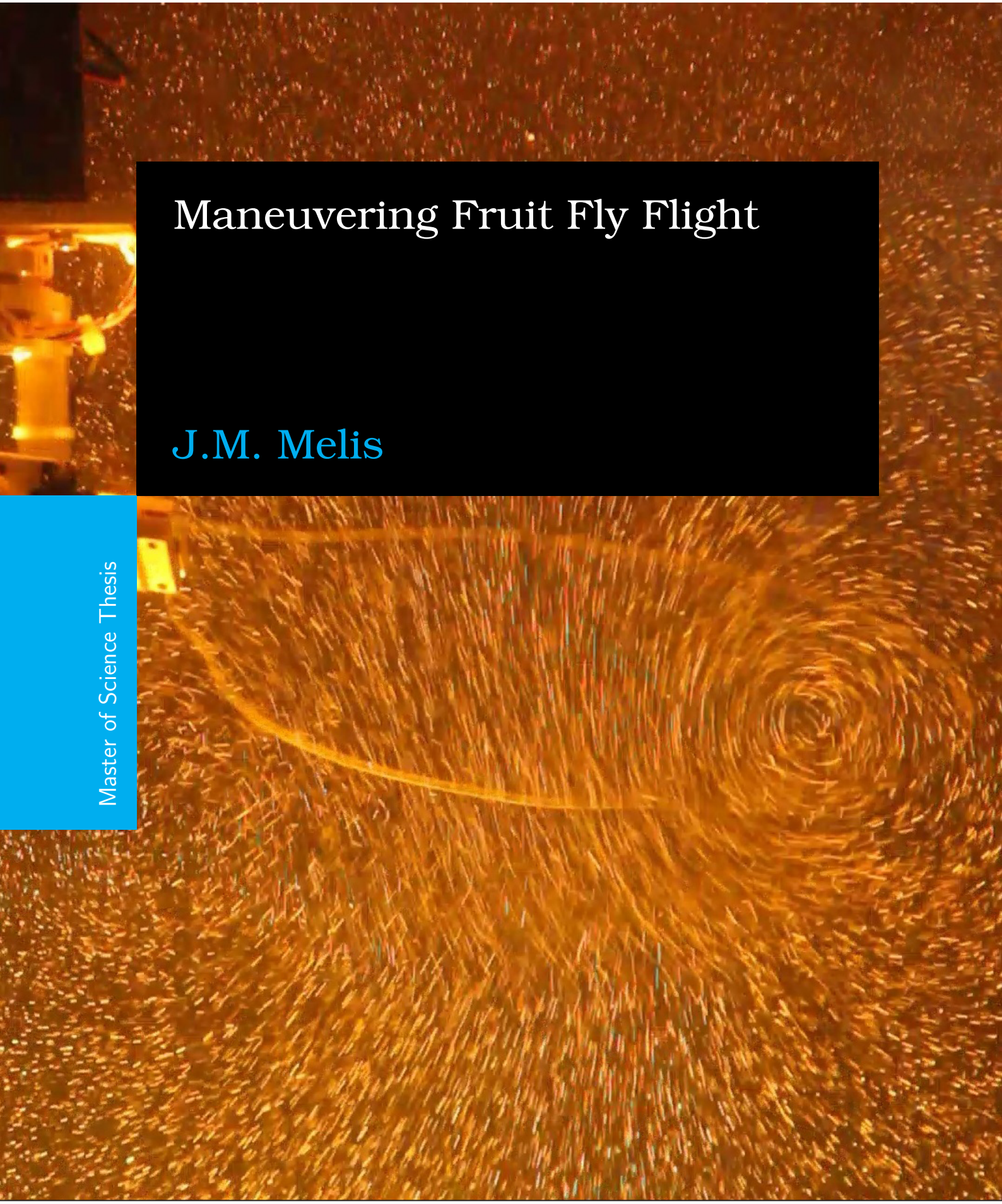

Maneuvering Fruit Fly Flight

J.M. Melis

Master of Science Thesis

Aerodynamics

Faculty of Aerospace Engineering

TU Delft

Delft University of Technology

Maneuvering Fruit Fly Flight

Master of Science Thesis

For obtaining the degree of Master of Science in Aerospace Engineering
at Delft University of Technology

J.M. Melis

January 22, 2014

Faculty of Aerospace Engineering · Delft University of Technology

Delft University of Technology

DELFT UNIVERSITY OF TECHNOLOGY
DEPARTMENT OF AERODYNAMICS

The undersigned hereby certify that they have read and recommend to the Faculty of Aerospace Engineering for acceptance the thesis entitled **"Maneuvering Fruit Fly Flight"** by **J.M. Melis** in fulfillment of the requirements for the degree of **Master of Science**.

Dated: January 22, 2014

Supervisors:

Dr. ir. B.W. van Oudheusden

Dr. ir. F.T. Muijres

Ir. B.D.W. Remes

MSc. M. Perçin

Preface

This rather voluminous report will be the capstone of the time I was a student at Delft University of Technology. During my study in Delft Ive had a great time for which I can blame my friends, the seven and a half year of studying aerospace were filled with numerous random crazy events which were above all much fun. I would like to thank my roommates for their wisdom and in-depth dinner conservations.

For the research of this thesis, I have spent ten months at the Dickinson lab at the University of Washington in Seattle. First of all, I would like to thank my supervisor Florian Muijres for providing me the opportunity to investigate such a fascinating subject and for the support and freedom I experienced during my graduation. I am also very grateful to my roommate and friend, Ambar, who made me feel at home in the US immediately at the day of my arrival. To my new friends in the US, I hope to catch up with you soon.

Finally I would like to express my gratitude to my parents for their reliance, patience and unconditional support which was of great value during my study.

Johan Melis
Delft, January 2014

Summary

The goal of the thesis was to establish and validate a model for maneuvering fruit fly flight. Fruit flies are capable of rapidly changing direction and accelerating away from a threat during so-called escape maneuvers. The maneuverability and control of these escape maneuvers are of interest for the development of small unmanned aircraft (Micro Aerial Vehicles) and for the field of neurobiology where the wing kinematic response of fruit flies on visual stimuli is heavily studied.

For the analysis of maneuvering flight the following methodologies have been used. The experimental data has been obtained from an experimental rig which is specially designed to trigger fruit flies performing escape maneuvers in front of three high-speed cameras. An automated flight tracking program reconstructs the orientation and position of the body and wings of the fly during the maneuver. The flight tracking results are inherently noisy and therefore a Kalman filter has been developed to remove the noise and to compute the derivatives of the position and orientation data. During the analysis it is necessary to parameterize the body and wing characteristics, which resulted in the definition of body and wing parameters as wing kinematic angles, the strokeplane and some aerodynamic and inertial characteristics of the specific fly. In order to compare all the wingbeats obtained from the high-speed video data, a uniform definition of a wingbeat is necessary. This uniform definition must be independent of variations in body and wing dimensions between flies and differences in wingbeat duration. Defining the wing kinematic angles by a polynomial fit using Legendre polynomials proved to be successful.

The methodologies described in the previous paragraph are sufficient to obtain a model of maneuvering flight. What remains is to determine the validity of the maneuvering flight model. Two techniques are used; dynamically scaled experiments and a dynamic simulation. In the dynamically scaled experiments the flow conditions generated by the wings of the fly are recreated on much larger robotic flapping wings. The robotic flapper is called the RoboFly and it can measure the aerodynamic forces and moments during a wingbeat. RoboFly experiments shows how well the predicted forces and moments of the maneuvering flight model actually represent the actual flow conditions. The second technique is the dynamic simulation; an aerodynamic model (quasi-steady aerodynamic model) and an inertial model in combination with the gravity forces are combined in an implicit Runge-Kutta scheme to compute the body motion due to the wing kinematics. The dynamic simulation can be used to compare the computed body motion and the actual body motion observed in the high-speed video

sequences.

The analysis of maneuvering fruit fly flight started with a qualitative analysis of the observed escape maneuvers. The focus of the qualitative analysis was on two extreme maneuvers: the roll maneuver and the pitch-up maneuver. The wing kinematics during these maneuvers were clearly distinguishable from the hovering flight wing kinematics and the wing kinematics could be linked to the body motion. The general escape strategy of the fly is to direct its strokeplane away from the looming threat which means that the thrust used for weight support is now fully dedicated for acceleration.

The maneuvering flight model was established by the regression of the difference in polynomial coefficients of maneuvering wingbeats and average wingbeats used for hovering flight and the associated non-dimensional forces and moments produced by the maneuvering wing kinematics under stationary body conditions. Using this regression the maneuvering flight model is independent of variations in body and wing dimensions between flies and the effects of aerodynamic and inertial damping. The maneuvering flight model is able to capture subtle wing motions whilst there is a significant scatter in the regression data. RoboFly experiments show that the predicted forces and moments by the maneuvering flight model are close to the produced forces and moments by the maneuvering wing kinematics, except for the pitch maneuvers. In case of pitching moments, the quasi-steady aerodynamic model overestimates the pitch moment. The maneuvering flight model uses the quasi-steady aerodynamic model and the wing kinematics for the pitch maneuvers are likely to be an underestimation of the actual wing kinematics.

The dynamic simulation model has been used to compute the body dynamics of hovering and maneuvering wingbeats. The body acceleration computed by the dynamic simulation compares well to the acceleration found in the video sequences. The body angular acceleration is however computed poorly by the dynamic simulation. There are several factors which make the dynamic simulation inaccurate, however the overestimation of the pitch moment by the quasi-steady aerodynamic model has definitely effects on the resultant moment vector. The dynamic simulation has been used to simulate the effects of aerodynamic and inertial damping. Aerodynamic and inertial damping are not strong enough to end fast rotations, a substantial counter-torque is needed to end a rotation. The effects of inertial damping are usually negligible, however for strong roll rates the effects of inertial damping can add up to 20%. The results of dynamic simulations are useful to study the trends in aerodynamic and inertial damping however for quantitative results the model needs to be improved.

The maneuvering wing kinematics resulting from the maneuvering flight model showed an important role of the so-called *downward plunge*. The downward plunge plays an important role during the roll maneuver and for the generation of forces perpendicular to the strokeplane. Flow visualization experiments on the RoboFly of the downward plunge used during a roll maneuver show that the downward plunge uses mainly wing drag to generate a force normal to the strokeplane. The flow visualizations suggest that added mass helps generating this drag force, a more detailed model of added mass in the aerodynamic and inertial model could reveal more about the role of added mass during the downward plunge.

Table of Contents

List of Figures

List of Tables

Part I

Introduction

Chapter 1

Motivation & Strategy

1.1 Motivation

For centuries mankind has tried to build aircraft inspired by bird flight. Large flapping wings were constructed in order to generate sufficient lift to take to the skies. In 1903, Orville Wright flew the first motorized heavier-than-air machine for 12 seconds. The *Wright Flyer* was an abstract and simple aircraft when compared to nature. The design of the aircraft was based on extensive analyses in a wind tunnel instead of copying the geometry of a bird's wing. The development of aircraft since that windy Thursday morning in 1903 went fast. Nowadays aircraft are very complex technical systems, while the design of aircraft has generally little resemblance to nature. However recently there is a renewed interest in flapping flight among aerospace engineers. Due to advances in electronics and battery capacity it is possible to miniaturize UAVs to so-called MAVs, ranging in span from 25 to 5 $[cm]$. These MAVs are especially useful for missions indoors, their limited size and good maneuverability are helping to stay within confined spaces. Bio-inspired flapping wing MAVs have proven to be very suited for indoor missions. Just as insects, flapping wing MAVs are able to hover and perform fast and controlled maneuvers. An example of such a MAV is the *RoboBee*, Fig. 1.1. Although the RoboBee is able to perform pitch, yaw and roll maneuvers, the speed of these maneuvers comes nowhere near the maneuverability of actual insects. A fruit fly for example can turn its flight direction with 90 degrees in less than an eye blink, Ref. [6]. These 90 degrees changes in direction are called saccades. Still little is known about how insects perform these maneuvers exactly.

The research phase of this thesis was performed at the Dickinson lab at the University of Washington in Seattle. The Dickinson Lab studies the neural and biomechanical basis of behavior in the fruit fly, *Drosophila*. The research in the Dickinson Lab is primarily focused on flight control of fruit flies. A rather complex set-up which is frequently used to study how the fruit flys sensory system, control system and motor-system cooperate is the so-called

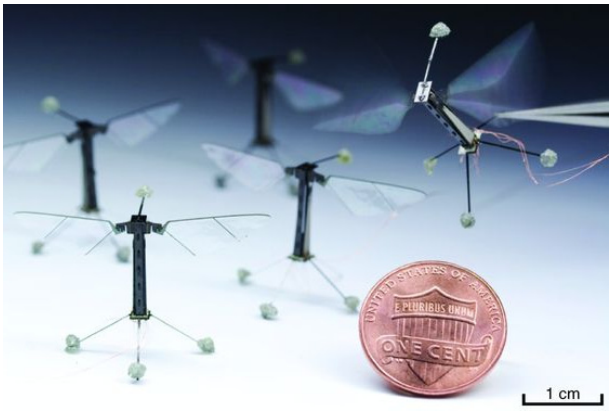

Figure 1.1: The RoboBee, Ref. [29].

electronic flight simulator. The electronic flight simulator is built around a tethered fruit fly which is looking at a screen consisting of Light Emitting Diodes (LEDs) which are used to display moving patterns, Fig. 1.2. The moving patterns can elicit flight behavior of the fruit fly, the resulting wing kinematics are captured by a sensor which transforms the position of the shadow of a wing on the sensor into a voltage. The shadow is cast by an Infra-Red (IR) LED and the sensor is called a wingbeat analyzer. The eliciting of flight behavior by moving patterns is based on optic flow. Optic flow can best be explained by the sense of velocity one will get whilst driving a car through a lane with trees on the side. The trees will basically emerge from a point distant on the road ahead and will expand from that point upon the time they pass the car as a blur. Optic flow can be used to elicit turning flight by rotating a pattern around the fly. The response of the fly is measured by the wingbeat analyzer as a difference in stroke amplitude between the left and right wing . The response of the fly can be coupled to the patterns on the LED screen such that the set-up becomes interactive. Whilst the fly is tethered it is possible to record and stimulate neurons in the brain and motor system. This makes the electronic flight simulator a very powerful tool to unravel the flight system of a fruit fly.

The electronic flight simulator does not simulate all flight conditions, the tethering of the fly constrains the body motion of the fly. The fruit fly has a special sensory system to detect angular velocities, the halteres. The hovering wing kinematics of flies are substantially different under tethered flight conditions than in free flight, Ref. [17]. The wingbeat analyzer simplifies the observed wing kinematics significantly by only taking the stroke amplitude into account. To be able to interpret the flight behavior performed in the electronic flight simulator better, a more detailed model of maneuvers in free flight is necessary. In literature there are a couple of papers of yaw maneuvers of fruit flies in free flight, Ref. [16] and Ref. [2]. However these papers are sometimes contradicting and based on less than a dozen observed yaw maneuvers. A large scale and structured study of maneuvering fruit fly flight could give more insight in the strengths and weaknesses of the electronic flight simulator. The subject of maneuvering fruit fly flight is not extensively described in literature. Therefore making a predefined detailed research plan is difficult and restricts the research to an approach of which the outcomes are uncertain. In order to provide necessary flexibility in the research approach, a research strategy is defined instead of a detailed plan.

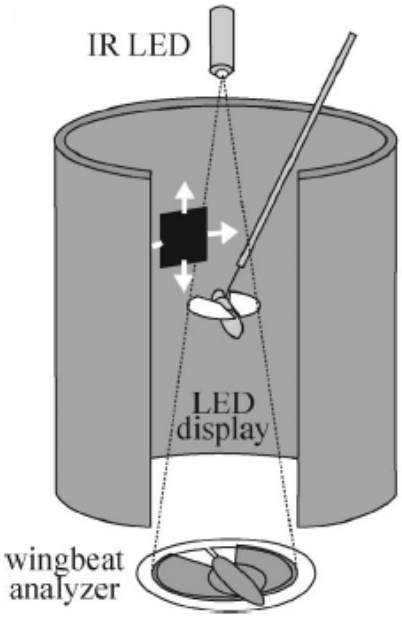

Figure 1.2: Lay-out electronic flight simulator, Ref. [8].

1.2 Strategy

Defining a strategy for the analysis of maneuvering fruit fly flight is difficult. As with most biological systems, a fruit fly is a highly complex system which means that there are generally no independent parameters of the system which can easily be implemented in a simple model. Another challenge in studying fruit fly flight is the large variation in body and wing size and shape between individuals. Research on hovering fruit fly flight shows that wing inertia, wing flexibility and the surrounding flow are highly interactive and form a complex dynamical system, Ref. [28]. Then there are several unsteady aerodynamic effects which are insignificant or uncommon for manned aircraft but play a leading role in lift and drag generation in fruit fly flight, Ref. [25]. The complexity of insect flight claimed several decades of research on insect aerodynamics before a satisfactory model of hovering flight was established. Although the current model of hovering fruit fly flight provides a sturdy basis, one cannot expect that the analysis of maneuvering fruit fly flight can follow a straightforward and preconceived research plan. Therefore instead of a research plan a research strategy was chosen, which offers more flexibility to tackle the problem.

The main objective of the thesis is:

> *Establish and validate a model of maneuvering fruit fly flight, linking wing kinematics to body dynamics and independent of variations in body and wing shapes and dimensions between individual fruit flies.*

In order to achieve this goal, just as it was the case with the aircraft of Wilbur and Orville Wright, an abstract and structured approach was chosen. The high-speed camera data is a rich source of information and allows for investigation of many aspects of insect flight. The approach of this thesis is a data-driven approach. Which means that the generation of the maneuvering flight model is closely linked to the data; the development of the model depends heavily on the data and is adaptable following new insights after progressive analysis of the data. Another aspect of the data-driven approach is to incorporate the complete dataset in the analysis. This does not mean that outliers cannot be removed from analysis, but the resulting maneuvering flight model must be applicable on the observed free flight maneuvers in the dataset as much as possible. In this way a robust maneuvering flight model can be established with a sturdy statistical basis. Using the data-driven approach the maneuvering flight model can be constructed in three steps.

- Create a uniform description of the wing kinematics and the body and wing parameters of the different flies. The goal of this uniform description is to exclude effects on the maneuvering flight model due to variations of parameters between individuals. The uniform description must allow for comparison of the wing kinematics obtained from different individuals and under different flight conditions.
- Characterize maneuvering flight and non-maneuvering flight and divide the wingbeats accordingly. Define a set of independent maneuver types and select the wingbeats performing these maneuver types. Develop a methodology to find the relation between the wing kinematics and the resulting body dynamics of a maneuver.
- Validate the established maneuvering flight model and investigate the underlying physics of the model. The validation of the maneuvering flight model can be based on two benchmark results. In the first place there are the filtered results from the video sequences. Secondly it is possible to recreate the flow conditions of the observed wing kinematics on a dynamically scaled model, the so-called *RoboFly* Fig. 1.3.

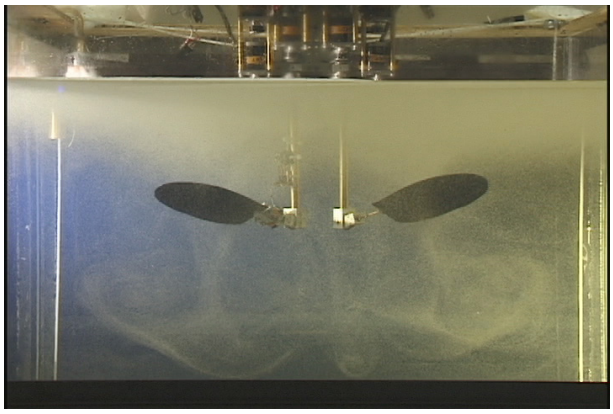

Figure 1.3: The RoboFly, Ref. [7].

Chapter 2

Literature Review

Insect flight differs in many aspects from conventional flight; the flow around the wing experiences strong linear and rotational accelerations, the aerodynamic forces on the wing are complex and unsteady and the wake influences the flow around the wing significantly. After this chapter it is assumed that the reader is familiar with the most important unsteady aerodynamic effects in insect flight and with the general lay-out of the wingbeat of a fruit fly. This short literature review gives a summary of the definitions of a wingbeat of a fruit fly and the unsteady aerodynamic effects which are important during the wingbeat of a fruit fly.

The Wingbeat of a Fruit Fly

Before focusing on the unsteady aerodynamic effects related to the acceleration and deceleration of the wing it is useful to present the accelerations encountered during a typical wingbeat of a fruit fly. The reciprocating motion during a wingbeat can be divided into two strokes; the downstroke and the upstroke. The downstroke is when the wing is moving from the dorsal side of the fly to the ventral side of the fly and the upstroke is the wing motion in opposite direction. Both strokes consist of a rapid acceleration of the wing at the start of the stroke and a rapid deceleration at the end of the stroke. At the end of a stroke the wing not only starts to change in direction of motion but also in orientation, the wing will rotate around its spanwise axis. The wing rotation phase in the wingbeat is called pronation when it happens at the dorsal side of the fly and supination for the ventral side of the fly. A hovering wingbeat of a fruit fly in free flight is depicted schematically in Fig. 2.1 in combination with a recap of the wingbeat terms.

The wing motion can be described with respect to the body using the wing kinematic angles. The wing kinematic angles are a set of three Euler angles which define the orientation of the wing with a reference frame. Usually this reference frame is the strokeplane reference frame; the strokeplane is the plane spanned by the supination point and the pronation point and is

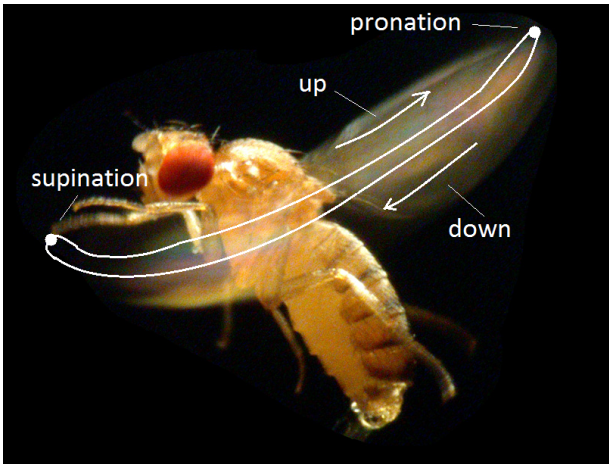

Figure 2.1: The downstroke, upstroke, point of pronation and point of supination in a wingbeat.

orthogonal to the body symmetry plane. The position of the projection of the wing in the strokeplane is given by the first Euler angle, the stroke angle. The angle between projection of the wing in the strokeplane and the actual wing is given by the deviation angle. Finally the rotation angle around the spanwise axis is given by the geometric angle of attack. An example of how the strokeplane and wing kinematic angles can be defined is given in Fig. 2.2.

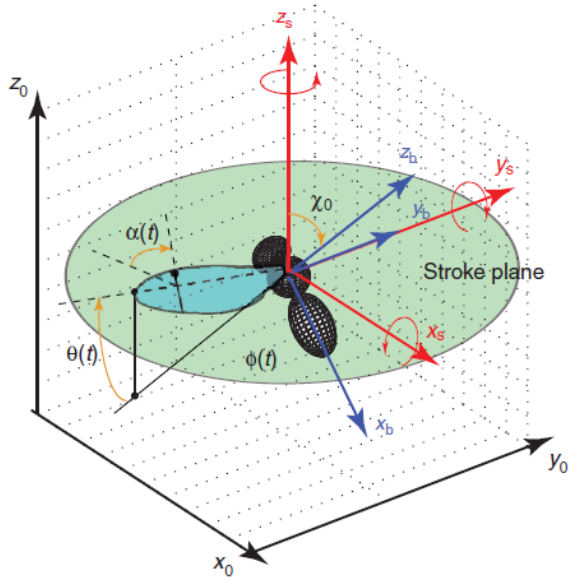

Figure 2.2: Definition of wing kinematic angles and the strokeplane according to Ref. [5]. The angle $\phi(t)$ is the stroke angle, $\theta(t)$ the deviation angle and $\alpha(t)$ the geometric angle of attack. The angle χ_0 defines the angle between the body reference frame and the strokeplane reference frame.

Unsteady Aerodynamic Effects

On the scale of insect flight effects which are insignificant in conventional aircraft aerodynamics become important whilst important parameters from aircraft aerodynamics become unimportant. For example, when looking closely at the cross-section of a fly wing one can see that the airfoil is everything but smooth, however due to the much stronger effects of viscosity at the scale of small insects, airfoil-shape seems to be of little importance, Ref. [9]. During the fast flapping motion of a fruit fly the air surrounding the wings is rapidly accelerated and decelerated, these kinds of flows are seldom encountered in aircraft aerodynamics and often negligible. These flow phenomena are commonly summarized in one single term; unsteady aerodynamic effects.

The Wagner Effect

Whenever an inclined airfoil is impulsively started from rest it will take some time before the circulation on the wing reaches its steady-state value. This is due to two phenomena which are jointly labeled as the Wagner effect, Ref. [25]. The first phenomenon is the delay in establishing the Kutta-condition. The Kutta-condition places the stagnation point of the flow leaving the airfoil on the sharp trailing edge (TE) of the airfoil. When an airfoil is impulsively started the Kutta-condition is not met immediately, it will take some time before the Kutta-condition is established and the circulation has reached its steady-state value. The second phenomenon is the influence of the starting vortex on the build-up of circulation. When an airfoil is impulsively started it will shed a starting vortex. The starting vortex has a circulation which opposes the circulation on the wing. The opposite circulation suppresses the circulation on the wing, as long as the wing is close to the starting vortex this opposing circulation will affect the build-up of circulation negatively, Fig. 2.3. As with every stroke in a wingbeat the wing accelerates and decelerates the Wagner effect will reduce the amount of produced lift. So the Wagner effect reduces the efficiency of flapping wings, however at the scale of fruit fly wings the viscosity is quite strong which limits the influence of the starting vortex. Experiments have shown that the Wagner effect is small for fruit fly flight, Ref. [25], and can be neglected.

Delayed Stall

When research on insect flight started it became soon clear that according to standard flow theory the steady-state lift values of the flat thin insect wings were not sufficient to provide weight support during hovering flight. The assumption was that a Leading-Edge Vortex (LEV) is responsible for increasing the lift coefficient of insect wings. It took however decades before this assumption was confirmed by smoke-visualization on a hawk moth, Ref. [13]. The LEV increases the lift in two ways; in the first place the vortex attached to the wing creates an area of low pressure on the upper side of the wing, secondly there is a mechanism called *delayed stall*. The low pressure area directly increases the normal force on the wing, the

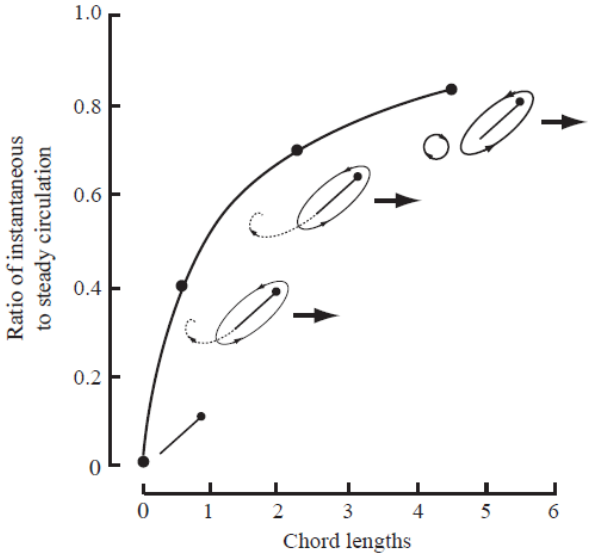

Figure 2.3: Relation between build-up in circulation and the distance travelled by the wing in combination with the formation and shedding of a starting vortex, Ref. [25].

delayed stall mechanism increases the lift indirect. A conventional aircraft airfoil can increase its lift production under a certain velocity by increasing the angle-of-attack. A higher angle-of-attack will lead to a higher lift coefficient, there is however a limit. For a certain angle-of-attack the flow is not able to stay attached to the wing resulting in flow separation or stall. When an airfoil stalls the lift will decrease whilst the drag increases significant, for a conventional airfoil this will happen for an angle of attack around 15 degrees. A LEV can delay stalling and therefore the angle of attack can be increased to the maximum obtainable lift coefficient, Fig. 2.4. The LEV on an insect wing is a consequence of the sharp LE of the wing. Due to the sharp LE the flow from the lower side of the wing is not able to follow the curvature of the wing and separates immediately. Under influence of the surrounding flow, the separated flow will slowly curve back to the airfoil, until it reattaches on the airfoil. At this point a stagnation point will emerge, the pocket of separated flow will form the LEV and the surrounding flow will flow towards the TE such that the Kutta condition is still satisfied. The LEV is often unstable, it turns out that the stability of the LEV is inherent to the dynamics of flapping flight as performed by insects and birds. A distinction must be made between linear flapping motion and rotational flapping motion; in the case of linear flapping motion the airfoil undergoes a reciprocating motion in a two-dimensional plane, the rotational flapping motion is similar to a swinging pendulum. During rotational flapping flight there are three accelerations acting on a fluid volume near the wing; angular, centripetal and Coriolis accelerations. These accelerations play a key-role in stabilizing the LEV, even when the LEV is unstable, the angular accelerations will keep the LEV. This happens during a so-called spiral-burst where the LEV grows significantly in size and the flow will become turbulent. In Fig. 2.5 a schematic overview of the LEV stability is given, the three axes are three non-dimensional parameters. The first parameter is the Reynolds number at the radius

of gyration:

$$Re_g = \frac{\rho \bar{U}_g c}{\mu},$$

in which ρ is the air density, $\bar{U}_g$ the air velocity at the radius of gyration, c the mean chord and μ the viscosity of air. The Reynolds number represents the ratio between inertial and viscosity effects. The second parameter is the dimensionless stroke amplitude:

$$A^* = \frac{A}{c},$$

in which A is the actual stroke amplitude. The dimensionless stroke amplitude represents the ratio between the amplitude of the wingtip and the average chord of the wing. Finally the Rossby number, linking the radius of rotation R to the wing chord:

$$Ro = \frac{R}{c}.$$

The Rossby number links the radius of rotation to the chord length linking the slenderness of the wing to the rotational velocity of the flapping wing. When $Ro = \infty$ there is no longer a rotational flapping motion, the wing will undergo a translational flapping motion. It turns out that the Rossby number is determining the stability, a Rossby number of order one will guarantee an attached LEV. The dimensionless stroke amplitude is important for the formation of a LEV under translational flapping motion. Surprisingly the Reynolds number does not affect the stability of the LEV, although it is important for the spiral-burst phenomenon. This means that the LEV is not confined to insect flight but is also available for birds and bats for example, with the only condition being flapping flight.

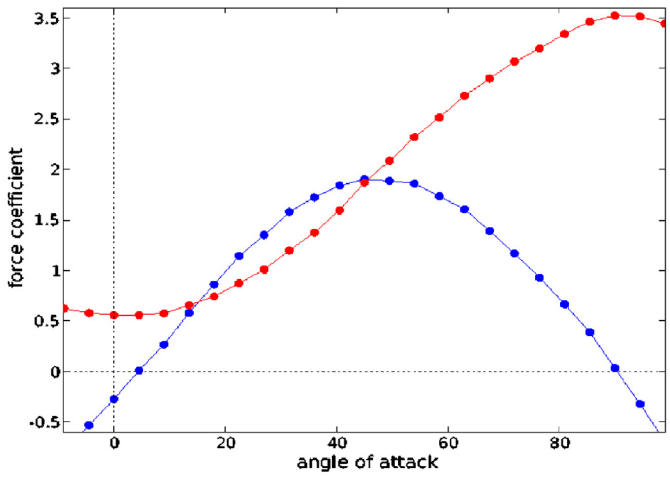

Figure 2.4: The lift- and drag-coefficients, blue and red respectively, versus the angle-of-attack for a fruit fly wing with LEV present, Ref. [11].

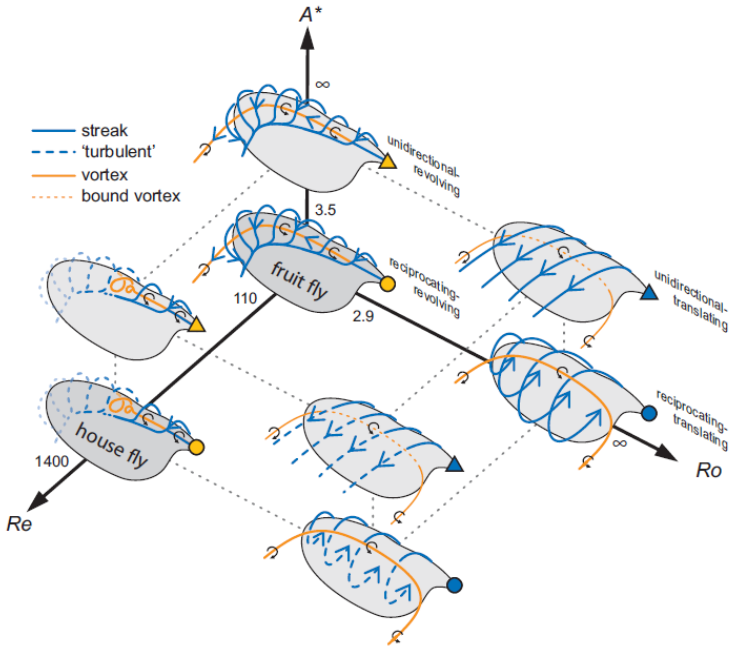

Figure 2.5: Schematic overview LEV stability and attachment for different Ro, Re and A^*, Ref. [21].

Rotational Lift

During stroke reversal the wing rotates rapidly around its axis. This rotation is a source of circulation which can generate a lift force, Ref. [10]. The aerodynamic mechanism which causes this force is called the Kramer effect. The effect shows much resemblance with the Magnus effect with the difference that the Magnus effect describes the lift force generated by rotating cylinders whilst the Kramer effect applies to rotating flat plates. In case of the Magnus effect, lift is generated by the fact that on one side of the cylinder the air is accelerated by the rotation of the cylinder, which means a decrease of pressure on that side of the cylinder. On the opposing side of the cylinder air is decelerated, which means that the pressure increases. This pressure difference causes a force which can have a positive or negative contribution to the lift force, depending on the direction of the air flow and the rotation direction. The Kramer effect works in a similar way, although the flow is more complex than for the cylinder. The difference is that the force is always normal to the wing surface for the Kramer effect. The rotational force can add to the lift generation on a flapping wing when the rotation of the wing is such that the angle-of-attack increases. The timing of wing rotation in a wingbeat is important, if wing rotation happens prior to stroke reversal it will have a positive effect on the lift generation, whilst the other way around will decrease the lift, Ref. [10]. The rotational force counter-acts the lift force when the angle-of-attack decreases. The effect can be described quite well by a formula for the rotational force acting on a blade-element in the quasi-steady model:

$$F_{rot} = C_{rot}\rho U\dot{\alpha}c^2\Delta R,$$

in which $\dot{\alpha}$ is the time derivative of the wing pitch angle, C_{rot} the rotational force coefficient ($C_{rot} = 1.55$) and ΔR the width of the blade-element.

Added Mass and Wake Capture

Besides the forces generated by translational and rotational motion there are also complex effects due to wing acceleration and deceleration and interaction between the wing and its wake. The effect of these forces are much smaller than the translational and rotational motion, however they can be dominant during stroke reversal. Added mass and wake capture are difficult to distinguish from each other and from the translational and rotational motion, as they are difficult to isolate from the other aerodynamic forces.

Added Mass

Whenever a wing accelerates or decelerates it will also accelerate or decelerate the air around the wing. The volume of air which is accelerated or decelerated depends on a lot of terms but viscosity and the translational and rotational circulation are significant. The acceleration and deceleration of the volume of air will exert a force on the wing. The added mass effect is usually modeled as a fixed volume of air around the wing and the mass of that volume. As it is very complicated to compute the volume, usually a fixed volume around the wing is chosen.

During a wingbeat the effects of added mass are the strongest at stroke reversal where the wing decelerates and subsequently accelerates. It is usually difficult to separate the translational and rotational circulation and the added mass force in experiments. When an inclined airfoil is impulsively started with a strong acceleration a peak in lift and drag force occurs, Fig. 2.6. This force peak is not present when the acceleration is low. The force peak is primarily due to added mass. During the wingbeat of a fruit fly, force peaks are present at the start of each stroke when the wing starts accelerating. In this case it is not clear whether the force peak is caused by added mass or wake capture, which will be explained in the next section. As the wing is moving in or close to the wake of the previous stroke wing-wake interactions can occur. Wake capture can also cause a force peak at the start of the stroke.

A 2D Compuational Fluid Dynamics (CFD) study of an accelerating NACA 0012 airfoil at a Reynolds number of $Re = 100$ shows how added mass can cause a peak at the start of a wing stroke, Ref. [19]. Fig. 2.7 shows the NACA 0012 airfoil accelerated from standstill to a velocity U within the non-dimensional time, $\tau = \frac{tU}{c}$ in which c is the chord of the airfoil. The airfoil has an angle of attack of $\alpha = 35\,^{\circ}$. Around the airfoil in Fig. 2.7 positive and negative vorticity layers are depicted. A negative vorticity layer is present around the LE and upper surface of the airfoil, at the lower surface of the airfoil a positive vorticity layer is present. The force exerted by a fluid on a solid body can be written in non-dimensional form as:

$$F^* = -\frac{d\gamma^*}{d\tau} + \frac{2}{c^2}\frac{d}{d\tau}\int_A V^* dA$$

in which $F^* = 2F/\rho U^2 c$, $\gamma^* = \gamma/Uc^2$ and $V^* = V/U$ where V is the velocity of a point

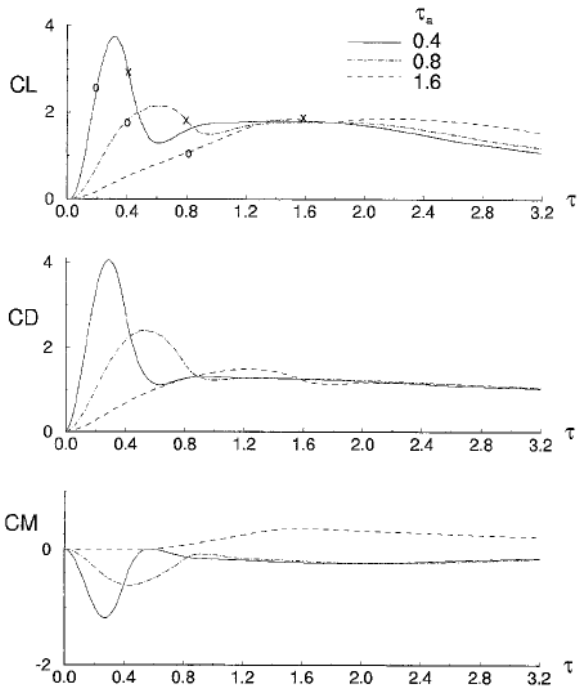

Figure 2.6: Force and moment coefficients vs. τ. The airfoil is accelerated from rest to U (Symbol 'o' denotes the maximum acceleration point, symbol 'x' the end of the acceleration), Ref. [19].

within A the section area of the airfoil. The total first moment of vorticity γ^* is the voriticity present in the flow and on the body. When the airfoil is accelerating the second term is small compared to the first term of the expression for F^*. The force peak at the start of an accelerating motion, Fig. 2.6, can be expressed as the time rate of change of the total moment of vorticity. For a fast acceleration the time rate of change of the total moment of vorticity is large whilst for a slow acceleration the gradient is small. When looking at Fig. 2.7 one can see that for the fast accelerating airfoil the amount of vorticity in the flow and the area of air encaptured by the vorticity is larger for the fast acceleration as for the slow acceleration. As the undisturbed flow has zero vorticity, the vorticity layers indicate the area of air which is influenced by the accelerating wing. The total first moment of vorticity can be used to model added mass forces. A detailed overview of vorticity distrubtions around an accelerating wing is difficult to obtain experimentally. Detailed three-dimensional CFD studies of the vorticity field around a flapping wing could help to establish an accurate model of added mass.

Wake Capture

Wake capture takes place during stroke reversal and is generally associated to the large peaks during the start of a stroke. At stroke reversal both the LEV and the Rotational Starting Vortex (RSV) are shed in the wake. The LEV and RSV have opposite vorticity and will generate a strong fluid jet in between them. When the wing motion stops and reverse direction, the wing will travel through this fluid jet. Depending on the orientation of the wing

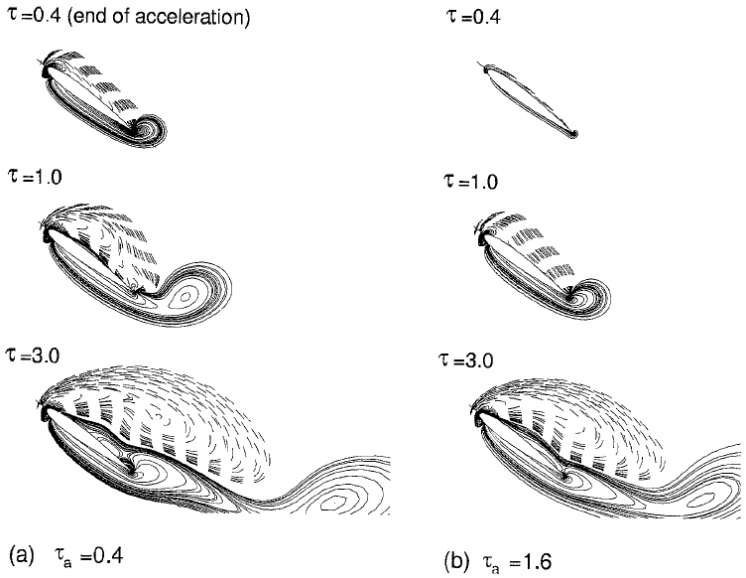

Figure 2.7: Vorticity plots at different times τ. In subplot (a) the airfoil is accelerated from standstill to U in $\tau = 0.4$. In subplot (b) the airfoil is accelerated from standstill to U in $\tau = 1.6$, Ref. [19].

the fluid velocity of the fluid jet will cause a negative or a positive lift force. In both cases there will also be a drag force. In Fig. 2.8 a flow visualization study of wake capture during a wing stroke is shown.

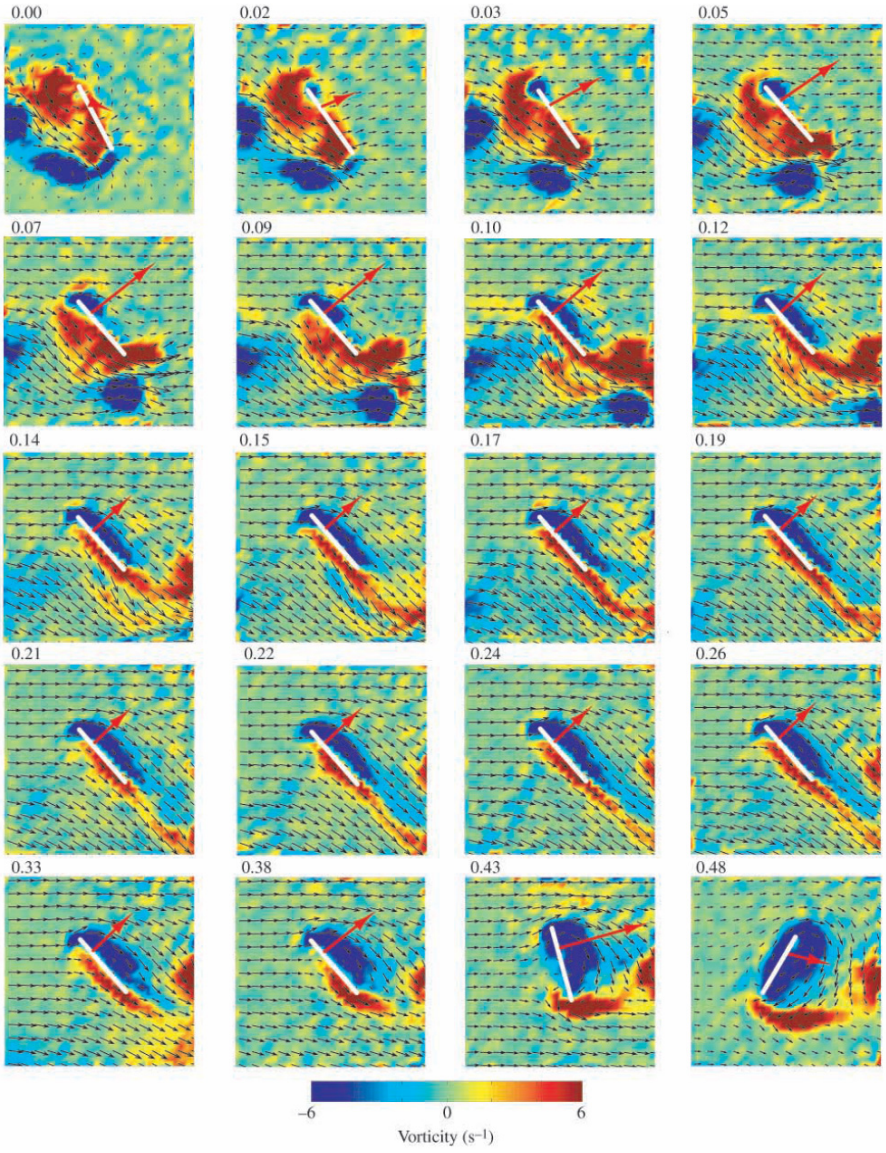

Figure 2.8: Flow visualization of wake capture at the start of a stroke. The velocity and vorticity field are both depicted in the figure and at the start of the stroke the fluid jet between the shedded LEV and RSV is visible, Ref. [3].

Part II

Methodologies

Chapter 3

Experimental Methods

The approach used in this thesis to study maneuvering fruit fly flight is based on a combination of experiments and simulations. The experimental methods used in this thesis were: high-speed videography of fruit flies in free flight and the measurement of aerodynamic forces and moments on the RoboFly. The experimental set-ups were already available at the Dickinson lab which means that the design and building of these set-ups were not a part of the thesis. Both set-ups are the result of the work of several researchers and years of fine-tuning; therefore the experimental set-ups are rather complex. In the subsequent chapters the high-speed videography data will be used to obtain a model of maneuvering flight. The RoboFly is used to recreate the flow conditions associated to a set of predefined wing kinematics, which allows for a comparison with the aerodynamic model used in this thesis and an investigation of the wake dynamics of maneuvering flight. Both experimental set-ups are of vital importance for the thesis, therefore a detailed description of the experimental methodologies will be given in this chapter.

3.1 High-Speed 3D Videography

High-speed 3D videography is the keystone in studying insect behavior in free flight as it is the most accurate and least intrusive method available. The high-speed cameras are integrated in an experimental rig which maximizes the chance that flies perform an escape maneuver in the focal volume of the cameras and on the other hand minimizes the disturbance of the fly's natural behavior, Fig. 3.1. The whole experimental environment can be divided into the experimental rig itself and the tracking software which derives the body and wing kinematics from the video images.

Experimental Set-up

Although saccades are often performed by flies in free flight it requires a lot of luck to catch such a saccade on camera. Therefore the experimental set-up is optimized to maximize the chance of a fly performing a saccade in the focal volume of the camera. This optimization is achieved by focusing on three different aspects of the set-up: the experimental animals, the eliciting of saccades and the high-speed cameras.

Experimental Animals

The choice for fruit flies as experimental animals might not seem logical. Most fruit flies have wings of just 2 mm in length and their flap frequency is around 200 Hz. Both the temporal as the spatial scales are very small and getting an accurate estimate of the weight of an individual is almost impossible. From this perspective another fly species like the much larger housefly would be more suited for the experiments. There are however three reasons why the fruit fly is the preferred choice.

The first reason has to do with the limitations of the cameras as there is a restricted volume in the field of view of the camera which is in focus. The bigger this so-called focal volume, the more distance is needed between the camera and the volume. The larger housefly has generally a much higher speed than the fruit fly which means that the focal volume has to be big in order to capture the whole maneuver. The distance could be shortened by using lenses; however these lenses would bring more distortion of the image. The experimental rig to study maneuvering houseflies would need to be significantly larger than the current one studying fruit flies. Another advantage of fruit flies is that they have a short life and are easy to breed. This means that there are sufficient numbers of flies available each day. By having many flies in the experimental rig, the chance that one of them performs a saccade inside the focal volume increases. Usually the rig contains around 50 flies. Most of the time these flies are resting or walking around in the rig but once in a while a few of them will take flight. The main reason however why fruit flies were selected has to do with biological research, especially research in the field of neuroscience. The fruit fly is a model organism in many fields of biology and many aspects of fruit flies have been thoroughly researched. For example the full genome of the fruit fly is mapped which has helped the development of genetic tools which can influence behavior and physical features of the flies. The Dickinson lab is focusing on the neural and biomechanical basis of behavior in the fruit fly. Better understanding of maneuvering flight would be very beneficial for the fields of neuroscience and biomechanics.

The specific species of fruit flies, *Drosophila*, which was chosen is the *Drosophila hydei*, both males and females. The *Drosophila hydei* was chosen because it is one of the largest *Drosophila* species with a wing length of about 3 mm, which made the tracking of the wings easier. The flies released in the experimental set-up were between one and five days old. The flies were deprived of food and water to increase activity. An experimental session usually runs from 9 h till 17 h each day. Flies are added every day to keep the number of flies in the rig roughly constant, at the end of the week all flies are replaced. During these 8 hours of experiments, usually between the 6 and 8 maneuvers are captured on camera.

Eliciting saccades

Besides the high-speed cameras, the experimental rig has a system which can trigger saccade maneuvers when the fruit fly is in the focal volume. The center of the rig is a transparent plastic cylinder with a height and diameter of 21 cm. This is a rather small volume such that the chance becomes bigger that the flies will fly through the focal volume. Yet it is still large enough for the flies to perform free flight. The average speeds of the flies in the rig are rather low, 20 cm/s in comparison to the cruise speed outdoors, which lies between the 1 and 1.5 m/s. It turns out that the saccade itself is not affected by the dimensions of the cylinder. The focal volume is in the center of the cylinder and the deceleration necessary to avoid the walls will happen outside of the focal volume. There are no indications that the flies restrict their acceleration at the start of the maneuver due to the confined space.

The saccade response of the fruit fly is elicited by an electronic simulation of a fast approaching object. The walls of the cylinder are surrounded by a wall of green LED panels on which patterns can be played at a frequency high enough to make sure the flies cannot observe flickering of the images, Fig. 3.1. The default state of the LED wall is a uniform green lighting. The simulation of a fast approaching object or the *looming stimulus*, is performed by switching the LEDs off such that a black expanding circle is displayed. This expansion happens quite quickly and has stopped long before the flies have processed the image and start with the escape response. The looming stimulus must be shown when the flies are within the focal volume. This is achieved by an infra-red (IR) cross-beam laser system, which can detect whether the fly flies through a sphere of 2 mm in diameter in the middle of the focal volume. The laser system works in the infra-red spectrum as the eyes of the fly are not able to perceive light in the IR-spectrum. Once the laser system is triggered, the looming stimulus will be displayed and a command is sent to the high-speed cameras to save the buffer of the continuously running cameras. The buffer contains a recording window of 372 ms before and 372 ms after the trigger time. In that way both the flight before the stimulus and the response are captured.

High-speed cameras

In order to be able to reconstruct the three-dimensional body and wing dynamics from video images of fruit flies in free flight a minimum of three synchronized high-speed cameras is necessary. This is exactly the amount of cameras used in the set-up, the cameras are placed on orthogonal angles w.r.t. each other such that there is a top-, front- and side- view. The focus of the three cameras is overlapping on one volume such that there is a focal volume of $20 \times 20 \times 20mm$. In order to make sure that all three cameras are in focus on this volume a calibration method has been developed, which is executed at the start of each experiment session. The calibration method also makes sure that the laser trigger is centered in the focal volume. The high-speed cameras are backlit by three arrays of IR LEDs. The camera recording frequency is 7500 Hz with a shutter speed of 1/30000 seconds and an image resolution of 1024 by 1024 pixels. Typically a captured wingbeat will consists of 35 to 40 frames. The IR LEDs are grouped in a 10 by 10 array, in front of each array an opaque diffuser is placed such that the background is more uniform. IR LEDs are chosen to provide sufficient lighting whilst not disturbing the flies. Backlighting with visible light would be very

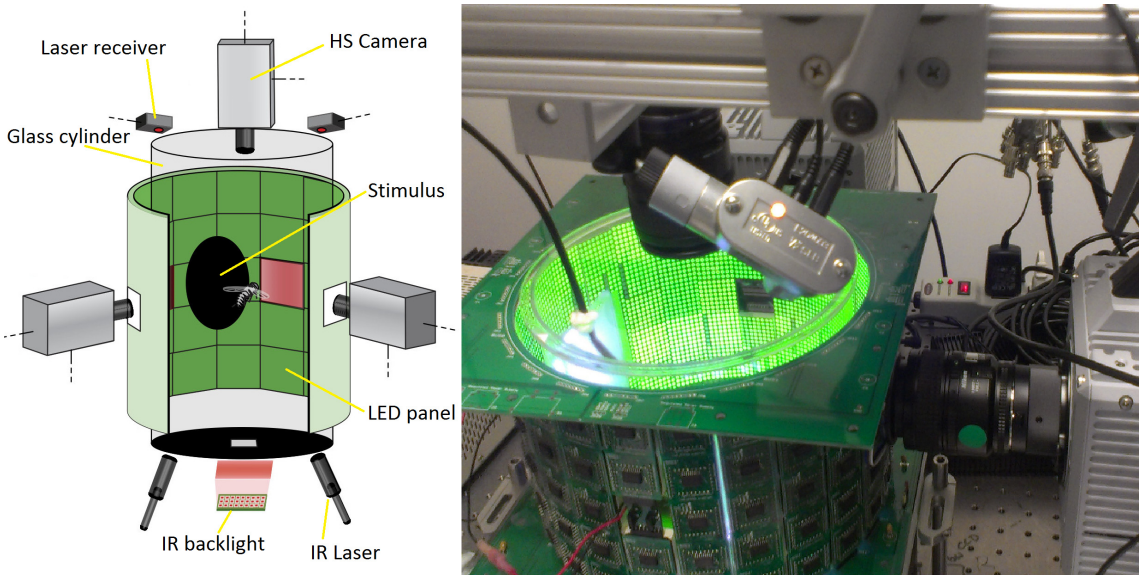

Figure 3.1: Schematic lay-out and picture of the experimental set-up.

intense such that the flies probably will avoid the focal volume. In order to reduce the heat production of the IR LEDs they are synchronized with the cameras by using a LED strobe controller. Still the heat production of the LEDs is quite severe such that the glass cylinder in which the LEDs are placed is cooled by blowing cold air over the walls of the cylinder. Using a thermometer as feedback system for the air conditioner keeps the temperature inside the cylinder between $24 - 27\,^{\circ}\mathrm{C}$.

Flight Tracking

The tracking system is a custom-build program which was the result of the PhD thesis of E.I. Fontaine, Ref. [15]. The tracking system uses model-based computer vision technique to establish a three-dimensional image out of the three simultaneous frames. Model-based computer vision uses a three-dimensional geometric model of the object which is present in the two-dimensional images in order to obtain the position and orientation of the object. The model-based technique is preferable as it is the most robust computer vision technique for the low lighting and the resolution of the movie frames. In this section the lay-out of the system will be described.

Foreground segmentation

The first step of the tracking procedure is background subtraction. This procedure subtracts the background pixels from the picture in order to capture the silhouette of the fly. The background is the diffusive panel backlit by the array of IR LEDs, the uniformity in intensity of the background allows for easy removal of the pixels belonging to the background. The area on the image containing the wings and legs is generally lighter than the body, which is used by the program to distinguish the body from the wings and legs. This procedure is called

foreground segmentation and the procedure will divide the pixels in two groups: body pixels and wing/leg pixels. The division in groups is done by fitting two Gaussians in the histogram of pixel intensities, Fig. 3.2. The Gaussians correspond to the difference in intensities of the wing/leg pixels and the body pixels measured over 200 images. Although the actual intensity distributions in an image are seldom two Gaussians, this fitting procedure is still quite robust.

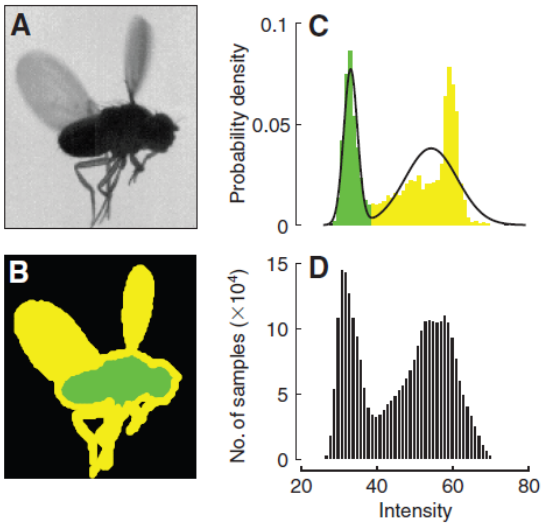

Figure 3.2: A: raw image. B: background subtraction and foreground segmentation. C: Density vs. intensity of body pixels and wing/leg pixels. D: Density distribution vs. intensity over 200 images. Ref. [15].

Model-based image tracking

The model-based image tracking is a procedure in which a three-dimensional model, in this case a geometric fruit fly model, is positioned and oriented such that the two-dimensional top-, front- and side-views of the model have the best fit with the actual movie frames. The model-based image tracking starts with a manual tracking procedure in which the initial state of the position and orientation of the body and the wings is determined. The manual tracking procedure is also used to determine the specific physical features of the individual fruit fly in the movie sequence. For example the actual shape of the body and wing is determined in this manual tracking, as well as the locations of the wing joints and the body axis. The standard geometric fruit fly model is updated after the procedure by altering the b-splines of the model After the manual tracking the automatic tracking procedure will use the initial state and updated geometric model to keep track of the body and wings. The model-based image tracking is not a fast method and without a good initial guess of the position and orientation of the body and wings the procedure may never find a solution. The initial guess is provided by a Sigma Point Kalman filter (SKF) which uses the previous state and a model of the dynamics of the fruit fly to estimate the state of the body and wings in the next frame. The model of the dynamics of the fruit fly is based on a database of already tracked wingbeats. At the start of the project the database consisted only of well-tracked wingbeats

which were manually tracked, later on in the project the database was extended with well-tracked wingbeats obtained from the automatic image tracking. Once the initial guess is provided by the SKF an iterative method will establish the best fit to the image frames.

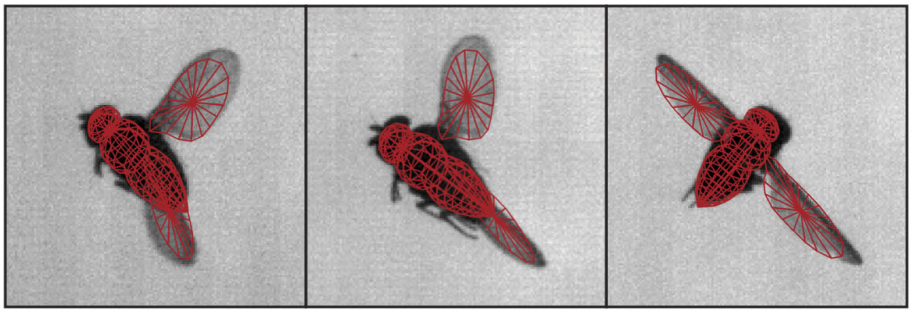

Figure 3.3: Typical model fitting to the three synchronized views.

Tracking performance

As a part of the validation of the tracking program, a comparison has been made between the program and a more elaborate semi-automated method to determine the wing kinematics from the study of Card and Dickinson, Ref. [4]. This comparison is not perfect, as also the method of Card and Dickinson cannot always derive the exact orientations and positions, however the comparison study can provide a qualitative analysis of the performance of the tracker. Using the video sequences of the study of Card and Dickinson, the following weaknesses were discovered. It turned out that both methods had severe difficulties in estimating the roll angle of the body. Due to the fact that the body is nearly rotationally symmetric, the roll angle has to be determined by the orientation of the wing joints. As these wing joints are not easy to distinguish, the roll angle can vary a lot between two subsequent frames. In the automated tracking program the roll angle is determined by assuming wing symmetry, Fig. 3.4. The solution enhances assuming a symmetric wingbeat w.r.t. the flys symmetry plane and rolling the body if the orientation of the body differs from this condition. Generally the symmetry assumption holds, however one must be cautious regarding the body roll angle. During the tracking of a movie sequence it might happen that the tracker will not be able to follow one or both of the wings. Once this occurs, the orientation of the wings and the body might be anything. The position of the body is rather easy to track, however the orientation of the body also depends on the wings hence its orientation might be a different story. Often when the tracker loses track of one wing it might capture that wing again one wingbeat later. Points where the tracker often loses track are; when the wings are in front or behind the body in one image, during stroke reversal where rotational velocities of the wings are high and during maneuvers in which the wingbeat will deviate from the wingbeats in the model database. When analyzing the tracked wingbeats one must be cautious to check whether the wings were properly tracked.

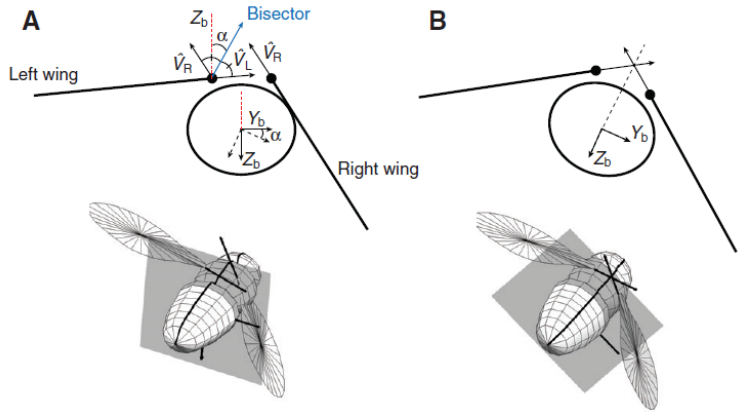

Figure 3.4: A: Body roll angle before wing symmetry correction. B: Body roll angle after correction, Ref. [15].

3.2 The RoboFly

Reproducing and measuring the flow characteristics generated by a certain set of wing kinematics at the actual size and wingbeat frequency of a fruit fly is practically impossible. By applying dynamic scaling the flow characteristics can be reproduced at a more convenient spatial and temporal scale. The dynamic scaling is achieved by keeping the ratio between inertial and viscous forces, or the Reynolds number, the same. The Reynolds number of flapping flight is defined as:

$$Re_{fly} = \frac{n_{fly} \cdot R_{fly}^2}{\nu_{air}},$$

where n_{fly} is the frequency of the wingbeat, R_{fly} the wing length and ν_{air} the kinematic viscosity of the air. The Reynolds number of the dynamically scaled model has the same definition:

$$Re_{robo} = \frac{n_{robo} \cdot R_{robo}^2}{\nu_{oil}},$$

but now the kinematic viscosity of the air is changed for the kinematic viscosity of the test fluid, which is mineral oil. A higher kinematic viscosity allows a slower wingbeat frequency and larger wing length to be applied. The wing length of the RoboFly is 230 mm and the kinematic viscosity of the mineral oil is $\nu_{oil} = 115 \cdot 10^{-6}\left[m^2/s\right]$ at 25 °C, Ref. [16]. The average wing length of the *Drosophila hydei* is 3 mm and the average wingbeat frequency is 189 Hz. The kinematic viscosity of air is $\nu_{air} = 15.7 \cdot 10^{-6}\left[m^2/s\right]$ at 25 °C, now all parameters necessary to compute the flap frequency at which the RoboFly needs to operate are there:

$$\frac{n_{robo}}{n_{fly}} = \left(\frac{\nu_{oil}}{\nu_{air}}\right)\left(\frac{R_{fly}}{R_{robo}}\right)^2\left(\frac{\hat{r}_2^2\,(S)_{robo}}{\hat{r}_2^2\,(S)_{fly}}\right).$$

Using this formula the flap frequency turns out to be 0.26 Hz. The values for $\hat{r}_2^2\,(S)_{robo}$ and $\hat{r}_2^2\,(S)_{fly}$ are 0.35 and 0.40 respectively. The two terms represent the normalized second

moment of wing area and are used to scale the effect of a small notch at the base of the robotic wing. The aerodynamic forces generated in flapping flight scale with $\rho R^2 U^2$ as the area of the wing scales with the wing length. The velocity of the wing scales with the wingbeat frequency and the wing length, $U = n \cdot R$. So the ratio of forces can be defined as:

$$\frac{F_{robo}}{F_{fly}} = \left(\frac{\rho_{oil}}{\rho_{air}}\right)\left(\frac{\nu_{oil}}{\nu_{air}}\right)^2 \left(\frac{\hat{r}_2^2\,(S)_{robo}}{\hat{r}_2^2\,(S)_{fly}}\right) \approx 3.5 \cdot 10^4.$$

in which the density of the mineral oil is $0.88 \cdot 10^3\ kg \cdot m^{-3}$ at 25 °C and the density of the air $1.18\ kg \cdot m^{-3}$ at 25 °C in the experimental set-up.

The hardware is designed such that the stroke angle (ϕ), the deviation angle from the stroke-plane (θ) and the rotation angle of the wing (η) can be controlled independently on both wings. The definition of the wing kinematic angles is comparable to Fig. 2.2. The stroke position of each wing is controlled by a stepper motor, whilst the deviation angle and rotation angle are controlled by digital servo motors. The stroke axes of the two wings are parallel and separated by 0.11 m. The wing motor assemblies are attached to a base plate and the base plate is attached to a frame outside the tank of the RoboFly which makes sure that the RoboFly is immovable. Between the base plate and the frame there are force and torque sensors which can measure the force and moment generation of the RoboFly in 6 degrees of freedom, the lay-out is shown in Fig. 3.5. The tank around the RoboFly, filled with mineral oil, has dimensions of $1 \times 2.4 \times 1.2$ m. These dimensions are sufficient to make sure that the walls will not influence the flow around the RoboFly.

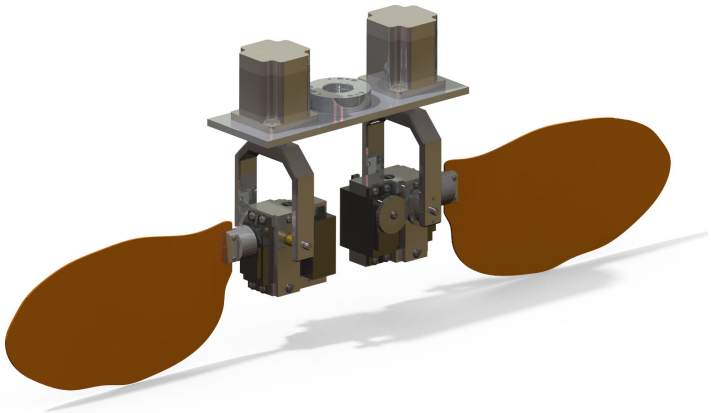

Figure 3.5: Flapping wing system RoboFly.

Chapter 4

Body & Wing Model

One of the most challenging aspects of biological research is creating a simplified model of the biological system whilst still capturing all relevant parameters. The complexity of even a small creature like a fruit fly is so large that for example after decades of research there is still not a complete model of how the flight-muscles actuate the wings. In this chapter a simple model of the aerodynamic and inertial aspects of fruit fly flight will be established. Subsequently a definition of the wing kinematics will be given in combination with its relation to the description of the body and wing orientation. The conventions defined in this chapter will be used throughout the thesis.

4.1 Geometric Model

The geometric model used by the model-based image tracking of Chapter 3, will be used for the estimation of aerodynamic and inertial parameters. As the geometric model of the flight tracker is fitted to the images of the fruit fly, it will be unique for every fly. Using the geometric model all, fly specific aerodynamic and inertial parameters can be found.

Fly Model

The fly model consists of three rigid body parts, being the body, the left wing and the right wing. The wings are connected to the body by ball joints, giving the wings three Degrees Of Freedom (DOF) w.r.t. the body. The rigid body assumption is not true to nature, especially considering the wings. During flight the wings deform considerably due to aerodynamic and inertial forces and these deformations are affecting the lift and drag force on the wing. Although wing flexibility is not negligible it cannot be included in the tracking procedure as the amount of possible model configurations would make it impossible to use the tracking

program. The body can also deform as the body consists of three parts; the head, the thorax and the abdomen, which are able to rotate with respect to each other. These rotations are however rather small and for simplicity the body as a whole is considered to be rigid. During the fitting procedure of the tracking program, all the individual parts consisting of b-splines are scaled to the best fit in the three orthogonal images. In order to obtain the actual dimensions of the fly, the image is corrected for lens distortion. This makes sure that the size and shape of the resulting model resembles the actual dimensions. Fig. 3.3 shows a typical fly model obtained from the tracking program and an actual fruit fly, one can see that the wings and the different body parts correspond to a reasonable degree. The fit of the fly model to the images is not always perfect but usually important modeling parameters like the wing length, wing area and body volume are captured rather well such that the fitted fly model gives good fly specific parameters.

With the wings and body scaled and shaped to the individual fly in the video sequence there is only one thing remaining; the determination of the position of the wing joints. During the manual tracking procedure at the start of the video sequences the positions of the joints are tracked. Now the positions of the joints are known the model is geometrically defined, however in order to be able to track the position and orientation of the fly one needs reference points. The first reference point is on the body and corresponds to the body center of gravity (c.g.). This point is estimated on the scale of the body. The c.g. is positioned at the longitudinal axis of the body within the abdomen at a distance of 40% of the body length, measured from the tail. At the c.g. of the body, the origin of the so-called body reference frame is placed. In Fig. 4.1 the body reference frame is shown, in combination with the reference frames of the left and right wings. In the next paragraph the position and orientation of the three reference frames w.r.t. the fly will be given.

The x-axis of the body reference frame aligns with the body longitudinal axis and is positive when pointing to the head of the fly. The y-axis is parallel to the vector running from the left wing joint to the right wing joint. The z-axis is pointing to the ventral side of the fruit fly. When the fly is in hovering flight the z-axis is partly pointing downwards with respect to the inertial reference frame. This might seem a bit counter intuitive as the gravity vector is a positive force in the body reference frame. However this definition of the reference frame is called the aerodynamic reference frame and is useful especially in the aerodynamic analysis when for example the angle of attack needs to be defined. The reference frames of the wings are also aerodynamic reference frames. The reference frame of the left wing has its origin at the left wing joint. The x-axis of the left wing reference frame is parallel to a chord section of the left wing and is defined positive when pointing towards the leading edge of the wing. The y-axis is aligned with the line between the wing joint and the wing tip, for the wing model this line is exactly orthogonal to the x and z axis of the fly reference frame. The y-axis is defined positive when pointing away from the left wingtip for the left wing, for the right wing the y-axis must be pointing towards the right wingtip to be positive. Finally the z-axis of the reference frames of the left and right wing must orthogonal on the x-axis and y-axis according to the definitions of a right-hand reference frame.

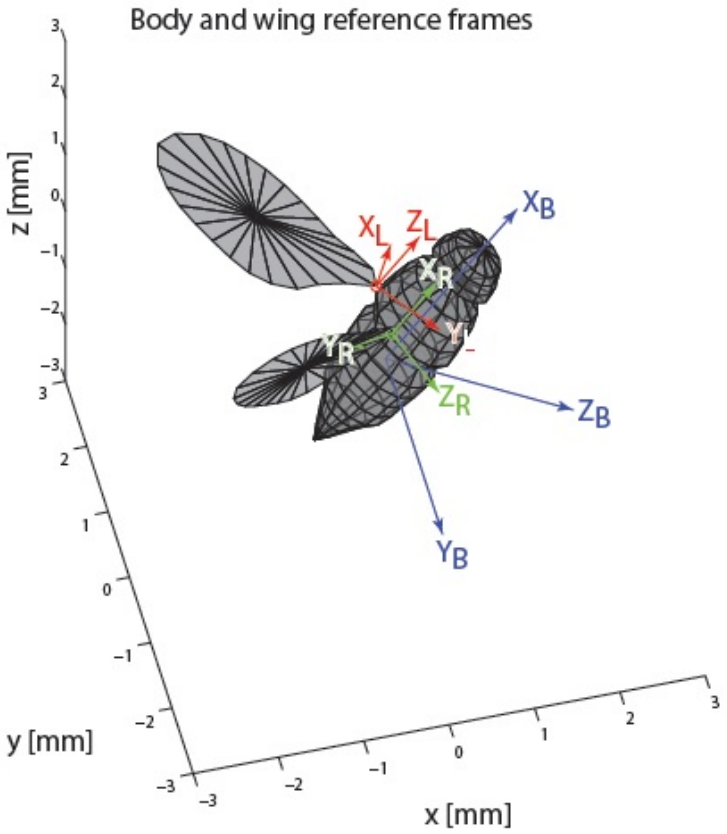

Figure 4.1: The fly model including the body reference frame (blue), left wing reference frame (red) and right wing reference frame (green).

Fly Mass

Knowing the mass of a fruit fly in flight is not a sinecure. The mass of a fruit fly is rather low, in case of the *Drosophila Hydei* on average $1.85 \cdot 10^{-6}$ $[kg]$. As a consequence of the small weight, the evaporation of body fluids can influence the mass significantly. It would be a rather tedious procedure to weigh each fly before the experiment and to identify each fly in the movie sequence. To obtain an estimate of the weight of a fly in a movie sequence, a different approach has been taken. It has been established that a fly's mass scales with its wing length, to be precise with the third power of the wing length. This relation is based on regression data of body mass and wing length for the *Drosophila Melanogaster* which is present at the Dickinson lab. By weighing 20 flies and establishing an average mass, the mass of a *Drosophila Hydei* is linked to the wing kinematics by:

$$m_{fly} = 1.85 \cdot 10^{-6} \left(\frac{L_w}{L_{w\ avg}} \right)^3 .$$

In which m_{fly} is in kg, L_w is the wing length in mm and $L_{w\ avg}$ is the average wing length of the *Drosophila Hydei* being 3.0 mm.

Wing Mass and Virtual Wing Mass

Considering the difficulties measuring a fly's mass as a whole, one can imagine what it would take to measure the mass of a single wing. Therefore also the wing weight is estimated based on the fly's dimensions. By using a relation established by C.P. Ellington, Ref. [14], the mass of the wing can be linked to the wing area:

$$m_w = L_w \cdot A_w \cdot \rho_{cuticle} \cdot h_w,$$

in which m_w is the wing mass in kg, A_w the wing area in mm^2, $\rho_{cuticle}$ the average $2D$ density of the wing in $(1200kg \cdot mm^{-2})$ and h_w the non-dimensional wing thickness being a constant with a value of $5.4 \cdot 10^{-4}$. In this way both the fly's mass as the wing mass are linked to the dimensions of the wing. The body mass can be obtained by subtracting the mass of both wings from the fly's mass. The mass of the wing is very low compared to the body, on average a single wing weighs only 0.28% of the flys total mass. It would however be a mistake to ignore the wing mass as due to the high angular velocities of the wing, inertial effects can be substantial even with a very light wing.

The story does not end after determining the wing mass, even with a very accurate wing mass the inertial effects would be underestimated significantly when neglecting the virtual wing mass. The virtual wing mass is the weight of the air which is accelerated and decelerated with the wing. The virtual wing mass represents the force on the wing due to added mass. One could argue that the added mass effects must be incorporated in the aerodynamic model and not in the inertia model by introducing the term of virtual mass. However modeling added mass effects accurately is quite complicated and computationally heavy whilst adding the virtual mass to the inertial model gives a reasonable estimate of added mass effects. The aerodynamic model of this thesis will not model added mass and as compensation the virtual mass is included in the inertial model. The size and the shape of the volume varies during the wingbeat, C.P. Ellington, Ref. [14], assumes a constant cylindrical volume of air around the contour of the wing which roughly corresponds average value of the virtual mass during a wingbeat. The volume of air used to establish the virtual wing weight is shown in Fig. 4.2. The virtual wing weight is added to the actual weight of the wing in the inertial model. The virtual mass adds roughly 50% to the wing mass.

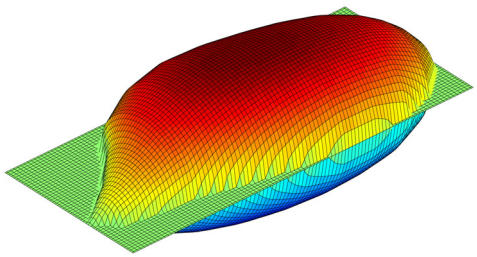

Figure 4.2: The volume of air forming the virtual wing.

Inertia and Virtual Inertia

Using the mass and polygonal model of the body and wing, the inertia tensors of the body and wings can be obtained. In case of the body first the volume of the polygonal model of the body is determined. By dividing the volume by the mass of the body, a uniform body density is obtained. The next step is dividing the body into segments along the x-axis. Each segment is a disk and the mass of each cylinder is obtained from its volume multiplied by the body density. Using the segments the actual center of gravity of the body can be obtained. Note that the c.g. of the tracking program is just a reference point and does not necessarily correspond to the actual c.g. of the fly. The segments can also be used to obtain the inertia tensor, the inertia tensor is defined as:

$$I_{seg} = \begin{bmatrix} I_{xx} & -I_{xy} & -I_{xz} \\ -I_{yx} & I_{yy} & -I_{yz} \\ -I_{zx} & -I_{zy} & I_{zz} \end{bmatrix},$$

with:

$$\begin{aligned} I_{xx} &= \bar{I}_{xx} + \left(y^2 + z^2\right) m_{seg}, \\ I_{yy} &= \bar{I}_{yy} + \left(x^2 + z^2\right) m_{seg}, \\ I_{zz} &= I_{zz} + \left(x^2 + y^2\right) m_{seg}, \\ I_{xy} &= I_{yx} = \bar{I}_{xy} + xy\ m_{seg}, \\ I_{xz} &= I_{zx} = \bar{I}_{xz} + xz\ m_{seg}, \\ I_{yz} &= I_{zy} = \bar{I}_{yz} + yz\ m_{seg}. \end{aligned}$$

Where $\bar{I}$ is the local inertia tensor centered around the c.g. of the segment and m_{seg} is the mass of the segment. The distances x, y and z are the distances between the c.g. of the segment and the c.g. of the body in the body reference frame. The local inertia tensor of a single segment is modeled as the inertia of a disc:

$$\bar{I} = \begin{bmatrix} \frac{1}{2} m_{seg} r^2 & 0 & 0 \\ 0 & \frac{1}{12} m_{seg} \left(3r^2 + \Delta x^2\right) & 0 \\ 0 & 0 & \frac{1}{12} m_{seg} \left(3r^2 + \Delta x^2\right) \end{bmatrix},$$

in which r is the radius of the disc and Δx the height of the disc. Adding up the all the inertia tensors of the segments yields the total inertia tensor of the body, a typical result of the body inertia tensor is:

$$I_{body} = \begin{bmatrix} 0.0280 & 0 & 0 \\ 0 & 0.1102 & 0 \\ 0 & 0 & 0.1102 \end{bmatrix} \cdot 10^{-5} \left[kg\ mm^2\right],$$

For the wing inertia a slightly different approach has been taken. The wing does not have any symmetry planes and therefore a more general approach is taken. The wing is rasterized by a grid in x and y direction, Fig. 4.3, and each cell will be checked whether it lies within the wing contour. Each cell within the wing contour gets a mass related to the area of the cell and the wing's inertia tensor is computed in a similar way as the body inertia. The only difference is that the local inertia tensor of each cell is assumed to be zero, which is justified

as the grid is sufficiently fine. A typical wing inertia tensor is shown below:

$$I_w = \begin{bmatrix} 0.2592 & -0.0123 & 0 \\ -0.0123 & 0.0502 & 0 \\ 0 & 0 & 0.3094 \end{bmatrix} \cdot 10^{-8} \left[kg\ mm^2\right],$$

In order to include the virtual mass effect in the inertia model, also the inertia of the volume of air around the wing must be taken into account. To achieve this, first the center of gravity of the wing + virtual mass must be obtained. This is done by the computation of the c.g. of the wing without virtual mass and the c.g. of the virtual mass without the wing and subsequently determining the position of the c.g. of the wing including virtual mass by using both previously determined points. Just as in the case of the wing without virtual mass, the space around the wing is rasterized. Only now the grid has also an extent in the z direction, the resulting volume of grid elements is shown in Fig. 4.2. The inertia tensor of the virtual mass in combination with the wing inertia tensor (adjusted to the new found c.g. for the wing including virtual mass) forms the wings virtual inertia tensor. The entries of the virtual wing inertia tensor are on average 50% larger than the wing inertia tensor without virtual mass. The virtual inertia tensor of the previously shown wing inertia tensor is:

$$I_{vw} = \begin{bmatrix} 0.3748 & -0.0193 & 0 \\ -0.0193 & 0.0889 & 0 \\ 0 & 0 & 0.4260 \end{bmatrix} \cdot 10^{-8} \left[kg\ mm^2\right],$$

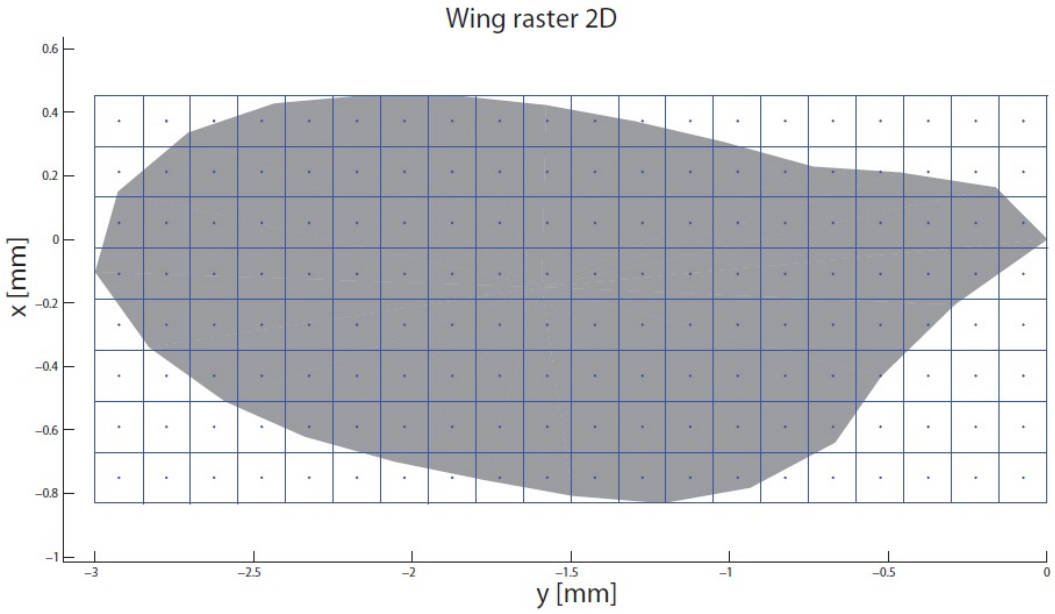

Figure 4.3: Raster placed on wing for inertia computations.

4.2 Quaternions and Rotation Matrices

The orientations of the reference frames of the body and wings w.r.t. each other and the inertial reference frame are given in quaternions. Quaternions are used as they are uniquely defined for every possible orientation, which is required as fruit flies are very maneuverable and can even fly upside down. However before considering the subject of quaternions, first a short introduction will be given to Euler angles. This is because an Euler sequence is a more intuitive way to define an orientation and also the wing kinematic angles are Euler angles. As an example of the way Euler angles work, the Tait-Bryan convention will be given. In the Tait-Bryan convention an aerodynamic reference frame is rotated from its start position to its final position by a yaw rotation ψ around the z-axis of the aerodynamic reference frame, followed by a pitch rotation θ around the y-axis of the rotated system and finally a roll rotation ϕ around the x-axis of the rotated system, Ref. [20]. In order to transform a vector in one reference frame to a vector defined w.r.t. another reference frame a rotation matrix is used. The rotation matrix of the Tait-Bryan transformation can be defined as:

$$R_{TB} = \begin{bmatrix} 1 & 0 & 0 \\ 0 & cos\,(\phi) & -sin\,(\phi) \\ 0 & sin\,(\phi) & cos\,(\phi) \end{bmatrix} \cdot \begin{bmatrix} cos\,(\theta) & 0 & sin\,(\theta) \\ 0 & 1 & 0 \\ -sin\,(\theta) & 0 & cos\,(\theta) \end{bmatrix} \cdot \begin{bmatrix} cos\,(\psi) & -sin\,(\psi) & 0 \\ sin\,(\psi) & cos\,(\psi) & 0 \\ 0 & 0 & 1 \end{bmatrix}.$$

The rotation matrix R_{TB} converts a vector in the inertial reference frame to the aerodynamic reference frame. By taking the transpose of the rotation matrix the vector can be transferred back to the inertial reference frame. A disadvantage of Euler angles in general is that certain orientations do not relate to a unique set of Euler angles. For example when using a pitch rotation of $90\,^{\circ}$ there are numerous combinations of roll and yaw which yield the same orientation. In order to have a unique description of every possible orientation quaternions are used. Quaternions define an orientation by defining an axis of rotation, the so-called Euler axis, by a unit vector $\mathbf{e}$ and performing a single rotation around this reference frame θ. The quaternion is derived from the Euler formula and consists of four identities:

$$\mathbf{q} = \begin{bmatrix} sin\left(\frac{\theta}{2}\right) e_x \\ sin\left(\frac{\theta}{2}\right) e_y \\ sin\left(\frac{\theta}{2}\right) e_z \\ cos\left(\frac{\theta}{2}\right) \end{bmatrix}.$$

The first three identities are called the vector part of the quaternion; the fourth identity is the scalar part which is a result of the derivation of a quaternion from Euler's formula. Opposite to the Euler angles, the identities of a quaternion are not independent which results and can be real or imaginary. This brings along some different algebra considering quaternions, multiplication of two quaternions for example is non-communicative. Quaternion operations used in this thesis are given in Appendix. A. A quaternion represents a rotation of the reference frame; however a quaternion cannot be used directly to transfer a vector from one reference frame to another. In order to do so, the quaternion needs to be converted to a rotation matrix. For convenience the identities of the quaternion are numbered:

$$\mathbf{q} = \begin{bmatrix} q_1 \\ q_2 \\ q_3 \\ q_4 \end{bmatrix},$$

in which q_4 is the scalar part. The rotation matrix can be written as:

$$R = \begin{bmatrix} q_4^2 + q_1^2 - q_2^2 - q_3^2 & 2q_1q_2 + 2q_3q_4 & 2q_1q_3 - 2q_2q_4 \\ 2q_1q_2 - 2q_3q_4 & q_4^2 - q_1^2 + q_2^2 - q_3^2 & 2q_2q_3 + 2q_1q_4 \\ 2q_1q_3 + 2q_2q_4 & 2q_2q_3 - 2q_1q_4 & q_4^2 - q_1^2 - q_2^2 + q_3^2 \end{bmatrix},$$

in order for the rotation matrix to be valid the norm of the quaternion needs to be 1. The orientations of the reference frames described earlier in this chapter can be captured in quaternions. The orientation of the body reference frame w.r.t. to the inertial reference frame can be described by quaternion $\mathbf{q}_b$. The rotation matrix associated to $\mathbf{q}_b$ is R_b. In order to transform from the body reference frame to the inertial reference frame the quaternion inverse can be used. The orientation of the left wing is defined w.r.t. the body reference frame and captured by the quaternion $\mathbf{q}_L$ and rotation matrix R_L. Also the right wing is defined w.r.t. body reference frame, $\mathbf{q}_R$ and R_R. One can transform directly from the inertial reference frame to the wing reference frame by multiplying by two rotation matrices, for example $R_L \cdot R_b$. A similar thing can be done with quaternions, using the quaternion multiplication $\mathbf{q}_L \otimes \mathbf{q}_b$ in which $\otimes$ is the quaternion multiplication operator. The definition of this operator and other characteristics of quaternions can be found in Appendix. A and in Ref. [12].

4.3 Body & Wing Kinematics

In most literature on fruit fly aerodynamics, the exact definition of the wing kinematic angles often differs per article. Usually the wing kinematic angles are Euler angles defining the orientation of the reference frame of a wing w.r.t. a strokeplane. This is also the definition of wing kinematics in this thesis. First the strokeplane will be described and subsequently the Euler sequence necessary to obtain the final orientation of the wing.

Strokeplane Reference Frame

An insect's wingbeat can be divided into four phases. The motion of the wing from the dorsal to the ventral side of the fruit fly is called the downstroke and the opposite motion the upstroke. The points where the wings reverse direction have also a name: pronation and supination. Pronation is the rotation of the wing at the dorsal side of the fly and supination at the ventral side. Usually the strokeplane is defined as the plane between the point of supination and pronation and the projection of those points in the symmetry plane of the fly. The points of pronation and supination vary a bit each wingbeat. In order to reduce complexity the orientation and position of the strokeplane is chosen to be constant w.r.t. the body reference frame. After determining the average pronation and supination points of more than hundred wingbeats of several different flies, the angle between the constant strokeplane reference frame and the body reference frame $\beta_{strk} = -55\,^\circ$. The strokeplane reference frame is depicted in Fig. 4.4, the z-axis is pointing downwards which is the definition of an aerodynamic reference frame. Usually when the fly is in steady flight, the strokeplane is roughly parallel to the horizon. The rotation around the x-axis is called roll, the rotation

around the y-axis is called pitch and the rotation around the z-axis is yaw. The definition of the roll, pitch and yaw rotation around the strokeplane reference frame is used throughout the thesis unless mentioned otherwise. One must be careful; the definition of roll, pitch and yaw are different from the roll, pitch and yaw definition in an Euler sequence like the Tait-Bryan angles. The rotation matrix to transform coordinates from the body reference frame to the strokeplane reference frame is:

$$R_{strk} = \begin{bmatrix} cos\left(\beta_{strk}\right) & 0 & -sin\left(\beta_{strk}\right) \\ 0 & 1 & 0 \\ sin\left(\beta_{strk}\right) & 0 & cos\left(\beta_{strk}\right) \end{bmatrix}.$$

The strokeplane reference frame is often used instead of the body reference frame to analyze velocities, angular velocities, accelerations, forces and moments of the fly. This is because the strokeplane reference frame is more intuitive than the body reference frame. The gravity force for example, is roughly pointing downwards and the aerodynamic force is roughly opposite to this force.

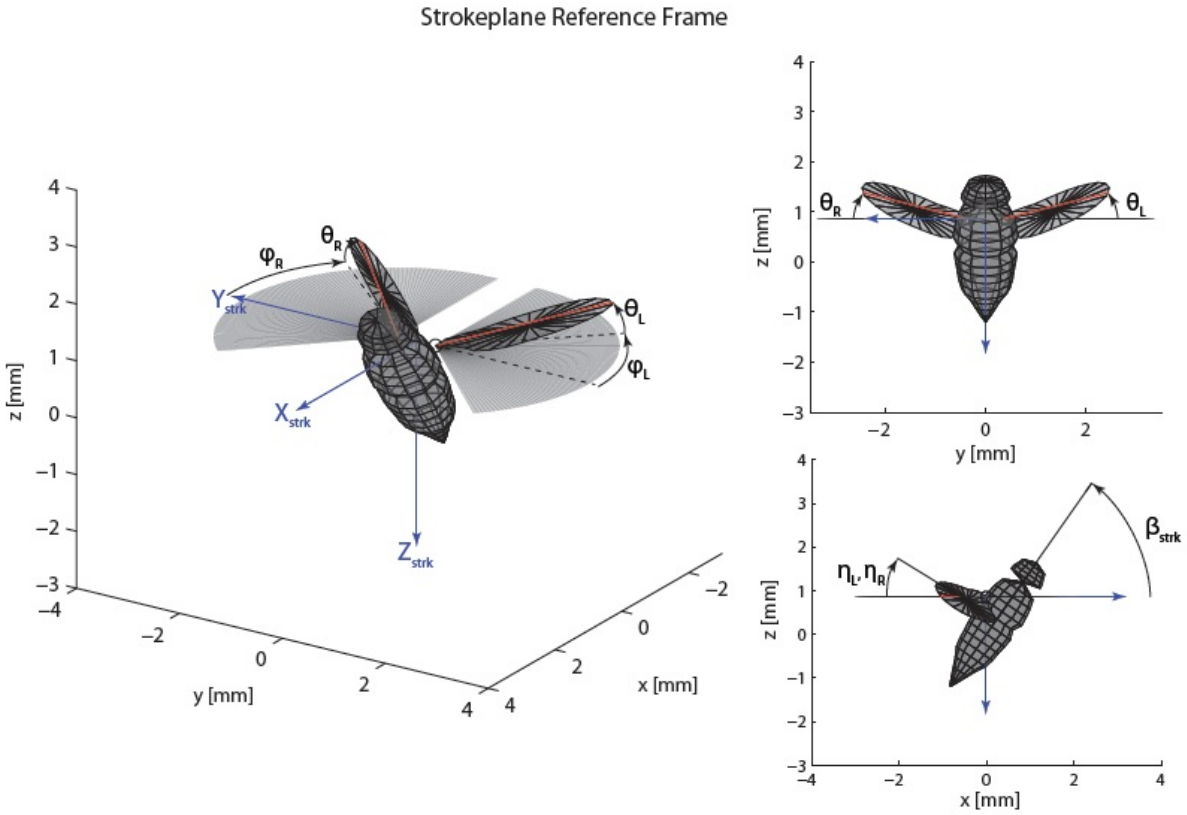

Figure 4.4: Definition of the strokeplane reference frame.

Wing Kinematic Angles

With the strokeplane reference frame defined the wing kinematic angles can be established. The wing kinematic angles consist of three Euler angles which orient the wing from a start position in the strokeplane reference frame to its final orientation. The first angle is the stroke amplitude angle ϕ which rotates the wing around the z-axis of the wing reference frame. The angle ϕ is defined as the angle between the y-axis of the strokeplane reference frame and the projection of the y-axis of the wing reference frame on the strokeplane. The angle ϕ is positive when the projection of the y-axis of the wing is at the dorsal side of the strokeplane. In Fig. 4.4 the strokeplane is shown in combination with the definition of the wing kinematic angles. After the first rotation of the wing reference frame by ϕ, the wing will be rotated around the x-axis of the wing reference frame by an angle θ. The angle θ is called the strokeplane deviation angle or just deviation angle and is positive when the wing's y-axis is elevated above the strokeplane. In this case elevation above the strokeplane is w.r.t. the head of the fruit fly and is thus opposite to the downward pointing z-axis of the strokeplane reference frame. The last angle is the wing pitch angle or wing rotation angle, η. This angle defines the rotation around the y-axis of the wing reference frame. The definition of η is that the angle is a function of the difference in ϕ and θ between a point on the y-axis of the wing and a point Δx away from that point. The angles defining the difference, $\Delta\phi$ and $\Delta\theta$, are combined in a tangent function:

$$\eta = arctan\left(\frac{\Delta\theta}{\Delta\phi}\right).$$

Unfortunately this definition of η would yield negative values for η during the whole wingbeat, as the postive rotation direction around the y-axis of the wing reference frame is opposite. For convenience η is multiplied by -1 and subsequently the wing is rotated 180 degrees around its y-axis such that the definition of eta is positive for the wingbeat. The rotation matrix to transform coordinates in the body reference frame to the wing reference frame can be described by a rotation to the strokeplane reference frame and subsequently rotations by the Euler sequence of the wing kinematic angles. For the left wing the rotation matrix, R_L, becomes:

$$R_L = R_{180} \cdot R_{\eta_L} \cdot R_{\theta_L} \cdot R_{\phi_L} \cdot R_{strk}.$$

And for the right wing:

$$R_R = R_{180} \cdot R_{\eta_R} \cdot R_{\theta_R} \cdot R_{\phi_R} \cdot R_{strk}.$$

The definitions of the rotation matrices of the wing kinematic angles and how these matrices relate the the angular velocities and angular accelerations of the wings are given in Appendix B.

Wingbeat Selection

With the wing kinematic angles the wingbeat is defined in space, what remains is the definition of the wingbeat in time. In this thesis a wingbeat will always start at the begining at the

downstroke and will stop at the end of the upstroke. However finding a good definition of when the wingbeat starts and ends is difficult. When analyzing the video sequences the time step between two subsequent frames is taken as a the minimum time step. The wingbeat can now be described as a sequence of frame numbers, there will be a frame number assigned to the start of the downstroke and a frame number for the start of the upstroke. The end of the downstroke is the frame before the start of the upstroke and the end of the upstroke is the frame before the start of the downstroke of the next wingbeat. In this way a movie sequence can be divided in a number of subsequent wingbeats and on a sub-wingbeat level in a downstroke followed by an upstroke. What is left is determining the start of a downstroke and an upstroke.

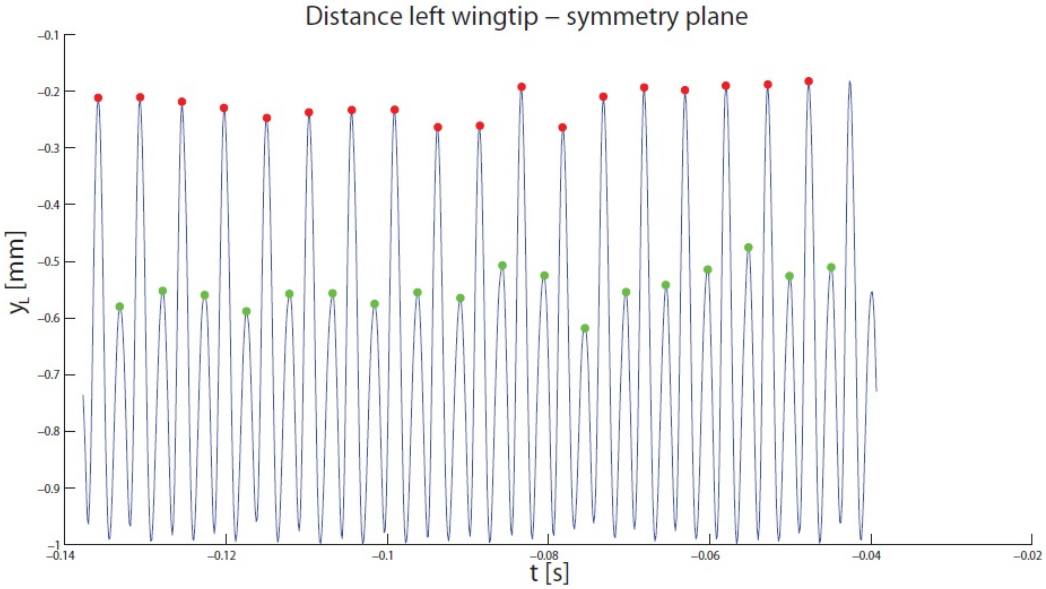

Figure 4.5: Wingbeat selection by the distance between the wingtip and the symmetry plane of the body, y_L. The start of the upstroke is marked by the green dots and the start of the downstroke by the red dots.

In this thesis the start of a downstroke or an upstroke is defined as the local minimum distance of the wingtip to the symmetry plane of the body spanned by the x and z-axis of the body reference frame, Fig. 4.5. Under some circumstances it might be the case that the wingtip crosses the symmetry plane, but even in these cases the negative value of the distance will still be the minimum. Due to physical limits the start of the downstroke is much closer to the symmetry plane than at the start of the upstroke. This can be used to distinguish the downstroke from the upstroke. Allthough it might be that for some unusual wingbeats the start of the upstroke is closer to the symmetry plane than the start of the downstroke, over a movie sequence one can clearly distinguish the two phases. An alternating series of small and big local minima shows the alternating sequence of down and upstrokes. Most of the times the left and right down and upstroke starts are in the same frame. However it might be the case that the left and right wingbeat differ a frame. Therefore the left wingtip is taken as the actual start of the up and downstroke. When a minimum of the right wingbeat differs more than two frames from the left wingbeat, the wingbeat as a whole is discarded. This is

justified as the left and right wing are dynamically coupled by the thorax and although the wing kinematic angles of the left and right wingbeat can differ a lot, it is physically impossible that the flap frequency of the left and right wingbeat can differ significantly. The maximum difference of two frames is based on a visual analysis of the wingbeats for more than ten sequences. Usually the wingbeats for which the left wingbeat definition differs more than two frames from the right wingbeat definition are poorly tracked or not tracked at all.

Aerodynamic Parameters

The aerodynamic analysis in the thesis uses the quasi-steady blade-element theory; the quasi-steady aerodynamic model. Blade-element theory is used to compute the lift and drag generation on propellers and similarly the quasi-steady model can compute the lift and drag on a flapping wing. In the quasi-steady model it is assumed that the aerodynamic effects can be modelled by the instanteneous values of for example the angle of attack and the flow velocity. Both blade element theory as the quasi-steady model divides the wing into a number of spanwise sections. For each section the local flow velocity and the local angle of attack of the flow is computed. Using these variables the lift and drag can be computed. In Chapter 7 the quasi-steady model, as used in this thesis, will be defined. With the wing kinematic angles and the quaternions defined it is possible to establish the definition of the local flow velocity and the local angle of attack which are needed in the quasi-steady model. The local flow velocity on the left wing at section k is defined as:

$$u_L^k = R_L v_b + [R_L \omega_b] \times \left[R_L J_L + y_{sectL}^k \right] + \omega_L \times y_{sectL}^k,$$

where; v_b and ω_b are the velocity vector and angular velocity vector of the body in the body reference frame, J_L is the distance from the c.g. of the body to the left wing joint and y_{sectL}^k is the distance from the center of segment k to the left wing joint in the left wing reference frame and ω_L the angular velocity vector of the left wing. The position vectors used for the computation of the local flow velocity in relation to the blade element are shown in Fig. 4.6. The operator $\times$ stands for the cross product and can be written as the cross product matrix, for example:

$$[\omega_L \times] = \begin{bmatrix} 0 & -\omega_L(3) & \omega_L(2) \\ \omega_L(3) & 0 & -\omega_L(1) \\ -\omega_L(2) & \omega_L(1) & 0 \end{bmatrix}.$$

The angle of attack is defined as the angle between the flow velocity running parallel to the chord of the section and the flow normal to the chord section. Spanwise flow is neglected as the quasi-steady model assumes zero spanwise flow. This analysis of the side-slip velocity angle β shows that this assumption holds during the stroke, only at stroke reversal β deviates from 0 for sections at a spanwise location measured from the wing base of more than 10% of the wing length. At the wing base and at stroke reversal the wing velocity is low such that the effects of the spanwise flow are small. The angle of attack at the left wing section k is defined as:

$$\alpha_L^k = atan2\left(u_L^k(3), u_L^k(1)\right).$$

The *atan*2 operator is a function in Matlab® which extends the continuous domain of the *arctan* operator from $-\pi$ to π. During the downstroke the angle-of-attack is positive and the lift and drag coefficients are directly dependent from α. However during the upstroke the angle of attack negative, therefore the absolute angle of attack $|\alpha|$ is used for both the downstroke as the upstroke.

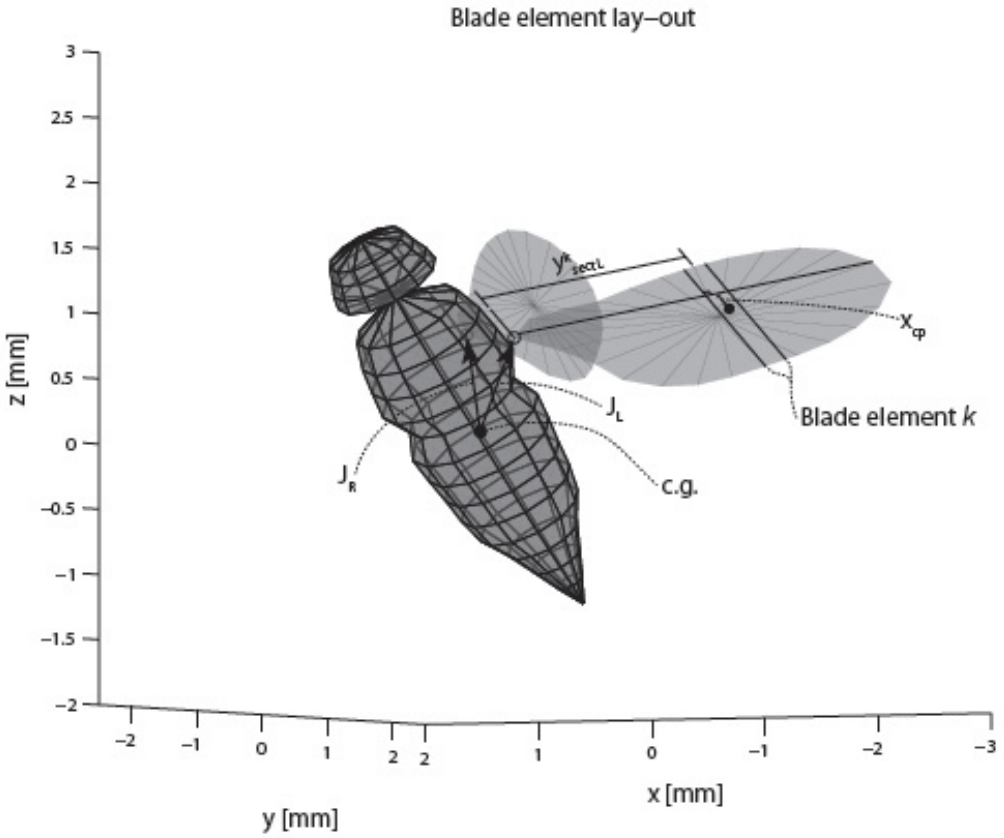

Figure 4.6: Blade element.

Chapter 5

Kalman Filter

The automated tracking software extracts the position and orientation of the flys body and the orientation of its wings for each frame. Using these results, the body and wing dynamics can be studied. The tracking results are however inherently noisy, the noise in the body and wing dynamics is too severe for a detailed analysis of fruit fly flight. In this chapter the procedure for filtering the data will be explained and discussed. There are several options for filtering noise from data, but in this thesis only Kalman filtering is considered. Kalman filtering is preferable above other noise-removing filters such as a Wiener filter or a Savitzky-Golay smoothing filter. There are two main reasons for this preference; in the first place the Kalman filter includes a physical model of the process it is filtering which reduces the influence of unphysical data points. Secondly the Kalman filter does not only filter the data but can also filter the derivatives of the data such that both the data and the derivatives are filtered proportional and according to the physical model. The filtering of the data will start with the filtering of the position data, which requires a linear Kalman filter. The linear Kalman filter is the most basic filter and serves as a good introduction to Kalman filtering. The orientation of the body and the wings is described in quaternions. The quaternion update step in a Kalman filter is no longer linear and therefore a non-linear Kalman filter is required. The Kalman filter which is chosen is an Extended Kalman Filter (EKF), which linearizes the quaternion update. This chapter will describe: the algorithms of the linear and extended Kalman filter, the implementation of the filters and the tuning and results of the filtering.

5.1 Linear Kalman Filter

The x, y and z coordinates from the tracking software, describing the position of the c.g. of the body in the inertial reference frame, contain noise as can be seen in Fig. 5.1. The deviation is not very large but the frequency is rather high, which would introduce significant errors in velocity and acceleration if no filtering is applied. Filtering a trajectory was one of the first implementations of a Kalman filter and the physical model of the filter is rather simple.

A Kalman filter is actually based on two different models and their uncertainties. When implementing a Kalman filter, one starts to define those models. The models are written in the state-space form which describes the update of the state of a system in time. The three main components of a state space system are the state vector, the system model and the measurement model.

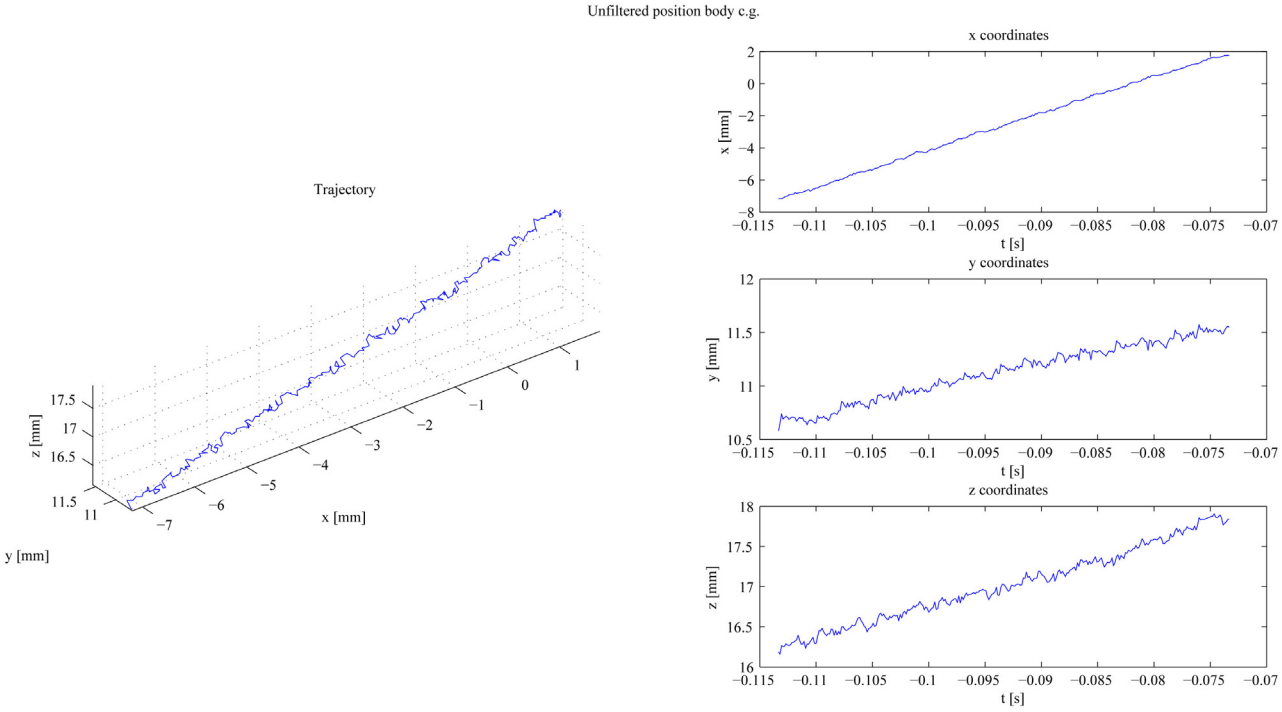

Figure 5.1: Unfiltered data position c.g. body in inertial reference frame.

State vector

The measurement data of the position of the c.g. of the fruit fly consists of a sequence of the x, y and z coordinates in the global reference frame separated by time step Δt. As the frame rate of the cameras is 7500 Hz, $\Delta t = 1.33 \cdot 10^{-4}$ $[s]$. Besides the position also the velocity and acceleration of the c.g. are of interest when analyzing fruit flies in free flight. As the time is updated with a constant time step it is convenient to replace the time series of the measurement data by a discrete integer sequence: $k = 1, 2, 3, ..., N$. Now $t(1)$ is the start time of the measurements and $t(N)$ the stop time. The state vector for a certain value of k is given by:

$$\mathbf{x}_k = [\ x(k),\ y(k),\ z(k),\ u(k),\ v(k),\ w(k),\ a_x(k),\ a_y(k),\ a_z(k)\ ]^T,$$

in which u, v and w are the velocities in the global frame in the x, y and z direction. The same convention is used for the acceleration terms.

System model

The system model describes the correlation between the state of the system at time t and the state of the system at time $t + \Delta t$ or the transform from state k to the state $k + 1$. As the time step Δt is rather small, using a point-mass model for the movement of the c.g. is a reasonable assumption. The point-mass model is a linear system and can be captured in the general system model of a discrete-time linear Kalman filter:

$$\mathbf{x}_{k+1} = \Phi_k \mathbf{x}_k + \mathbf{w}_k,$$

with:

$$\mathbf{w}_k = \mathcal{N}(0, Q_k).$$

The vector $\mathbf{w}_k$ contains the system noise in the update. Generally this noise is not known and is assumed to be normal distributed with covariance Q. The normal distribution assumption is necessary in order to let the Kalman filter algorithm work. The matrix Φ_k incorporates the linear model of the system. In this case the model of the system is a Taylor series expansion of the position around time t. The position vector is denoted as:

$$\mathbf{r} = \begin{bmatrix} x \\ y \\ z \end{bmatrix}.$$

Besides the position, also the velocity ($\dot{\mathbf{r}}$) and acceleration ($\ddot{\mathbf{r}}$) will be included in the Taylor series expansion:

$$\mathbf{r}(t + \Delta t) = \mathbf{r}(t) + \dot{\mathbf{r}}(t)\Delta t + \frac{1}{2}\ddot{\mathbf{r}}(t)\Delta t^2 + O(\Delta t^3),$$

the first derivative:

$$\dot{\mathbf{r}}(t + \Delta t) = \dot{\mathbf{r}}(t) + \ddot{\mathbf{r}}(t)\Delta t + O(\Delta t^2),$$

and the second derivative:

$$\ddot{\mathbf{r}}(t + \Delta t) = \ddot{\mathbf{r}}(t) + O(\Delta t).$$

This can be rewritten to the matrix equation of the system model with $\mathbf{x} = [\mathbf{r}, \quad \dot{\mathbf{r}}, \quad \ddot{\mathbf{r}}]^T$:

$$\mathbf{x}_{k+1} = \begin{bmatrix} 1 & 0 & 0 & \Delta t & 0 & 0 & \frac{1}{2}\Delta t^2 & 0 & 0 \\ 0 & 1 & 0 & 0 & \Delta t & 0 & 0 & \frac{1}{2}\Delta t^2 & 0 \\ 0 & 0 & 1 & 0 & 0 & \Delta t & 0 & 0 & \frac{1}{2}\Delta t^2 \\ 0 & 0 & 0 & 1 & 0 & 0 & \Delta t & 0 & 0 \\ 0 & 0 & 0 & 0 & 1 & 0 & 0 & \Delta t & 0 \\ 0 & 0 & 0 & 0 & 0 & 1 & 0 & 0 & \Delta t \\ 0 & 0 & 0 & 0 & 0 & 0 & 1 & 0 & 0 \\ 0 & 0 & 0 & 0 & 0 & 0 & 0 & 1 & 0 \\ 0 & 0 & 0 & 0 & 0 & 0 & 0 & 0 & 1 \end{bmatrix} \mathbf{x}_k = \Phi_k \mathbf{x}_k.$$

Measurement model

The measurement model transforms measured variables into state variables. The measurement model describes the measurements at time t as a linear function of the state at time t and normal distributed measurement noise with covariance R. The measurement model is given as:

$$\mathbf{z}_k = H\mathbf{x}_k + \mathbf{v}_k,$$

with:

$$\mathbf{v}_k = \mathcal{N}(0, R_k),$$

in which $\mathbf{z}_k$ is a vector with measured variables at instance k, H is a matrix containing the relations between the state vector and measurements and $\mathbf{v}_k$ contains the measurement noise. From the high-speed movies the position of the c.g. is directly determined which makes the measurement model simple:

$$\mathbf{z}_k = \begin{bmatrix} 1 & 0 & 0 & 0 & 0 & 0 & 0 & 0 & 0 \\ 0 & 1 & 0 & 0 & 0 & 0 & 0 & 0 & 0 \\ 0 & 0 & 1 & 0 & 0 & 0 & 0 & 0 & 0 \end{bmatrix} \mathbf{x}_k + \mathbf{v}_k.$$

Initialization

Before the algorithm can start, the initial conditions must be defined. First of all, there must be a state vector at $k = 1$. For the position the measurements of the position at $k = 1$ are a good estimate. The velocity is obtained by taking the difference between the position at $k = 1$ and $k = 11$ and dividing this difference by $10 \cdot \Delta t$. The interval of $10 \cdot \Delta t$ is chosen as the noise in the measurements is rather high which would result in large errors in the velocity estimation. The acceleration is assumed to be zero as estimating the acceleration from the estimated velocity is very inaccurate.

The second initial condition is the error covariance of the state at $k = 1$, P_1^-. It is very difficult to give an estimate of the covariance matrix as the error covariances Q and R of vectors $\mathbf{w}_k$ and $\mathbf{v}_k$ are unknown. Therefore the covariance matrix is set as an identity matrix.

Finally the error covariance matrices Q and R must be set. These matrices do however not only influence the initial conditions but the entire filtering procedure. The motivation of the choice for these matrices will be given in the section about tuning.

The initial settings of the Kalman filter in this case are rather crude. However it is observed that after $k = 20$ the influence of badly chosen initial conditions is ignorable. To make sure that also for $k < 20$ the results are not affected by the choice of initial conditions it is the procedure to run the Kalman filter (including the Rauch-Tung-Striebel smoother) for a second time. During the second time the initial state vector and initial covariance matrix P are the filtered results from the first run of the Kalman filter. This procedure generates a sufficiently accurate estimate of the initial conditions such that no effect of the initial conditions can be observed anymore in the results.

The algorithm

The algorithm of a Kalman filter consists basically of two phases: a prediction phase and a measurement update phase, Ref. [18]. In the prediction phase, a prediction of the state vector in the next frame is made and a prediction of the error covariance in the next frame. These predictions are based on the system model and the system noise covariance and the current state and error covariance. The prediction of the state, or the a priori estimate, is given by:

$$\mathbf{x}_{k+1}^{-} = \Phi_k \mathbf{x}_k^{+}.$$

The plus and minus signs for the state vectors in this equation stand for the filtered state (+) and the a priori estimate (−). The prediction of the error covariance in the next frame is:

$$P_k^{-} = \Phi_k P_k^{+} \Phi_k^T + Q_k.$$

After the prediction phase the measurement update phase starts. In this phase the prediction of the previous phase is compared with the measurement data. This comparison results in an update of the state vector and error covariance matrix. The relative weight of the measurement compared to the prediction of the state is captured by the filter gain $\bar{K}_k$. The gain is computed in the following way:

$$\bar{K}_k = P_k^{-} H^T \left[H P_k^{-} H^T + R_k \right]^{-1}.$$

Using the gain, the state can be updated:

$$\mathbf{x}_k^{+} = \mathbf{x}_k^{-} + \bar{K}_k \left[\mathbf{z}_k - H \mathbf{x}_k^{-} \right].$$

The update of the error covariance is given by:

$$P_k^{+} = \left[I - \bar{K}_k H \right] P_k^{-}.$$

By alternating the two phases the algorithm runs through the data. The updated states ($\mathbf{x}_k^{+}$) are saved as the filtered data, however also the estimated states and the estimated and updated error covariances are saved. This data is used for the smoothing procedure after applying the algorithm.

Rauch-Tung-Striebel Smoother

The filtered data of the Kalman filter is influenced by the measurements and the system model. The influence of the models on the data can be tuned. When both the measurements and the system model have sufficient influence on the filtering, the algorithm will produce a smoothened data set. The amount of smoothing can be increased by applying a smoothing algorithm on the filtered data. However there is a second and more important reason to apply a smoothing algorithm. The Kalman filtering algorithm introduces a temporal lag in the data. This lag can be removed by applying a smoothing algorithm. The Rauch-Tung-Striebel smoother is one of the most used smoothers and also easy to implement. It basically

is a Kalman filter running backwards through the data. In this way the lag is removed and some additional smoothing is applied on the data.

The algorithm will run from $k = N$ to $k = 1$. It will use the filtered state and the state estimates generated by the Kalman filter in combination with the updated error covariance and the estimated error covariance. The smoothened state, $\hat{\mathbf{x}}_k$, is generated by:

$$\hat{\mathbf{x}}_k = \mathbf{x}_k^+ + A_k \left(\hat{\mathbf{x}}_{k+1} - \mathbf{x}_{k+1}^- \right)$$

with;

$$A_k = P_k^+ \Phi_k^T P_{k+1}^-.$$

If the user is interested in the error covariance of the smoothened solution, the error covariance matrix also needs an update:

$$\hat{P}_k = P_k^+ + A_k \left(\hat{P}_{k+1} - P_{k+1}^- \right).$$

Tuning and Results

The tuning of a Kalman filter can be an art in itself. There are several algorithms available to automatize this procedure but they do not work very well for non-linear problems, Ref. [23]. Luckily for the system matrix of position, velocity and acceleration the tuning can be based on the accuracy of the Taylor approximation. It is assumed that the measurements of position are first order accurate ($O(\Delta t)$), scaling with velocity. As the tuning is based on the ratio between the Q and R matrix it is convenient to set the R matrix to identity. In the tuning only the diagonals of the Q and R matrix are important as the covariance between the state variables is assumed to be zero, a common assumption in Kalman filtering. The accuracy of the system according to the Taylor series is $O\left(\Delta t^3\right)$. As the diagonal of the measurement covariance matrix is set to one, the value of the diagonal values in Q corresponding to the position variance are Δt^2, being the ratio in orders of magnitude between the system and the measurements. The variance of the derivative of the position measurements scales with the acceleration which has an order of magnitude $\left(O\left(\Delta t^2\right)\right)$. The variance of the derivative of the Taylor series representing the system also scales with $\left(O\left(\Delta t^2\right)\right)$, which makes the ratio between system and measurement variance 1. Finally the same procedure is used for the acceleration and the following covariance matrices are obtained:

$$R = \begin{bmatrix} 1 & 0 & 0 \\ 0 & 1 & 0 \\ 0 & 0 & 1 \end{bmatrix},$$

$$Q = \begin{bmatrix} \Delta t^2 & 0 & 0 & 0 & 0 & 0 & 0 & 0 & 0 \\ 0 & \Delta t^2 & 0 & 0 & 0 & 0 & 0 & 0 & 0 \\ 0 & 0 & \Delta t^2 & 0 & 0 & 0 & 0 & 0 & 0 \\ 0 & 0 & 0 & 1 & 0 & 0 & 0 & 0 & 0 \\ 0 & 0 & 0 & 0 & 1 & 0 & 0 & 0 & 0 \\ 0 & 0 & 0 & 0 & 0 & 1 & 0 & 0 & 0 \\ 0 & 0 & 0 & 0 & 0 & 0 & \frac{1}{\Delta t^2} & 0 & 0 \\ 0 & 0 & 0 & 0 & 0 & 0 & 0 & \frac{1}{\Delta t^2} & 0 \\ 0 & 0 & 0 & 0 & 0 & 0 & 0 & 0 & \frac{1}{\Delta t^2} \end{bmatrix}.$$

The results for these filter settings are very satisfactory. In Fig. 5.1 a typical flight path during a filmed flight sequence is displayed. The model fitting is not so accurate for the body which means that the position of the center of gravity is distributed randomly around the actual trajectory of the body. The linear Kalman filter is very capable to handle this level of noise, not only is the position a smooth curve over time, Fig. 5.2, also the velocity, Fig. 5.3, and the acceleration, Fig. 5.4, are smooth over time. This is achieved without losing too much temporal resolution; only oscillations around the frame rate frequency are filtered out of the solution. Due to the body inertia these oscillations have a rather small effect on the position of the c.g. such that the solution is not affected much by filtering out these high frequencies.

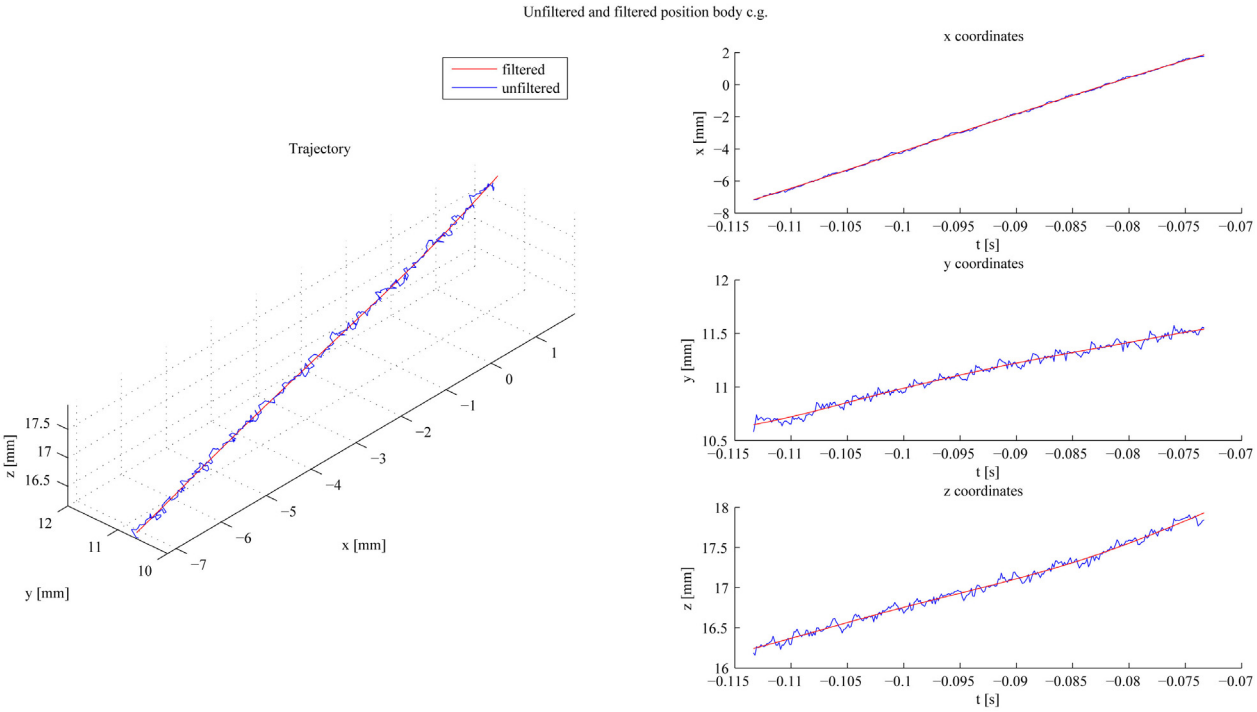

Figure 5.2: Unfiltered and filtered data position c.g. body in inertial reference frame.

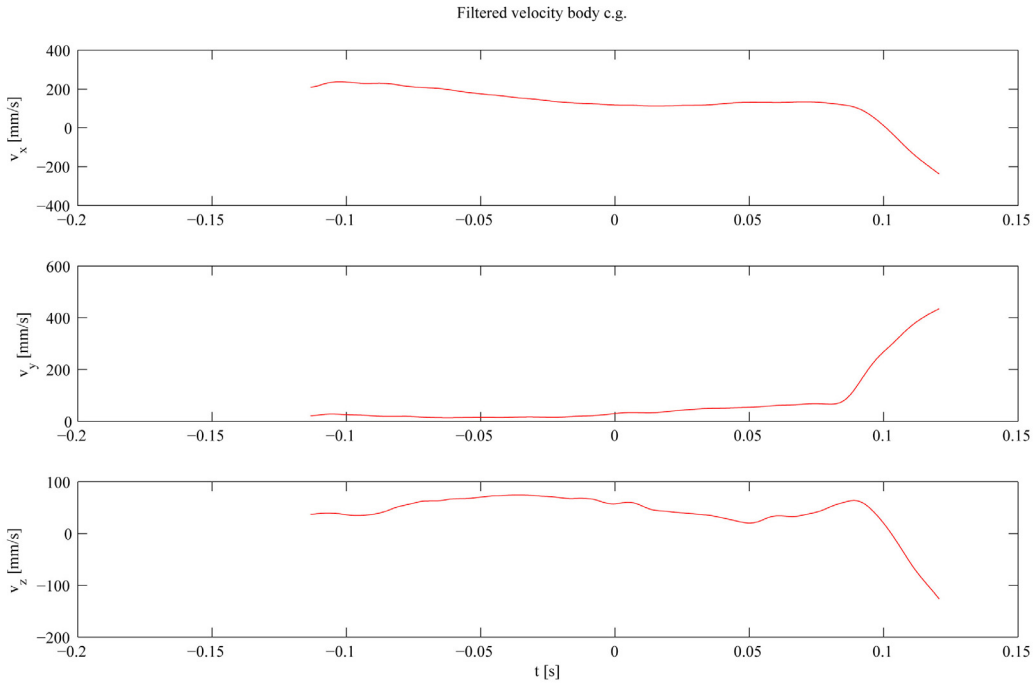

Figure 5.3: Filtered velocity c.g. body in inertial reference frame.

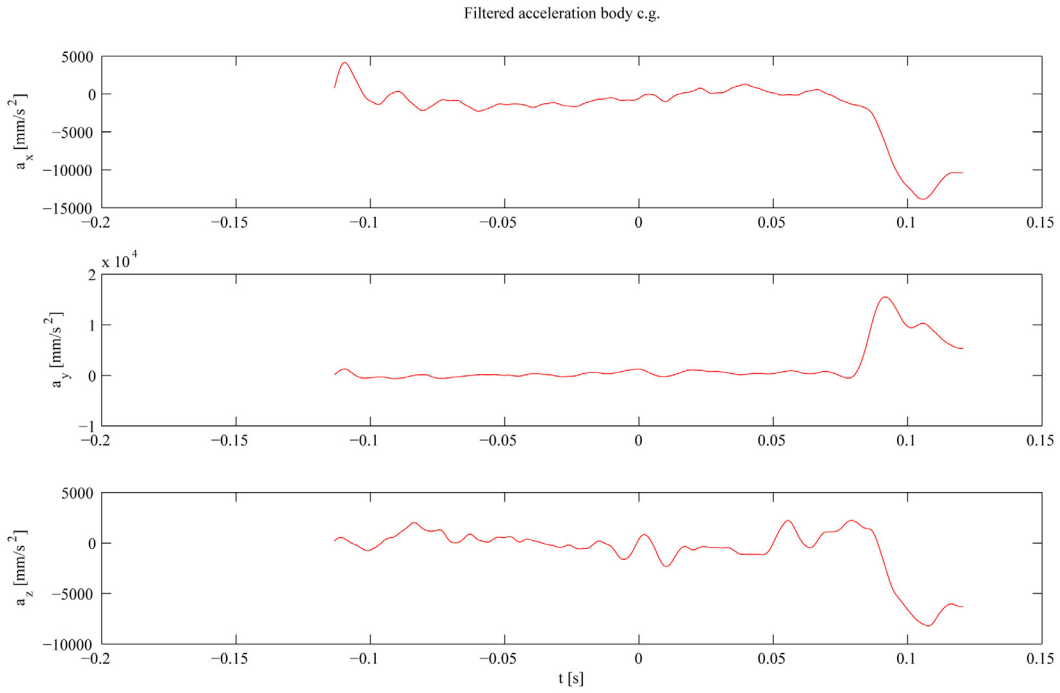

Figure 5.4: Filtered acceleration c.g. body in inertial reference frame.

5.2 Extended Kalman Filter

The Extended Kalman Filter (EKF) is basically a linear Kalman filter with some adaptations to handle the non-linear system. The unaltered parts of the algorithm of the linear Kalman filter will not be repeated in this section.

State Vector

The orientation of the body and both wings in each frame is given in quaternions. The quaternion derivative is a function of the angular velocity ω, which is an important parameter. The angular acceleration $\dot{\omega}$ is also included in the state vector in order to improve the model. The complete state vector is given as:

$$\mathbf{x}_k = [\dot{\omega}_x,\ \dot{\omega}_y,\ \dot{\omega}_z,\ \omega_x,\ \omega_y,\ \omega_z,\ q_1,\ q_2,\ q_3,\ q_4\ ].$$

System Model

The predicted state is given by $\hat{\mathbf{x}}_{k+1} = f(\mathbf{x}_k) + \mathbf{w}_k$ where $f(\mathbf{x}_k)$ is a non-linear function. The non-linear function can be linearized around the state $\mathbf{x}_k$:

$$\mathbf{x}_{k+1} = \frac{\partial f(\mathbf{x}_k)}{\partial \mathbf{x}} \cdot \mathbf{x}_k + \mathbf{w}_k.$$

The Jacobian matrix $\frac{\partial f(\mathbf{x}_k)}{\partial \mathbf{x}}$ is the system matrix Φ_k. Matrix Φ_k is a function of $\mathbf{x}_k$ and changes every time step. The matrix Φ_k is given by:

$$\Phi_k = \begin{bmatrix} 1 & 0 & 0 & 0 & 0 & 0 & 0 & 0 & 0 & 0 \\ 0 & 1 & 0 & 0 & 0 & 0 & 0 & 0 & 0 & 0 \\ 0 & 0 & 1 & 0 & 0 & 0 & 0 & 0 & 0 & 0 \\ \Delta t & 0 & 0 & 1 & 0 & 0 & 0 & 0 & 0 & 0 \\ 0 & \Delta t & 0 & 0 & 1 & 0 & 0 & 0 & 0 & 0 \\ 0 & 0 & \Delta t & 0 & 0 & 1 & 0 & 0 & 0 & 0 \\ 0 & 0 & 0 & \frac{q_4\Delta t}{2} & -\frac{q_3\Delta t}{2} & -\frac{q_2\Delta t}{2} & 1 & \frac{\omega_3\Delta t}{2} & -\frac{\omega_2\Delta t}{2} & \frac{\omega_1\Delta t}{2} \\ 0 & 0 & 0 & \frac{q_3\Delta t}{2} & \frac{q_4\Delta t}{2} & -\frac{q_1\Delta t}{2} & -\frac{\omega_3\Delta t}{2} & 1 & \frac{\omega_1\Delta t}{2} & \frac{\omega_2\Delta t}{2} \\ 0 & 0 & 0 & -\frac{q_2\Delta t}{2} & \frac{q_1\Delta t}{2} & \frac{q_4\Delta t}{2} & \frac{\omega_2\Delta t}{2} & -\frac{\omega_1\Delta t}{2} & 1 & \frac{\omega_3\Delta t}{2} \\ 0 & 0 & 0 & -\frac{q_1\Delta t}{2} & -\frac{q_2\Delta t}{2} & -\frac{q_3\Delta t}{2} & -\frac{\omega_1\Delta t}{2} & -\frac{\omega_2\Delta t}{2} & -\frac{\omega_3\Delta t}{2} & 1 \end{bmatrix}.$$

The function $f(\mathbf{x}_k)$ is given by a Taylor series for ω and $\dot{\omega}$. The quaternion update is described in Appendix A. The system matrix is an adapted version of the system matrix used in Ref. [30] in which an extended Kalman filter was used to model human limb motion.

Measurement Model

The measurement model is first represented by a simple 4 by 10 identity matrix, inserting the quaternion measurements in the filter. Unfortunately, due to high frequency (faulty) oscillations in the body orientation, the noise levels of the angular velocity and acceleration are too high to be useful. By smoothing the quaternions severely the noise level can be reduced. However the filtered angular velocities are still not sufficiently smooth. Therefore the following solution is used. In a first filtering step the quaternions are smoothed as much as possible whilst maintaining the required temporal resolution. The resulting angular velocity and quaternions are subsequently inserted in a second filtering step with a measurement matrix (7 by 10 identity matrix). In the second filtering step the quaternions are smoothed minimally, the angular velocity and angular acceleration however are smoothed upon the required level.

The Algorithm

The extended Kalman filter deviates from a linear Kalman filter in two ways, in the first place the system matrix Φ_k needs to be updated every time step, secondly the predicted and the updated quaternions in the algorithm need to be normalized every time step. Similar to the linear Kalman filter, a Rauch-Tung-Striebel smoother is applied in order to apply extra smoothing and remove the lag.

Tuning and Results

In case of the linear Kalman filter the tuning could be based on the order of magnitude of the error of the system and the assumed order of magnitude of the error of the measurements. Unfortunately this is not the case anymore for an extended Kalman filter. The ratio between the covariance matrices Q and R can no longer be directly derived from the properties of the system. Although there are iterative procedures to tune the matrices, such as the Autocovariance Least-Squares (ALS) method, generally these procedures yield very meager results, Ref. [23]. The tuning of the extended Kalman filter therefore requires some trial-and-error steps before reaching a satisfactory tuned filter. As mentioned before there are two filtering steps. For the body orientation the first step smoothens the quaternions such that the filtered data contains sufficiently smoothened angular velocities. Again the measurement covariance matrix R is set to identity again, the diagonal of the Q matrix is split up into three variables

a, b and c:

$$Q = \begin{bmatrix} a & 0 & 0 & 0 & 0 & 0 & 0 & 0 & 0 & 0 \\ 0 & a & 0 & 0 & 0 & 0 & 0 & 0 & 0 & 0 \\ 0 & 0 & a & 0 & 0 & 0 & 0 & 0 & 0 & 0 \\ 0 & 0 & 0 & b & 0 & 0 & 0 & 0 & 0 & 0 \\ 0 & 0 & 0 & 0 & b & 0 & 0 & 0 & 0 & 0 \\ 0 & 0 & 0 & 0 & 0 & b & 0 & 0 & 0 & 0 \\ 0 & 0 & 0 & 0 & 0 & 0 & c & 0 & 0 & 0 \\ 0 & 0 & 0 & 0 & 0 & 0 & 0 & c & 0 & 0 \\ 0 & 0 & 0 & 0 & 0 & 0 & 0 & 0 & c & 0 \\ 0 & 0 & 0 & 0 & 0 & 0 & 0 & 0 & 0 & c \end{bmatrix}.$$

For the first filtering step a and b are set to zero whilst $c = 0.003$. The second filtering step sets a, b and c to $0.0001/\Delta t^2$, 0.0001 and 1 respectively. The wings undergo a similar procedure but the wing quaternions require much less smoothing. The first step sets a, b and c to 0, 0 and 1 respectively. The second step sets a, b and c to 0, $1/\Delta t^2$ and 1 respectively.

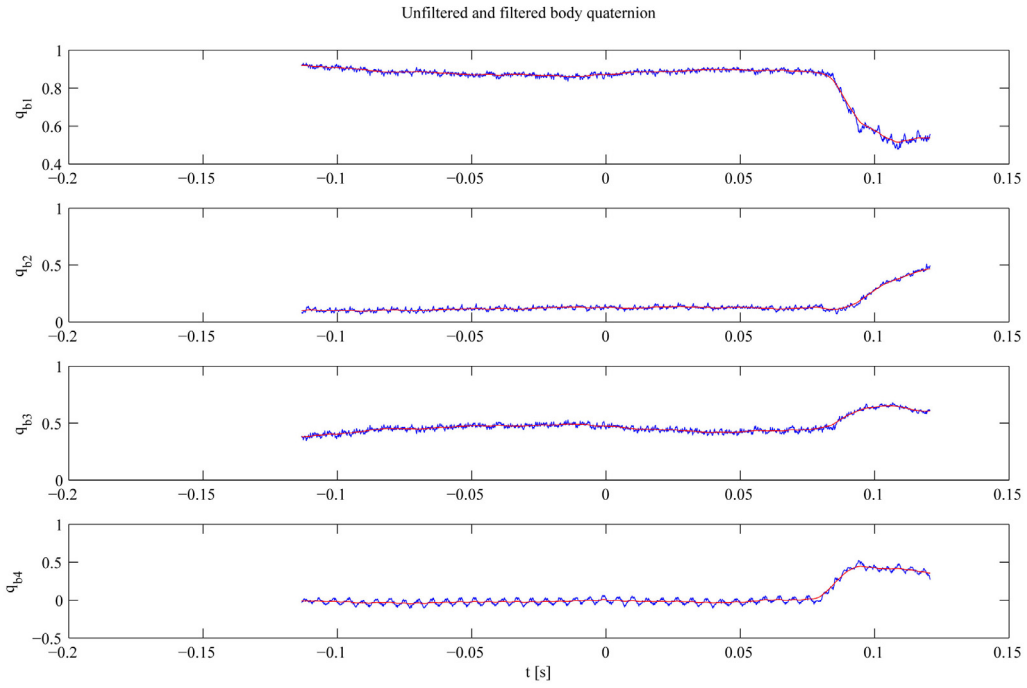

Figure 5.5: Unfiltered (blue) and filtered (red) body quaternion.

In Fig. 5.5 and Fig. 5.6 the filtered body quaternion and the filtered body angular velocity are depicted respectively. As can be seen in the angular velocity and to a lesser degree in the quaternion, there is a rather strong oscillation at the wingbeat frequency present in the data. This is due to the induced wing motion on the body quaternion due to the roll fitting of the body based on the orientation of the wings. This oscillation is not that problematic for

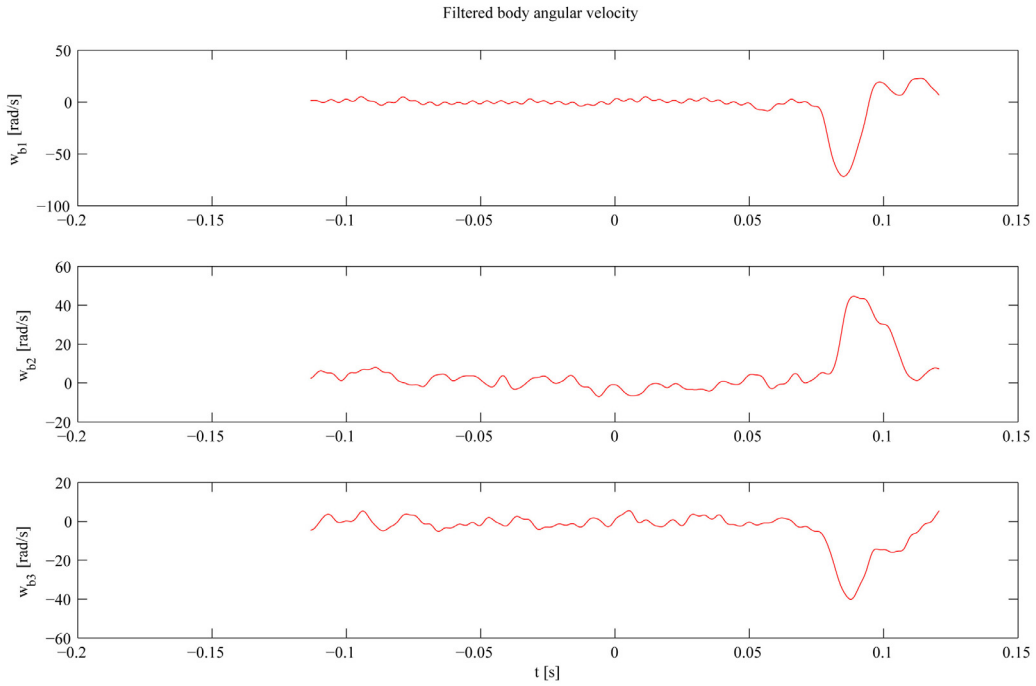

Figure 5.6: Filtered body angular velocity in body frame of reference.

the body orientation itself, however the derivative of the quaternion, the angular velocity, is greatly affected by this oscillation. The filtering greatly reduces this oscillation, however at the price of reduced temporal resolution.

In Fig. 5.7 the wingtip path during a sequence of the left and right wings are projected on a sphere. Both the filtered and unfiltered wingtip paths are depicted. Fig. 5.7 shows the strength of the extended Kalman filter, as the filter uses the motion of the hinged wing system in areas where the measurements are uncertain. This can particularly be seen at stroke reversal where the wing tracking is uncertain. The Kalman filter creates nice rounded wingtip paths at stroke reversal instead of the jerky measured wingtip path. This reduces unwanted peaks in the angular velocity and angular acceleration and makes the filtered data usable for simulations or experiments. Fig. 5.8 shows how the left wing quaternion is filtered. The wing quaternions do not contain as much noise as the body quaternion and the amount of filtering of the wing quaternions is kept minimal. The same yields for the filtering of the wing's angular velocity, Fig. 5.9, although the peaks in wing angular velocity at stroke reversal are lower than in the angular velocity derived from the unfiltered wing quaternion. The lower velocities around stroke reversal are an effect of the more rounded trajectories at stroke reversal produced by the filtering procedure.

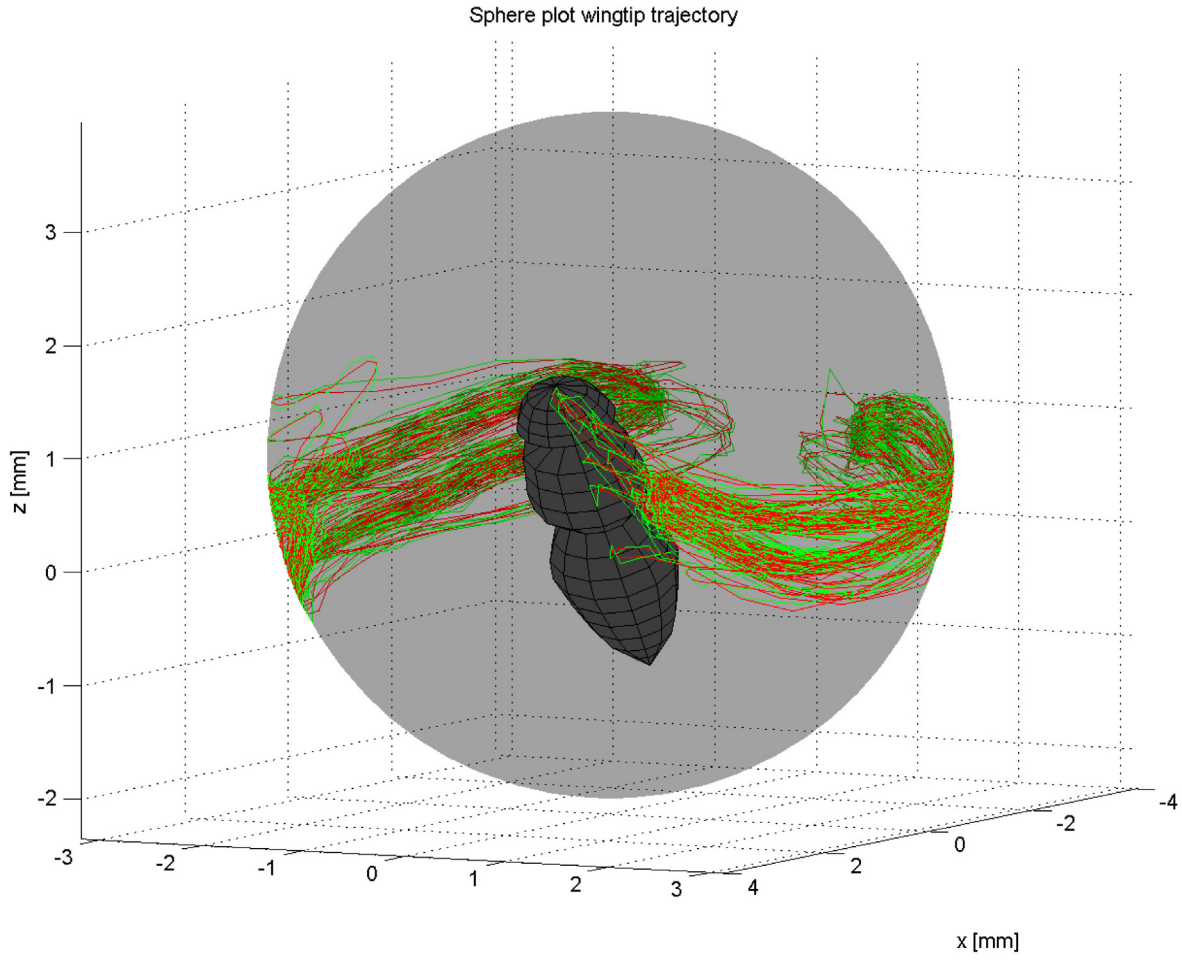

Figure 5.7: Wingtip paths of unfiltered (green) and filtered (red) left and right wing.

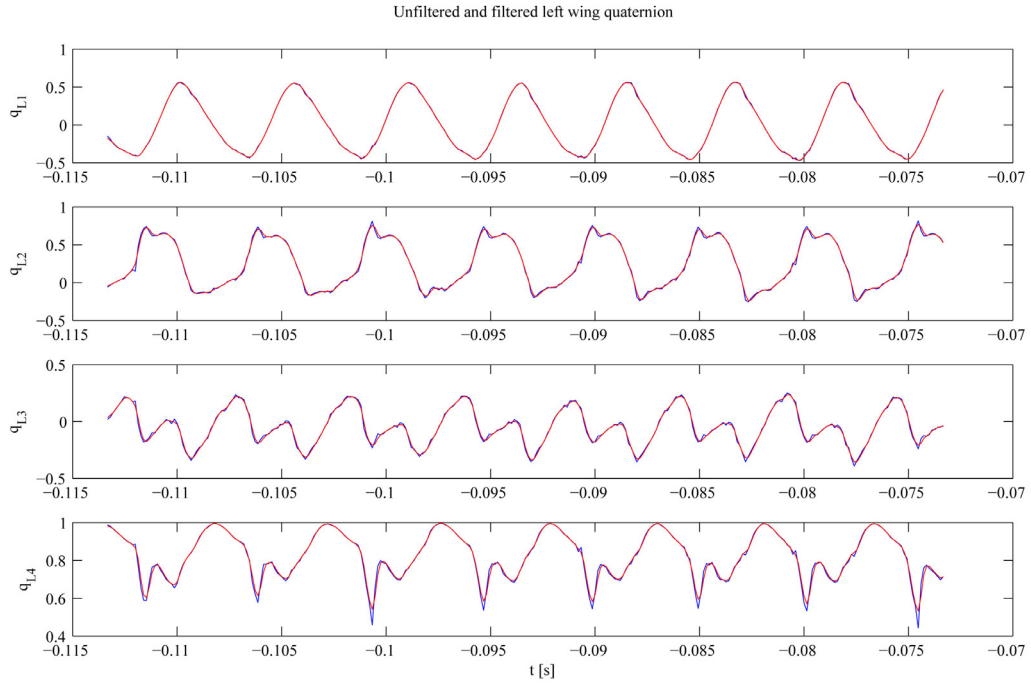

Figure 5.8: Unfiltered (blue) and filtered (red) left wing quaternion.

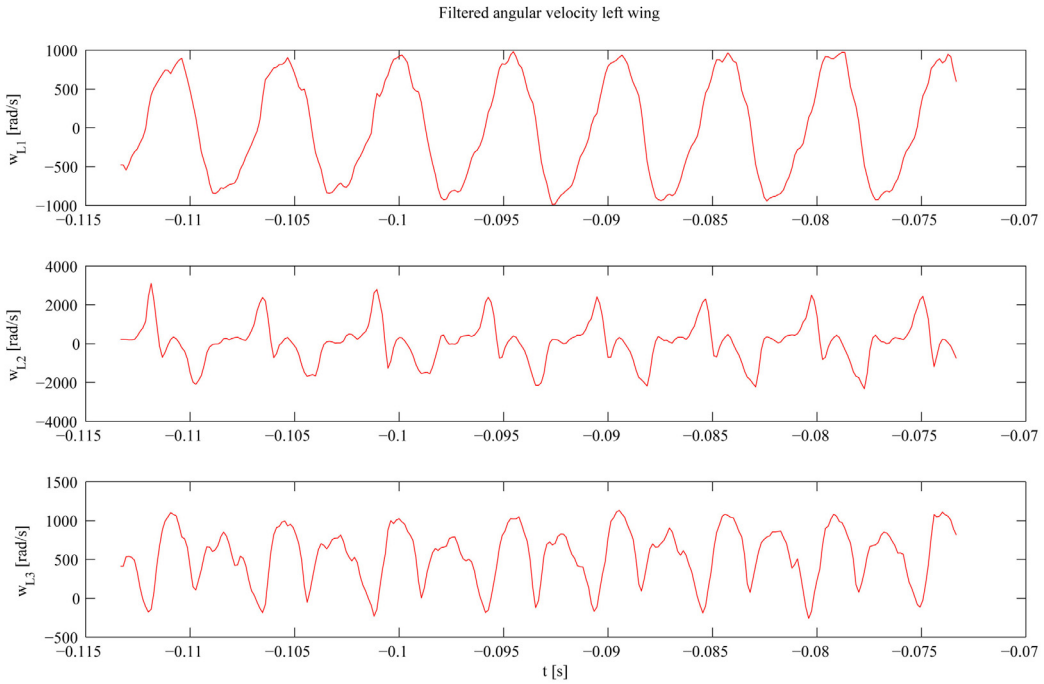

Figure 5.9: Filtered angular velocity left wing in wing reference frame.

Chapter 6

Polynomial Fit

The wing kinematic angles derived from the filtered quaternions $\mathbf{q}_L$ and $\mathbf{q}_R$ can be used directly to study and simulate hovering and maneuvering flight of fruit flies. However the combination of wing kinematics of the left and right wing of a fruit fly differ per fly. Establishing a general model for steady and maneuvering flight of fruit flies will be very difficult because even during hovering flight the wingbeat of the left and right wing differ as well as the wingbeats differ over time. Apparently some variation in wing kinematics does not have much effect on the body kinematics. Beside this variability the assumption of symmetry, used in the geometric model, is not really valid for fruit flies. There are differences in wing length, wing shape and wing area between the left and right wing. This can be due to differences in growth, or one wing can be damaged. It seems to be the case that the fruit fly adjust its wing kinematics in order to compensate for these imbalances. Besides the symmetry also the duration and the ratio between the downstroke and upstroke differ per wingbeat. At least the temporal dynamics of the left and right wings are symmetric. To be able to compare wingbeats with different durations a polynomial is fitted to the wing kinematic angles. The polynomials used are Legendre polynomials which have several advantages over other options. However the Legendre polynomials are defined over a limited domain and therefore at the edges the polynomial fit needs to be "stitched" together using a restricted least-squares fit. The restricted least-squares fit guarantees a smooth transition between the two polynomials and their derivatives. Now a polynomial description of the wing kinematics over the full movie sequence is obtained; it is possible to extract symmetric wing kinematics from the observed wing kinematics. Symmetric wing kinematics are necessary as the geometric model is symmetric and does not incorporate the asymmetric body and wing features of the fly. Finally the polynomial fit also allows establishing an average wingbeat for a movie sequence.

6.1 Legendre Polynomials

When it comes to curve fitting there are a lot of options to transform a number of points into a function. After analysis of the different options it became clear that Legendre polynomials are the most suited function to fit to the wing kinematics. When considering curve-fitting there are a few trade-off criteria; the order of the function used, the number of parameters of the function w.r.t. the number of measurement points available, the goodness of the fit and the boundary conditions of the function. The first option considered are b-splines, b-splines are piecewise polynomials which meet at knots. At those knots the transition between the piecewise polynomials is continuous and smooth. The curvature between the knots is defined by control points which are defined in $2D$. The second option is using Fourier series as a curve, Fourier series are a combination of sines and cosines. The third and final option considered is the use of polynomial regression using Legendre polynomials. The specific choice of Legendre polynomials as polynomial basis of the regression has to do with the characteristics of Legendre polynomials which make them very suited to analyze harmonics.

Trade-off curve fitting

The most common used b-spline is a cubic spline, which uses piecewise polynomials of the third order. However in this case the use of a third order polynomial will not suffice. In the dynamic model the second derivative of the wing kinematic angles is used to compute the wing's angular acceleration. The angular acceleration is used for example to compute the rotational lift and has significant influence on the wing inertia. The second derivative of the wing kinematic angles needs to be continuous and smooth. Therefore upon the fourth derivative the spline needs to be continuous, which requires the usage of higher order splines. Unfortunately generally higher order splines tend to increase the curvature of the spline between two knots, such that the smoothness decreases. Also the higher order splines require a higher number of control points.

The Fourier series seems an attractive alternative as sine and cosine functions are usually used to describe harmonic motions such as a flapping wing. There is however one big disadvantage of Fourier series, which is that they describe periodic functions. This means that the kinematic angles and their derivatives must be equal at the start and end of the wingbeat, such that the same wingbeat can be iterated over and over again in time. This is a very useful aspect of Fourier series considering average wingbeats which have the periodic boundary condition. However when analyzing actual wingbeats this periodic boundary condition is not valid anymore and Fourier series can no longer be used to describe the wingbeat.

A Legendre polynomial basis consists of alternating symmetric and anti-symmetric polynomials in the domain spanned. This combination of symmetric and anti-symmetric polynomials is convenient when considering harmonics, as they allow to analyze both periodic and non-periodic curves. The description of a periodic motion by Legendre polynomials might be better than using sines and cosines. For example the downstroke and upstroke duration are not equal, however they are close to each other. Using a Fourier fit with an insufficient

order would result in the assumption of sinusoidal behavior of the wingbeat, which is not the case. As for the b-splines, also the Legendre polynomials must be continuous up to the fourth derivative. Another problem which is inherent to polynomial fitting is the so-called Runge-phenomenon, which occurs at the boundaries of the polynomial domain. The Runge-phenomenon makes that the polynomial fit starts to oscillate between the data points it is supposed to fit such that the fit is perfect on the data points but the interpolation between the data-points is unrealistic. The Runge-phenomenon is suppressed by a restricted least-squares fit at both boundaries which guarantees the fourth derivative continuity. The Legendre Polynomial does not make a fit through the data points as well as a b-spline could, however this generates some additional smoothing and keeps the order of the polynomials low. A low order polynomial is preferable as the amount of polynomial fitting coefficients describing the wingbeat will be low which makes the analysis of the wingbeat easier.

Legendre Polynomial Basis

The Legendre polynomial basis is defined on the domain between $x = -1$ and $x = 1$ and can be described by the following formula:

$$P_{n+1}(x) = \frac{2n+1}{n+1} x P_n(x) - \frac{n}{n+1} P_{n-1}(x),$$

in which n is the order of the polynomial and the starting conditions of the formula are the polynomials: $P_0 = 1$ and $P_1 = x$. In Fig. 6.1 the polynomials upon $n = 5$ are given. In order to keep the order of the polynomials low, the wingbeat is split into two domains each having their own independent set of polynomials. One domain is assigned to the downstroke and the other to the upstroke. Besides at the start and the end of the wingbeat a restricted least-squares fit is also necessary between the downstroke and upstroke. After inspection of dozens of wingbeats it has become clear that during steady flight and maneuvers the downstroke and upstroke are relatively uncoupled, which justifies the split. For the restricted least-squares fit the derivatives of the Legendre polynomials are necessary. The k^{th} derivative of a Legendre polynomial is given by:

$$P^k_{n+1}(x) = (2n+1) \cdot P^{k-1}_n(x) + P^k_{n-1}(x),$$

with as starting conditions: $P^k_0(x) = 0$, $P^k_1(x) = P^{k-1}_0(x)$ and $P^k_2(x) = 3P^{k-1}_1(x)$. However as the derivatives of the Legendre polynomials are also used as time derivatives it is necessary to scale the domains with the ratio between the downstroke time and upstroke time. By multiplication with a scaling factor the differences in domain size are balanced, for the downstroke:

$$P^k_n(x) = \left(\frac{t_{wb}}{t_{down}}\right)^k \cdot P^k_n(x)$$

and for the upstroke:

$$P^k_n(x) = \left(\frac{t_{wb}}{t_{up}}\right)^k \cdot P^k_n(x),$$

in which t_{wb} is the wingbeat time, t_{down} the downstroke time and t_{up} the upstroke time.

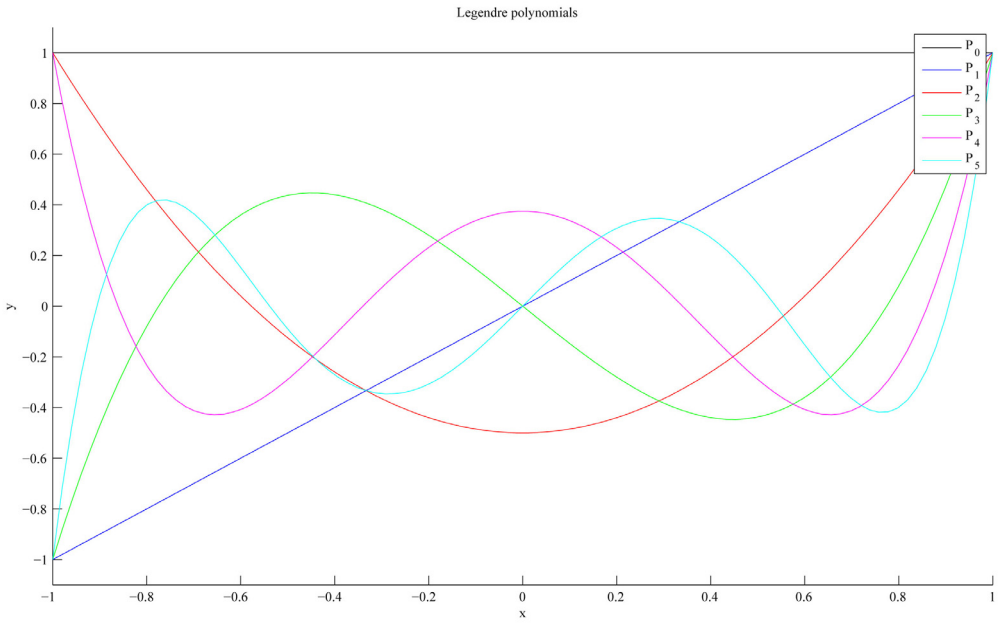

Figure 6.1: Legendre polynomial basis up to order 5.

6.2 Restricted Least-Squares Fit

The restricted least-squares fit enforces boundary conditions on the edges of the domain of the polynomial fit. This allows for a piecewise polynomial fit to be "stitched" together with the guarantee that the transition between the pieces is continuous upon a certain derivative. The restricted least-squares fit starts with obtaining a local least-squares fit. All the local least-squares fits are joined in one vector, β. The vector β is corrected for the boundary conditions in one matrix operation which results in the restricted least-squares fit, β^*.

The ordinary least-squares fit for one piece, i, is defined as $\beta_i = \left(X_i^T X_i\right)^{-1} X_i^T y_i$ where the relation between the measurement vector y_i and the fit β_i is $y_i^* = X_i \beta_i$. The local Vandermonde matrix X_i is constructed of Legendre polynomials upon order n_{pol}. The x values of the polynomials are distributed uniformly over the Legendre domain between -1 and 1. The number of x values corresponds to the number of measurement points y_i. Every measurement point corresponds to the value of the wing kinematic angle at a certain frame. The frame intervals which make up all the pieces of the piecewise polynomial fit for a whole sequence are an alternating series of down and upstrokes. In contradiction to the definition of the wingbeat in the thesis in this case the boundaries of the down and upstroke overlap, which means that the end of the downstroke is the start of the upstroke and vice versa. All the local fits β_i are stacked upon each other such that they form one vector β.

The vector β is corrected for the boundary conditions at the pieces to become the restricted least-squares fit β^*. The correction consists of a single Vandermonde matrix X combining

all local Vandermonde matrices, the restriction matrix R contains the boundary conditions, the measurement vector y of the whole sequence and a restriction vector v_r. The restricted least-squares fit is defined as:

$$\beta^* = \beta - \left(X^T X\right)^{-1} R^T \left(R \cdot \left(X^T X\right) \cdot R^T\right)^{-1} \left[R \cdot \beta - v_r\right].$$

The Vandermonde matrix X consists of the local Vandermonde matrices X_i, at the boundaries the local fit of one stroke overlaps with the next stroke. At the boundaries the average of the two adjacent fits is used by multiplying the values for the Legendre polynomials at the right and left boundary of the Legendre domains with 0.5. The structure of X can be given in a schematic representation, Fig. 6.2.

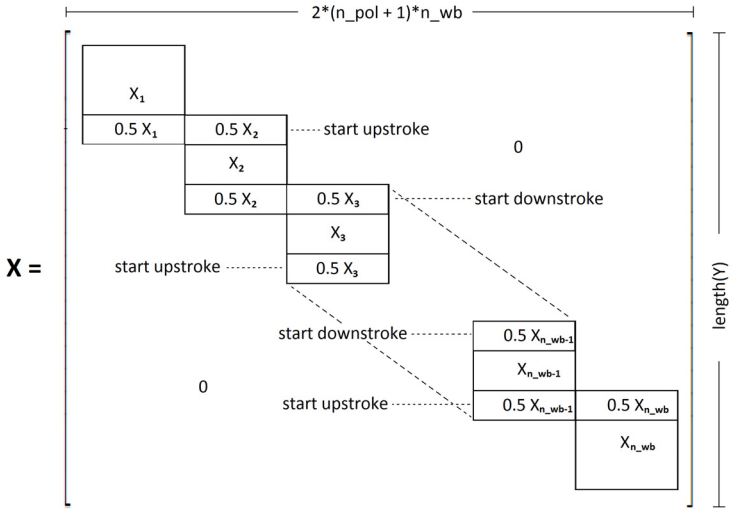

Figure 6.2: Vandermonde matrix X for the restricted least-squares fit.

The restriction matrix R makes sure that the transition between the strokes is continuous upon a given order. In this case the transition between two pieces must be continuous upon the fourth derivative, which is done by making the local fit of the end of the stroke equal to the local fit of the start of the next stroke. This is done for the Legendre basis and its first four derivatives resulting in a matrix of $(n_{deriv} + 1) \cdot (n_{strokes} + 1)$ rows by $(n_{pol} + 1) \cdot n_{strokes}$ columns, in which n_{deriv} is the number of derivatives (4) and $n_{strokes}$ the number of strokes in the sequence. It is possible to define the boundary conditions at the start of a stroke and at the end of a stroke as two sub-matrices of R; R_{start} and R_{end}. The matrix R_{start} contains the Legendre basis and its four derivatives at $x = -1$ upon the order of polynomials used, R_{end} is a similar matrix at $x = 1$. The matrix R is constructed with R_{start} and R_{end}, which is given in a schematic representation:

$$\mathbf{R} = \begin{bmatrix} R_{start} & & & & \\ -R_{end} & R_{start} & & 0 & \\ & -R_{end} & R_{start} & & \\ & & \ddots & \ddots & \\ & 0 & & -R_{end} & R_{start} \\ & & & & R_{end} \end{bmatrix},$$

with:

$$R_{start} = \begin{bmatrix} P_1^0(-1) & P_2^0(-1) & \cdots & P_{n_{pol}+1}^0(-1) \\ P_1^1(-1) & P_2^1(-1) & \cdots & P_{n_{pol}+1}^1(-1) \\ P_1^2(-1) & P_2^2(-1) & \cdots & P_{n_{pol}+1}^2(-1) \\ P_1^3(-1) & P_2^3(-1) & \cdots & P_{n_{pol}+1}^3(-1) \\ P_1^4(-1) & P_2^4(-1) & \cdots & P_{n_{pol}+1}^4(-1) \end{bmatrix}$$

and:

$$R_{end} = \begin{bmatrix} P_1^0(1) & P_2^0(1) & \cdots & P_{n_{pol}+1}^0(1) \\ P_1^1(1) & P_2^1(1) & \cdots & P_{n_{pol}+1}^1(1) \\ P_1^2(1) & P_2^2(1) & \cdots & P_{n_{pol}+1}^2(1) \\ P_1^3(1) & P_2^3(1) & \cdots & P_{n_{pol}+1}^3(1) \\ P_1^4(1) & P_2^4(1) & \cdots & P_{n_{pol}+1}^4(1) \end{bmatrix}.$$

At the start and end of a movie sequence there is one adjacent stroke missing, this is solved by replacing the sub-matrix of the adjacent stroke by a vector of constants. These vectors are captured in a single restriction vector v_r which consists of zeros except for the start and end of the sequence. The values for the constants are obtained by mirroring the stroke w.r.t. the boundary. At the start of the sequence the values of v_r are obtained by $R_{start} \cdot \beta_1$ and at the end of the sequence $R_{end} \cdot \beta_{n_{strokes}+1}$, which results in the vector:

$$v_r = \begin{bmatrix} R_{start} \cdot \beta_1 \\ 0 \\ \vdots \\ 0 \\ R_{end} \cdot \beta_{n_{strokes}+1} \end{bmatrix}.$$

Once the restricted least-squares fit is applied on a sequence, a polynomial coefficient vector for a single wingbeat can be constructed. The polynomial fitting coefficients of the downstroke and the upstroke in a single wingbeat are taken from vector β^* and stacked upon each other to become the vector a_{fit}. The vector a_{fit} has $(n_{pol}+1)\cdot 2$ elements and the value of the resulting polynomial fit can be found by multiplying by the so called wingbeat Legendre matrix, X_{wb}, which consist of the Legendre basis of the downstroke and upstroke. For all the values of the polynomial fit the values are either created by the downstroke polynomial coefficients or the upstroke polynomial coefficients, with the exception of the point at the start of the upstroke. At the start of the upstroke the results of the downstroke polynomial fit and the upstroke polynomial fit are averaged. The amount of sampling points of the polynomial fit in time can be determined by the user.

What is left in order to represent a wingbeat as a polynomial fit is determining the order of the polynomials which generates the best fit. Usually the goodness of a fit is used for determining the order of the polynomials. However in this case it is important to have an order of polynomials which is high enough to describe the fourth derivative proper as well. Therefore the goodness of a fit is not used as a decision factor but a visual inspection of how well the fit works for the wing kinematic angle and its derivatives and how robust this fit is for all possible wingbeats. For the wing kinematic angles θ, η and ϕ it was derived that

the order of the polynomials of; $n_{pol\ \theta} = 12$, $n_{pol\ \eta} = 14$ and $n_{pol\ \phi} = 10$ yields the best fit w.r.t. the data points, the derivatives up to the fourth order whilst using a minimal number of polynomials. The original wing kinematic angles and their polynomial fits for a movie sequence are given in Fig. 6.3.

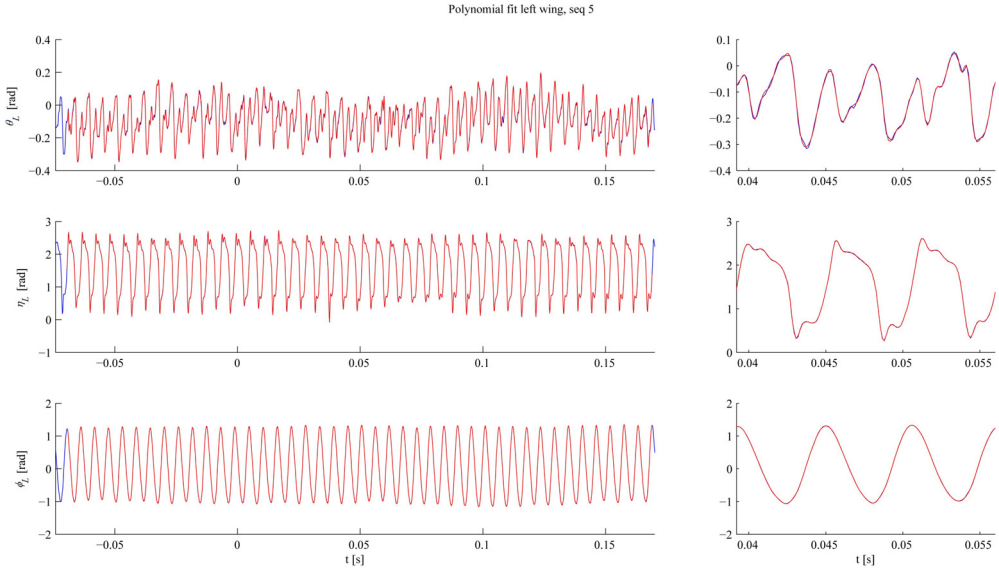

Figure 6.3: Original wing kinematics (blue) and the polynomial fit (red).

The restricted least-squares fit procedure can now be applied and the result will be a description of each wingbeat by a set of six vectors and two scalar values. The six vectors consist of the polynomial fitting coefficients for the three wing kinematic angles of the left and right wingbeat; a_{θ_L}, a_{η_L}, a_{ϕ_L}, a_{θ_R}, a_{η_R} and a_{ϕ_R}. The two scalar values are the wingbeat frequency f and the downstroke to upstroke ratio *down_up*. The result for the global average wingbeat, which is an average wingbeat which's definition will be given later on in this chapter, is shown in Table. 6.1. In case of an arbitrary the polynomial coefficients of the left and right wing will differ, however the table shows how the polynomial fit of a whole wingbeat is defined.

Polynomial fit global wingbeat						
	a_{θ_L}	a_{η_L}	a_{ϕ_L}	a_{θ_R}	a_{η_R}	a_{ϕ_R}
downstroke	-0.0684	2.2054	0.0306	-0.0684	2.2054	0.0306
	-0.0007	-0.1824	-1.3703	-0.0007	-0.1824	-1.3703
	0.1161	-0.4300	0.1446	0.1161	-0.4300	0.1446
	-0.0165	0.2174	0.2227	-0.0165	0.2174	0.2227
	-0.0448	-0.2517	-0.0398	-0.0448	-0.2517	-0.0398
	0.0257	0.1047	0.0081	0.0257	0.1047	0.0081
	-0.0250	-0.0031	-0.0066	-0.0250	-0.0031	-0.0066
	0.0055	-0.1395	-0.0039	0.0055	-0.1395	-0.0039
	0.0140	0.1241	0.0044	0.0140	0.1241	0.0044
	-0.0099	-0.0030	0.0006	-0.0099	-0.0030	0.0006
	-0.0010	-0.0677	-0.0007	-0.0010	-0.0677	-0.0007
	0.0023	0.0346		0.0023	0.0346	
	-0.0003	0.0010		-0.0003	0.0010	
		-0.0091			-0.0091	
		0.0045			0.0045	
upstroke	-0.1557	0.7948	0.0803	-0.1557	0.7948	0.0803
	-0.0122	0.1528	1.3977	-0.0122	0.1528	1.3977
	0.2022	0.6026	0.0664	0.2022	0.6026	0.0664
	-0.0230	-0.2684	-0.2687	-0.0230	-0.2684	-0.2687
	-0.0560	0.3870	-0.0014	-0.0560	0.3870	-0.0014
	0.0493	0.0122	0.0123	0.0493	0.0122	0.0123
	-0.0179	-0.2598	-0.0192	-0.0179	-0.2598	-0.0192
	-0.0285	0.1622	0.0019	-0.0285	0.1622	0.0019
	0.0283	0.0440	0.0072	0.0283	0.0440	0.0072
	0.0096	-0.1076	-0.0004	0.0096	-0.1076	-0.0004
	-0.0119	0.0356	-0.0010	-0.0119	0.0356	-0.0010
	-0.0015	0.0285		-0.0015	0.0285	
	0.0017	-0.0295		0.0017	-0.0295	
		-0.0024			-0.0024	
		0.0068			0.0068	
$down\_up = 0.5384$						
$f = 189.0\,[Hz]$						

Table 6.1: Global wingbeat

6.3 Average Wingbeat

The description of the wingbeat by polynomial coefficients is uniform and allows comparing wingbeats. However the steady wingbeat seems to differ for each fruit fly and the asymmetry between the left and right wing kinematics makes it still very difficult to analyze maneuvering wing kinematics w.r.t. steady wing kinematics over multiple flies. An average wingbeat of the steady flight part of a movie sequence with symmetric wing kinematics will allow for a better comparison between fruit flies and also is better suited to the symmetric geometric model of the fly.

The average wingbeat of a movie sequence is taken from the time before the fruit fly triggers the laser trigger. At this phase the fruit fly is flying at low speeds or hovering through the focal volume most of the time, therefore this phase is called the steady flight phase. During the steady flight phase the fly might perform some maneuvers, however the duration of these maneuvers is much longer than for escape maneuvers. However to make sure that occasional maneuvers in the steady flight phase do not affect the average wingbeat significantly; a weighted average is taken. Usually the steady flight phase takes between the 50% and 80% of the duration of the movie, such that there is a sufficient amount of wingbeats. The minimum amount of wingbeats for which an average will be generated is 5 wingbeats. At the start and end of the piecewise polynomial fit one of the boundary conditions consists of a mirrored image of the wingbeat, it turns out that this definition of the boundary conditions causes a mild Runge phenomenon. Although the Runge phenomenon is almost always damped out within the first stroke, the first two wingbeats of a sequence are not included in the average wingbeat.

The average wingbeat procedure starts with obtaining an average left wingbeat and an average right wingbeat. This is done by taking an average of the polynomial coefficients of each wing kinematic angle. As the polynomial fit is a linear fit it is allowed to take the average over the fitting coefficients instead of the resulting polynomial fit. The weighted average is obtained by multiplying each coefficient vector of each wingbeat by its own weight scalar and taking the sum of all the weighted coefficient vectors to get one average polynomial coefficient vector. The element i of the average polynomial coefficient vector $\bar{a}$ is defined as:

$$\bar{a}(i) = \frac{\sum_{j=1}^{m} w_j(i) a_j(i)}{\sum_{j=1}^{m} w_j(i)},$$

where the weight $w_j(i)$ is:

$$w_j(i) = \sum_{k=1}^{m} \frac{1}{\left(a_k(i) - a_j(i)\right)^4}.$$

The polynomial coefficient vectors a_k and a_j are the same sequence of polynomial coefficient vectors of the wingbeats used for the average. The weight takes the difference between one coefficient of one wingbeat and the same coefficient of other wingbeats. In this way a wingbeat of which the coefficients deviate too much from the other wingbeats has almost negligible

influence on the average wingbeat. This makes sure that a maneuver in the sequence of wingbeats used to obtain the average has not too much effect.

Now the weighted average is obtained there is one condition which is not fulfilled. This is the periodic boundary condition, for simulation purposes it is necessary to be able to iterate the average wingbeat over time. The periodic boundary condition can be established by using the restricted least-squares fit. In this case the ordinary least-squares fit vector β does not consists of the local polynomial fits of subsequent strokes but of $\bar{a}$ repeated several times. The repetition of $\bar{a}$ makes that the boundary at the start of the wingbeat will equal the end of the wingbeat upon the fourth derivative. As at the start and the end of vector β the Runge phenomenon might occur, a number of 9 average wingbeats is used in β and only the wingbeat in the middle of β^* is used as the periodic average wingbeat.

Using the procedure just described the average left and right wingbeat kinematic angles are obtained; $\bar{a}_{\theta_L}$, $\bar{a}_{\eta_L}$, $\bar{a}_{\phi_L}$, $\bar{a}_{\theta_R}$, $\bar{a}_{\eta_R}$ and $\bar{a}_{\phi_R}$. Using the left and right average wingbeat, the wing kinematics of a fruit fly can be corrected for their asymmetry. This is done by the so-called deviation coefficient, a^{dev}, which is the difference between the actual polynomial fit of a wingbeat and the average polynomial fit. For the left wing kinematics for this becomes; $a^{dev}_{\theta_L} = a_{\theta_L} - \bar{a}_{\theta_L}$, $a^{dev}_{\eta_L} = a_{\eta_L} - \bar{a}_{\eta_L}$ and $a^{dev}_{\phi_L} = a_{\phi_L} - \bar{a}_{\phi_L}$. The definition is exactly the same for the right wingbeat, using the right average polynomial fit. The difference between the left and right average wing kinematics is now corrected by constructing a single set of average wing kinematics which yields for both wings. The average symmetric wingbeat, $\bar{a}_{LR}$ is obtained by the same procedure as for the average left and average right wingbeat, the difference is that the average is taken over the left and right polynomial fits combined. Also the weights of the weighted average take now the variation between the left and the right polynomial fits into account. In Fig. 6.4; the average left wing kinematics, the average right wing kinematics and the symmetric average wing kinematics are displayed. With the average symmetric wing kinematics established, $\bar{a}_{\theta_L R}$, $\bar{a}_{\eta_L R}$ and $\bar{a}_{\phi_L R}$, the symmetry correction on the actual polynomial fits of the left and right wingbeat can be performed. This is simply done by adding the deviation coefficients of the wing kinematics to the symmetric average wingbeat: $a^*_{\theta_L} = \bar{a}_{\theta_L R} + a^{dev}_{\theta_L}$, $a^*_{\eta_L} = \bar{a}_{\eta_L R} + a^{dev}_{\eta_L}$ and $a^*_{\phi_L} = \bar{a}_{\phi_L R} + a^{dev}_{\phi_L}$. The symmetry correction for the right wingbeat is done in the same way. By obtaining all the symmetric average wingbeats from all the tracked movie sequences the so-called global average wingbeat can be established. The polynomial fit of the global average polynomial fit, a_{glob}, is given in Table. 6.1 in combination with the global average frequency and *down_up* ratio.

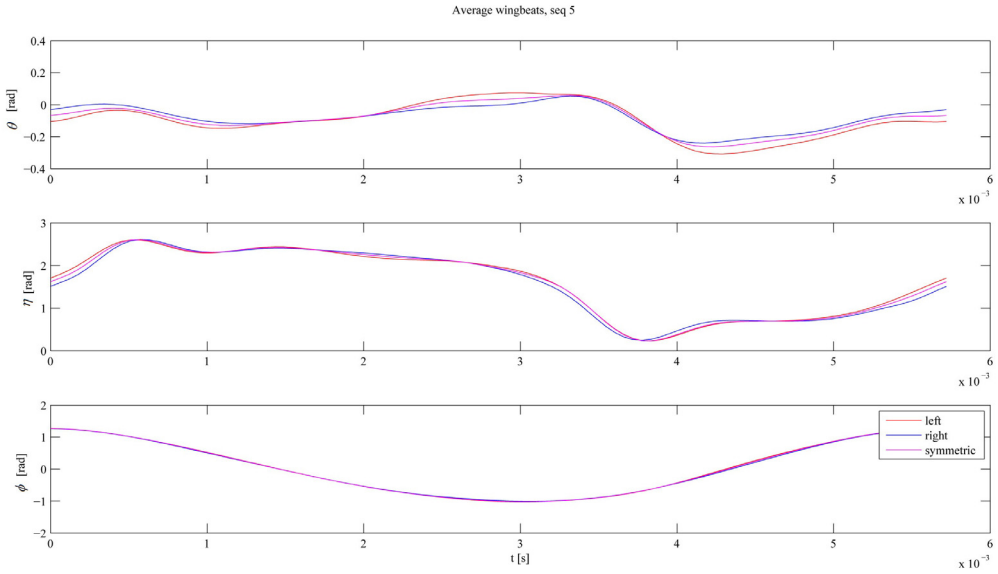

Figure 6.4: Average left, average right and symmetric wingbeat.

Chapter 7

Dynamic Simulation Model

The dynamic simulation model combines the body and wing model (Chapter 4), the polynomial coefficients of the wing kinematics (Chapter 6), the body dynamics, an inertial model and an aerodynamic model in one time-integration method to simulate steady and maneuvering flight of an individual fruit fly. Although the wing kinematics and the body and wing model for the dynamic simulation have been constructed carefully, the amount of uncertainty of these parameters in combination with the buildup in error due to the open-loop character of this simulation will make the simulation only realistic for a few subsequent wingbeats. Nonetheless these wingbeats have significant importance because they can test the validity of maneuvering wing kinematics under free flight conditions. The RoboFly is designed to simulate wingbeats under hovering flight conditions. During its use the apparatus has been adjusted such that it can simulate forward and backward translational motion and yaw motion as well. However the other DOF of the fly cannot be modeled yet. Also most maneuvers have an acceleration or rotation vector which does not align with one of the principal axes, an arbitrary translational or rotational motion is even more difficult to simulate on the RoboFly. Finally the inertia of the body and wing of the fly do not scale with the Reynolds number as is the case for the inertia of the fluid. The selected aerodynamic and inertial model are relatively simple. One could argue that by setting up the problem as a fluid-structure interaction problem and solving this problem by using a Computational Fluid Dynamics (CFD) code for the flow in combination with a finite-element method for modeling the structure, could yield much more accurate results. However one of the drawbacks of this approach is that the more detailed modeling also requires more details about for example the structure of the fly's wing. Getting a detailed image about the stiffness of the fruit fly's wing is quite difficult. Also the computation time of such a fluid-structure interaction problem would be huge. For example, a very recent study of the structure of the wake of a fruit fly needed more than a day to simulate just one wingbeat, Ref. [1]. The computation times and complexity of a fluid-structure interaction problem do not fit in the approach of this thesis to perform large scale analysis on the complete data-set of video sequences.

7.1 Aerodynamic Model

The quasi-steady aerodynamic model of insect flight has transformed from a rather crude model based on blade-element theory and the so-called pulsed momentum disc theory of C.P. Ellington, Ref. [14], towards the current quasi-steady model which is quite accurate in predicting forces and moments during hovering flight. The current quasi-steady model is based on extensive RoboFly experiments and unsteady aerodynamic effects like the LEV and rotational lift are included in the model, Ref. [11]. These two unsteady aerodynamic effects are also the most significant contributors to the lift and drag generation during flapping hovering flight. As these two models of force generation are relatively simple and robust only translational and rotational forces are included in the aerodynamic model of this thesis.

Translational Forces

The translational lift and drag force on a blade-element in the quasi-steady model has the same definition of translational forces in the traditional blade-element theory. The difference is in how the lift and drag coefficients are obtained, in this case the relation between the lift and drag coefficients and the angle of attack is obtained by dynamically scaled experiments with insect wings. These experiments are performed such that the rotational velocities and accelerations on the wing are the same as in flapping flight; however the local free stream airspeed for the blade-elements is constant as well as the local angle of attack, Ref. [9]. After some start-up effects, the LEV on the wing is steady and one can obtain constant lift and drag coefficients of the wing including the LEV. Using this methodology the following relations for the local lift and drag coefficient were found:

$$c_l(\alpha) = 0.225 + 1.58 \cdot sin(2.13\alpha - 7.2)$$

and:

$$c_d(\alpha) = 1.92 - 1.55 \cdot cos(2.04\alpha - 9.82)$$

in which α is the local angle of attack in degrees, Ref. [10]. Using these coefficients the local value of the lift and drag force can be computed:

$$L_{trans} = \frac{1}{2}\rho c\left(u_x^2 + u_z^2\right) c_l(|\alpha|)\,\Delta R \cdot 10^{-3}\,[N]$$

and:

$$D_{trans} = \frac{1}{2}\rho c\left(u_x^2 + u_z^2\right) c_d(|\alpha|)\,\Delta R \cdot 10^{-3}\,[N]\,.$$

The air velocity is defined in the wing reference frame and spanwise flow is excluded from the lift and drag calculations as the wingtip velocity is significantly larger than the body velocity. Therefore spanwise flow is only noticeable during stroke reversal and compared to the lift and drag generation during the stroke the effects can be ignored. The lift and drag force must be converted to the wing reference frame, as the wing flips during the wingbeat

one must distinguish the downstroke from the upstroke. This is done by looking at the sign of the angle of attack, in this case the downstroke is defined when $\alpha \geq 0$:

$$F_{trans} = \begin{bmatrix} L_{trans}\ sin\left(|\alpha|\right) - D_{trans}\ cos\left(|\alpha|\right) \\ 0 \\ -L_{trans}\ cos\left(|\alpha|\right) - D_{trans}\ sin\left(|\alpha|\right) \end{bmatrix} [N]$$

and the upstroke when $\alpha < 0$:

$$F_{trans} = \begin{bmatrix} L_{trans}\ sin\left(|\alpha|\right) - D_{trans}\ cos\left(|\alpha|\right) \\ 0 \\ L_{trans}\ cos\left(|\alpha|\right) + D_{trans}\ sin\left(|\alpha|\right) \end{bmatrix} [N]\,.$$

In this case the air density is given in $\left[kg \cdot mm^3\right]$. The individual force vectors on the blade elements can be summed up to a single force vector for each wing. Multiplication by the rotation matrices R_L^T and R_R^T yields the force of the left and right wing in the body reference frame. By multiplying and summing the local force vectors with the distance of the blade element from the wing joint the torque at the wing joint in $[N \cdot mm]$ in the wing reference frame. Conversion of the left and right torque vector to the body reference frame and adding the contributions of the left and right force vectors of the wing yields the aerodynamic torque at the c.g.

Rotational Forces

The rotational force at a blade element is a function of the magnitude of the air velocity and the derivative of the angle of attack, $\dot{\alpha}$. The rotational force is always normal to the wing surface and its sign depends on whether α is increasing or decreasing. The local rotational force can be expressed as:

$$F_{rot} = \begin{bmatrix} 0 \\ 0 \\ C_{rot}\ \rho\ \sqrt{u_x^2 + u_z^2}\ \dot{\eta}\ c^2\ \Delta R \cdot 10^{-3} \end{bmatrix} [N]\,, \tag{7.1}$$

with $C_{rot} = 1.55$, Ref. [26], and just as with the translational forces spanwise flow is neglected. The angular velocity $\dot{\eta}$ is the time derivative of the wing pitch angle η. The procedure for the right wing is similar. The vector $y_{sect\ L}$ is the distance from the center of the blade element to the wing joint in the wing reference frame. Just as in the case of the translational force, also the values of the local rotational forces can be added up and transformed to the c.g. of the body. The translational and rotational forces and moments can be combined to form the aerodynamic force and aerodynamic moment, F_{aero} and M_{aero} respectively.

7.2 Inertia Model

The inertia of a fruit fly is rather complex, even the simple geometric model consisting of three rigd bodies still has a lot of complexity. The weight of the wings and their virtual mass

is less than 1% of the body mass, however due to the high angular velocities and angular accelerations the wings influence the inertia of the fruit fly significantly. The method used to model all the inertial effects like the Coriolis and centrifugal forces is based on Langrangian dynamics, Ref. [27]. Using Lagrangian dynamics it is possible to establish the Lagrange's equations of motion. In these equations of motion the gravity and aerodynamic forces are modeled as external forces and moments, which leaves the resulting forces and moments in the equations as the inertial forces and moments. These inertial forces and moments can be divided into forces and moments as the result of the linear and angular acceleration of the body and the forces and moments as a result of linear and angular body velocity and the angular velocities and accelerations of both wings.

Lagrangian Dynamics

Lagrangian dynamics are based on the energy stored in the system for which the equations of motion have to be obtained. The standard Lagrange's equation can be written as:

$$\frac{d}{dt}\left(\frac{\partial L}{\partial \dot{q}_k}\right) - \frac{\partial L}{\partial q_k} = Q_k \quad k = 1, 2, ..., n$$

where L is the Lagrangian of the system which is the difference between the kinetic and potential energy of the system, q_k are the generalized coordinates and Q_k are the generalized forces. The generalized coordinates q_k are in this case the position vector r (which runs from the origin of the inertial reference frame to the c.g. of the body) and the orientation of the body. The derivative of the position gives the velocity which can be transformed to the body reference frame. The orientation of the body is given by the body quaternion q_b and the derivative of the body quaternion is $\dot{q}_b$. As $\dot{q}_b$ is not independent this is problematic in the standard Lagrange's equation. However as $\dot{q}_b$ is a linear function of the angular velocity of the body ω_b the generalized coordinate $\dot{q}_b$ can be replaced by the quasi-coordinate ω_b, Ref. [22] and Ref. [24]. The quaternion derivative can be written as $\dot{q}_b = [\beta]\,\omega_b$, where $[\beta]$ is a matrix built up by the identities of q_b. The quasi-coordinate can be inserted in Lagrange's equation yielding:

$$\frac{d}{dt}\left(\frac{\partial \bar{L}}{\partial \omega}\right) + [\beta]^T [\gamma] \left(\frac{\partial \bar{L}}{\partial \omega}\right) - [\beta]^T \left(\frac{\partial \bar{L}}{\partial q}\right) = (N)$$

with ω as the quasi-coordinates, q the generalized coordinates, N the adjusted generalized forces and $\bar{L}$ the Lagrangian rewritten as a function of ω_k and q_k. Inserting the generalized position vector r and the quasi-coordinate q_b in the rewritten Lagrange's equation gives the specific Lagrange's equation for this problem:

$$\frac{d}{dt}\left(\frac{\partial L}{\partial v_b}\right) + [\omega_b \times] \frac{\partial L}{\partial v_b} - R_b \frac{\partial L}{\partial r} = F_b$$
$$\frac{d}{dt}\left(\frac{\partial L}{\partial \omega_b}\right) + [v_b \times] \frac{\partial L}{\partial v_b} + [\omega_b \times] \frac{\partial L}{\partial \omega_b} - R_\varphi \frac{\partial L}{\partial \varphi_b} = M_b$$

where φ stands for the Euler angles needed to express the body orientation in independent coordinates. The matrix R_φ stands for the transformation matrix necessary to transform the

Euler angle rates $\dot{\varphi}$ to the body angular velocity ω_b. The vector F_b stands for the generalized body force and the vector M_b the generalized body moment, both in the body frame of reference. The matrix $[\omega_b\times]$ stands for the cross product matrix of ω_b.

Now it is time to focus on the Lagrangian L, which is the difference between the kinetic energy and potential energy, $L = T - V$. In this case the dynamic system consisting of three rigid bodies coupled by two ball joints does not have any potential energy. This is convenient as the derivative of the Lagrangian w.r.t. the generalized coordinates becomes zero, yielding:

$$\frac{d}{dt}\left(\frac{\partial L}{\partial v_b}\right) + [\omega_b\times]\frac{\partial L}{\partial v_b} = F_b$$
$$\frac{d}{dt}\left(\frac{\partial L}{\partial \omega_b}\right) + [v_b\times]\frac{\partial L}{\partial v_b} + [\omega_b\times]\frac{\partial L}{\partial \omega_b} = M_b$$

The kinetic energy T is defined as:

$$T = \frac{1}{2}\int \left[v_b,\ \omega_b,\ \omega_L^b,\ \omega_R^b\right]^T \left[v_b,\ \omega_b,\ \omega_L^b,\ \omega_R^b\right] dm$$

which can be rewritten as a matrix equation:

$$T = \frac{1}{2}\left[v_b,\ \omega_b,\ \omega_L^b,\ \omega_R^b\right]^T [M] \left[v_b,\ \omega_b,\ \omega_L^b,\ \omega_R^b\right]$$

in which $[M]$ is the mass matrix and the upper score b indicates that the angular velocities ω_L^b and ω_R^b are in the body reference frame. The mass matrix can be divided into 16 block matrices:

$$M = \begin{bmatrix} M_{11} & M_{12} & M_{13} & M_{14} \\ M_{21} & M_{22} & M_{23} & M_{24} \\ M_{31} & M_{32} & M_{33} & M_{34} \\ M_{41} & M_{42} & M_{43} & M_{44} \end{bmatrix}$$

The mass matrix is symmetric and the block matrices are defined as:

$$M_{11} = \begin{bmatrix} m_{fly} & 0 & 0 \\ 0 & m_{fly} & 0 \\ 0 & 0 & m_{fly} \end{bmatrix},$$

$$M_{12} = m_{vw}\left(-\left[J_L\times\right] - R_L^T\left[c_L\times\right]R_L\right) + m_{vw}\left(-\left[J_R\times\right] - R_R^T\left[c_R\times\right]R_R\right),$$

$$M_{13} = m_{vw}\left(-R_L^T\left[c_L\times\right]R_L\right),$$

$$M_{14} = m_{vw}\left(-R_R^T\left[c_R\times\right]R_R\right),$$

$$M_{21} = M_{12}^T,$$

$$\begin{aligned} M_{22} = {} & I_b + R_L^T I_{vw\ L}R_L + R_R^T I_{vw\ R}R_R + m_{vw}\left(-J_L - R_L^T\left[c_L\times\right]R_L\right)^T\left(-J_L - R_L^T\left[c_L\times\right]R_L\right) \\ & + m_{vw}\left(-J_R - R_R^T\left[c_R\times\right]R_R\right)^T\left(-J_R - R_R^T\left[c_R\times\right]R_R\right), \end{aligned}$$

$$M_{23} = R_L^T I_{vw\ L}R_L + m_{vw}\left(-J_L - R_L^T\left[c_L\times\right]R_L\right)^T\left(-R_L^T\left[c_L\times\right]R_L\right),$$

$$M_{24} = R_R^T I_{vw\ R}R_R + m_{vw}\left(-J_R - R_R^T\left[c_R\times\right]R_R\right)^T\left(-R_R^T\left[c_R\times\right]R_R\right),$$

$$M_{31} = M_{13}^T,$$

$$M_{32} = M_{23}^T,$$

$$M_{33} = R_L^T I_{vw\ L}R_L + m_{vw}\left(R_L^T\left[c_L\times\right]R_L\right)^T\left(R_L^T\left[c_L\times\right]R_L\right),$$

$$M_{34} = \begin{bmatrix} 0 & 0 & 0 \\ 0 & 0 & 0 \\ 0 & 0 & 0 \end{bmatrix},$$

$$M_{41} = M_{14}^T,$$

$$M_{42} = M_{24}^T,$$

$$M_{43} = M_{34}^T,$$

$$M_{44} = R_R^T I_{vw\ R}R_R + m_{vw}\left(R_R^T\left[c_R\times\right]R_R\right)^T\left(R_R^T\left[c_R\times\right]R_R\right).$$

The block matrices contain some terms which have been defined in Chapter 4 and some new body & wing related terms: R_L and R_R are the rotation matrices of the left and right wing, I_b is the body inertia matrix, $I_{vw\ L}$ and $I_{vw\ R}$ are the virtual inertia tensors of the left and right wing, c_L and c_R are the position vectors of the c.g. of the left and right wing (including virtual mass) w.r.t. the wing joint and defined in the wing reference frame, m_{vw} is the wing mass plus virtual wing mass of a single wing and m_{fly} the mass of the fly (body and wing mass without virtual wing mass). Fig. 4.6 shows how J_L and J_R are located in the body of the fly.

Equations of Motion

With the Lagrangian L known, $L = T$, it is possible to construct the Lagrange's equations of motion. Therefore it is necessary to obtain the derivatives of the Lagrangian. The derivatives w.r.t. the velocities v_b and ω_b are:

$$\begin{aligned}\frac{\partial L}{\partial v_b} =& \frac{1}{2}\left(v_b^T M_{11} + \omega_b^T M_{21} + \omega_L^{b^T} M_{31} + \omega_R^{b^T} M_{41}\right) + \frac{1}{2}\left(M_{11} v_b + M_{12}\omega_b + M_{13}\omega_L^b + M_{14}\omega_R^b\right)\\ \frac{\partial L}{\partial \omega_b} =& \frac{1}{2}\left(v_b^T M_{12} + \omega_b^T M_{22} + \omega_L^{b^T} M_{32} + \omega_R^{b^T} M_{42}\right) + \frac{1}{2}\left(M_{21} v_b + M_{22}\omega_b + M_{23}\omega_L^b + M_{24}\omega_R^b\right)\end{aligned}$$

and their time derivatives:

$$\begin{aligned}\frac{d}{dt}\left(\frac{\partial L}{\partial v_b}\right) =& \frac{1}{2}\left(a_b^T M_{11} + \omega_b^T \dot{M}_{21} + \dot{\omega}_b^T M_{21} + \omega_L^{b^T} \dot{M}_{31} + \dot{\omega}_L^{b^T} M_{31} + \omega_R^{b^T} \dot{M}_{41} + \dot{\omega}_R^{b^T} M_{41}\right)\\ &+ \frac{1}{2}\left(M_{11} a_b + \dot{M}_{12}\omega_b + M_{12}\dot{\omega}_b + \dot{M}_{13}\omega_L^{b^T} + M_{13}\dot{\omega}_L^{b^T} + \dot{M}_{14}\omega_R^{b^T} + M_{14}\dot{\omega}_R^{b^T}\right)\\ \frac{d}{dt}\left(\frac{\partial L}{\partial \omega_b}\right) =& \frac{1}{2}\left(a_b^T M_{12} + v_b^T \dot{M}_{12} + \omega_b^T \dot{M}_{22} + \dot{\omega}_b^T M_{22} + \omega_L^{b^T} \dot{M}_{32} + \dot{\omega}_L^{b^T} M_{32} + \omega_R^{b^T} \dot{M}_{42} + \dot{\omega}_R^{b^T} M_{42}\right)\\ &+ \frac{1}{2}\left(M_{21} a_b + \dot{M}_{21} v_b + \dot{M}_{22}\omega_b + M_{22}\dot{\omega}_b + \dot{M}_{23}\omega_L^b + M_{23}\dot{\omega}_L^b + \dot{M}_{24}\omega_L^b + M_{24}\dot{\omega}_L^b\right)\end{aligned}$$

The time derivatives of the mass matrix require differentiation of the various rotation matrices involved. The time derivative for a rotation matrix is defined as $\frac{d}{dt}(R) = [\omega\times]\, R$ and using

the product rule the following matrix derivatives are obtained:

$$\dot{M}_{12} = m_{vw}\left[-R_L^T\left[\omega_L\times\right]\left[c_L\times\right]R_L - R_R^T\left[\omega_R\times\right]\left[c_R\times\right]R_R\right]$$

$$\dot{M}_{13} = m_{vw}\left[-R_L^T\left[\omega_L\times\right]\left[c_L\times\right]R_L\right]$$

$$\dot{M}_{14} = m_{vw}\left[-R_R^T\left[\omega_R\times\right]\left[c_R\times\right]R_R\right]$$

$$\dot{M}_{21} = \dot{M}_{12}^T$$

$$\begin{aligned}\dot{M}_{22} =& R_L^T\left[\omega_L\times\right]I_{vw\ L}R_L + R_R^T\left[\omega_R\times\right]I_{vw\ R}R_R + R_L^T I_{vw\ L}\left[\omega_L\times\right]^T R_L + \\ & R_R^T I_{vw\ R}\left[\omega_R\times\right]^T R_R + m_{vw}\left[-R_L^T\left[\omega_L\times\right]\left[c_L\times\right]R_L\right]^T\left[-\left[J_L\times\right] - R_L^T\left[c_L\times\right]R_L\right] + \\ & m_{vw}\left[-\left[J_L\times\right] - R_L^T\left[c_L\times\right]R_L\right]^T\left[-R_L^T\left[\omega_L\times\right]\left[c_L\times\right]R_L\right] + \\ & m_{vw}\left[-R_R^T\left[\omega_R\times\right]\left[c_R\times\right]R_R\right]^T\left[-\left[J_R\times\right] - R_R^T\left[c_R\times\right]R_R\right] + \\ & m_{vw}\left[-\left[J_R\times\right] - R_R^T\left[c_R\times\right]R_R\right]^T\left[-R_R^T\left[\omega_R\times\right]\left[c_R\times\right]R_R\right]\end{aligned}$$

$$\begin{aligned}\dot{M}_{23} =& R_L^T\left[\omega_L\times\right]I_{vw\ L}R_L + R_L^T I_{vw\ L}\left[\omega_L\times\right]^T R_L + \\ & m_{vw}\left[-R_L^T\left[\omega_L\times\right]\left[c_L\times\right]R_L\right]^T\left[-R_L^T\left[c_L\times\right]R_L\right] + \\ & m_{vw}\left[-\left[J_L\times\right] - R_L^T\left[c_L\times\right]R_L\right]^T\left[-R_L^T\left[\omega_L\times\right]\left[c_L\times\right]R_L\right]\end{aligned}$$

$$\begin{aligned}\dot{M}_{24} =& R_R^T\left[\omega_R\times\right]I_{vw\ R}R_R + R_R^T I_{vw\ R}\left[\omega_R\times\right]^T R_R + \\ & m_{vw}\left[-R_R^T\left[\omega_R\times\right]\left[c_R\times\right]R_R\right]^T\left[-R_R^T\left[c_R\times\right]R_R\right] + \\ & m_{vw}\left[-\left[J_R\times\right] - R_R^T\left[c_R\times\right]R_R\right]^T\left[-R_R^T\left[\omega_R\times\right]\left[c_R\times\right]R_R\right]\end{aligned}$$

The generalized forces and moments, F_b and M_b of the Lagrange's equations of motion can be divided in aerodynamic and gravitational forces. Inserting the derivatives of the Lagrangian in the equations of motion yields:

$$M_{11}a_b + M_{12}\dot{\omega}_b = F_A + F_G - \left[\omega_b\times\right]\frac{\partial L}{\partial v_b} - \left(\dot{M}_{12}\omega_b + \dot{M}_{13}\omega_L^b + M_{13}\dot{\omega}_L^b + \dot{M}_{14}\omega_R^b + M_{14}\dot{\omega}_R^b\right)$$

$$\begin{aligned}M_{21}a_b + M_{22}\dot{\omega}_b =& M_A - \left[v_b\times\right]\frac{\partial L}{\partial \omega_b} - \left[\omega_b\times\right]\frac{\partial L}{\partial \omega_b} - \\ & \left(\dot{M}_{21}v_b + \dot{M}_{22}\omega_b + \dot{M}_{23}\omega_L^b + M_{23}\dot{\omega}_L^b + \dot{M}_{24}\omega_R^b + M_{24}\dot{\omega}_R^b\right)\end{aligned}$$

The inertia terms in the equation of motion can be divided into inertial forces and moments, $F_{I_{acc}}$ and $M_{I_{acc}}$, due to accelerations and inertial forces and moments due to velocities, $F_{I_{vel}}$ and $M_{I_{vel}}$. The equations of motion can be written as:

$$\begin{bmatrix} F_{I_{acc}} \\ M_{I_{acc}} \end{bmatrix} = \begin{bmatrix} F_A \\ M_A \end{bmatrix} + \begin{bmatrix} F_G \\ 0 \end{bmatrix} + \begin{bmatrix} F_{I_{vel}} \\ M_{I_{vel}} \end{bmatrix}.$$

The terms on the left side of the equation are the inertial acceleration forces and moments, the resulting terms on the right side besides the aerodynamic and gravitational terms are the inertial velocity terms.

7.3 Time Integration

The equations of motion of the previous section are defined as a state-space system and can be solved as a first order differential equation. The methodology used to solve the differential equation is an implicit Runge-Kutta method. The choice for an implicit Runge-Kutta method was not direct, first an explicit Runge-Kutta method was used as it is easier to implement. The build-up in error however is too severe for the explicit method to be useful. The implicit Runge-Kutta method used is a build-in function of Matlab® and will not be discussed here. The initial conditions and the state-space function used in the methodology however will be discussed.

The ODE solver of Matlab® selected to solve the differential equation is the *ode45* solver. The solver integrates a system of differential equations $\dot{y} = f(t, y)$ from t_0 to t_f with initial conditions y_0. The state-space function $f(t, y)$ uses the state-space definition of the equations to compute the time derivatives of the state, $y = [v_b, \omega_b]$. The state derivative $\dot{y}$ is obtained by:

$$\begin{bmatrix} a_b \\ \dot{\omega}_b \end{bmatrix} = \begin{bmatrix} M_{11} & M_{12} \\ M_{21} & M_{22} \end{bmatrix}^{-1} \begin{bmatrix} F_A + F_g + F_{I_{vel}} \\ M_A + M_{I_{vel}} \end{bmatrix} \cdot 10^3$$

The factor 10^3 is necessary as the acceleration is given in mm/s^2 instead of m/s^2. Throughout the dynamic simulation the length scale is in mm instead of m, the forces are given in $[N]$ and the moments in $[N \cdot mm]$. The aerodynamic forces and moments are dependent on the body and wing parameters of the specific fly, the wing kinematics and the body kinematics being v_b and ω_b. Also the inertial model is dependent on the body and wing parameters, the wing kinematics and body kinematics. As in the implicit Runge-Kutta method the time step is not constant and also not always increasing, it is necessary to have a continuous definition of the wing kinematics and body kinematics. The body kinematics are given with the function y and luckily the wing kinematics are independent of the body kinematics and therefore known in advance. By defining the wing kinematics at a time grid t_f and interpolating at the specific time t the instantaneous forces and moments can be obtained.

Unfortunately the gravity force is dependent on the body orientation which is not given in y but must be obtained by integration of the body angular velocity. In this case the body quaternion update is used, the quaternion update is defined in Appendix A. The time step Δt necessary for the quaternion update is obtained by retrieving the time of the previous iteration stored in a file outside the function. Also the body quaternion of the previous iteration is obtained in this way such that the current quaternion can be obtained. Transforming the current body quaternion into a rotation matrix yields the direction of the gravity vector in the body reference frame. The magnitude of the gravity force vector is obtained by multiplying the mass of the fly by the gravitational acceleration, 9.81 $[m/s^2]$. The quaternion update

turns out to be rather accurate over the simulation. During simulated wingbeats with high body angular velocities the gravity vector diverges from the z-axis of the inertial reference frame by a negligible angle.

The initial conditions for the function, y_0, consist of the initial position and orientation of the c.g. of the body and the initial velocity and angular velocity of the body. There are two different cases of analysis which require two different sets of initial conditions. The first case analyzes only the effect of inertial forces and moments generated by the wing motion on the dynamics of the body. In this case the body can be positioned and oriented in any way, it is however convenient to keep the strokeplane horizontal. This is done by obtaining the quaternion of the transpose of the strokeplane reference frame multiplied by a rotation matrix of a rotation of 180 degrees along the x-axis of the strokeplane reference frame in order to get the z-axis of the strokeplane pointing downwards. The position does not affect the dynamic simulation in any way and is therefore taken to be $[0, 0, 0]$ in the inertial reference frame.

The second case analyzes wingbeats obtained from the movie sequences including the aerodynamic and gravitational forces. The initial orientation and initial velocities are obtained from the first frame linked to the specific wingbeat. However the inclusion of the aerodynamic and gravitational forces yields some problems. In the first place the aerodynamic model usually underestimates the force production necessary for weight support. Also the inertia of the wings and the position of the aerodynamic center in the strokeplane generates a moment around the y-axis of the strokeplane. This pitching moment is rather strong and makes it difficult to compare the simulated wingbeat with the actual wingbeat. The c.g. of the body is determined carefully, however it would be very coincidental that the c.g. of the geometric model really coincides with the actual c.g. Even when it does it might be very well the case that the pitch rate of the body in real flight is stabilized over multiple wingbeats and that it is not necessarily zero over a single wingbeat. It is possible to construct a hovering average wingbeat in which the c.g. is placed such that there is no resulting average pitching moment. However the iterative method would require a significant amount of iterations before a satisfactory result is obtained and still the weight support issue is not solved. Therefore another approach is used, for an average hovering wingbeat in which the body is oriented such that the strokeplane is horizontal the resulting forces and moments are determined. This will generate two average resultant forces, $\bar{F}_{I_{acc}}$ in the x direction and $\bar{F}_{I_{acc}}$ in the z direction, and one average resultant moment, $\bar{M}_{I_{acc}}$ around the y-axis, all in the strokeplane reference frame. As the wing kinematics are symmetrical and the strokeplane is horizontal, there are no average resultant asymmetric forces and moments. The resultant forces and moments are used as an extra initial condition F_0 and M_0. This extra initial condition is used in the state-space function:

$$\begin{bmatrix} a_b \\ \dot{\omega}_b \end{bmatrix} = \begin{bmatrix} M_{11} & M_{12} \\ M_{21} & M_{22} \end{bmatrix}^{-1} \begin{bmatrix} F_A + F_g + F_{I_{vel}} - F_0 \\ M_A + M_{I_{vel}} - M_0 \end{bmatrix} \cdot 10^3$$

The effect of F_0 and M_0 is that the disturbing effects of the limited weight support and the pitching moment can be removed from a hovering wingbeat. Usually F_0 and M_0 need to be refined to obtain a stable hovering wingbeat. The refinement is done by obtaining F_0 and M_0 from a dynamic simulation of an average hovering wingbeat and use these initial conditions in another dynamic simulation of the same wingbeat. By determining the resultant forces and moments of the last simulation and adding them to the F_0 and M_0 previously used the

resultant forces and moments of a new simulation are small enough to make the effects of the resulting pitching moment and weight support no longer noticeable for a single hovering wingbeat. This procedure is easy to implement and not as tedious as determining a new c.g. The stable hovering wingbeat offers a good basis for analyzing maneuvering wing kinematics.

7.4 Validation

The dynamic simulation described in the previous sections is quite a complex model and obtaining a proper image of the validity of the model as a whole is difficult. In Chapter 10 simulated wingbeats will be compared with the actual wingbeats obtained from the movie sequences. This gives a very good impression of how well the body and wing model, the polynomial fits of the wing kinematics, and the dynamic simulation are able to represent the actual dynamic behavior of a fruit fly. However before this analysis it is necessary to check the validity of the different components of the dynamic simulation.

Aerodynamic Model

Hovering insect flight has been documented quite well in literature and a comparison between the aerodynamic force production during hovering flight and the quasi-steady model. The validity of the quasi-steady model during maneuvering flight is not well described in literature and this is one of the subjects in which this thesis can be an addition to existing literature. In order to validate the aerodynamic model; the results of the quasi-steady model will be compared with a paper over the force generation during hovering *Drosophila* flight, Ref [17].

In Fig. 7.1, the results of the quasi-steady model for a symmetric average wingbeat are given. In Fig. 7.2, the force and moment development over time in the strokeplane reference frame of the same wingbeat as in Fig. 7.1 is given. In Chapter 4 a relation between the mass of the fly and the wing length was established. Using this relation and comparing the weight of a fruit fly with a certain wing length and the vertical aerodynamic force generation for its symmetric average wingbeat learns us that usually between 80 and 95% of the weight support can be delivered by the quasi-steady model of this thesis. In Fig. 7.3, the vertical force production for Robofly experiments and a quasi-steady model of Ref [17] is shown. When comparing the results of Fig. 7.2 and Fig. 7.3 the results are rather similar. The hovering wingbeat of the *Drosophila Hydei* and *Drosophila Melanogaster* both produce more lift during the upstroke than the downstroke and in both cases the drag of the downstroke opposes the drag of the upstroke. In Fig. 7.2 the peaks at the start of both strokes are stronger than in Fig. 7.3 which indicates that the rotational lift is stronger in the first case. The wing kinematics are in both cases quite similar, however for the *Drosophila Hydei* the downward motion at the start of the upstroke is more pronounced whilst the downstroke is roughly parallel to the strokeplane.

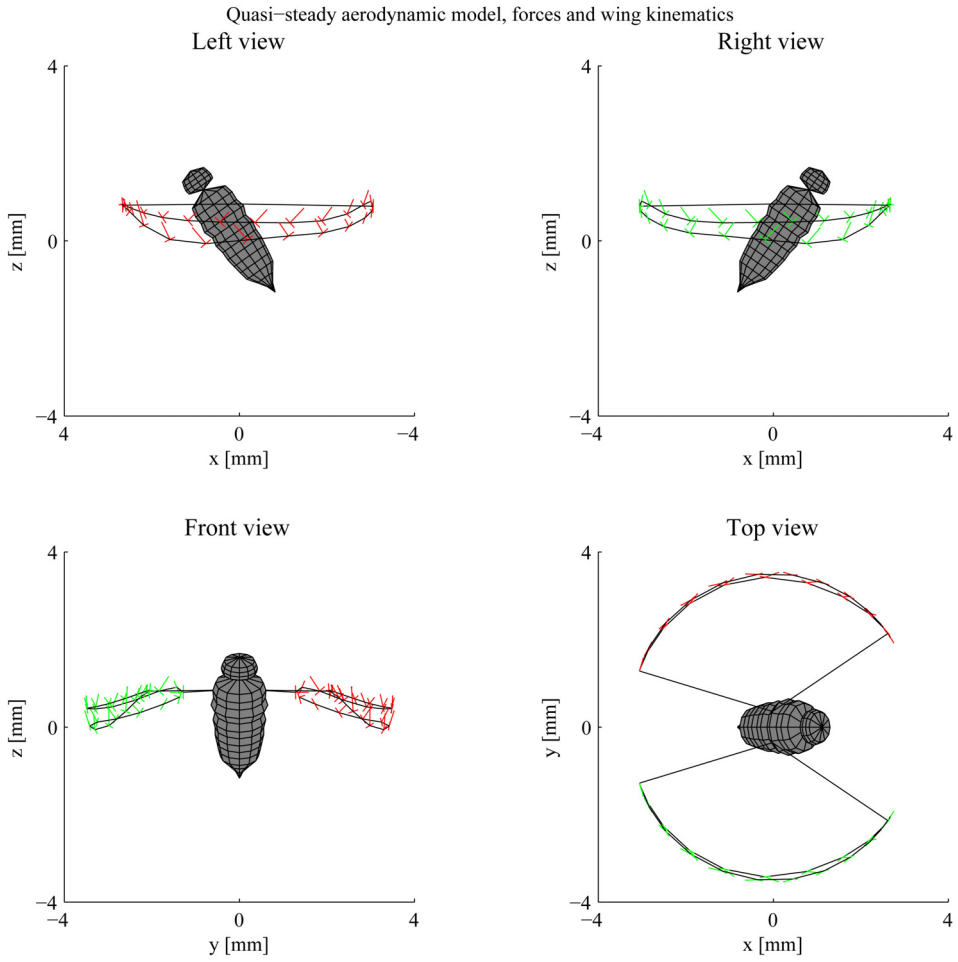

Figure 7.1: Schematic presentation of the relation between the wing kinematics and the force production of the quasi-steady model during the average symmetric wingbeat, a_{glob}.

Inertia Model

Due to the high wingbeat frequency the angular velocities and accelerations of the wings have considerable influence on the body motion. Effects like the Coriolis force are significant and might result in some counter-intuitive effects. In the dynamic simulation it is possible to analyze the inertial model without aerodynamic and gravitational forces. The inertia model is rather complex and it is quite difficult to obtain measurements of just the inertial forces generated by a fruit fly in free flight. However when analyzing the wing kinematics in vacuum there are a few conditions of the inertia model which must be satisfied. In the first place the average inertial forces over the wingbeat must be zero, such that the average position of the fruit fly remains stationary. Also the linear and angular momentum of the wingbeat must be conserved during the wingbeat.

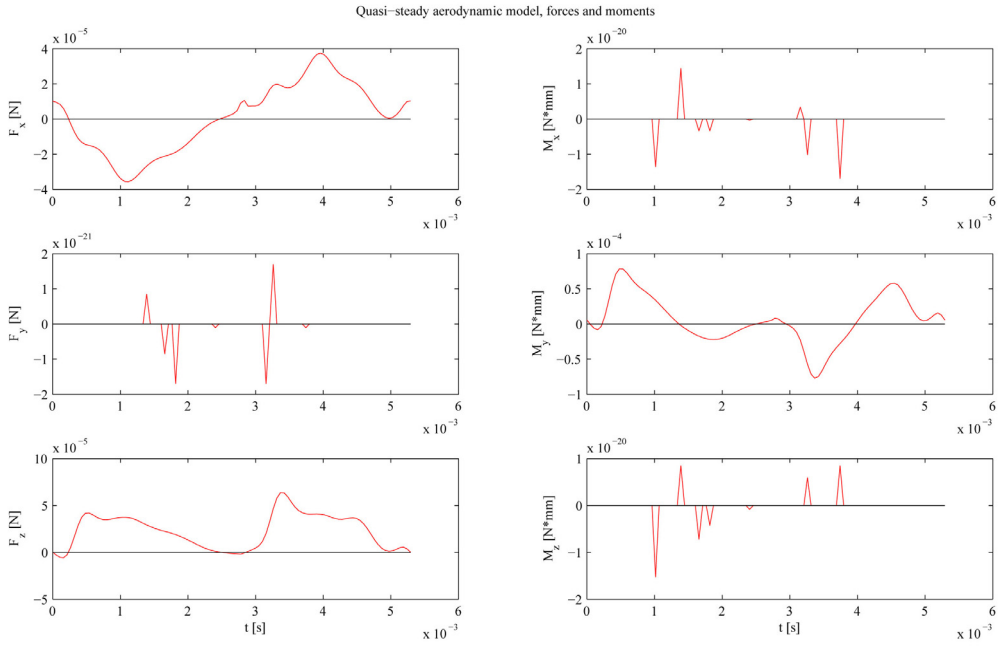

Figure 7.2: Forces and moments of the quasi-steady model during the average symmetric wingbeat, a_{glob}. For comparison purposes the y and z-axes of the strokeplane reference frame in this figure are flipped.

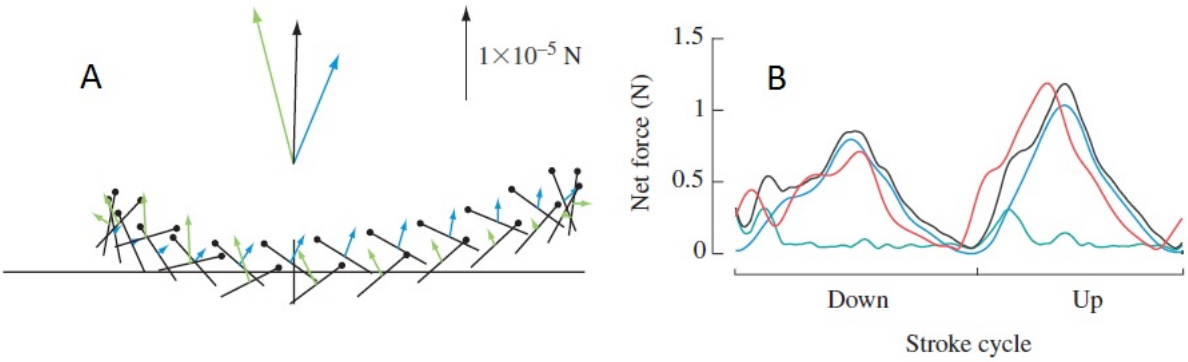

Figure 7.3: Aerodynamic force generation during a hovering wingbeat of a *Drosophila Melanogaster*, Ref [17]. A: side-view wingbeat, the motion to the left is the downstroke and the motion to the right is the upstroke. B: Lift-force generation; Robofly measurements (red), quasi-steady model translational and rotational lift (black), quasi-steady model translational lift (blue), quasi-steady model rotational lift (cyan).

Linear and angular momentum, LM and AM, are defined as:

$$\begin{bmatrix} LM \\ AM \end{bmatrix} = \begin{bmatrix} I \cdot m_{fly} & -m_{vw}\left([c_{J_L}\times] + [c_{J_R}\times]\right) \\ m_{vw}\left([c_{J_L}\times] + [c_{J_R}\times]\right) & I_b + R_L^T I_{vwL} R_L + R_R^T I_{vwR} R_R - \\ & m_{vw}\left([c_{J_L}\times]^2 + [c_{J_R}\times]^2\right) \end{bmatrix} \begin{bmatrix} v_b \\ \omega_b \end{bmatrix} - \begin{bmatrix} m_{vw} R_L^T [c_L\times] R_L & m_{vw} R_R^T [c_R\times] R_R \\ -R_L^T I_{vwL} R_L + & -R_R^T I_{vwR} R_R + \\ m_{vw}[c_{J_L}\times]\left[R_L^T [c_L\times] R_L\right] & m_{vw}[c_{J_R}\times]\left[R_R^T [c_R\times] R_R\right] \end{bmatrix} \begin{bmatrix} \omega_L^b \\ \omega_R^b \end{bmatrix}$$

with $c_{J_L} = \left[J_L + R_L^T c_L\right]$ and I the identity matrix. For convenience the initial body velocity and body angular velocity are taken such that the linear and angular momentum are zero during the wingbeat. The velocities v_{b_0} and ω_{b_0} necessary to obtain zero linear and angular momentum can be computed by:

$$\begin{bmatrix} v_{b_0} \\ \omega_{b_0} \end{bmatrix} = \begin{bmatrix} I \cdot m_{fly} & -m_{vw}\left([c_{J_L}\times] + [c_{J_R}\times]\right) \\ m_{vw}\left([c_{J_L}\times] + [c_{J_R}\times]\right) & I_b + R_L^T I_{vwL} R_L + R_R^T I_{vwR} R_R - \\ & m_{vw}\left([c_{J_L}\times]^2 + [c_{J_R}\times]^2\right) \end{bmatrix}^{-1} \cdot \begin{bmatrix} m_{vw} R_L^T [c_L\times] R_L & m_{vw} R_R^T [c_R\times] R_R \\ -R_L^T I_{vwL} R_L + & -R_R^T I_{vwR} R_R + \\ m_{vw}[c_{J_L}\times]\left[R_L^T [c_L\times] R_L\right] & m_{vw}[c_{J_R}\times]\left[R_R^T [c_R\times] R_R\right] \end{bmatrix} \begin{bmatrix} \omega_L^b \\ \omega_R^b \end{bmatrix}$$

at time t_0. The dynamic simulation of the inertia model is first performed on a generated set of wing kinematics consisting of sine and cosine functions. The choice for generated profiles instead of directly using the polynomial fits has two reasons In the first place the polynomial fit cannot be differentiated indefinitely and therefore the derivatives are less accurate than the original function, this generates small errors. The second reason is that most of the average wingbeats obtained from the movie sequence do not have conservation of angular momentum. The wingtips of both wings travel around a loop-like trajectory which generates a pitching moment. The generated wing kinematic set is:

$$\begin{aligned} \theta_L &= \theta_R = \theta_{L_0} + A_{\theta_L} cos\left(4\pi f t\right) \\ \eta_L &= \eta_R = \eta_{L_0} + A_{\eta_L} sin\left(2\pi f t\right) \\ \phi_L &= \phi_R = \phi_{L_0} + A_{\phi_L} sin\left(2\pi f t\right) \\ f &= 189\ [Hz] \end{aligned}$$

with $\theta_{L_0} = \frac{5\pi}{180}$, $\eta_{L_0} = \frac{\pi}{2}$, $\phi_{L_0} = \frac{10\pi}{180}$, $A_{\theta_L} = \frac{10\pi}{180}$, $A_{\eta_L} = \frac{45\pi}{180}$ and $A_{\phi_L} = \frac{60\pi}{180}$. The resulting linear and angular momentum of the dynamic simulation and the resulting body kinematics are given in Fig. 7.4 and Fig. 7.6. The linear and angular momentum are all zero so conservation of momentum is satisfied. Also the resulting body kinematics, v_b and ω_b, are periodic and the wingbeat average body velocities are zero. If a normal average wingbeat is used, conservation of angular momentum is no longer satisfied, as can be seen in Fig. 7.5 and Fig. 7.7. Now the momentum is slow but steadily increasing over time, with as result

that also the wingbeat averaged body velocity and angular velocity is slowly increasing. In the full dynamic simulation with gravity forces and aerodynamic forces however this slowly increasing momentum is not really noticeable as the wingbeat averaged aerodynamic forces and moments are generally stronger.

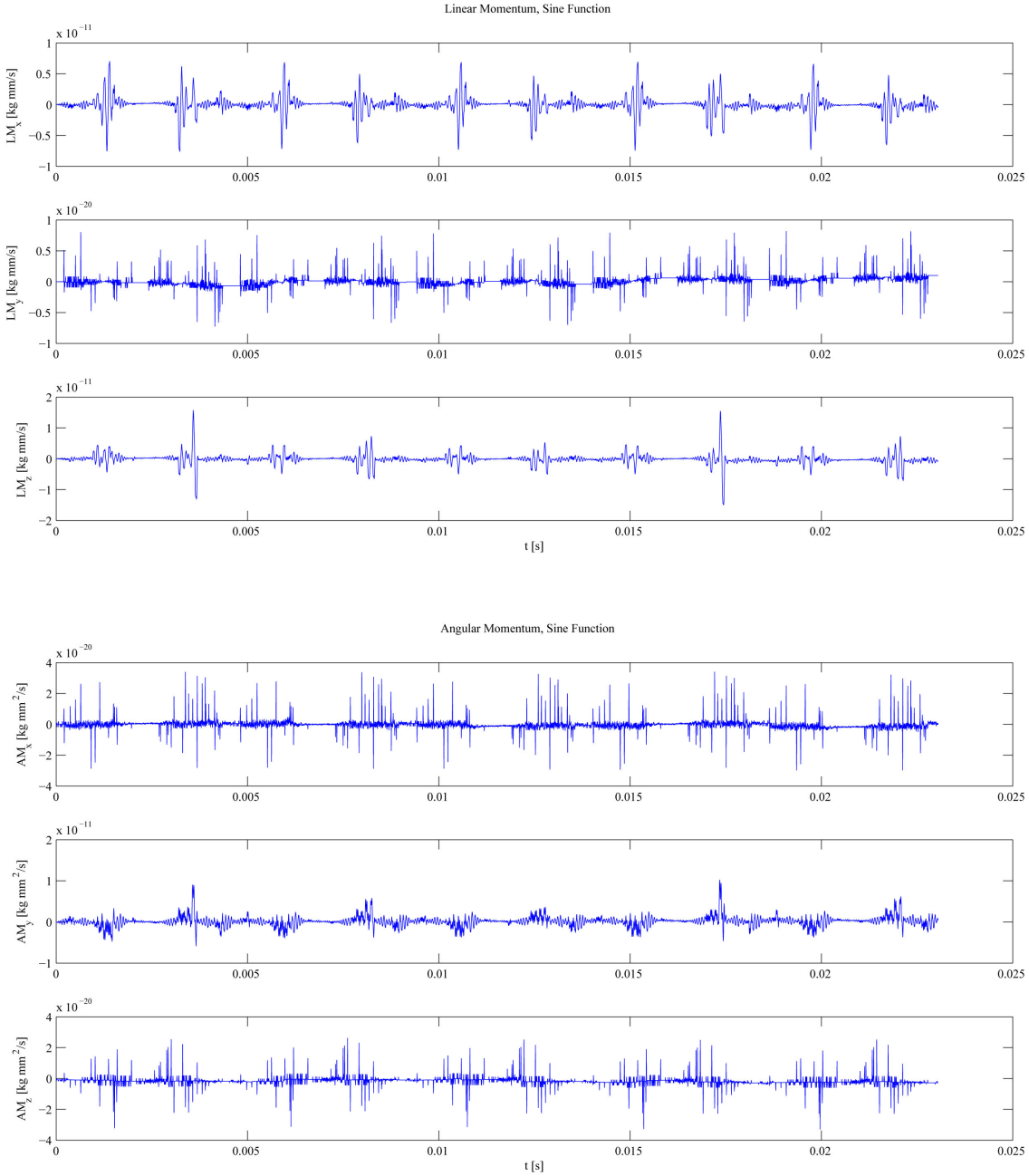

Figure 7.4: Linear and angular momentum simulation of 5 wingbeats defined by sine and cosine functions.

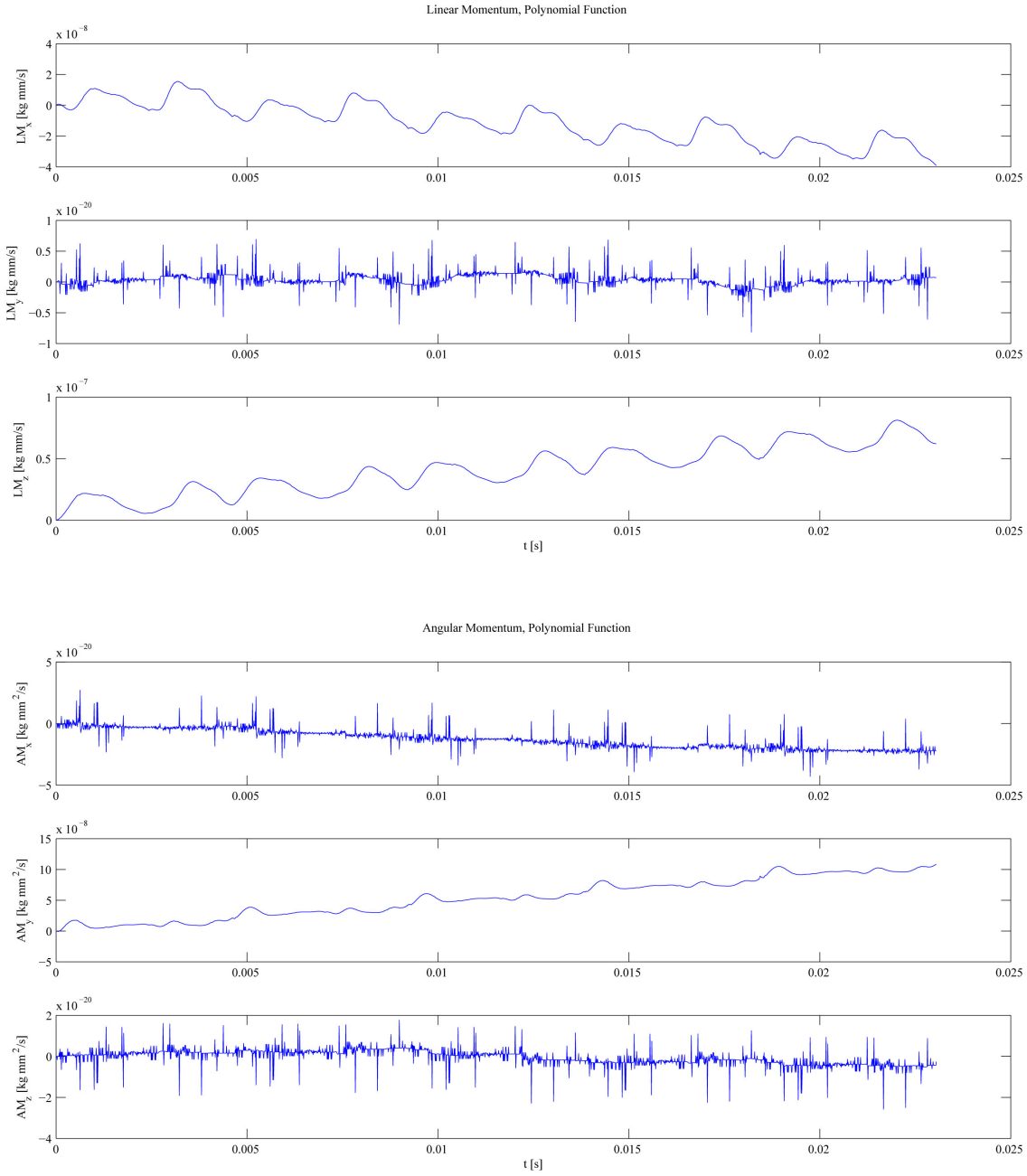

Figure 7.5: Linear and angular momentum simulation of 5 wingbeats defined by polynomial functions.

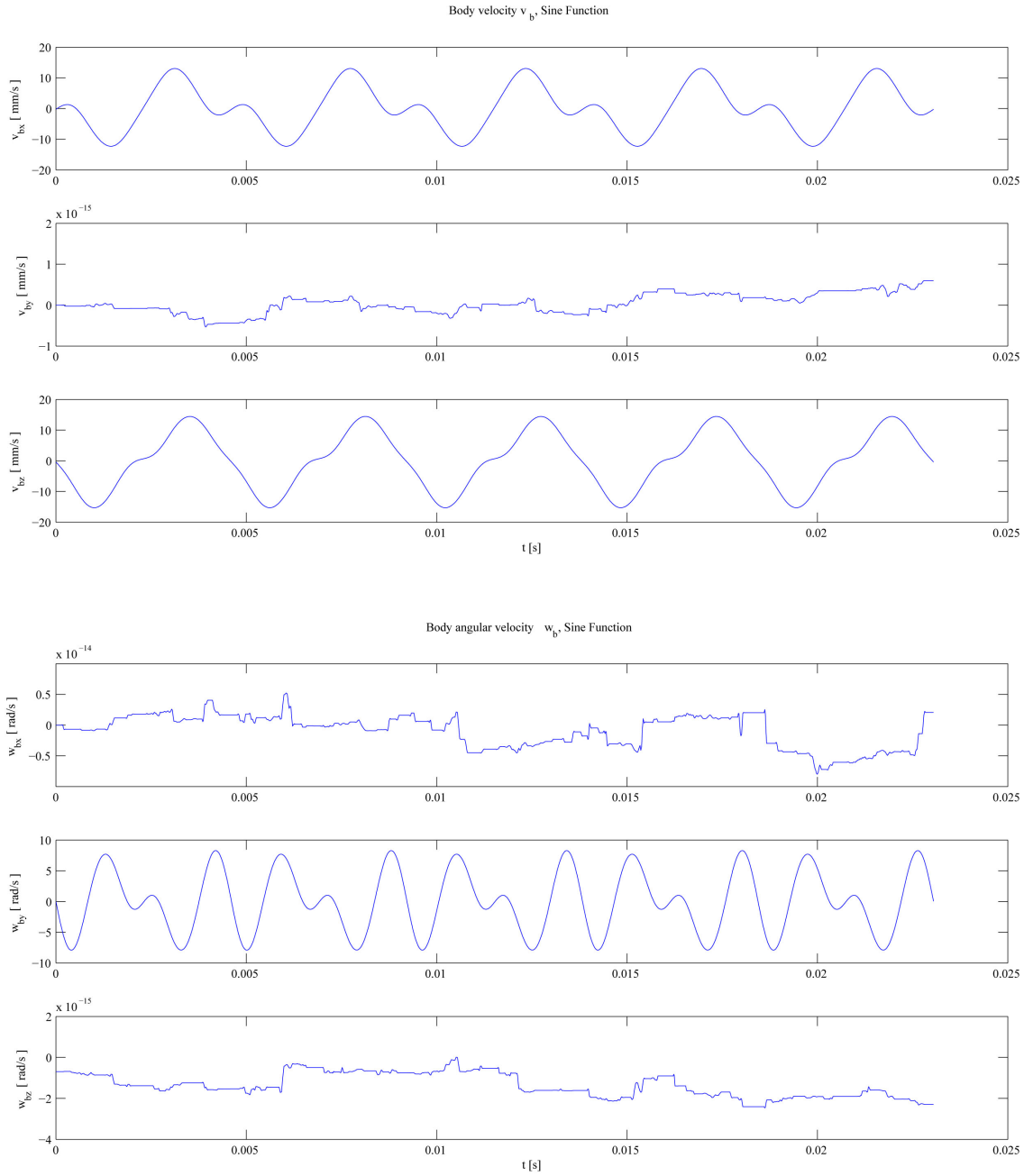

Figure 7.6: Body velocity and angular velocity in the body reference frame during the linear and angular momentum simulation of 5 wingbeats defined by sine and cosine functions.

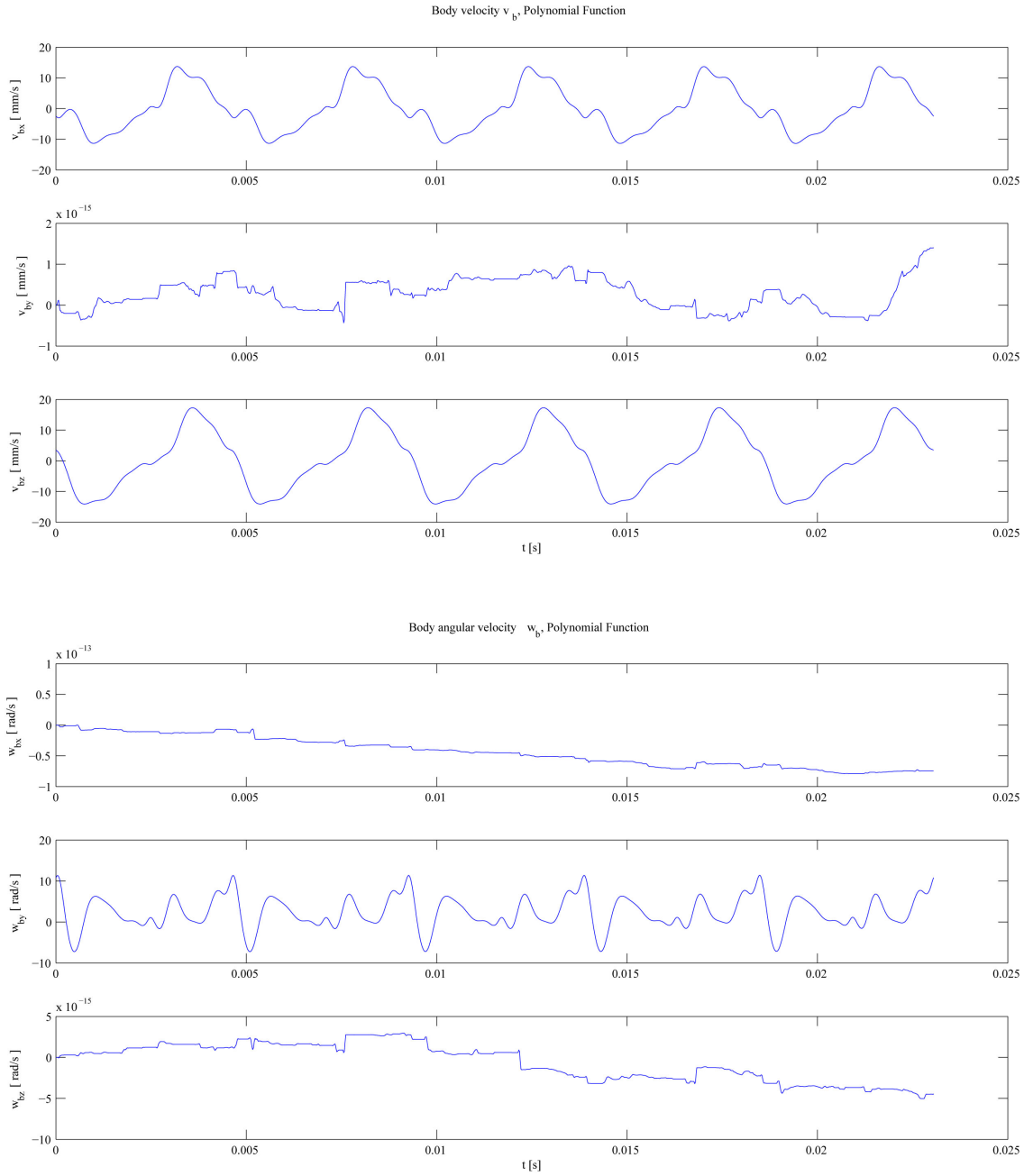

Figure 7.7: Body velocity and angular velocity in the body reference frame during the linear and angular momentum simulation of 5 wingbeats defined by polynomial functions.

Part III

Results

Chapter 8

Escape Maneuvers

The filtered body and wing kinematics are sufficiently smooth to permit a qualitative aerodynamic analysis of the wing kinematics and their effect on the flight path. After this chapter the wingbeats of all the sequences will be grouped in one big database. In order to be able to analyze the wingbeats of different flies a symmetry correction of the wing kinematics and a non-dimensionalization of the forces and moments will be applied. However a maneuver usually consists of multiple wingbeats, so just the analysis of single maneuvering wingbeats will not yield a proper image of maneuvering flight. In this chapter the flight of a fruit fly before and during the escape response will be discussed. Before the escape response the flight of the fly is marked as steady flight. This often consists of hovering or slow forward flight, a maneuver might occur but the duration of this maneuver is significantly larger than escape maneuvers. Once the fly notices the visual stimulus it will start its escape maneuver. Depending on the direction of the visual stimulus w.r.t. the fly and the flight conditions of the fly at the moment it perceives the visual stimulus, the fly performs a certain maneuver. The two clearly different maneuvers can be observed; a roll maneuver which directs the strokeplane away from the stimulus, or a pitch-up maneuver which accelerates the fly backwards to evade a stimulus usually coming from the front. Usually the fly does not use a pure roll or a pure pitch maneuver but a combination of both maneuvers, in this chapter the roll maneuver and pitch-up maneuver will be shown to have examples of a rolling and pitching wingbeats. In order to get a clear view of the effect of the wing kinematics on the maneuver the aerodynamic force and moment generation of the wing kinematics must be known. The quasi-steady aerodynamic model is used in this chapter to obtain force and moment estimates. The quasi-steady aerodynamic model will be defined in Chapter 7 where it is used extensively in the dynamic simulation.

8.1 Steady Flight

This section will analyze the characteristics of the steady flight wingbeats, or steady wingbeats. Comparison of the obtained wing kinematic angles of steady wingbeats with literature for hovering flight of *Drosophila Melanogaster*, Ref. [17], shows that the general outline of the reported hovering wingbeat kinematics of the *Drosophila Melanogaster* is very similar in structure to the wing kinematic angles observed in the video sequences. However when looking at the wingtip path of these steady wingbeats it becomes clear that there is relatively small but not negligible variation between subsequent steady wingbeats in a sequence and steady wingbeats of different flies. These steady wingbeats are very characteristic for each fly, as there is a large variation in body and wing shapes and dimensions and there are often small asymmetries in the body and wings. This leads to a specific tuning of the wing kinematics for each fly in order to enable hovering flight. Although there is a large variation in wing kinematics for steady wingbeats between flies, the variation of the steady wingbeat during the steady flight phase is minimal. In Fig. 8.1 and Fig. 8.2 two subsequent steady wingbeats are displayed. The two wingbeats are taken from the steady flight part of sequence 71 in which a roll maneuver is performed, the position of the two subsequent wingbeats is shown in Fig. 8.4. In the two subfigures on the right of Fig. 8.1 and Fig. 8.2 the computed forces of the quasi-steady model are shown. As one can see the forces of the left and right wing are relatively symmetric and there is also little variation between the two subsequent wingbeats. In appendix C some additional steady wingbeats are added to the sequence. Looking at the forces one might argue that the start of the left upstroke in Fig. 8.2 produces significantly more force than the start of the left upstroke in Fig. 8.1, however the difference in force does not lead to significant changes in body dynamics. This strengthens the assumption that body attitude is corrected over multiple wingbeats and that small variations in wing kinematics do not directly affect the body attitude.

Despite the variation in wing kinematics between flies, there are several characteristics of the steady wingbeat which are uniform over all sequences. When looking at multiple steady wingbeats it becomes clear that the downstroke is more constant than the upstroke. There are often variations in the wingtip path of the upstroke but the downstroke is usually very similar to the previous downstroke and the next downstroke. This might have something to do with the fact that the wingtip velocity during the downstroke is lower than during the upstroke. This velocity difference is a direct effect of the downstroke to upstroke ratio, the downstroke usually takes up around 53% of the wingbeat. The angle-of-attack during the downstroke is also rather constant compared to the upstroke, the angle of attack during the downstroke is around the $50\,^\circ$ whilst during the constant part of the upstroke the angle of attack it is $40\,^\circ$, Fig. 8.3. The values of the angle of attack are quite high in comparison to angles of attack experienced on conventional aircraft wings. This shows the dominant role of the LEV in insect flight.

The absolute stroke angle of the supination point is smaller than the absolute stroke angle of the pronation point, which means that the average stroke angle is not zero and the center of pressure of a wingbeat lies behind the wing joints in the strokeplane reference frame. This misalignment between the center of pressure and the wing joints generates on average a pitch down moment over the wingbeat. This pitch down moment must be counter-acted

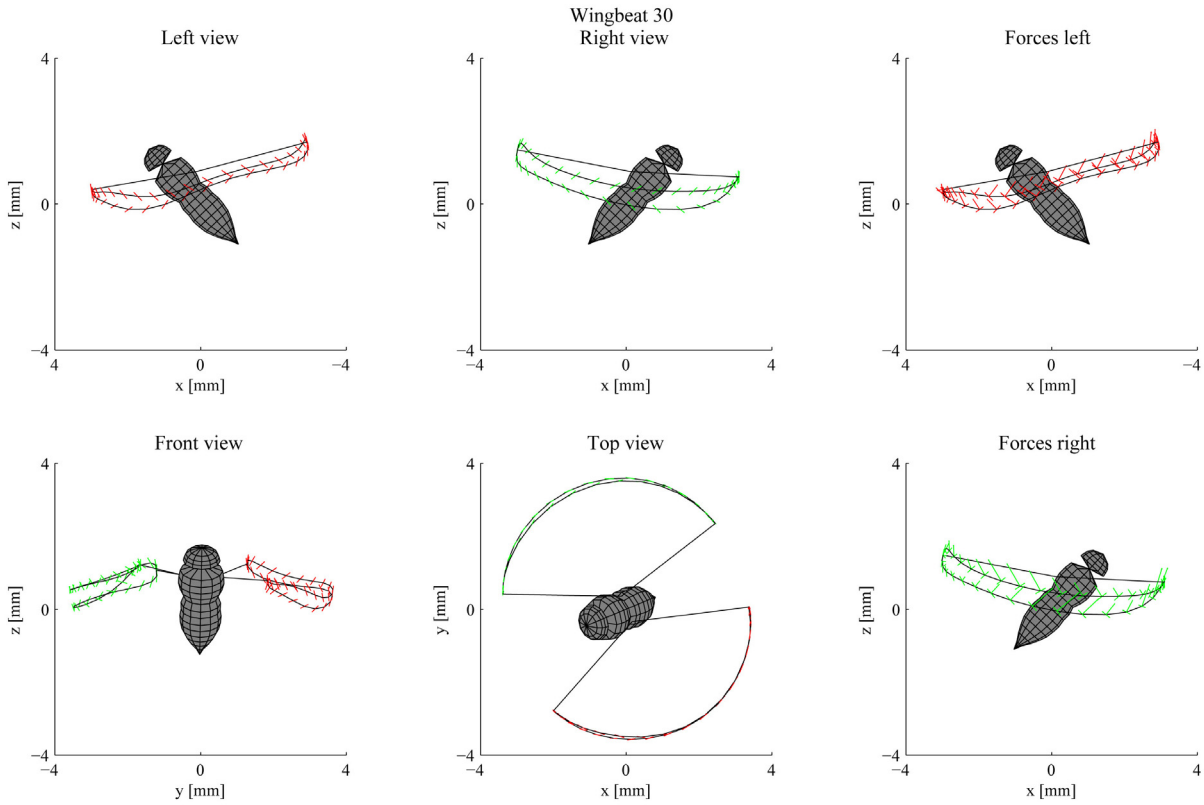

Figure 8.1: Example of a steady wingbeat. The view angles are aligned with one of the principal axes of the strokeplane reference frame. In the left and the right view only pitch motion is applied on the body. The front view only applies roll motion and the top view only yaw motion.

for hovering flight, which is performed by generating extra force at the start of the upstroke. This extra force is generated by a so-called *downward plunge* at the start of the upstroke. The downward plunge starts at the point of supination after which the wing is plunged rapidly downwards w.r.t. the strokeplane and ends when the downward motion gradually shifts to motion parallel to the strokeplane. After the downward plunge the wing moves parallel to the strokeplane with a constant angle of attack, a situation which is similar to the downstroke. During the downward plunge the wing is oriented almost orthogonal on the direction of motion of the wing and the angle of attack is close to 90 °. This very high angle of attack generates very high drag forces normal to the wing surface and the downward plunge can be compared to a paddling motion. At the end of the downward plunge the wing rotates such that the angle of attack becomes around the 40 ° such that the lift force becomes bigger than the drag force. As mentioned before, the wingtip path of the upstroke varies more compared to the downstroke, this can also be a result of the downward plunge. After a study of dozens of steady wingbeats it became clear that the deviation angle of the downward plunge varies over the steady wingbeats. It might be that the downward plunge plays a significant role in stabilization of the body.

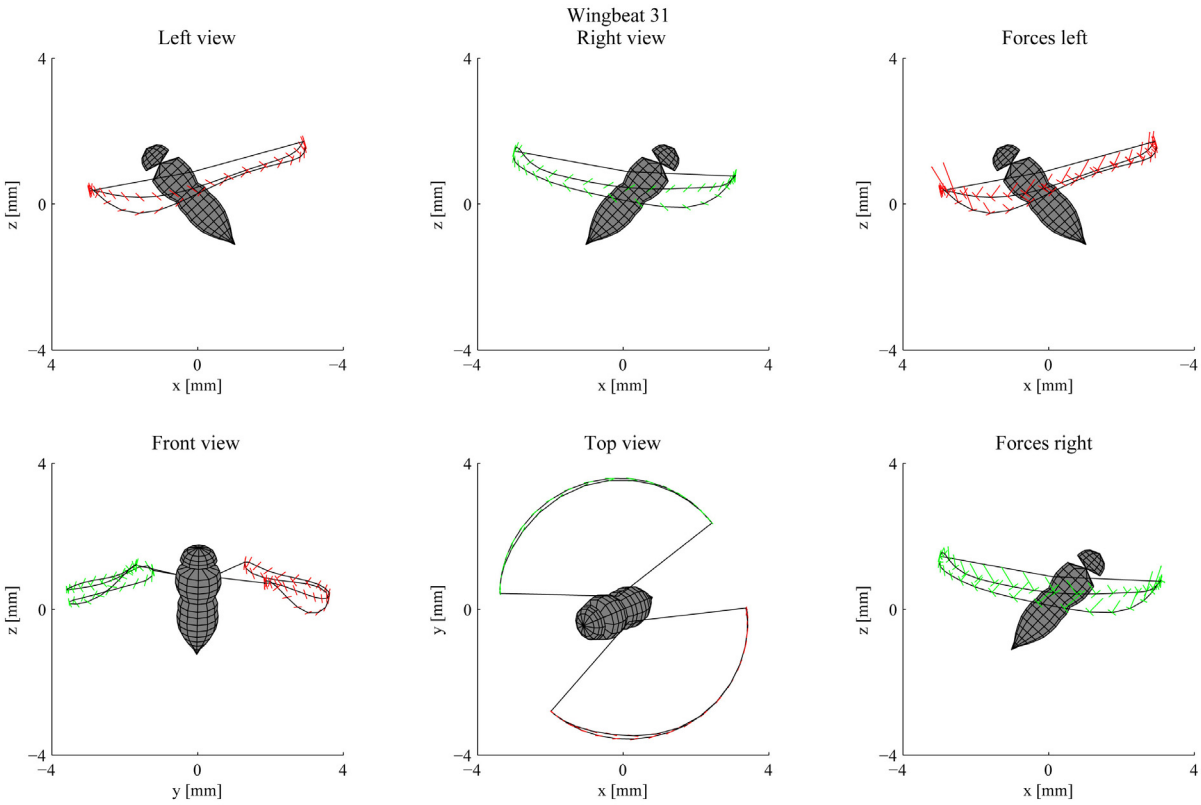

Figure 8.2: Example of a steady wingbeat.

The claim that all variation of the wing kinematics during the phase called steady flight in the sequences is part of hovering wing kinematics might be a bit strong. In Fig. 8.4 the fly performs a yaw turn before the escape maneuver starts and also the fly descends and ascends slowly. In this sequence the duration of the yaw turn is much longer than for example the roll turn at the start of the escape maneuver. Although the duration of turns during the steady flight phase is usually longer than the duration of turns during the escape maneuver, it is not reasonable to mark the wingbeats during such turns as steady wingbeats. In the determination of the average wingbeat in Chapter 6 measures are taken to exclude these turning wingbeats from the average wingbeat. Apart from possible turns during the steady flight phase the wingbeats during the steady flight phase can be marked as hovering flight wingbeats. The velocity during the steady flight phase is rather low, usually between the 10 and 20 cm/s. The effect of body velocity on the aerodynamic force generation at these speeds can be ignored. The body speed is low due to the confined space of the test set-up which only allows high speed flight for short instances.

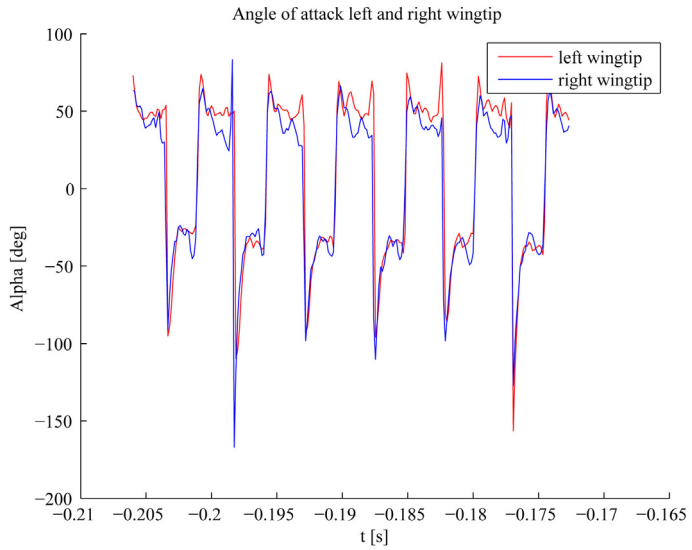

Figure 8.3: The angles of attack of the left and right wingtips for 6 wingbeats under steady flight conditions.

8.2 Roll Maneuver

In order to escape from the visual stimulus, the fly needs to change direction and accelerate away from the stimulus as fast as possible. This can be done by a roll maneuver which is the most common option observed in the studied escape maneuvers. The roll maneuver consists of a fast roll in which the fly usually rolls its body to a roll angle of approximately 90 °, followed by an acceleration phase in which the fly flies away from the stimulus and slowly corrects the strokeplane to a more horizontal orientation. This section will describe an example of such a roll maneuver and will describe the relation between the escape maneuver and the wing kinematics.

In Fig. 8.4 an example of a roll maneuver is depicted. The average position and orientation of the fly during a wingbeat is shown by plotting the body and strokeplane. During the steady flight phase in Fig. 8.4 the speed of the fly is rather low, which can be seen by the close distances between the subsequent fly models in the figure. During the steady flight phase the fly makes a yaw turn and is sometimes side-slipping a bit, however the body velocity always remains low. When the fly flies through the center of the focal volume it will trigger the laser-trigger system. As the laser beam is in the IR-spectrum, the fly will not be disturbed by the beam. Once the laser-trigger system is activated almost immediately a visual stimulus will be shown on the LED-screens. The visual stimulus is a circular expansion and it will take some time before the expansion, starting from a single pixel, has reached its maximum area. The visual system of the fruit fly is one of the fastest in the animal kingdom, however also the visual system and the fly's brain will need some time before it recognizes the visual stimulus as a treat and will initiate the escape response. The behavioral and sensory aspects of the escape maneuver will not be a part of the thesis, fact is however that the fly will not immediately respond to the visual stimulus in time. In Fig. 8.4 the wingbeat in which the

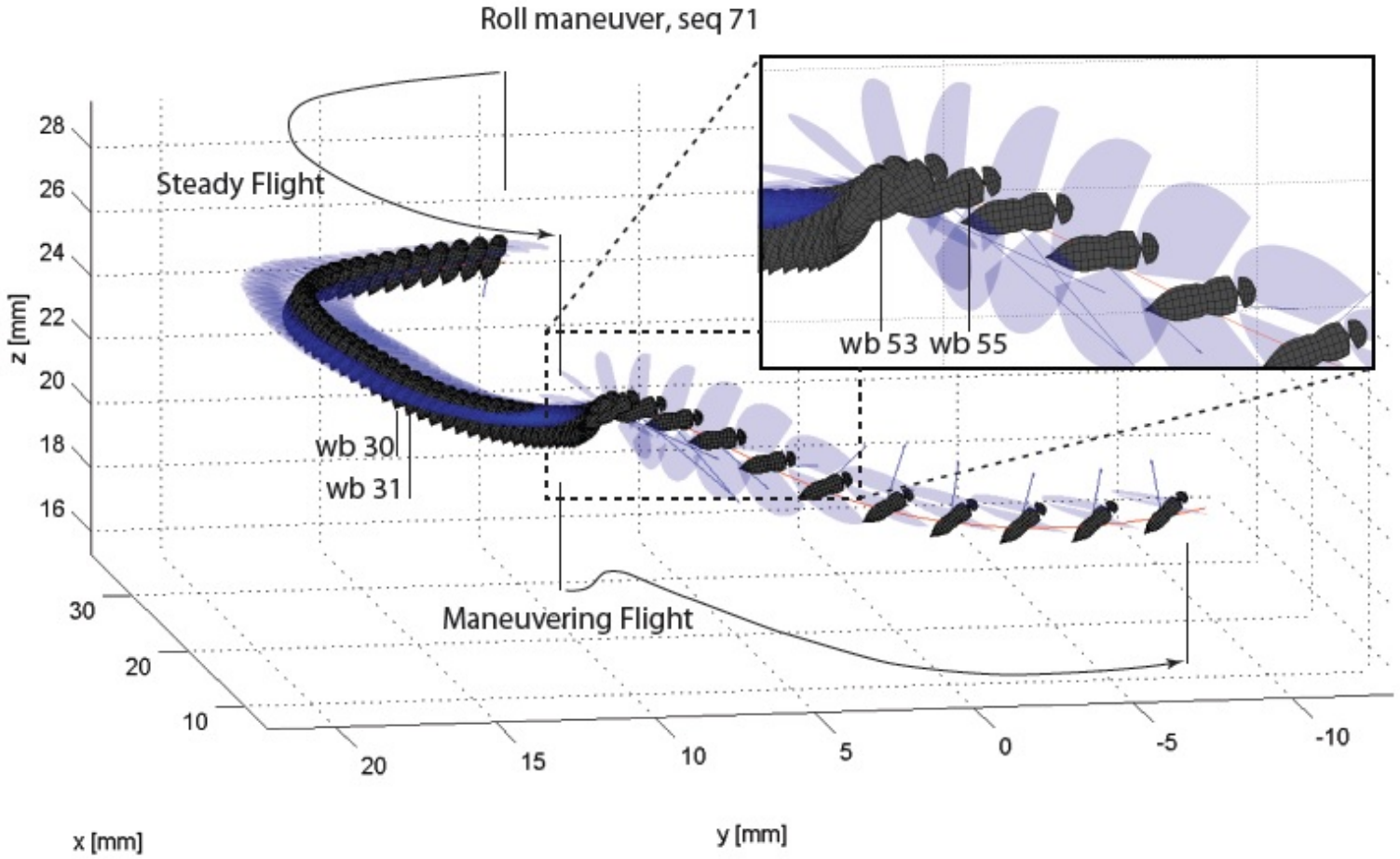

Figure 8.4: Flight path of a sequence including a roll maneuver. The average position and orientation of the fruit fly for each wingbeat is given by a schematic representation, for visualization purposes the fruit fly model is 0.5 times the original size. The blue arrow shows the acceleration vector. The location of different wingbeats is marked by their wingbeat number.

visual stimulus is displayed on the LED-screen is marked.

Once the visual stimulus is perceived by the fly an escape maneuver will be started. In this example the escape maneuver starts with a fast roll of the body to the left, directing the head of the body away from the stimulus. One of the two wingbeats which generates the moment necessary for the roll rate is shown in Fig. 8.5. Comparison to the steady wingbeats of Fig. 8.1 and Fig. 8.2 shows quite some differences in wing kinematics. The left wing is lowered and the downward plunge of the steady wingbeat is absent. Due to the lowering of the wingtip path of the left wing the wingbeat averaged force vector of the left wing is tilted to the left. The absence of the downward plunge results in a lowered force production of the left wing. Both effects help in generating a rolling moment as the left wingbeat average force vector normal to the strokeplane becomes smaller The right wing kinematics differ spectacularly from the steady wingbeat, during the downstroke the wing is raised almost

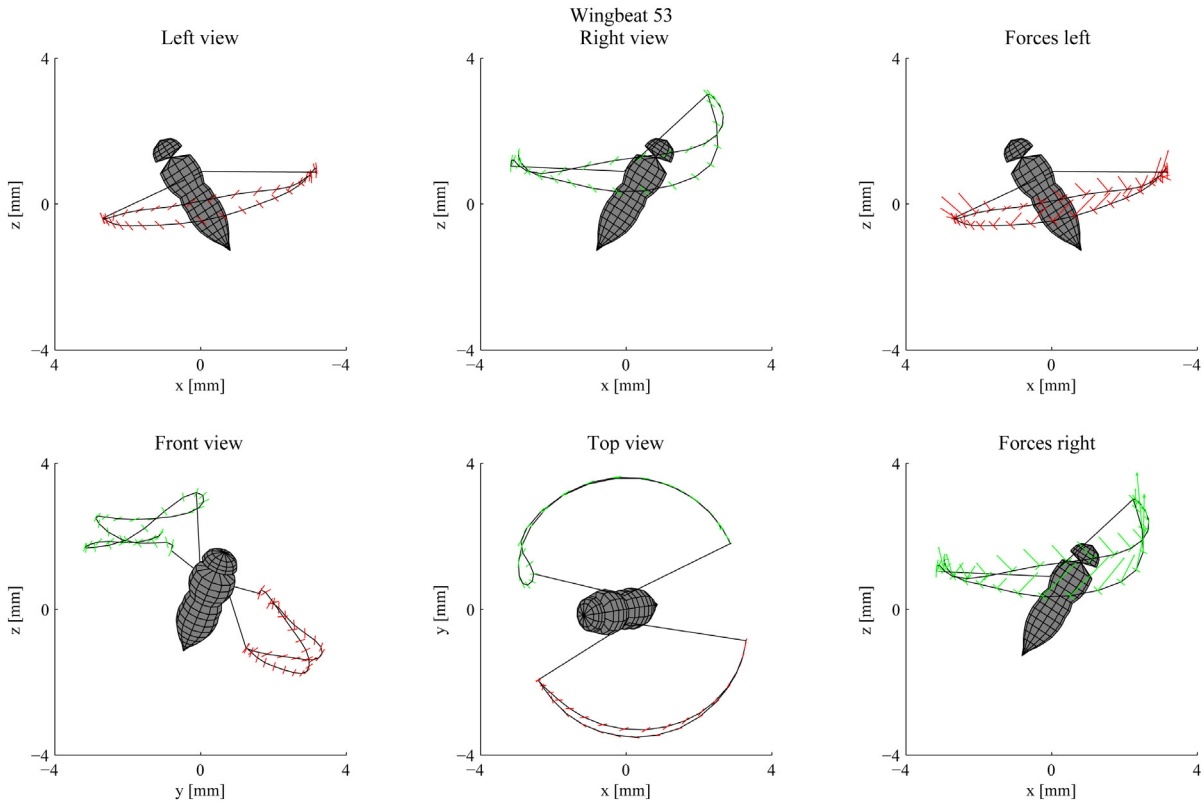

Figure 8.5: Wingbeat initiating roll maneuver.

above the head of the fly. The upstroke starts with plunging the wing downwards from this elevated position, the duration of this downward plunge takes up the largest part of the upstroke. The downward plunge results in a significant amount of force production on the right wing, which in combination with the left wing produces a strong roll moment. The wingbeat in Fig. 8.5 does not only produce a rolling moment but also smaller pitch and yaw moments. All the maneuvering wingbeats of this example can be found in appendix C. Wingbeat 52, the wingbeat preceding the wingbeat in Fig. 8.5, also generates a roll moment in the same way as wingbeat 53. However wingbeat 53 has a much stronger contribution in the roll moment production. After wingbeat 53 the body of the fly has reached a large roll rate, it takes just two more wingbeats to achieve a roll angle of approximately 90°. As during the generation of the roll moment, also a pitching moment is generated the fly also experiences a pitch-up motion. Once the fly has reached a roll angle of 90° the pitch and roll moments have rotated the strokeplane in such a way that it is almost perfectly normal to the direction of the visual stimulus. The force used for weight support under steady flight conditions is now fully dedicated to the acceleration of the fly in the horizontal plane. Changing the orientation of the strokeplane is not the only thing which happens once the escape response is initiated. To increase the force production as a whole also the wingbeat amplitude and wingbeat frequency are increased, leading to a larger wing velocity and thus higher aerodynamic forces. The increase in frequency and amplitude builds up over more

than one wingbeat and it usually takes around the 5 wingbeats before the frequency reaches its final value for the escape maneuver. The rotation of the strokeplane and the increase in force production enable the fly to reach accelerations up to 2 g during escape maneuvers. Remarkable of the maneuver is the speed of it, the fly can rotate to 90 ° in 4 wingbeats, which takes 0.02 seconds, Fig. 8.7. The duration of a human eye-blink is minimally 0.1 second and it does not require the complexity and coordination involved in the roll maneuver.

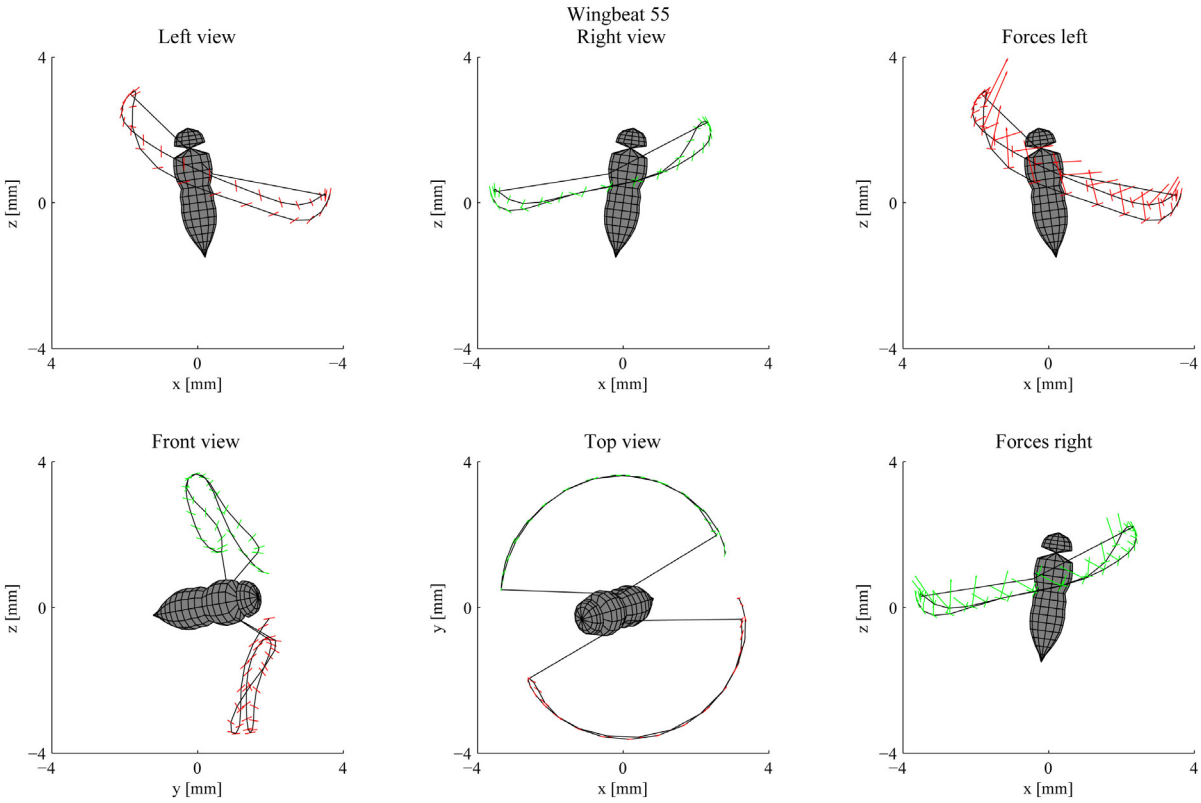

Figure 8.6: Counter-roll wingbeat.

The escape maneuver however does not stop after the 90 ° roll. In the first place the roll rate is not zero after the 90 ° roll and the fly would end upside down if the roll rate is not reduced to zero. A counter-rolling moment is necessary, wingbeat 55 generates such a moment, Fig. 8.6. The moment of the counter-roll wingbeat is produced in the same way as in wingbeat 53, however the size of the duration of the downward plunge in this case is smaller. This is because aerodynamic damping is helping in generating the counter-roll moment and has also reduced the roll rate during wingbeat 54. It takes 2 wingbeats before the roll rate is reduced to zero, wingbeat 55 and 56. Interesting is the small downward plunge at the start of the downstroke in Fig. 8.6. This is generating additional force in a similar way as the downward plunge at the start of the upstroke. The downward plunges at the start of the upstroke and downstroke are used in order to increase the force production as a whole, just as the wingbeat frequency and amplitude do. Once the strokeplane is rotated to a roll angle of 90 °, the fly

starts accelerating away from the stimulus, Fig. 8.8. With the strokeplane at 90° there is no weight support which means that the fly also starts accelerating downwards. At the start of the escape maneuver this might be beneficial to increase the magnitude of the acceleration vector, however later on in the maneuver the fly will recover to a roll angle of zero. This is done by a gradual correction in orientation by means of a yaw rotation and a pitch down rotation. Due to the angle between the strokeplane and the body of 55°, a yaw rotation of about 90° will result in a more level strokeplane such that the weight of the fly is supported again. The pitch down motion is necessary to keep the resultant aerodynamic force vector of the strokeplane tilted forward, such that the fly continuous accelerating away from the stimulus. The wing kinematics during this phase are also adapted such that the resultant force vector of the strokeplane is tilted forward.

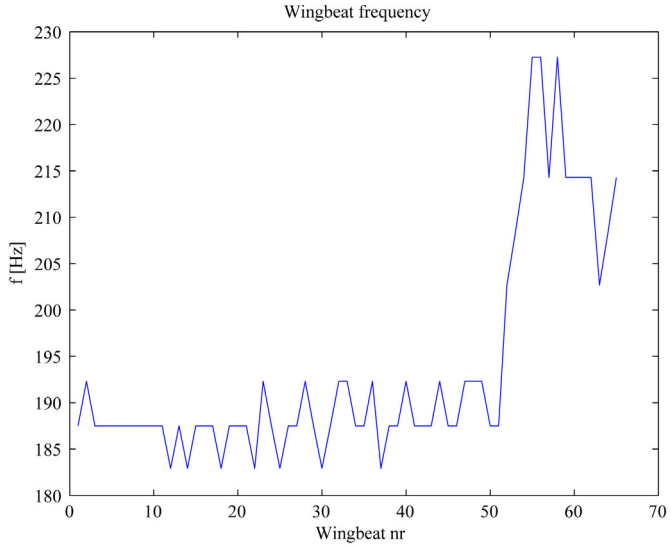

Figure 8.7: Wingbeat frequency of the wingbeats of sequence 71.

The roll escape maneuver just described is the most frequently used escape maneuver and is very stereotypical. Depending on the direction of the stimulus the fly rolls up to 90° or a somewhat smaller roll angle. When the stimulus is in front of the fly it sometimes uses a different escape strategy, the pitch-up maneuver. When looking at the way the fly uses the orientation of its strokeplane to maneuver is analogous to the maneuvering of a helicopter. A helicopter also uses the orientation of its rotor plane to perform maneuvers. The most astonishing part of the maneuver is the rapidity of the roll. The way in which the fly rolls in combination with the pitch-up motion is very stereotypical over all observed sequences. Previous studies of saccades have always described saccades as a fast yaw rotation as the basis of the rapid change in flight direction observed in saccades, Ref. [2]. The rapid roll observed in the escape maneuvers can yield much faster saccades however. When using just a yaw maneuver, the strokeplane is not tilted as drastically as in a roll maneuver, which means that the resultant force and therefore acceleration is much lower. In case of a roll maneuver the rotated strokeplane yields much stronger accelerations.

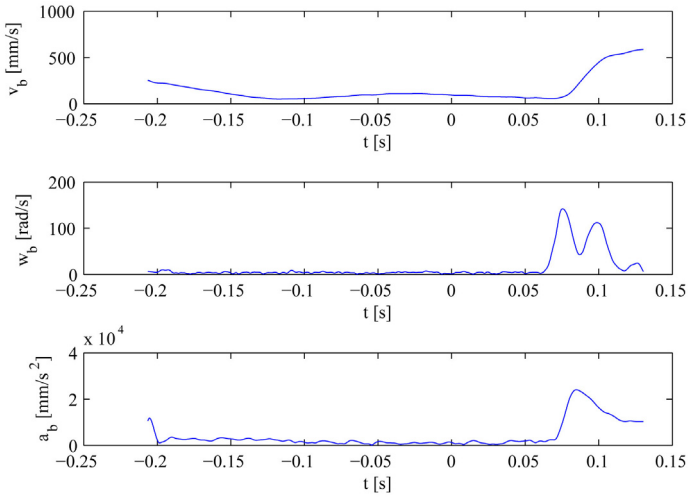

Figure 8.8: Body dynamics of sequence 71. Respectively, the absolute body velocity, absolute body angular velocity and absolute body acceleration are given.

8.3 Pitch-Up Maneuver

Besides the roll maneuver there is a second, less frequent, strategy employed by the flies in order to escape from the stimulus. When the stimulus is coming from the front, sometimes the fly prefers a roll maneuver and sometimes a so-called pitch-up maneuver. In the pitch-up maneuver the fly pitches upwards and simultaneously decelerates, the upward pitching positions the strokeplane roughly normal to the direction of the visual stimulus and the fly starts accelerating backwards, away from the stimulus. The wing kinematics necessary for this pitch-up maneuver will be described in this section.

In Fig. 8.9 the trajectory of the pitch-up maneuver is given. Once the fly has perceived the visual stimulus it starts to pitch-up, during 6 wingbeats the fly orients its body from a pitch angle of approximately 60 ° towards 100 °. The first two wingbeats of the pitch-up maneuver generate a symmetric pitch-up motion, however in the third wingbeat also a roll moment is generated. In combination with a yaw motion, the roll motion will slowly rotate the body such that the strokeplane provides more weight support. This happens whilst the fly is flying backwards and after the roll/yaw correction the fly is facing away from the stimulus and continues accelerating forward.

In Fig. 8.10 the wing kinematics generating a pitch-up moment are displayed. The wing kinematics of the pitch-up moment deviate less drastically from the steady wingbeat than the wing kinematics generating a roll moment. The pitch-up moment is generated by several aspects of the wing kinematics in Fig. 8.10. In the first place there is a shift in the average stroke angle such that the center of pressure is shifted forwards in the strokeplane, which creates a pitch-up moment. Secondly both on the left as the right wing the downward plunge is stronger than during steady flight also generating a pitch-up moment. Finally the pronation

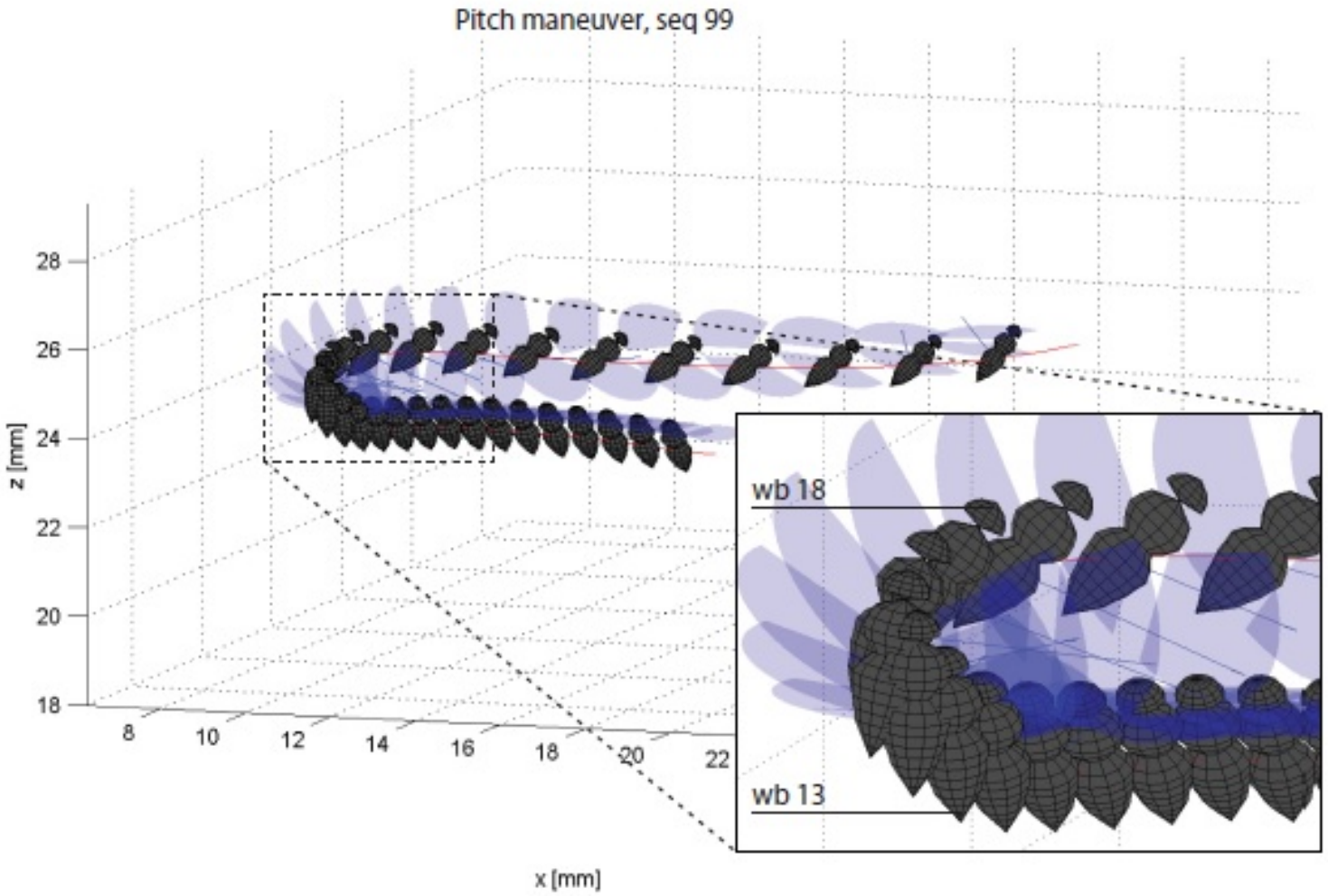

Figure 8.9: Flight path of a sequence including a pitch-up maneuver. The average position and orientation of the fruit fly for each wingbeat is given by a schematic representation, for visualization purposes the fruit fly model is 0.5 times the original size. The blue arrow shows the acceleration vector. The location of different wingbeats is marked by their wingbeat number.

point is lowered such that the wingbeat average aerodynamic force is tilted backwards; this helps to accelerate backwards and induces a pitch-up moment. The relative strength of these three effects is difficult to analyze in a qualitative way, this will be done in Chapter 9 when establishing the quantitative maneuvering flight model.

Fig. 8.11 shows a wingbeat in which the pitch-up maneuver has stopped and the body has already started rolling. A small counter-roll moment is generated in order to stop the rolling motion. Just as in the roll maneuver the force production is increased gradually and in wingbeat 18 the force production has reached its maximum. In case of the pitch maneuver it is not really clear whether the fly uses a counter-pitch moment or whether the aerodynamic and perhaps inertial damping is sufficient to stop the pitch rate. In Fig. 8.11 the pronation point is more backwards compared to wingbeat 13. This generates a pitch down moment,

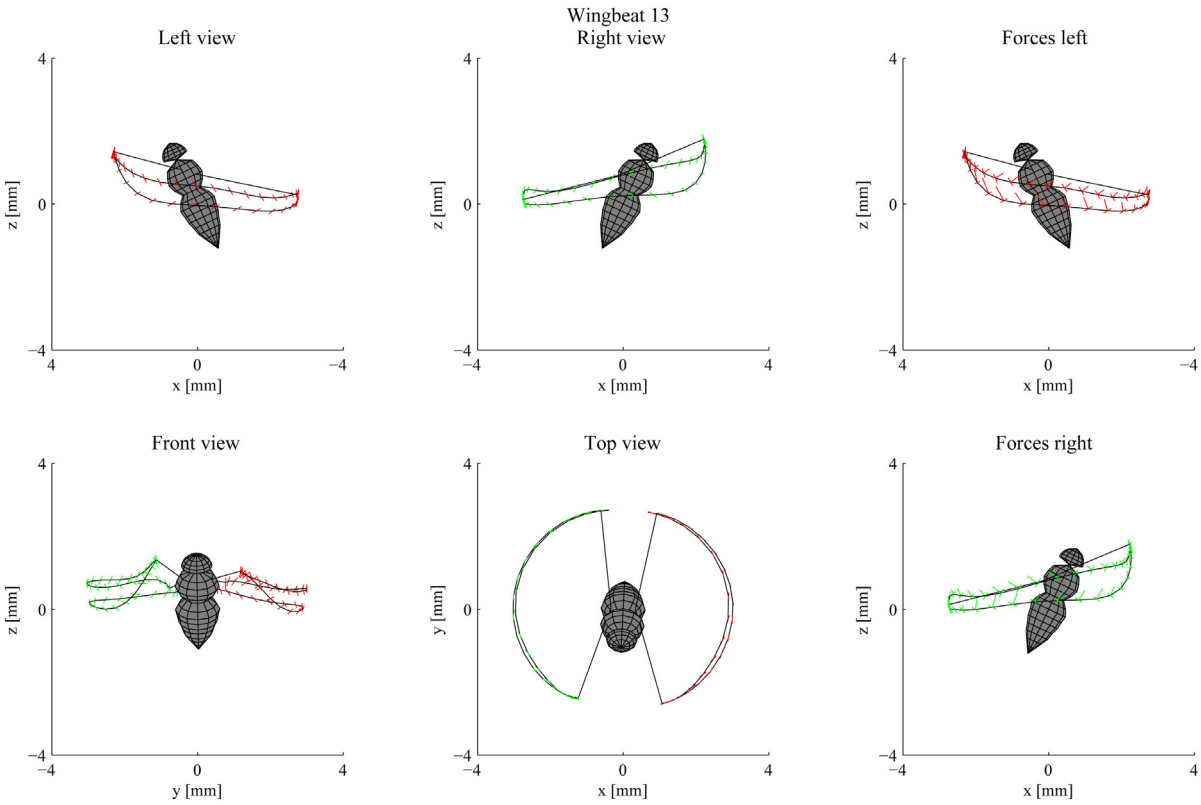

Figure 8.10: Pitch up wingbeat.

but is also part of maximizing force production. To answer these ambiguities it is necessary to establish a quantitative maneuvering flight model.

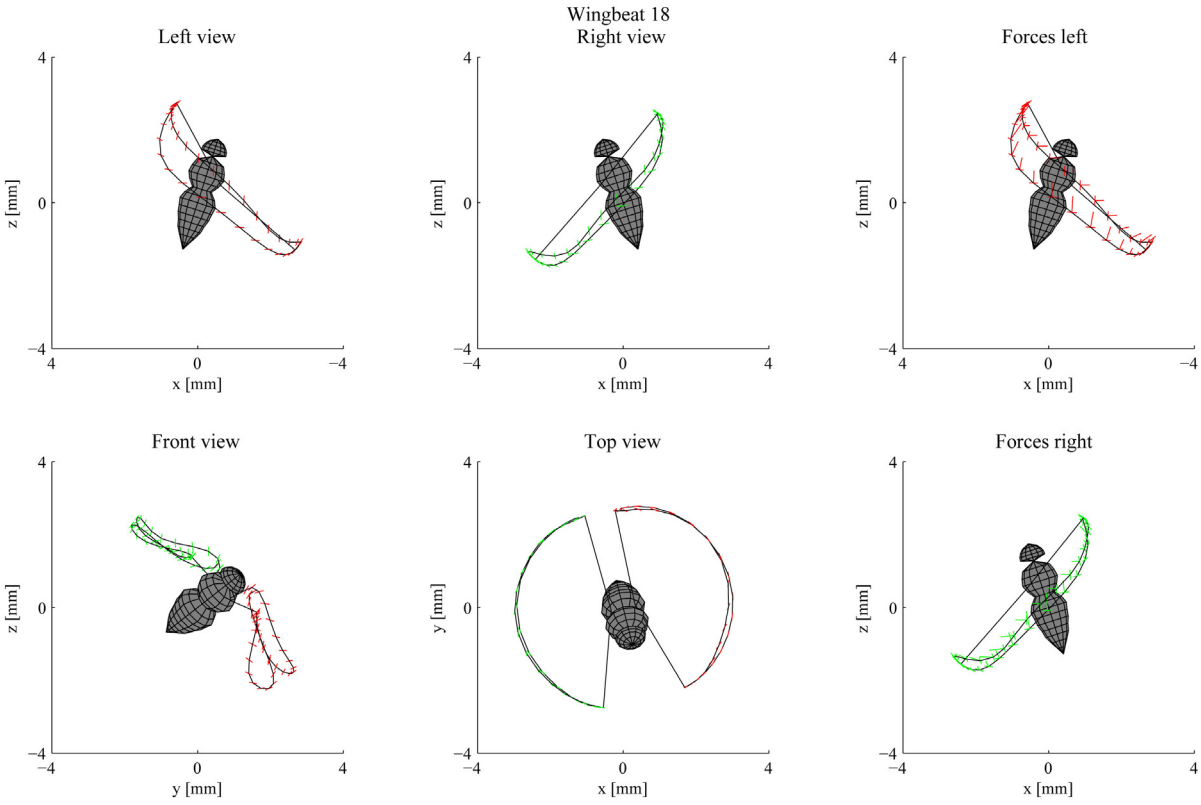

Figure 8.11: Roll and yaw correction.

Chapter 9

Maneuvering Flight Model

Establishing a general model for maneuvering fruit fly flight is rather challenging. The wide variety in body and wing parameters and steady wingbeats makes it difficult to compare maneuvers of different flies. Although the escape maneuvers are quite stereotypical, the speed with which the maneuvers are performed, the rotation axis and the line of action of the maneuvers all show a large variety. As soon as a fruit fly obtains some rotational velocity, aerodynamic and inertial damping occur which means that the force and moment generation over the duration of the maneuver differ. In order to tackle these variations it is necessary to eliminate the effects of aerodynamic and inertial damping and the difference in body and wing parameters between fruit flies. This is achieved by using the quasi-steady model to obtain an estimate of the aerodynamic force and moment generation whilst the body is stationary and subsequently non-dimensionalizing these forces and moments. The stationary simulation excludes any damping due to body velocity and the non-dimensionalization excludes fruit fly specific parameters like body mass and wing length from the results. The polynomial deviation coefficients of the maneuvering wingbeats (the polynomial deviation coefficients express the deviation of the wing kinematic angles during a wingbeat w.r.t. the wing kinematic angles of the symmetric average wingbeat of the specific movie sequence) can be compared with the generated stationary non-dimensional aerodynamic forces and moments. Summarizing: the goal is to find a relation between the body stationairy aerodynamic forces and moments generated by a maneuvering wingbeat and the deviation from that maneuvering wingbeat w.r.t. the symmetric average wingbeat. By finding relations between the polynomial coefficients and the force and moment generation, a maneuvering flight model can be established with the wingbeat defined in polynomial coefficients. This will generate a maneuvering flight model which is, just as the polynomial description of a wingbeat, not sensitive for differences in average wingbeats or different wingbeat frequencies and downstroke to upstroke ratios.

9.1 Non-dimensional Forces and Moments

Before the stationary aerodynamic forces and moments are obtained, first the maneuvering wingbeats must be selected. This is done by determining the wingbeat averaged body acceleration and rotational velocity in the strokeplane reference frame. To every wingbeat in the wingbeat database 6 wingbeat averaged values of the body dynamics are attached to the wingbeats; $\bar{a}_x$, $\bar{a}_y$, $\bar{a}_z$, $\bar{\omega}_x$, $\bar{\omega}_y$ and $\bar{\omega}_z$. The wingbeats in the database are considered maneuvering wingbeats when one or more of the 6 values exceeds a threshold, being a_{thresh} for the acceleration and ω_{thresh} for the angular velocity. The maneuvering wingbeats are divided into 6 groups: wb_{a_x} when $\bar{a}_x$ exceeds a_{thresh}, wb_{a_y} when $\bar{a}_y$ exceeds a_{thresh} and so on. This selection will create following groups: wb_{a_x}, wb_{a_y}, wb_{a_z}, wb_{ω_x}, wb_{ω_y} and wb_{ω_z}. One maneuvering wingbeat might show up in multiple groups and the values of a_{thresh} and ω_{thresh} are 4000 $[mm/s^2]$ and $6 \cdot \pi$ $[rad/s]$ respectively.

Now the maneuvering wingbeats are identified the polynomial fits of the wingbeats can be used to establish the wing kinematics necessary to obtain the aerodynamic forces and moments from the quasi-steady model. The quasi-steady model does not include body motion which excludes aerodynamic damping from the results. The results of the quasi-steady model will only give the aerodynamic forces and moments of a wingbeat and no inertial or gravitational forces and moments. A single maneuvering wingbeat is needs two runs of the quasi-steady model, first to obtain the forces and moments of the symmetric average wingbeat using the polynomial fit $\bar{a}_{LR}$ and second to obtain the forces and moments of the maneuvering wingbeat using the polynomial fit $\bar{a}_{LR}$+a_L^{dev} and $\bar{a}_{LR}$+a_R^{dev}. For convenience the wingbeat averaged forces and moments of the average wingbeat are grouped in a 6 by 1 vector $FM_{avg} = [F_{avg}, M_{avg}]$ and likewise for the maneuvering wingbeat $FM_{man} = [F_{man}, M_{man}]$.

The average wingbeat related to the maneuvering wingbeat is obtained to exclude variations in the symmetric average wingbeat between flies. The definition of the non-dimensional analysis has to be chosen such that the fruit fly specific differences in wing kinematics, body and wing dimensions are minimized as well as the supra wingbeat maneuver characteristics. The last issue is tackled by subtracting the symmetric average force and moment production of the symmetric average wingbeat from the average force and moment production of the maneuvering wingbeat. In this way the fruit fly specific average wingbeat and the differences in the direction of the acceleration vector and rotation axis are removed. Every maneuvering wingbeat has an incremental force and incremental moment vector (defined with respect to the three orthogonal axes of the strokeplane reference frame) which are used to perform the maneuver. The body and wing variations can be removed by non-dimensionalization, as a force in $[N]$ is defined as $kg \cdot m/s^2$ it is necessary to find the specific mass, length and time scale to make the force non-dimensional. The chosen mass scale is the fly's weight, m_{fly}, the chosen length scale is the wing length, L_w and the time scale is the wingbeat frequency f. The non-dimensional force is defined as:

$$F^* = \frac{F_{man} - F_{avg}}{m_{fly} f^2 L_w}$$

with the forces in $[N]$, m_{fly} in $[kg]$, f in $[Hz]$ and L_w in $[mm]$. For the non-dimensional moment a similar procedure is applied only the wing length is squared as $M = r \times F$ resulting

in:

$$M^* = \frac{M_{man} - M_{avg}}{m_{fly} f^2 L_w^2}$$

After non-dimensionalization of the maneuvering wingbeats there are 6 groups of forces and moments: $FM^*_{a_x}$, $FM^*_{a_y}$, $FM^*_{a_z}$, $FM^*_{\omega_x}$, $FM^*_{\omega_y}$ and $FM^*_{\omega_z}$.

9.2 Deviation Coefficients

In order to obtain the maneuvering wing kinematics, the wing kinematics are compared to the generated non-dimensional forces and moments. Just as the difference in forces and moments between the maneuvering and average wingbeat are used for the non-dimensional forces and moments, for the maneuvering wing kinematics only the polynomial deviation fit is taken into account. Using the axes of the strokeplane reference frame, 9 independent maneuvers can be defined. They depend on the force or moment generation around one of the three axes and also the sign of these forces and moments. The maneuvers can be divided into symmetric and asymmetric maneuvers. The symmetric maneuvers are: F_x *forward*, F_x *back*, F_z *down*, F_z *up*, M_y *down* and M_y *up*. The asymmetric maneuvers are: F_y, M_x and M_z. The maneuvers are after whether they generate a force or a moment, the axis on which the force or moment is generated and if necessary the direction in which they generate the force or moment. The force maneuvers are defining an acceleration in a certain direction and the moment maneuvers an angular acceleration and indirectly a rotational velocity around a specified rotation axis.

For the maneuvering flight model the polynomial deviation coefficients of the maneuvering wingbeats are plotted against the non-dimensional forces and moments. The symmetric maneuvers are caused by symmetric wing kinematics and therefore the left and right wing kinematics can be combined, $a^{dev}_{LR} = \frac{a^{dev}_L + a^{dev}_R}{2}$. The symmetric maneuvering wingbeats in a certain direction have to be divided into two groups. For the force generation along the strokeplane's x-axis for example the maneuvering wingbeats have to be divided into F_x *forward* and F_x *back*, which is done by dividing the wingbeats based on whether F_x is positive or negative respectively. In Fig. 9.1 several polynomial deviation coefficients of F_x *forward* are plotted against their non-dimensional F_x value. Fig. 9.1 shows the six most influential polynomial deviation coefficients for the downstroke, the six most influential polynomial coefficients of the upstroke are shown in Fig. 9.2. Although there is a large scatter of values; usually it is possible to establish a linear trend between the deviation coefficients and the non-dimensional force or moment. For the lower order Legendre polynomials there is usually a trend between the value of the deviation coefficients and the non-dimensional maneuvering force or moment. For every symmetric maneuver three trends can be obtained being b_θ, b_η and b_ϕ, which are the slopes of the trend lines of $a^{dev}_{\theta_{LR}}$, $a^{dev}_{\eta_{LR}}$ and $a^{dev}_{\phi_{LR}}$. By multiplication with the non-dimensional force or moment the deviation coefficients of the maneuvering wing kinematics generating the specific non-dimensional force can be obtained.

For the asymmetric maneuvers the left and right wing kinematics are not symmetric. For example a roll maneuver to the left and a roll maneuver to the right use anti-symmetric wing

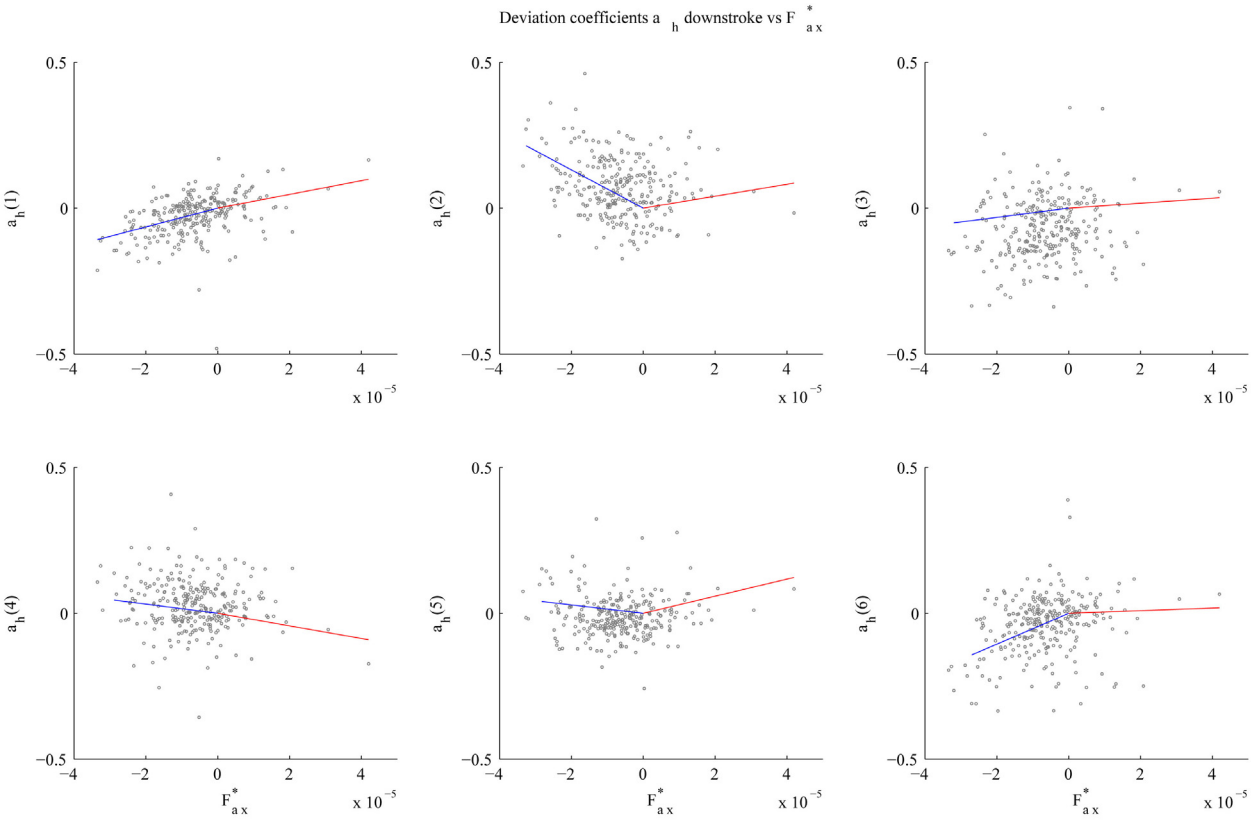

Figure 9.1: First 6 deviation coefficients $a^{dev}_{\eta_{LR}}$ for maneuvers which cause an acceleration along the x axis of the strokeplane reference frame. The first 6 deviation coefficients correspond to the most important polynomials of the downstroke. The deviation coefficients are plotted against the non-dimensional force F^*_x and the trend lines show the trends of the F_x *back* maneuver (blue) and the F_x *forward* maneuver (red).

kinematics. In order to increase the sample size the roll maneuvers to the left are mirrored to the right, by switching the sign of the non-dimensional moment and switching the left and right wing kinematics. In this way all roll maneuvers are to the right and trends can be found for the left and right wing kinematics. In Fig. 9.3 and Fig. 9.4 several polynomial deviation coefficients are plotted versus the non-dimensional force or moment. Just as for the symmetric wingbeats, fits are obtained only now there are six instead of three slopes; b_{θ_L}, b_{η_L}, b_{ϕ_L}, b_{θ_R}, b_{η_R} and b_{ϕ_R}.

In Appendix D the trend lines for all the maneuvers are given. The trend lines for F_z *down* are not given as there are only 10 wingbeats used for the trend lines, which is an insufficient sample size. The sample sizes for the other maneuvers are considerably higher: F_x *forward*: $N = 70$, F_x *back*: $N = 204$, F_y: $N = 455$, F_z *up*: $N = 414$, M_x: $N = 330$, M_y *down*: $N = 57$, M_y *up*: $N = 141$ and M_z: $N = 422$. In order to make the obtained maneuvering wing kinematics useable for the dynamic simulation model and for RoboFly experiments it is necessary to ensure periodic boundary conditions over the downstroke and upstroke. This

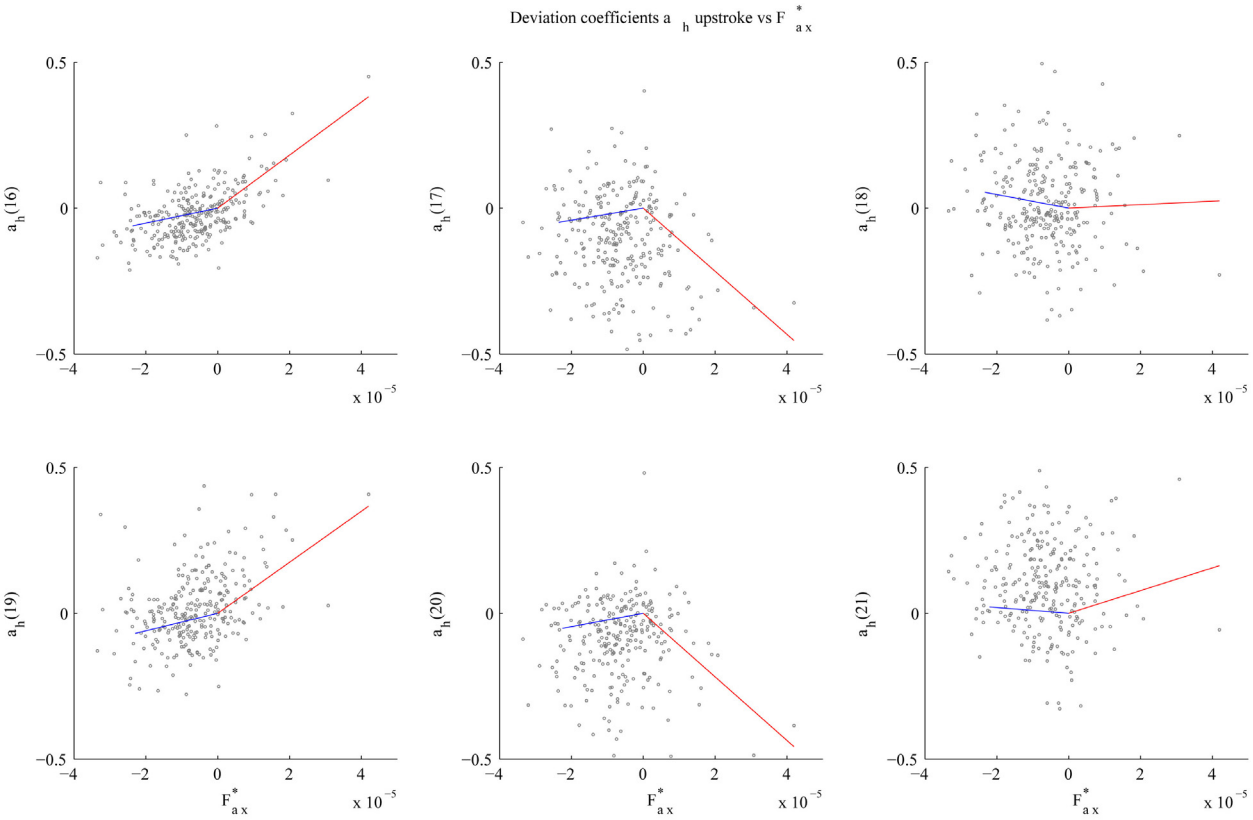

Figure 9.2: Deviation coefficients 16 - 21 of $a_{\eta_{LR}}^{dev}$ for maneuvers which cause an acceleration along the x axis of the strokeplane reference frame. Deviation coefficients 16 - 21 correspond to the most important polynomials of the upstroke. The deviation coefficients are plotted against the non-dimensional force F_x^* and the trend lines show the trends of the F_x *back* maneuver (blue) and the F_x *forward* maneuver (red).

is done by the same procedure as was used to enforce periodic boundary conditions on the average wingbeat in Chapter 6.

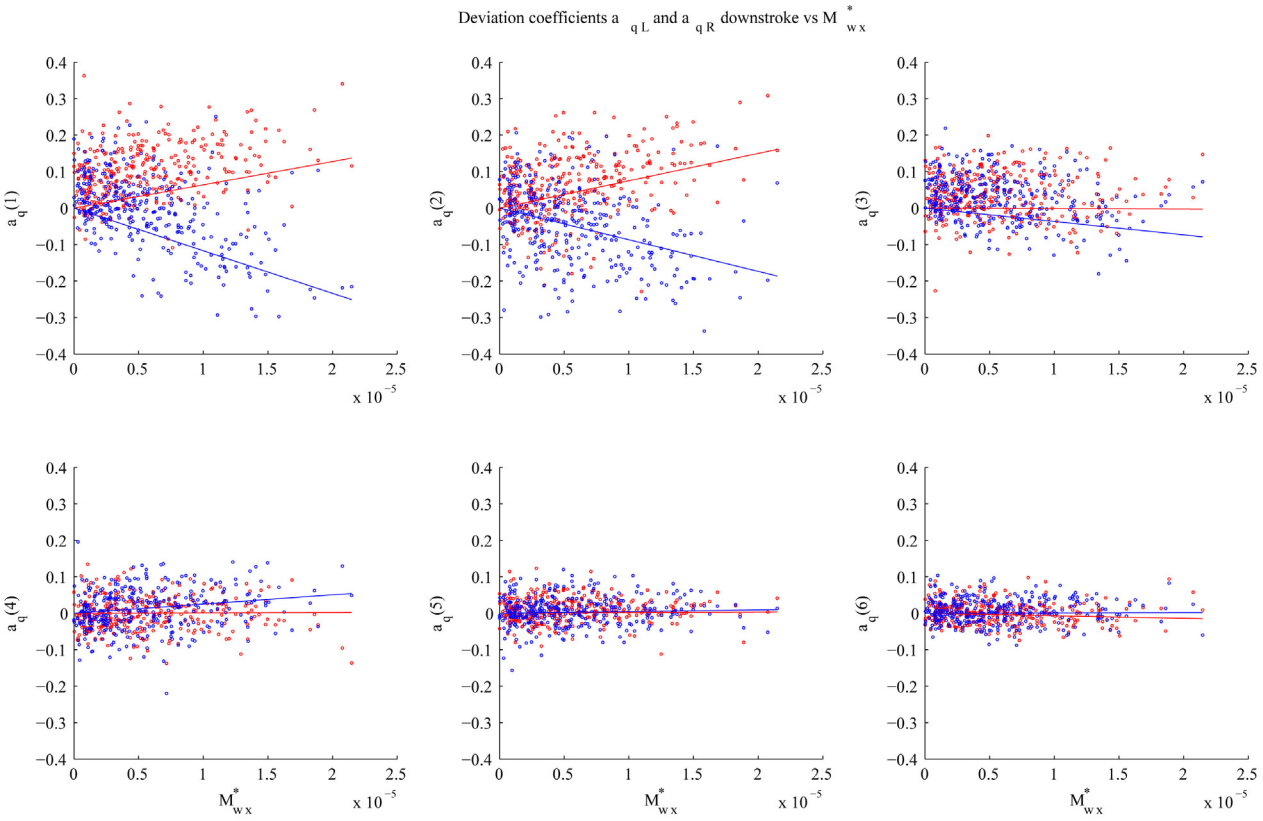

Figure 9.3: First 6 deviation coefficients $a_{\theta_L}^{dev}$ (red) and $a_{\theta_R}^{dev}$ (blue) for maneuvers which cause a rotational acceleration along the x axis of the strokeplane reference frame. The first 6 deviation coefficients correspond to the most important polynomials of the downstroke. The deviation coefficients are plotted against the non-dimensional moment M_x^* and the trend lines show the trends of the left wing kinematics (red) and the right wing kinematics (blue).

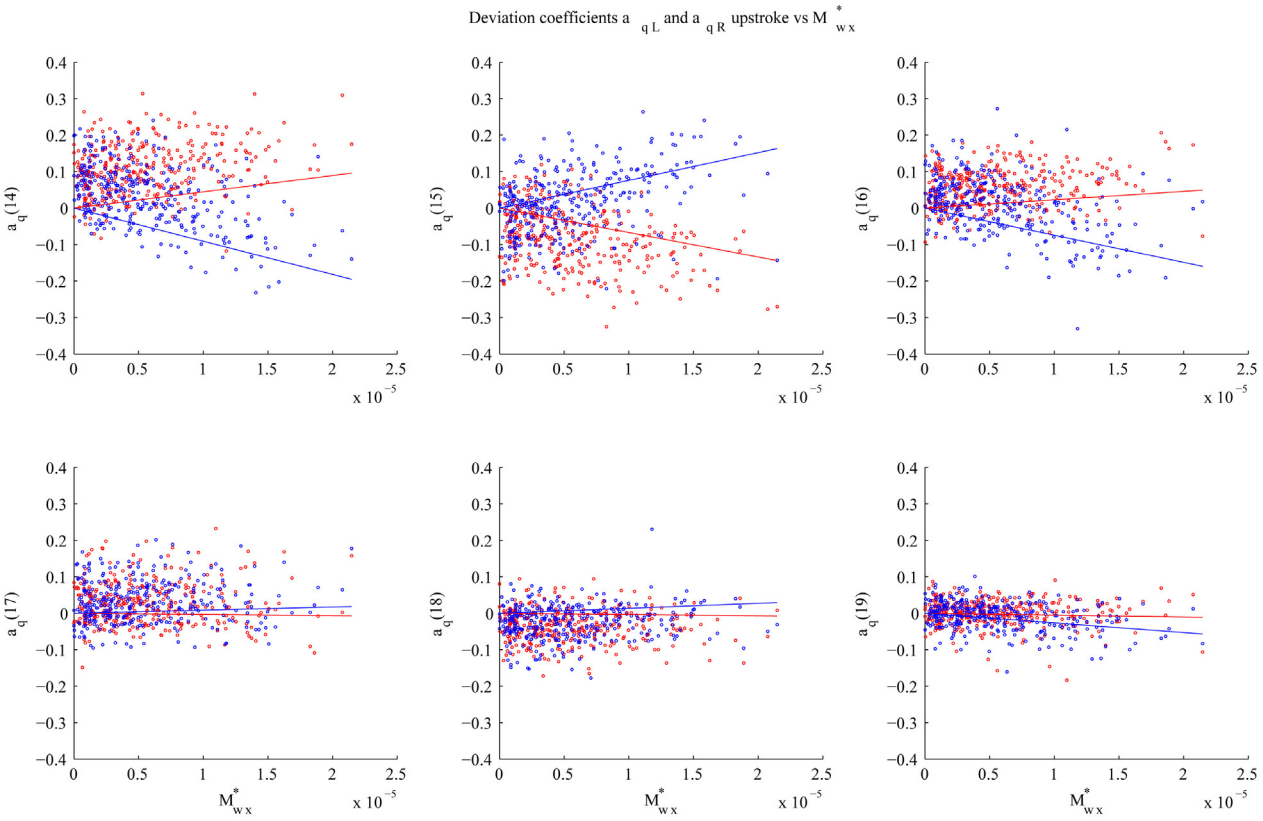

Figure 9.4: Deviation coefficients 14 - 19 of $a_{\theta_L}^{dev}$ (red) and $a_{\theta_R}^{dev}$ (blue) for maneuvers which cause a rotational acceleration along the x axis of the strokeplane reference frame. Deviation coefficients 14 - 19 correspond to the most important polynomials of the upstroke. The deviation coefficients are plotted against the non-dimensional moment M_x^* and the trend lines show the trends of the left wing kinematics (red) and the right wing kinematics (blue).

9.3 Maneuvering Wing Kinematics

The maneuvering wing kinematics can now be generated by first establishing the polynomial symmetric average wingbeat, subsequently adding the maneuvering polynomial deviation coefficients and finally obtaining the wing kinematic angles from the polynomial fits. The maneuvering polynomial deviation coefficients are established by multiplying the trend line b of a maneuver with the non-dimensional force or moment. In this way the maneuvering wing kinematics for all eight maneuvers can be obtained. In Fig. 9.5 and Fig. 9.6 the maneuvering wingbeats are depicted for the eight maneuvers. In the figures ten maneuvering wingbeats are given for each maneuver, starting from the average wingbeat upon the maneuvering wingbeat obtained from 1.2 times the maximum non-dimensional force or moment for that maneuver out of all measured maneuvers. The maneuvering wingbeats between the average wingbeat and the maximum wingbeat are uniformly increasing. The maneuvering wingbeats in Fig. 9.5 and Fig. 9.6 are created for RoboFly experiments, which induces sometimes limitations on the maneuvering wing kinematics. The maximum stroke angle ϕ in the RoboFly is 90 degrees and the maximum deviation angle θ is 30 degrees. When a maneuvering wingbeat exceeds these values the factor of 1.2 times the maximum wingbeat is downscaled. The factors and the non-dimensional force or moment related to the maximum wingbeat of a maneuver are also given in Fig. 9.5 and Fig. 9.6.

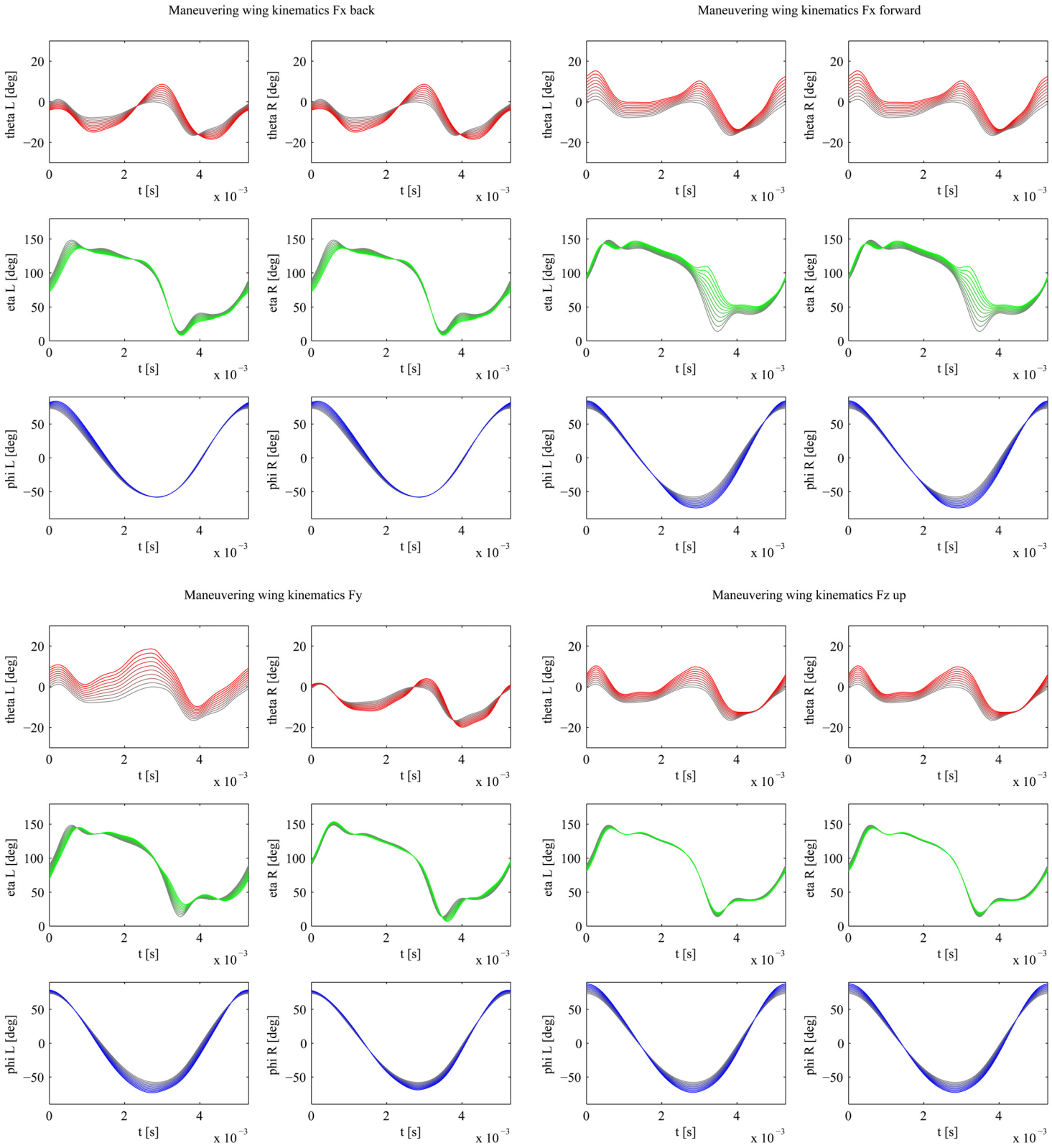

Figure 9.5: Force maneuvers

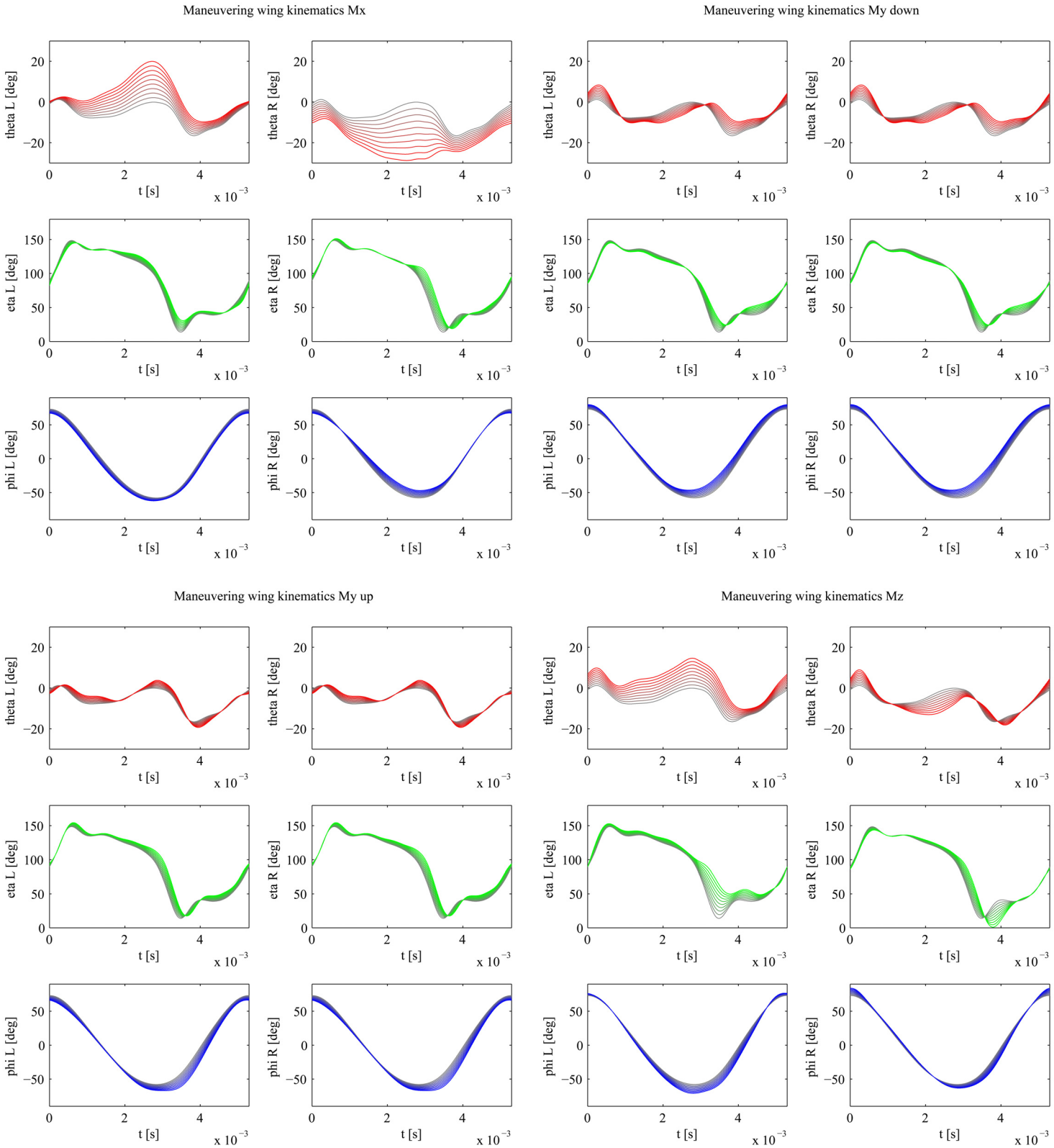

Figure 9.6: Moment maneuvers

Chapter 10

Results

The results can be categorized under five sections; RoboFly results, the maneuvering flight model, dynamic simulation results, aerodynamic and inertial damping and the results of flow visualization experiments. The high-speed video sequences provide a vast source of information and unfortunately not all the aspects of the observed flights could be researched. The five categories presented in this section are selected to present the established maneuvering flight model as complete as possible. Besides the model itself also the validation results and the limitations of the model will be presented in this chapter.

10.1 RoboFly Experiments

The maneuvering flight model of this thesis relies heavily on the quasi-steady aerodynamic model. The quasi-steady model gives a good estimate of the force production during hovering flight. However the validity of the quasi-steady model for the maneuvers observed in the video sequences is not known. The RoboFly is designed to replicate the flow around fruit fly wings under hovering flight conditions, but is restricted in simulating maneuvering flight. Roll and pitch motion cannot be simulated on the current set-up of the RoboFly. Therefore the RoboFly simulations are without body motion or rotation. The purpose of the RoboFly experiments is to validate the maneuvering flight model and the quasi-steady aerodynamic model.

Average Wingbeat Results

Fig. 10.1 shows the RoboFly results for the average wingbeat of all sequences, a_{glob}. Besides the forces and moments scaled to fruit fly size measured by the RoboFly, also the quasi-steady estimate with and without rotational lift is shown. Comparison of the forces and moments

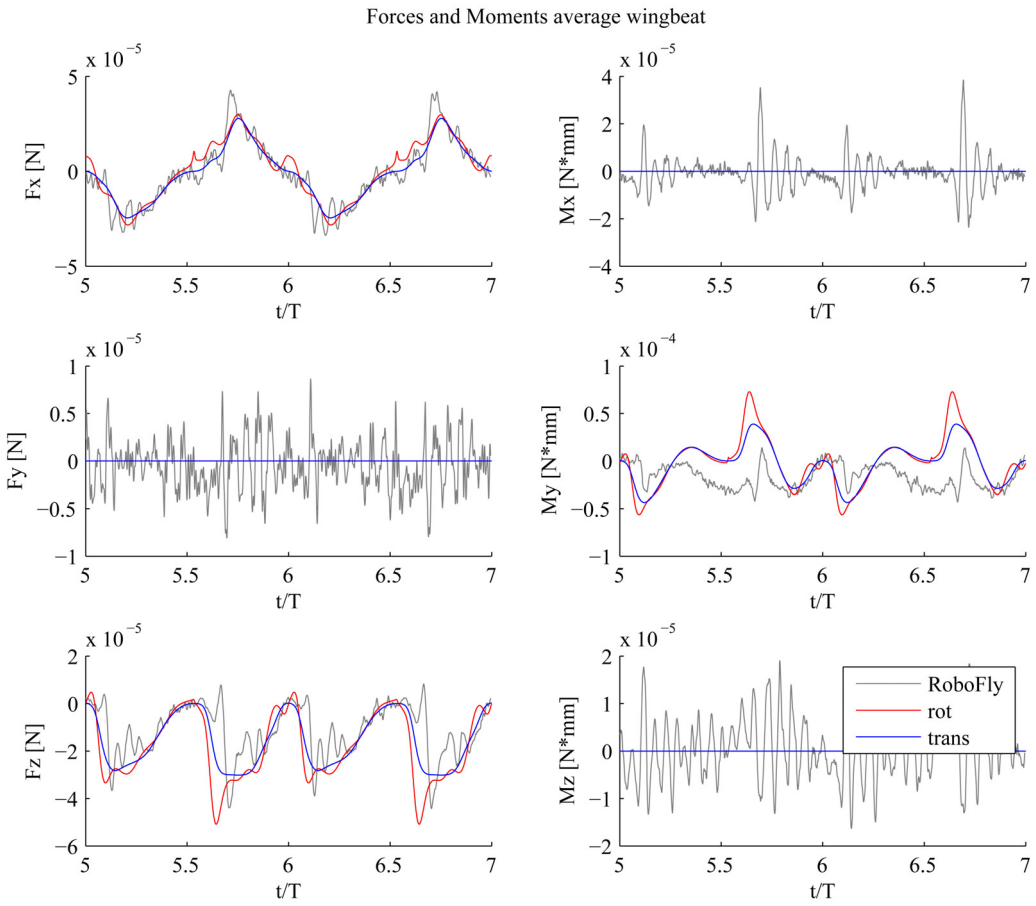

Figure 10.1: Quasi-steady aerodynamic model (erroneous rotational force model) for the global average wingbeat; RoboFly (grey), quasi-steady aerodynamic model translational forces only (blue) and quasi-steady aerodynamic model translational + rotational forces (red).

in Fig. 10.1 of the RoboFly results and the quasi-steady model, yields that the quasi-steady model generally predicts the forces quite accurate. However when looking at the results for the quasi-steady model including rotational lift, one can see that the force peaks are over estimated. This is due to a misinterpretation of the formula for rotational lift in Chapter 7, eq. 7.1. Instead of the time derivative of the wing pitch angle $\dot{\eta}$, the time derivative of the time derivative of the angle of attack $\dot{\alpha}$ has been used. The correct definition of the rotational forces leads to an improved prediction of the forces although the gradients of force peaks in the RoboFly experiments are generally sharper, Fig. 10.2. One might have noticed in Fig. 10.1 and Fig. 10.2 only the sixth and seventh wingbeat are depicted. The RoboFly simulations consist of seven wingbeats, the main reason for this number of wingbeats is the fact that the wake needs a few wingbeats to develop. Therefore the first three wingbeats are not analyzed, the subsequent four wingbeats will be analyzed. Four wingbeats are used in order to obtain an average, however the variation in RoboFly results is minimal. More details on the set-up of the RoboFly experiments can be found in Appendix. **??**. The forces F_x and F_z measured

by the RoboFly correspond well to the quasi-steady aerodynamic model. The pitch moment M_y however is significantly overestimated by the quasi-steady aerodynamic model.

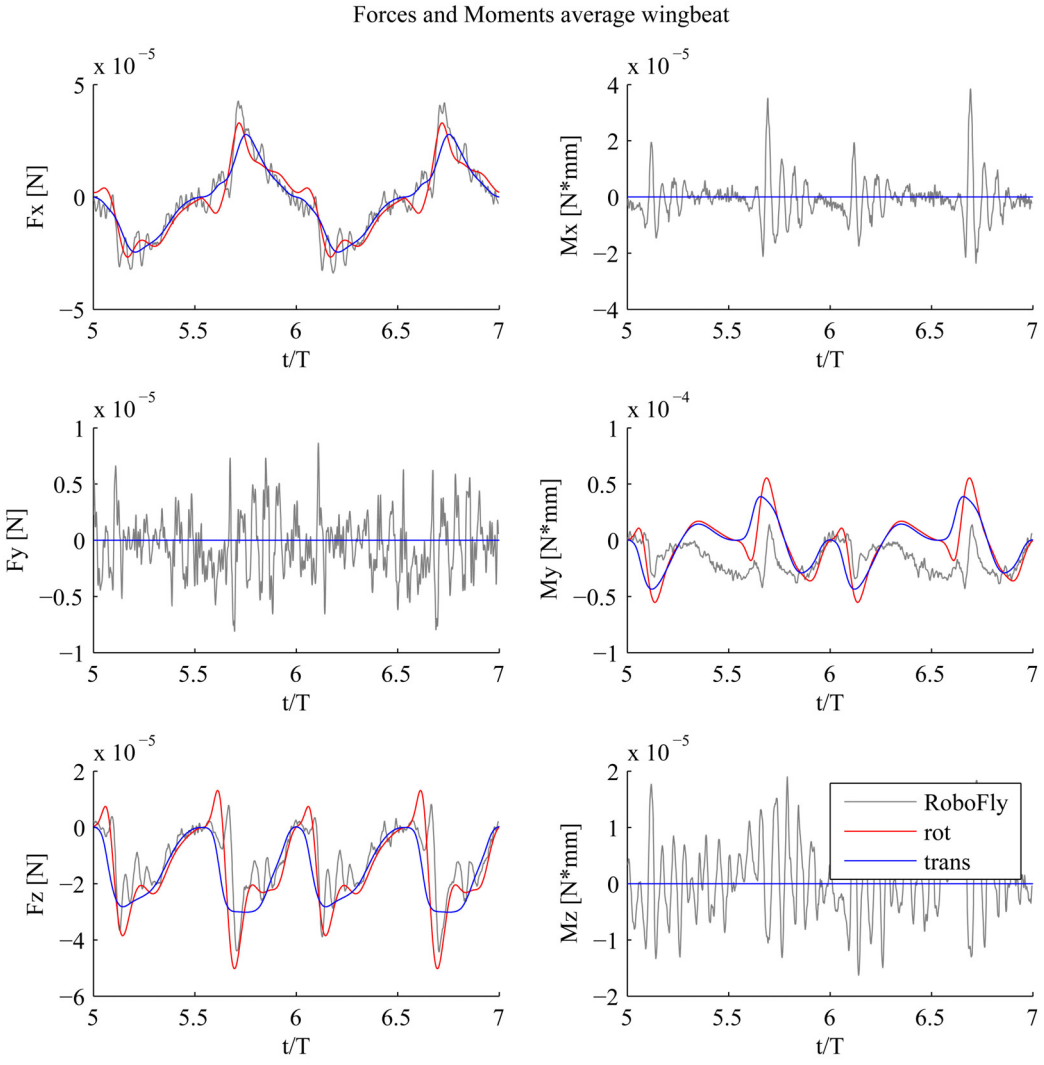

Figure 10.2: Quasi-steady aerodynamic model (corrected rotational force model) for the global average wingbeat; RoboFly (grey), quasi-steady aerodynamic model translational forces only (blue) and the revised quasi-steady aerodynamic model translational + rotational forces (red).

Unfortunately the erroneous formulation of the rotational forces in the quasi-steady model was discovered after the RoboFly experiments had been carried out. As the wing kinematics of the maneuvering flight model are established with the aid of the quasi-steady model the maneuvering wing kinematics of Chapter 9 are less pronounced than the actual wing kinematics. Due to time issues it was not possible to redo the RoboFly experiments with the maneuvering wing kinematics based on the revised quasi-steady model. However the main

goal of the RoboFly experiments was to validate the maneuvering flight model and the quasi-steady model under maneuvering wing kinematics. This validation is not threatened by the error in the rotational force model. In Chapter 9 the maneuvering wing kinematics are given in Fig. 9.5 and Fig. 9.6. In Fig. 9.5 and Fig. 9.6, 10 wingbeats are displayed per maneuver to keep the figures clear, in the RoboFly experiments there are 20 wingbeats per maneuver.

$\mathbf{F_x}$ back

Fig. 10.3 shows the RoboFly results for the maneuver F_x *back*. The maneuver F_x *back* is symmetric, so F_y, M_x and M_z are not affected by the maneuvering wing kinematics. When looking at F_x in Fig. 10.3 one can observe that the main force generation backwards in the x direction is produced in the middle of the downstroke. There are some slight changes in F_z and M_y but the change in forces is mainly in the x direction. When looking at the predicted F_x by the maneuvering flight model and the actual F_x following from RoboFly experiments it becomes clear that the erroneous rotational lift leads to a significant overprediction of maneuvering flight forces. This is due to two phenomena; in the first place the erroneous quasi-steady aerodynamic model overpredicts the effects of rotational forces which leads to less pronounced maneuvering wing kinematics of the maneuvering flight model, secondly the maximum non-dimensional force or moment will be an overestimation. The combined effect of the two phenomena is a much steeper slope of force prediction by the maneuvering flight model (black line in Fig. 10.3) compared to the RoboFly results (red line in Fig. 10.3). The quasi-steady model with only translational forces gives results which are close to the RoboFly experiments. The quasi-steady model with the corrected rotational model lies also close to the RoboFly results and for higher force production the model is more accurate than the translation only model. The contribution of the three wing kinematic angles is plotted in Fig. 10.3. The result of only changing the wing pitch angle, η, generates forces very similar to the full maneuvering wing kinematics. Changing only the stroke angle, ϕ, has a much smaller but also positive effect on the force generation in the x *back* direction. Changing only the deviation angle, θ, gives a negative contribution.

$\mathbf{F_x}$ forward

Fig. 10.4 shows the RoboFly results for the maneuver F_x *forward*. The force in x direction is primarily produced during the middle of the upstroke. The wingbeat averaged force production of F_z is not affected much by the maneuver, however the force peak at the start of the upstroke is suppressed whilst the force peak at the start of the downstroke is enforced. There are also some changes in M_y which results in a stronger pitch down moment. The predicted force F_x by the maneuvering wing kinematics is again a significant over estimation; this will be the case for all studied maneuvers. Considering the quasi-steady model in Fig. 10.4, there is a rather big difference between the translational forces only model and the model including rotational forces. The quasi-steady model with rotational forces matches the best with the RoboFly results. Just as was the case for F_x *back*, η is the dominant parameter in the force generation. However at higher force production the contribution of η becomes weaker whilst

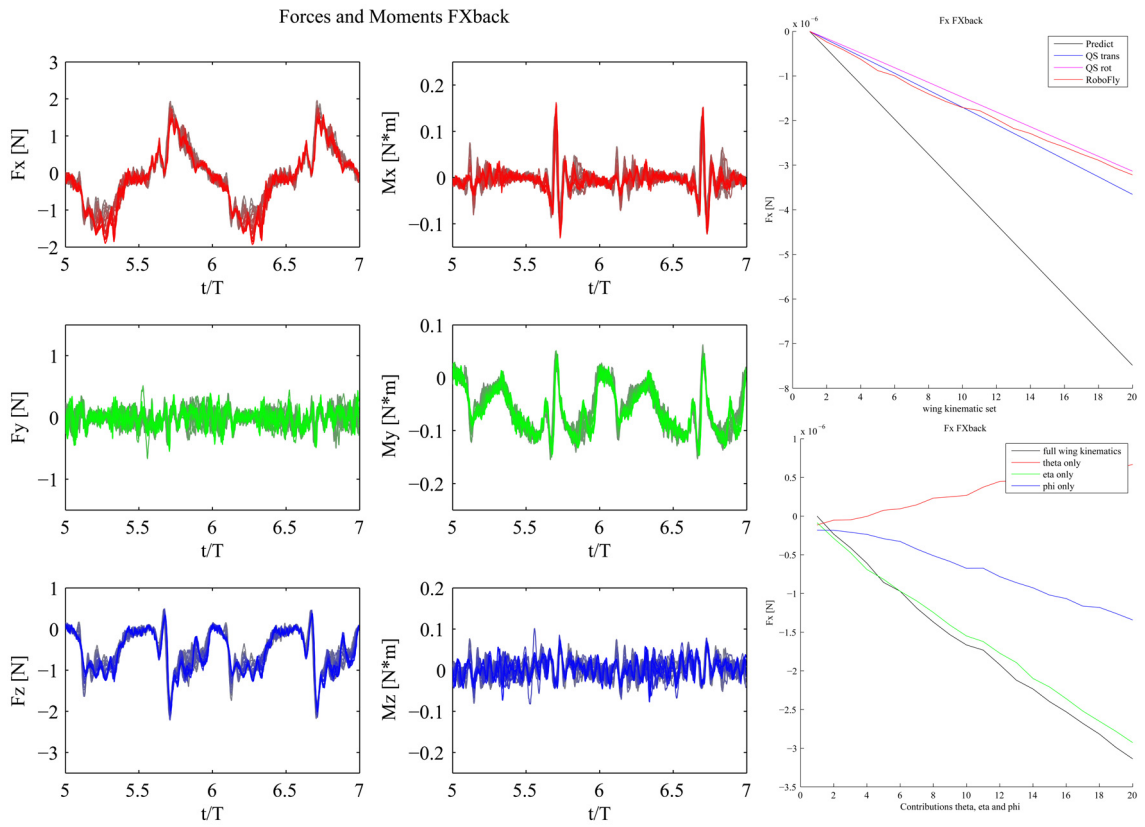

Figure 10.3: RoboFly experiments for F_x *back*. The left figure shows the forces and moments in the strokeplane reference frame, the grey wingbeat is the average wingbeat and the forces and moments slowly shift to the color red, green or blue when reaching their maximum predicted value. The figure in the right upper corner shows the force F_x against the set of 20 wingbeats. The black line shows the force predicted by the maneuvering flight model (based on the erroneous rotational force model), the red line gives the RoboFly results and the blue line the results for the quasi-steady model using only the translational force model. The magenta line shows the prediction of the quasi-steady model including the corrected rotational lift model. In the lower right corner the force F_x is plotted against the RoboFly results for the full set of maneuvering wing kinematics including θ, η and ϕ (black), the RoboFly results for a set of wing kinematics where η and ϕ are kept at the average wingbeat and θ is varied with maneuvering wingbeats (red) and a similar set-up for η only (green) and ϕ only (blue).

the contribution of ϕ increases. In this case the contribution of θ can be considered neutral.

$\mathbf{F_y}$

Fig. 10.5 shows the RoboFly results for the maneuver F_y. The force in y direction is produced during the downstroke and the upstroke, and there are some sharp peaks in force production during pronation and supination. As the F_y maneuver is an asymetric maneuver, all the forces and moments can be affected by the wing kinematics. For F_x there is an increase in force in the positive and negative direction, which can be considered as increased drag. There is a

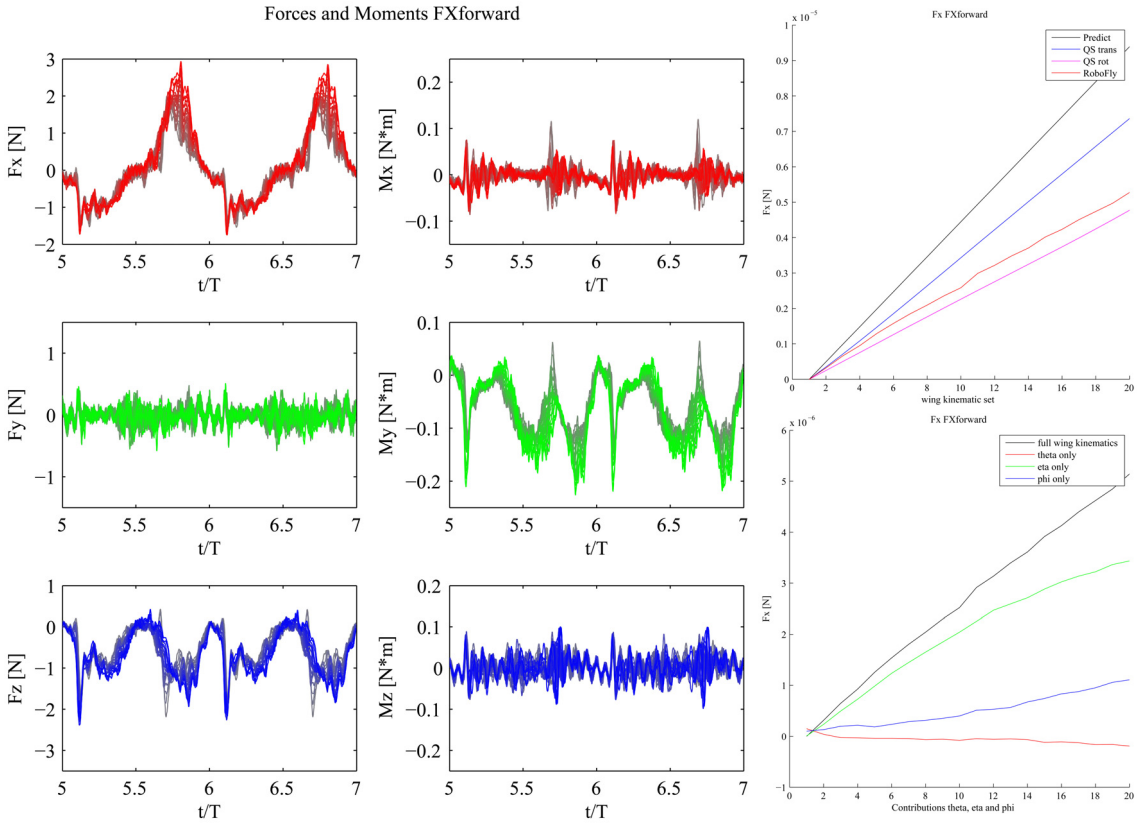

Figure 10.4: RoboFly experiments for F_x *forward*. For more information see the legend of Fig. 10.3.

slight increase in F_z during the upstroke. The moments M_x and M_z are not really affected by the maneuvering wing kinematics, the pitch moment M_y experiences an increase in amplitude however the wingbeat averaged pitch moment does not change a lot. The quasi-steady model results are close to the RoboFly results, with the model including rotational lift being closer to the RoboFly results. The dominant parameter in the F_y maneuver is η, but θ has also a positive influence. The stroke angle ϕ affects the force production in y direction slightly negative.

$\mathbf{F_z}$ up

Fig. 10.6 shows the RoboFly results for the maneuver F_z *up*. The force in z direction is produced during the downstroke and upstroke. The asymmetric forces and moments are not affected by the symmetric maneuver. Interesting to note is that there is only a small increase in amplitude of F_x compared to the increase in F_z. Also the amplitude of the pitch moment, M_y, is increasing however the wingbeat averaged value does not change much. The quasi-steady model overestimates the increase in F_z by approximately 15%. The translational and rotational quasi-steady model are lying very close together. The increase in F_z is mainly caused by ϕ and θ has also a contribution to the force generation, η contributes negatively.

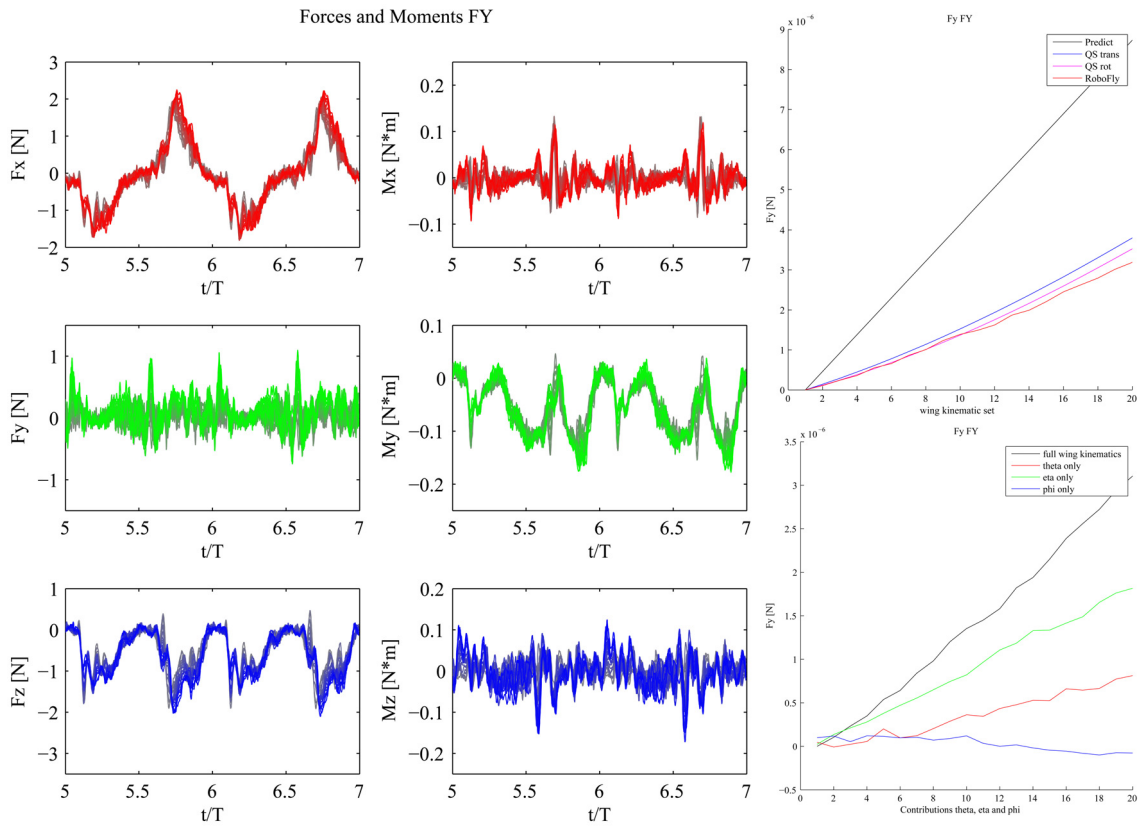

Figure 10.5: RoboFly experiments for F_y. For more information see the legend of Fig. 10.3.

$\mathbf{M_x}$

In Fig. 10.7 the results for the maneuver M_x are plotted. The moment around the x axis is generated during the start of the upstroke. There is a slight increase in force in the positive x direction for F_x. The oscillations in force of F_y increase, there is however not a significant change in the wingbeat averaged force. The force in z direction decreases and the moment M_y reduces in magnitude, becoming more pitch up. During the start of the upstroke there is not only the generation of the M_x moment but also the M_z moment. The strongest contributor to the M_x moment is θ, followed closely by ϕ. However in this case it is clear that the generation of the M_x moment is a joint effort of θ, η and ϕ.

$\mathbf{M_y}$ down

Fig. 10.8 shows the RoboFly results for the maneuver M_y *down*. The moment around the y axis is primarily generated at the end of the downstroke and the start of the upstroke. The force in x direction shifts a bit in time but the wingbeat averaged force remains zero. The force in z direction shows a shift in the peaks, there is a strong peak at the start of the downstroke whilst the peak at the upstroke diminishes. There is a large gap between

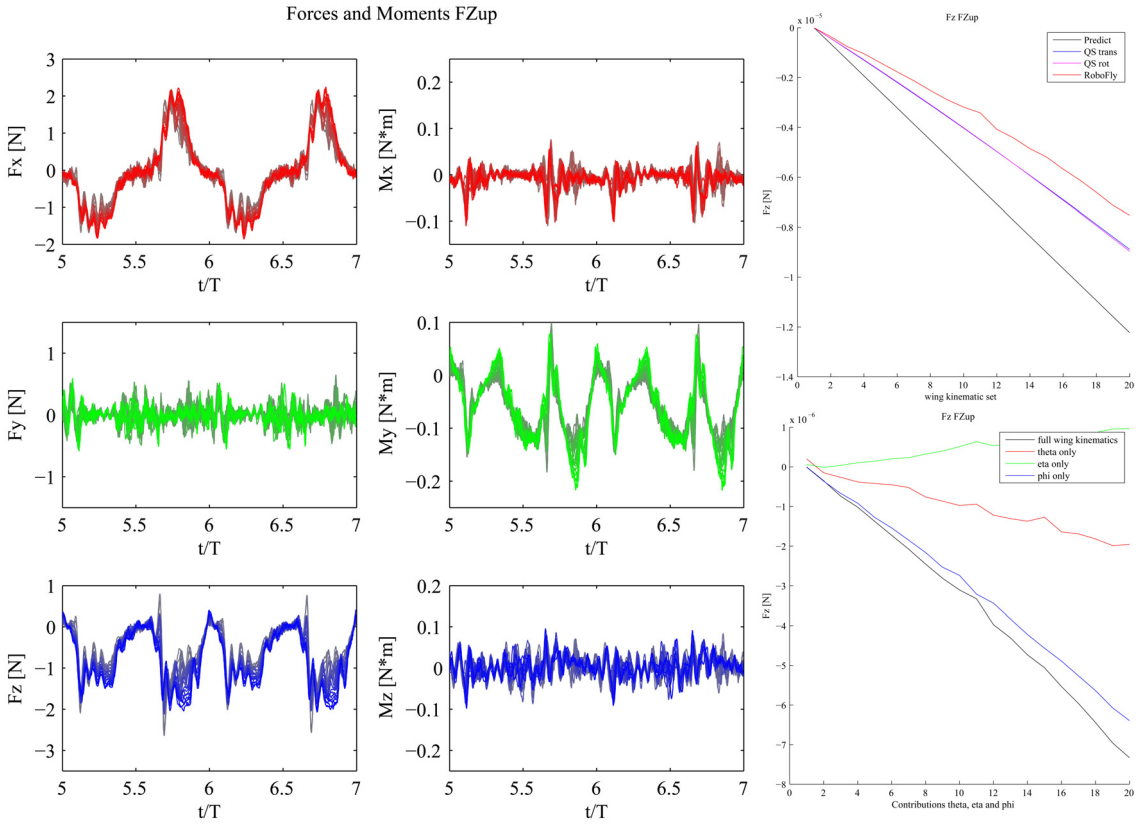

Figure 10.6: RoboFly experiments for F_z *up*. For more information see the legend of Fig. 10.3.

the results of the quasi-steady model and the RoboFly, the moment is overestimated by a factor 3. The biggest factor in generating the pitch-down moment is θ followed by ϕ. The contribution of η is small.

M_y up

Fig. 10.9 shows the RoboFly results for the maneuver M_y *up*. The moment around the y axis is generated during the whole stroke, with an additional increase at the start of the upstroke. At the start of the upstroke there is also an increase in force production in the x direction, generating a forward force. The force F_z is not altered much by M_y *up* although there is a small time shift in the peak at the start of the upstroke. Just as it was the case in M_y *down*, the pitch-up moment is strongly overestimated by the quasi-steady model with a factor of approximately 3. The biggest contributor to the pitch-up moment is ϕ, being even stronger than the three wing kinematic angles combined. This could be due to the fact that the maneuvering flight model was established using an erroneous definition of the rotational force model. But it could also be that the usage of ϕ only would generate more drag or that changing ϕ brings along inherit changes in θ and η. The wing kinematic angle θ has also a strong contributing effect on the pitch moment. The contribution of η is negative.

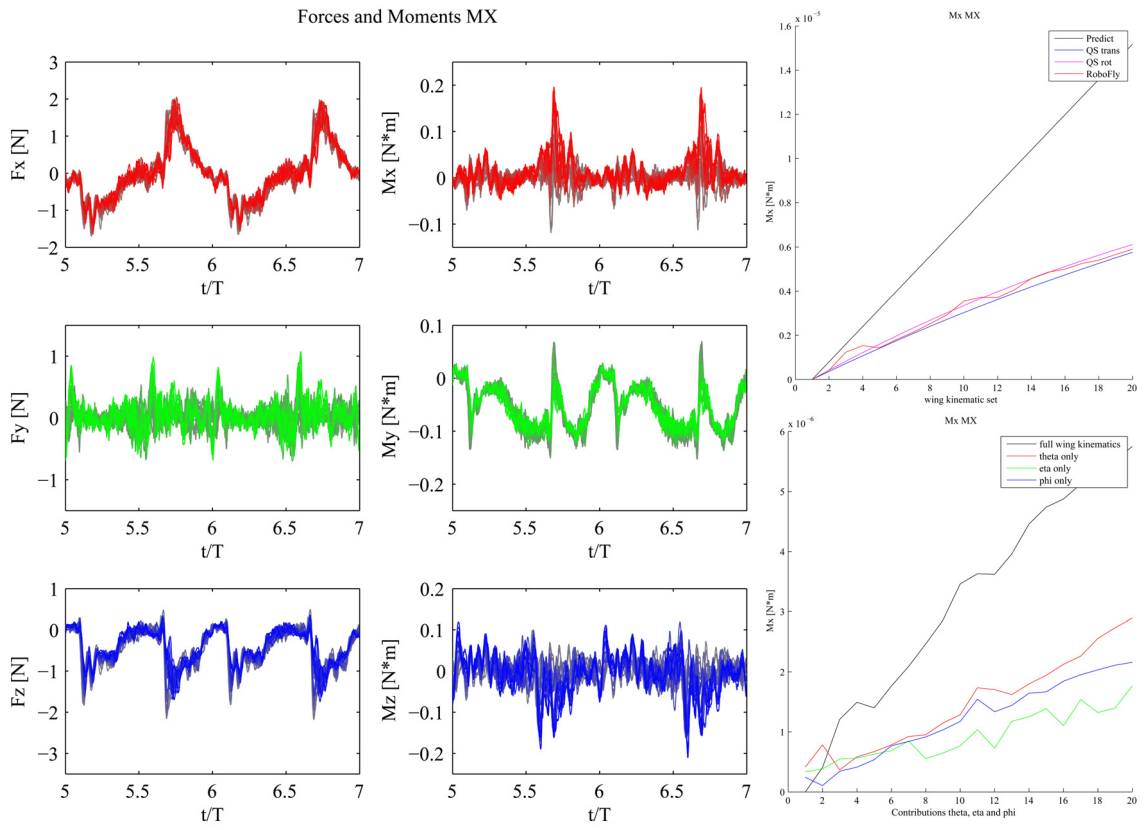

Figure 10.7: RoboFly experiments for M_x. For more information see the legend of Fig. 10.3.

$\mathbf{M_z}$

Fig. 10.10 shows the RoboFly results for the maneuver M_z. The moment around the z axis is mainly produced during the mid-part of the upstroke. The generation of the yaw moment also generates a slight increase in F_x in the forward direction and also a small time shift in force production during the usptroke. There is also an increase in F_z during the upstroke. The generation of M_z comes with a roll moment M_x a pitch down moment M_y. The pitch down moment and the roll moment are both quite significant but not as strong as for the M_y *down* and M_x maneuvers. The RoboFly results and the quasi-steady model including rotational forces show the best match, however the RoboFly results are about 15% stronger for high yaw moments. The yaw maneuver is mainly powered by η and θ is also slightly contributing. The stroke angle ϕ has a small negative effect on the yaw moment generation.

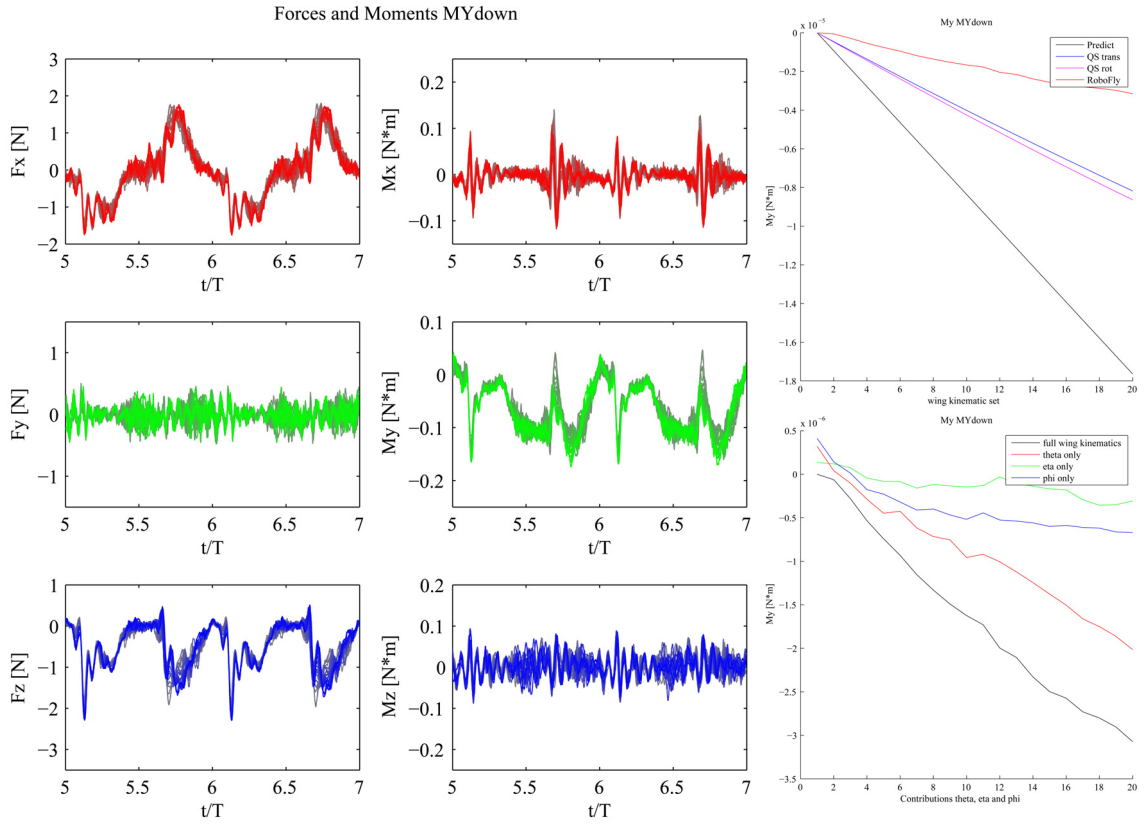

Figure 10.8: RoboFly experiments for M_y *down*. For more information see the legend of Fig. 10.3.

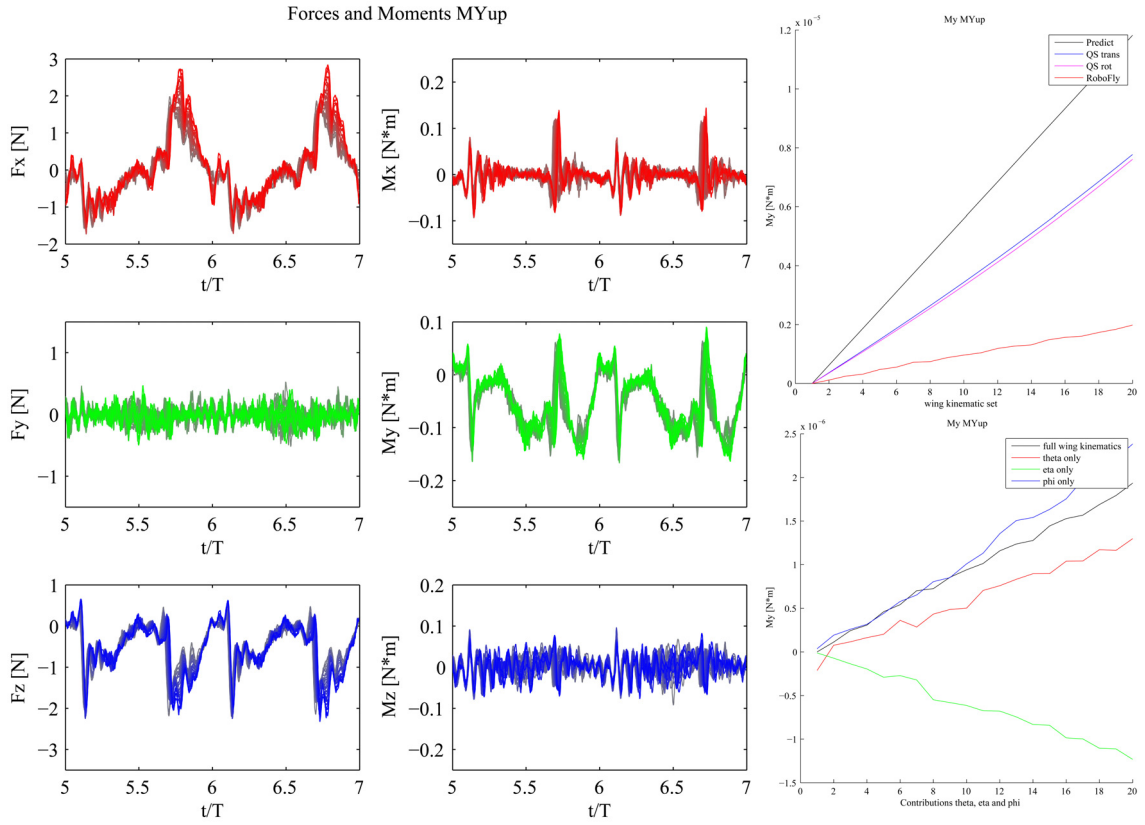

Figure 10.9: RoboFly experiments for M_y *up*. For more information see the legend of Fig. 10.3.

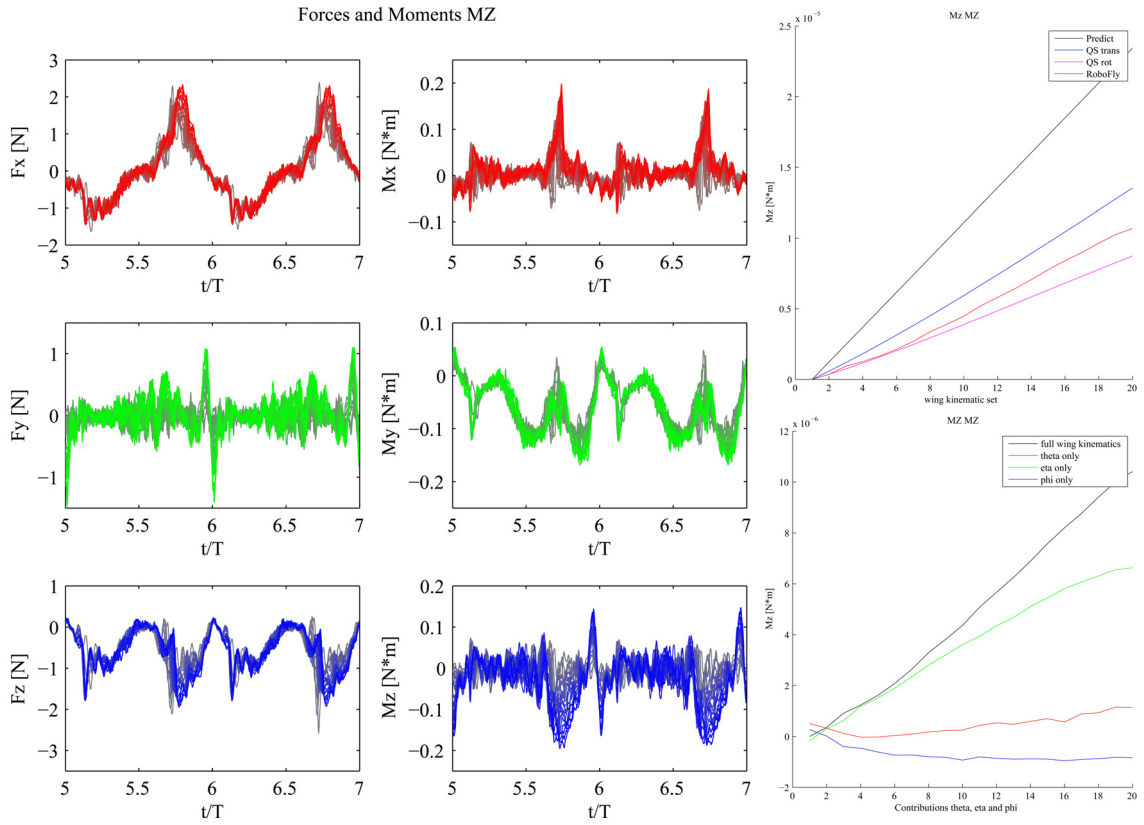

Figure 10.10: RoboFly experiments for M_z. For more information see the legend of Fig. 10.3.

10.2 Maneuvering Flight Model

As described in the previous section, the maneuvering flight model established in Chapter 9 is based on an erroneous aerodynamic model that overestimates the aerodynamic forces and moments significantly. Due to the late discovery of this error it was not possible to redo the RoboFly experiments. The RoboFly experiments from the previous section show however that the quasi-steady model with a revised rotational force model matches closely with the RoboFly results. Now the reliability of the quasi-steady model for maneuvering wingbeats is known a new maneuvering flight model can be established. This section will present the maneuvering flight model obtained by the same procedure as in Chapter 9 but now based on the corrected quasi-steady aerodynamic model.

The new maneuvering wing kinematics are given in Fig. 10.11 and Fig. 10.12. The wing kinematics in Fig. 10.11 and Fig. 10.12 are plotted in the same way as in Fig. 9.5 and Fig. 9.6, meaning that they are confined by the limits of the RoboFly set-up. The sample sizes for the maneuvers are: F_x *forward*: $N = 77$, F_x *back*: $N = 197$, F_y: $N = 455$, F_z *up*: $N = 405$, M_x: $N = 330$, M_y *down*: $N = 81$, M_y *up*: $N = 117$ and M_z: $N = 422$. The maximum non-dimensional forces and moments found in the maneuvering wingbeats dataset are: F_x *forward*: $F^*_{x_{max}} = 0.2412 \cdot 10^{-4}$, F_x *back*: $F^*_{x_{max}} = -0.4522 \cdot 10^{-4}$, F_y: $F^*_{y_{max}} = 0.4019 \cdot 10^{-4}$, F_z *up*: $F^*_{z_{max}} = -0.8327 \cdot 10^{-4}$, M_x: $M^*_{x_{max}} = 0.2145 \cdot 10^{-4}$, M_y *down*: $M^*_{y_{max}} = 0.2412 \cdot 10^{-4}$, M_y *up*: $M^*_{y_{max}} = -0.2626 \cdot 10^{-4}$ and M_z: $M^*_{z_{max}} = 0.4109 \cdot 10^{-4}$. The scaling factors are: F_x *forward*: 1.2, F_x *back*: 1.2, F_y: 1.2, F_z *up*: 0.93, M_x: 0.93, M_y *down*: 1.07, M_y *up*: 1.2 and M_z: 0.93. The trendlines b for the new maneuvering flight model can be found in Appendix. E.

Comparing the wing kinematics of Fig. 9.5 and Fig. 9.6 with the wing kinematics Fig. 10.11 and Fig. 10.12 shows that there are subtle differences between the two models. However the main trends in the maneuvering wing kinematics are present in both models without any exceptions. The small differences in wing kinematics in combination with the closely matched results of the quasi-steady model and the RoboFly experiments puts enough confidence in the newly established maneuvering flight model to reason how the forces and moments are generated by the wing kinematics. The maneuvering flight model predicts a linear increase in force or moment production as the maneuvering wing kinematics become stronger, this prediction is confirmed by the RoboFly experiments in Fig. 10.3 - Fig/ 10.9. The linearity of the RoboFly results confirms that the wing kinematics of (Fig. 9.5, Fig. 9.6) and (Fig. 10.11, Fig. 10.12) are similar. In Appendix. refApp:AppendixE the new trendlines for the maneuver are given. In order to reason how the forces and moments are generated by the wing kinematics; the RoboFly results of the previous section are used in combination with observations on maneuvering flight of Chapter 8. In Fig. 10.13 and Fig. 10.14 a schematic representation of the maneuvering flight model is given. The average wingbeat, a_{glob}, is printed in grey and the maneuvering wing kinematics for maximum non-dimensional force or moment are plotted on top of these wing kinematics. The left wing kinematics are plotted in red and the right wing kinematics in green, the views are aligned with the axes of the strokeplane reference frame.

$\mathbf{F_x}$ back

The subfigure in Fig. 10.13 on the upper left corner shows the maneuvering wing kinematics of F_x *back* at maximum force production. From the RoboFly experiments of the previous section that most of the force in the F_x *back* direction is produced during the downstroke. When looking at the wing pitch angle, the wing pitch angle is higher during the downstroke and smaller during the upstroke compared to the average wingbeat. The higher wing pitch angle during the downstroke tilts the force vector, which is due to the LEV almost always normal to the wing surface, more forward. The opposite is happening during the upstroke, where the force vector is tilted such that the force in the forward x direction is reduced. In this way a resultant force in the F_x *back* direction is generated. The way the force is generated has some resemblance with a paddling motion. In this paddling motion the wing pitch angle, η, is the most important parameter which corresponds to the RoboFly experiments. The supination point of the maneuvering wingbeat lies a bit higher than the supination point of the average wingbeat. The pronation point is lower for the maneuvering wingbeat compared to the average wingbeat. In this thesis the strokeplane is defined as a stationary plane with a constant angle with respect to the body's longitudinal axis. In literature however the strokeplane is usually defined as the plane between the pronation and supination point, in order to avoid confusion this definition of the strokeplane is called the *dynamic strokeplane*. If the wing pitch angle was defined with respect to the dynamic strokeplane, a slight rotation of the dynamic strokeplane can yield the difference in wing pitch angle between the upstroke and downstroke without changing the wing pitch angle w.r.t. the average wingbeat. The stroke angle ϕ has also a contribution to the force production in x direction, the amplitude is increased which means that the wing velocity increases. This means an increase in magnitude of the aerodynamic forces.

$\mathbf{F_x}$ forward

The subfigure in Fig. 10.13 on the upper right corner shows the maneuvering wing kinematics of F_x *forward* for $F_{x_{max}}$. The RoboFly experiments show that the force in x direction is mainly produced during the upstroke. Just as was the case for F_x *back*, also for F_x *forward* η is the most important parameter. The wing pitch angle is slightly smaller during the downstroke and bigger during the upstroke, which results in a paddling motion just as in F_x *back* but now in the opposite direction. The supination point of the maneuvering wingbeat lies a bit above the average wingbeat and the pronation point lies considerably higher than the average wingbeat, resulting in a pitch down rotation of the dynamic strokeplane. This tilts the wingbeat averaged force vector more forward resulting in a resultant force in the positive x direction. The generation of F_x *forward* is however not exactly opposite to F_x *back*. The downward plunge for F_x *forward* is much more stretched out in x direction and the wing pitch angle during this phase is orthogonal to the direction of motion. Large drag forces are created on the wing, generating a strong force in the positive x direction. The change in pitch angle during the downward plunge cannot be seen as a result of the tilt of the dynamic strokeplane, which is also visible in Fig. 10.11 as there is a time shift in η at the start of the upstroke. The stroke angle ϕ contributes to the force generation by increasing the amplitude

and thus the magnitude of the aerodynamic forces.

$\mathbf{F_y}$

The subfigure in Fig. 10.13 on the lower left corner shows the maneuvering wing kinematics of F_y. The RoboFly experiments show that the force in y direction is produced during both the upstroke and the downstroke. The wing pitch angle is identified as the biggest contributor to the force generation in y direction, followed by θ which has also a strong influence. For the left wing, η changes only at the start of the upstroke and the start of the downstroke. The wing pitch angle at these phases of the wingbeat is higher which leads to a paddling motion generating force in the positive y direction at the start of the upstroke and the start of the downstroke (see the front view). The increase in amplitude of ϕ helps to direct the force vector in the y direction during these two phases. The left wing is also slightly raised above the strokeplane, tilting the wingbeat averaged left force vector of the left wing into the y direction of motion. The right wing pitch angle does not show much variation w.r.t. the average wing pitch angle. The right wing is slightly lowered below the strokeplane, which also results in a tilt of the wingbeat averaged right force vector in the y direction. In this case the increase in stroke amplitude alone cannot generate a force in y direction. It is however imporant that the amplitude of ϕ is increased in order to enable the paddling motion in y direction.

$\mathbf{F_z}$ up

The subfigure in Fig. 10.13 on the lower right corner shows the maneuvering wing kinematics of F_z *up*. The RoboFly experiments show that the force in z direction is produced during both the upstroke and the downstroke. The stroke angle ϕ is by far the strongest contributor to the generation of vertical force, however the deviation angle θ has also influence. The wing pitch angle η does not really change w.r.t. the average wingbeat. The increase in amplitude of ϕ results in a higher magnitude of aerodynamic forces during both the upstroke and the downstroke. The angle θ changes such that the downward plunge at the start of the upstroke is strengthened. There is also a smaller downward plunge at the start of the downstroke. The combination of an increase in ϕ with the downward plunge motion reduces the generation of drag in the x direction of the strokeplane reference frame in comparison to the drag generation in case only ϕ was changed. This is due to fact that during a significant part of the downstroke and the upstroke the force vector normal to the wing is pointed upwards.

$\mathbf{M_x}$

The subfigure in Fig. 10.14 on the upper left corner shows the maneuvering wing kinematics of M_x. RoboFly experiments show that the moment M_x is primarily generated during the start of the upstroke. The contribution of the deviation angle θ is the strongest, however it is closely followed by ϕ and η respectively. The effect of θ, η and ϕ combined is much stronger

than the contribution of the single wing kinematic angles. The wing kinematics of the left wing do not differ much from the average wingbeat, however the supination point is elevated highly above the strokeplane. The elevation of the supination point creates a strong downward plunge taking up a significant part of the upstroke. For the right wing the supination point is lowered below the strokeplane, resulting in a decrease in ϕ and no downward plunge at the start of the upstroke. Both effects yield a decrease in force production on the right wing. The overall result is a strong increase in force on the left wing and a strong decrease in force on the right wing. Besides the generation of a roll moment, a pitch-up moment and a yaw moment are also generated. The pitch-up moment corresponds to the strong downward plunge on the left wing. The yaw motion corresponds to the tilting of the dynamic strokeplane of the left wing and the opposite tilting of the dynamic strokeplane of the right wing.

$\mathbf{M_y}$ down

The subfigure in Fig. 10.14 on the upper right corner shows the maneuvering wing kinematics of M_y *down*. RoboFly experiments show that θ has the strongest effect on generating a pitch down moment. The stroke angle ϕ is also a contributor, the wing pitch angle η is neutral. The differences between the wing kinematics of the maneuvering wingbeat do not differ as drastically from the average wingbeat as for the M_x maneuver. The main cause of the generation of the moment around the y axis is the reduction of the downward plunge at the start of the upstroke. A small downward plunge at the start of the downstroke is also present. The contribution of ϕ is marked by a small shift of the wingbeat averaged value of ϕ backwards in the x direction of the strokeplane reference frame. This results in a shift of the center of pressure of the wingbeat resulting in a pitch down moment.

$\mathbf{M_y}$ up

The subfigure in Fig. 10.14 on the lower left corner shows the maneuvering wing kinematics of M_y *up*. RoboFly experiments show that ϕ is the strongest contributor to the pitch up moment, whilst θ is also influential. Only changing η yields negative results. The pitch up moment is primarily generated at the start of the upstroke by increasing the strength of the downward plunge. The change in stroke angle also provides a pitch up moment by shifting the center of pressure more forward along the x axis of the strokeplane reference frame.

$\mathbf{M_z}$

The subfigure in Fig. 10.14 on the lower right corner shows the maneuvering wing kinematics of M_z. The RoboFly experiments showed that most of the yaw moment is generated during the middle part of the upstroke. The wing pitch angle is the dominant parameter although for higher yaw moments the influence of η declines whilst the contribution of θ becomes somewhat stronger. The stroke angle ϕ has a slightly negative contribution. The wing pitch angle of the left wing is during the downstroke quite similar to the downstroke of the average

wingbeat, however during the upstroke the pitch angle is much higher resulting in a paddling motion for the duration of the whole upstroke. The high drag forces due to the large angle of attack result in the generation of a yaw moment by the left wing. The downstroke of the right wing is also very similar to the downstroke of the average wingbeat considering η. During the upstroke of the right wing however the wing pitch angle is reduced significantly such that the there is almost no generation of F_x. This means that the right wing does not resist the yaw moment generated by the left wing during the upstroke. Interesting to note is what happens on the end of the right upstroke, the wing moves far back reaching a stroke angle of more than $90\,^\circ$. When the wing starts moving back during the downstroke it generates an additional yaw moment. Whether the large stroke angle at the end of the upstroke is an intended motion or just a result of the increased wing velocity during the upstroke due to the low wing pitch angle is unclear.

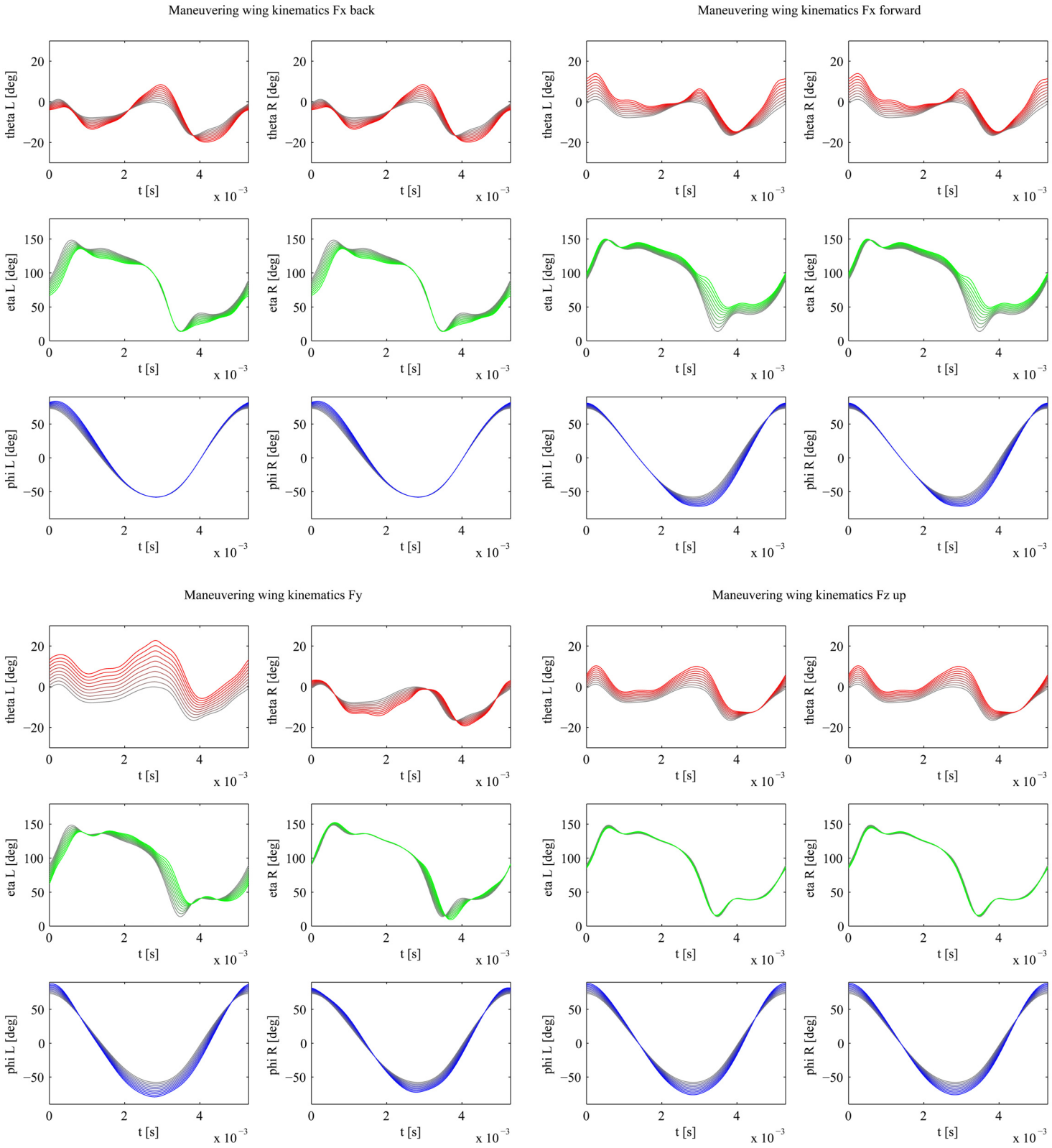

Figure 10.11: Force maneuvers

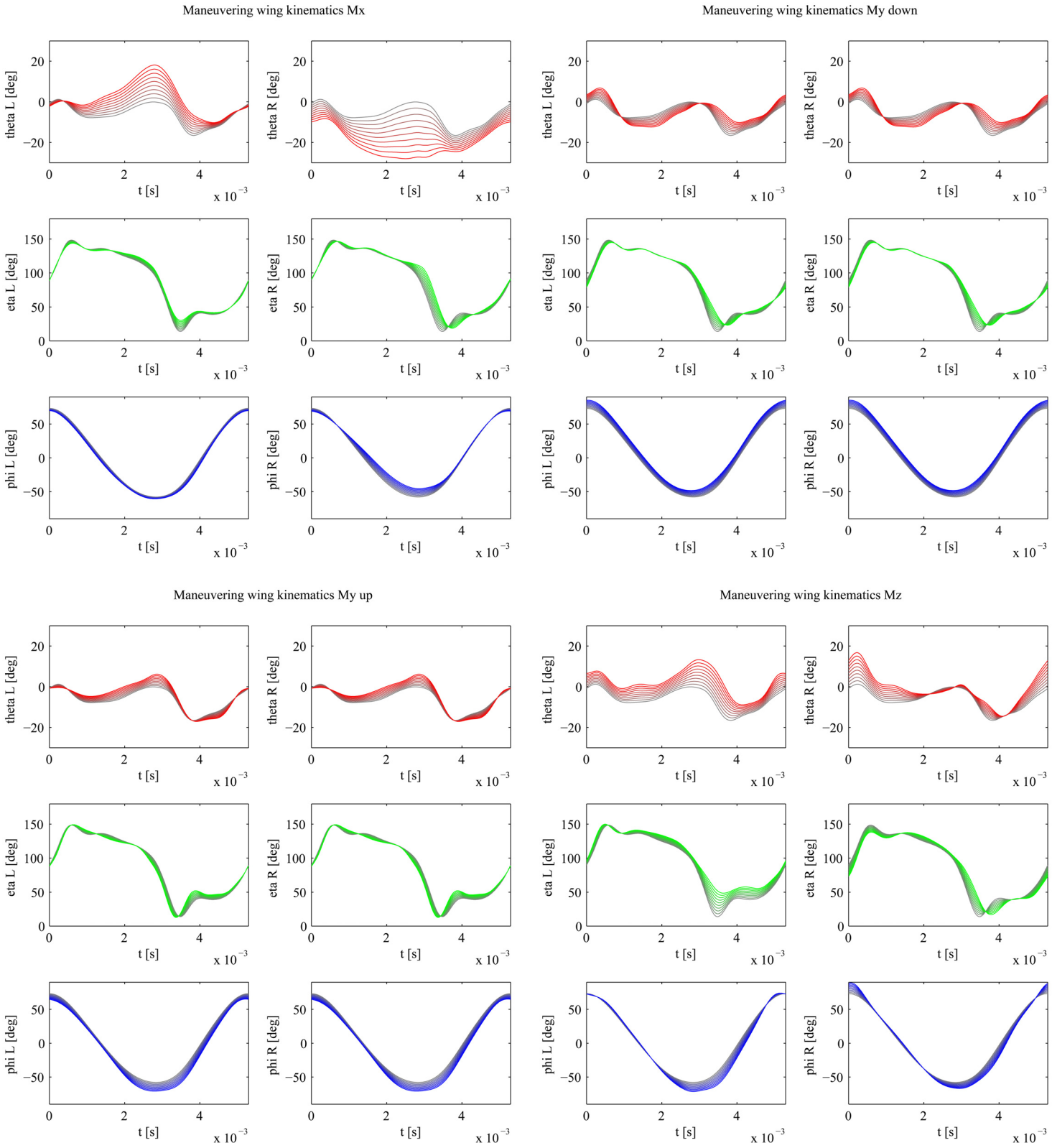

Figure 10.12: Moment maneuvers

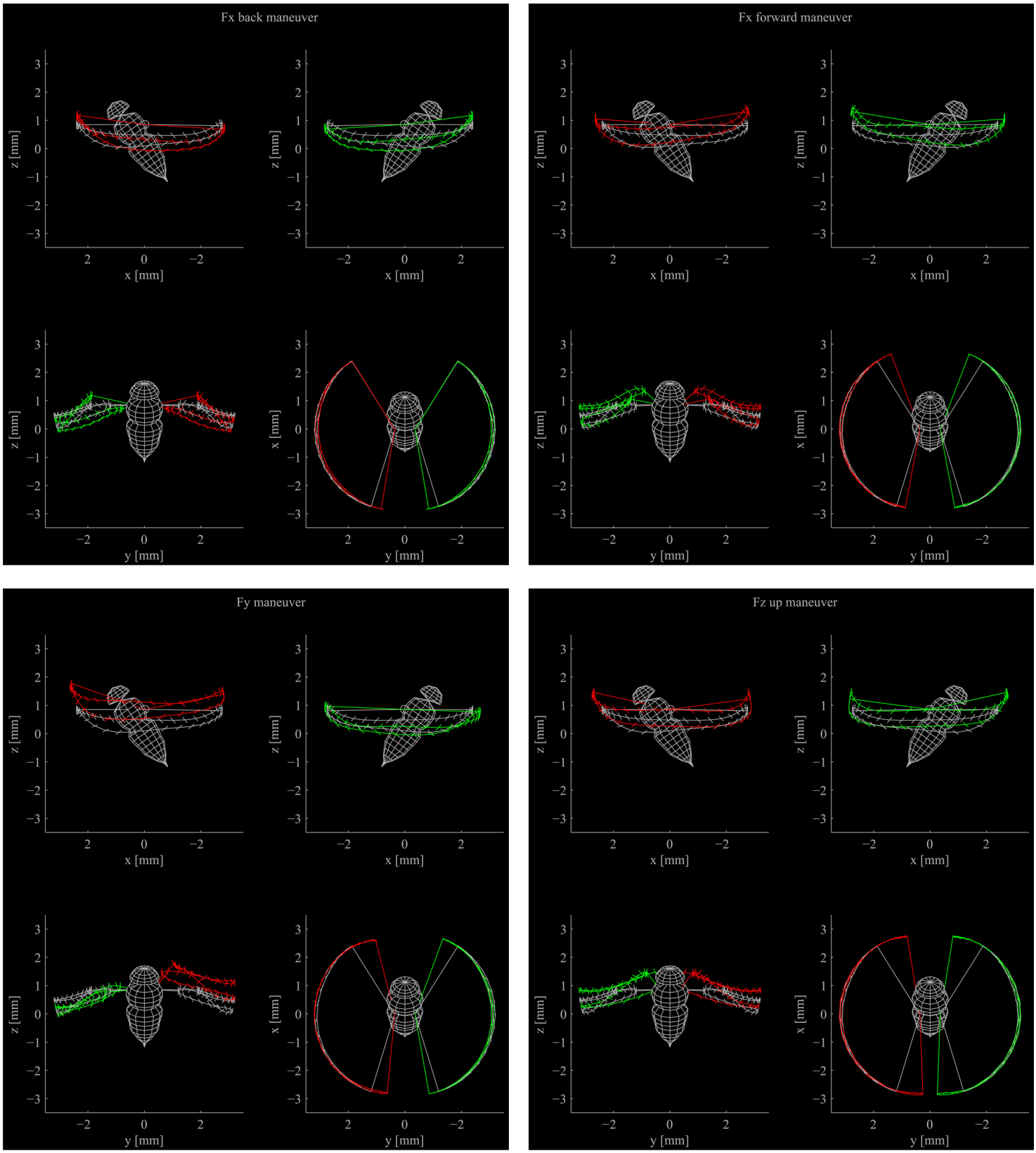

Figure 10.13: Force maneuvers

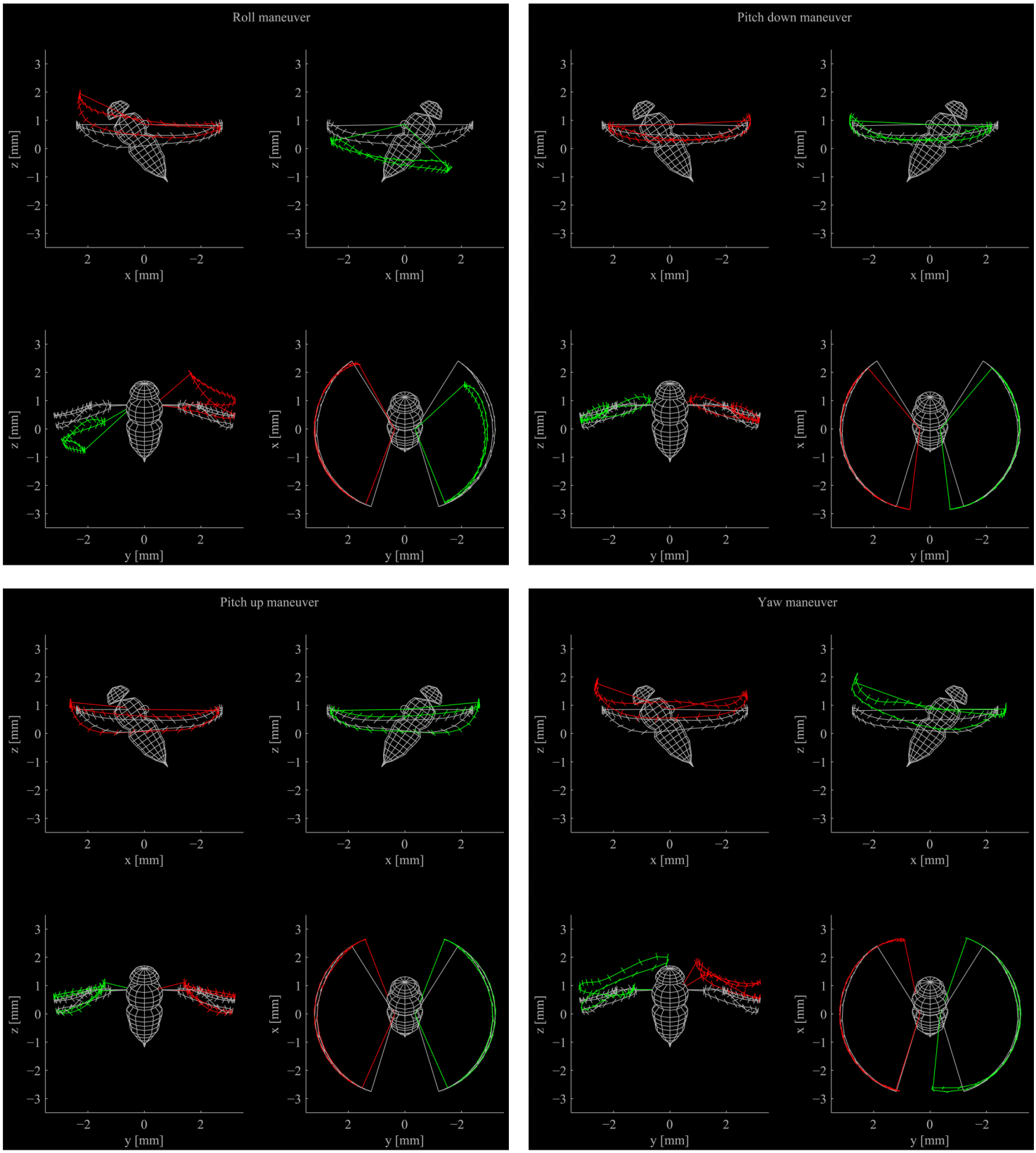

Figure 10.14: Moment maneuvers

10.3 Dynamic Simulation

The RoboFly experiments have shown the validity and limitations of the quasi-steady model and the validity of the maneuvering flight model. However the RoboFly experiments were performed without body motion and the effects of body and wing inertia experienced under free flight conditions. In order to investigate the performance of the maneuvering flight model under maneuvering flight conditions the dynamic simulation is used. However before the dynamic simulation is used to investigate the maneuvering flight model, first the validity of the dynamic simulation itself must be established for steady and maneuvering flight. This is done by selecting a single wingbeat from the high-speed video sequences and computing the wingbeat averaged values for the body dynamics, subsequently the selected wingbeat from the high-speed video sequence will be simulated in the dynamic simulation for the duration of a single wingbeat and finally the body dynamics of the video sequence and the dynamic simulation will be compared. This section enhances an elaborate verification of the dynamic simulation.

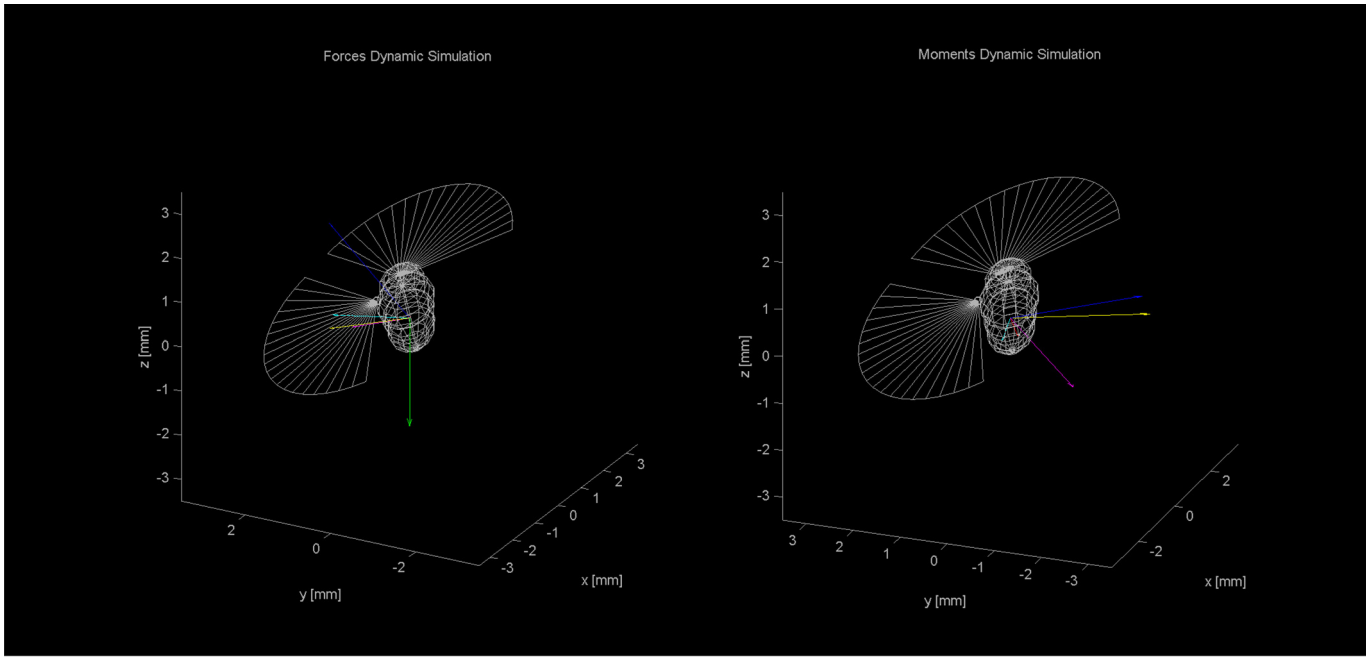

Figure 10.15: Overview of the force vectors and moment vectors involved in a maneuvering wingbeat. The left plot contains the following wingbeat averaged force vectors of the dynamic simulation: F_{aero} (blue), $F_{I\ vel}$ (red), F_g (green), $F_{I\ acc}$ (yellow). The force $F_{I\ acc}$ can be seen as the resultant force vector and F_{aero} is corrected by the initial force F_0 used to quarantee weight support for hovering flight. Beside forces there are also two acceleration vectors, a_{mov} (cyan) obtained from the Kalman filter and a_{sim} (purple) from the dynamic simulation. The right plot contains the following wingbeat averaged moment vectors: M_{aero} (blue), $M_{I\ vel}$ (red), $M_{I\ acc}$ (yellow). M_{aero} is corrected by the initial moment M_0 to cancel out the resultant pitch moment for hovering flight. There are two angular acceleration vectors: $\dot{\omega}_{mov}$ (cyan) and $\dot{\omega}_{sim}$ (purple).

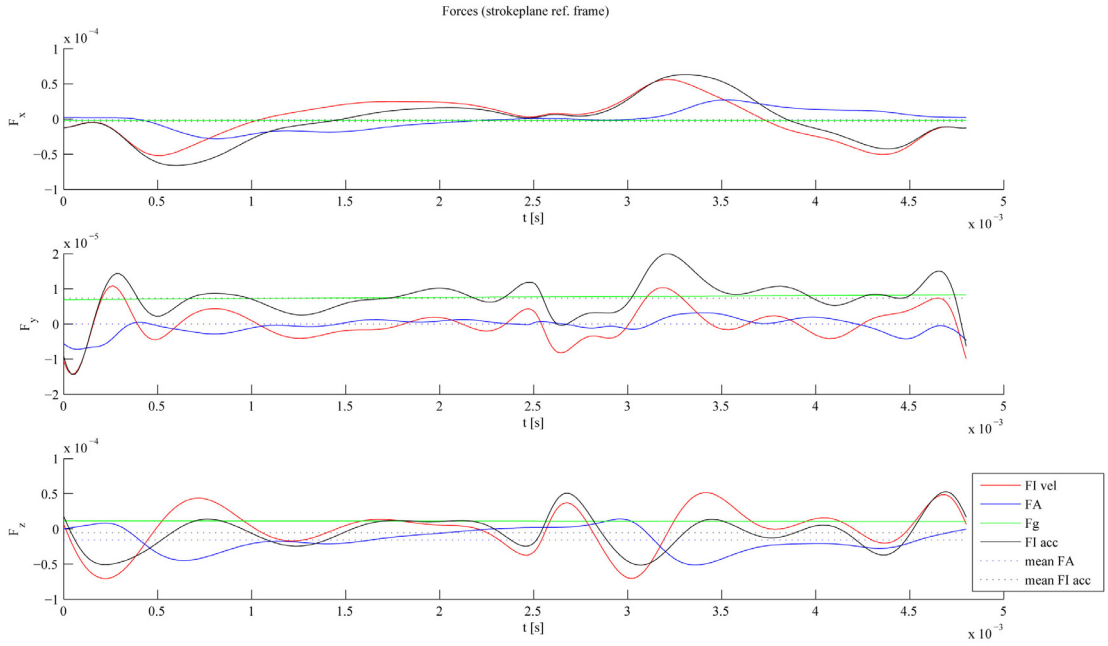

Figure 10.16: Forces of the dynamic simulation of the wingbeat presented in Fig. 10.15 in the strokeplane reference frame. The wingbeat averaged forces are: $F_{aero} = [-0.0240,\ -0.0048,\ -0.791]^T \cdot 10^{-4}$ $[N]$, $F_{I\ vel} = [-0.0206,\ 0.1748,\ -0.3169]^T \cdot 10^{-6}$ $[N]$, $F_g = [-0.0228, 0.0763, 0.1097]^T \cdot 10^{-4}$ $[N]$ and $F_{I\ acc} = [-0.3223, 0.7334, -0.5257]^T \cdot 10^{-5}$ $[N]$.

In the figures Fig. 10.15, Fig. 10.16 and Fig. 10.17 the results of the dynamic simulation are shown for a wingbeat in which the fly is accelerating and rotating. The definition of the dynamic simulation in Chapter 7 is used with one alteration, the rotational force model of the quasi-steady model is adjusted and uses $\dot{\eta}$ instead of $\dot{\alpha}$. The wing kinematics which are used for the dynamic simulation have a symmetry correction using the average polynomial fit and the deviation coefficients. The resulting polynomial coefficients are adjusted such that the wingbeat is periodic. This is necessary for the inertia model, the wingtip path needs to be a closed contour, otherwise the average inertial forces over a wingbeat are not close to zero anymore. This alteration in the wing kinematics can lead to some differences at the start of the downstroke and end of the upstroke, it would be better to simulate multiple subsequent wingbeats. The build-up in error is however too big to obtain a useful simulation of multiple wingbeats. The initial conditions are obtained from the Kalman filter results; the body position, body orientation, body velocity and body angular velocity at the start of the wingbeat will be used. The forces and moments, F_0 and M_0 are obtained by computing the wingbeat averaged resultant forces and moments from a dynamic simulation of the average wingbeat under hovering flight conditions. The average wingbeat is symmetric and corresponds to the flight sequence from which the maneuvering wingbeat is taken.

Fig. 10.15 consists of two plots, one plot containing the different force vectors used in the dynamic simulation, the other plot the moment vectors of the dynamic simulation. The fruit fly in Fig. 10.15 is accelerating backwards to the right in the perspective of the fly. This can be

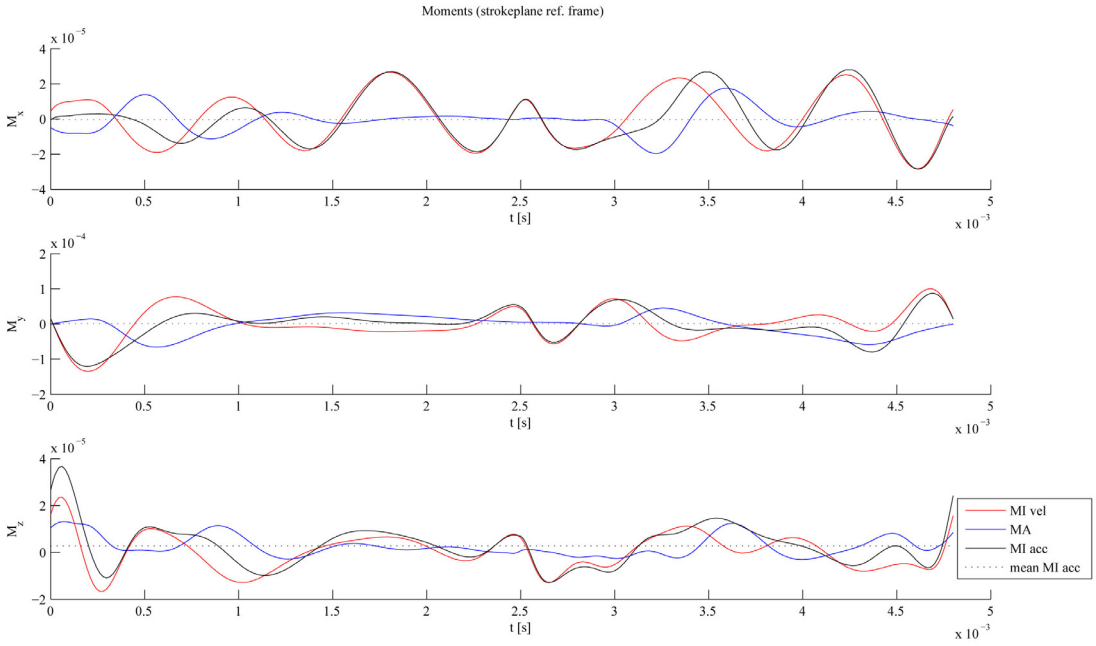

Figure 10.17: Moments of the dynamic simulation of the wingbeat presented in Fig. 10.15 in the strokeplane reference frame. The wingbeat averaged moments are: $M_{aero} = [-0.0389, -0.7400, 0.2627]^T \cdot 10^{-5}$ $[N \cdot mm]$, $M_{I\ vel} = [0.0306, -0.1311, 0.0837]^T \cdot 10^{-5}$ $[N \cdot mm]$ and $M_{I\ acc} = [-0.0358, -0.3101, 0.2711] \cdot 10^{-5}$ $[N \cdot mm]$.

seen by the direction of the acceleration vector a_{mov} in the figure. The simulated acceleration vector a_{sim} might be difficult to see because it is aligned with the resultant force vector, $F_{I\ acc}$. The two acceleration vectors are similar in magnitude and the angle between the two vectors is around the 15 °. The inertia force due to the effects of wing motion, $F_{I\ vel}$, is very small and not visible in the figure. This result corresponds to the fact that the inertia forces of the wing acting on the body are no external forces and should not generate a resultant force over longer timespans. This does not mean however that $F_{I\ vel}$ can be neglected, when looking at Fig. 10.16 it becomes clear that during the wingbeat the inertial forces of the wings have a significant influence on the body motion. A fact that has been established earlier in Fig. 7.7 where the wing motion in vacuum generates an oscillatory body motion. Altogether the prediction of the forces and the resulting acceleration of the wingbeat in Fig. 10.15 is predicted quite well by the dynamic simulation.

This situations alters for the prediction of the moments, presented in the right plot of Fig. 10.15. The wingbeat knows a moderate angular velocity mainly around the x and y axis, $\omega_{mov} = [34.8, 32.4, -5.2]^T$ $[rad/s]$ and the according angular acceleration vector is not large. The simulated angular velocity differs quite a bit, $\omega_{sim} = [22.2, 12.9, 19.9]^T$ $[rad/s]$, and the according angular acceleration vector has a magnitude which is much stronger. This can be seen clearly in Fig. 10.15 where the angular acceleration vector $\dot{\omega}_{mov}$ is small whilst the simulated angular velocity vector $\dot{\omega}_{sim}$ fills up the figure. The difference in magnitude is a factor 4 and the angle between the two vectors is about 40 °. The resultant moment $M_{I\ acc}$

and the angular velocity vector $\dot{\omega}_{sim}$ do not longer coincide as is the case for the simulated forces. This is because the angular velocity of the fly also plays a role in the equations of motion. A good example of this role can be given by looking at the Euler's equations of motion:

$$I\dot{\omega} + \omega \times [I \cdot \omega] = M,$$

where I is the inertia tensor of the body and M the moment vector. The product ω^2 can have a similar order of magnitude as $\dot{\omega}$. In the equations of motion of the dynamic simulation the angular acceleration of the body is also influenced by the body velocity, body acceleration and the wing inertia. The wingbeat averaged value of $M_{I\ vel}$ has the same order of magnitude as M_{aero}. During the wingbeat the effect of the wing inertia is even stronger, Fig. 10.17. Compared to the prediction of the acceleration vector of the dynamic simulation, the angular acceleration vector is predicted poorly. Besides the fact that the body and wing model of the fly and the dynamic simulation contain several simplifications and assumptions there are two main reasons why the angular acceleration is not predicted very well. The first reason is also observed in the RoboFly experiments, the quasi-steady aerodynamic model overestimates M_y. The difference between the results from the RoboFly experiments and the quasi-steady model is a factor 3. In the dynamic simulation this is also an issue, in almost every wingbeat there is a strong moment M_y. The relative importance of the moment becomes smaller when there is a strong moment around the x or z axis and for the steady wingbeats the moment M_0 cancels the dominating M_y partly. However for maneuvering wingbeats the wing kinematics change such that the moment M_0 is no longer accurate. Which is the second reason why the prediction of $\dot{\omega}$ is poor, the center of gravity is difficult to determine. A better algorithm to determine the center of gravity is needed, however without a better aerodynamic model for the pitching moment the dynamic simulation will not yield better results.

Besides the forces and moments, the dynamic simulation also computes body velocities, angular velocities, accelerations and angular accelerations. The Kalman filtering procedure also yields these body dynamics and the validity of the dynamic simulation can be tested by comparing the resulting body dynamics. Although the Kalman filtering procedure in combination with the tracking software have error terms, the results from the Kalman filter are deemed more reliable than the dynamic simulation. The filtering procedure also smoothens the body dynamics, which means a loss in temporal resolution. For a fair comparison the wingbeat averaged body dynamics are compared such that the difference in temporal resolution of the filtered results and the dynamic simulation makes no difference. In Fig. 10.18 - Fig. 10.21 the results of the comparison of 300 wingbeats is shown. The dynamic simulation of the body dynamics is performed under the same conditions as described in the previous paragraph.

Fig. 10.18 shows two different error parameters of the body velocity vector, in the strokeplane reference frame, of the dynamic simulation. The first parameter is the magnitude of the error, which is defined as the absolute difference between the velocity vector of the dynamic simulation and the velocity vector of the Kalman filter. The error magnitude is plotted against the value of the velocity of the Kalman filter. The second parameter is the so-called error angle, the error angle is the angle between the two velocity vectors computed by the dot product. The error angle is also plotted versus the velocity vector of the Kalman filter. The 300 simulated wingbeats are divided into 50 steady wingbeats and 250 maneuvering wingbeats both picked randomly from the wingbeat dataset. This means that all maneuver

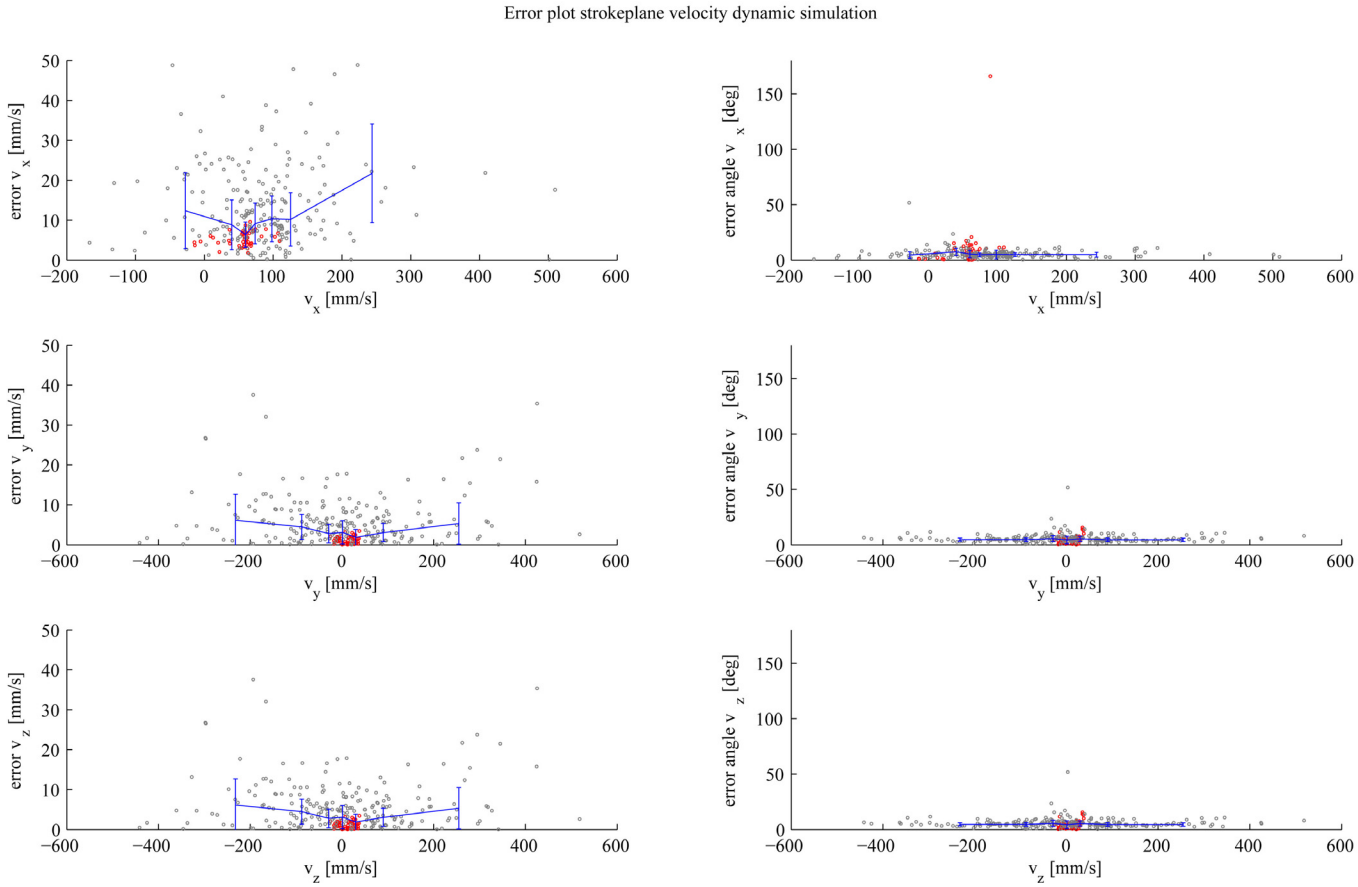

Figure 10.18: Plot of the error norm and error angle of the dynamic simulation of the body velocity for the three orthogonal axes of the strokeplane reference frame. The error norm of the dynamic simulation is defined as the absolute difference between the wingbeat averaged body velocity and the wingbeat averaged body velocity obtained from the video sequences. The error angle is the angle between the wingbeat averaged body velocity of the dynamic simulation and the wingbeat averaged velocity of the video sequence. The error norm and error angle are plotted versus the associated wingbeat averaged velocity of the video sequence. The red data points are the dynamics simulation results for steady wingbeats and the grey dots for maneuvering wingbeats, 50 steady wingbeats and 250 maneuvering wingbeats are simulated. The blue line is the weighted mean and the error bars show the variance of the weighted mean.

types are present, some categories like a_z and ω_z contain more wingbeats than others. The number of simulated wingbeats is however large enough to make sure that all maneuver types are statistically present in the validation. The steady wingbeats have a lower error magnitude than maneuvering wingbeats. This indicates that the dynamic simulation is more accurate for hovering flight conditions, which is an expected result as the quasi-steady model is designed for hovering flight. For the velocities v_y and v_z the mean velocity of the steady wingbeats is approximately zero, for v_x this mean velocity is around the 50 $[mm/s]$. The error angle of the steady wingbeats is generally higher than the maneuvering wingbeats, which is also an expected result. If the velocity vector is rather low the mean is also lower such that the variance becomes relatively stronger, meaning the signal-to-noise ratio decreases. As

the velocity deviates more from the mean steady wingbeat value the mean error magnitude and variance becomes larger. The mean error angle and variance decreases with increasing velocity. All together the error magnitude and angle are rather low and the body velocity is predicted accurately by the dynamic simulation. The mean velocity error magnitude and the mean velocity error in the x direction are higher than in the y and z direction.

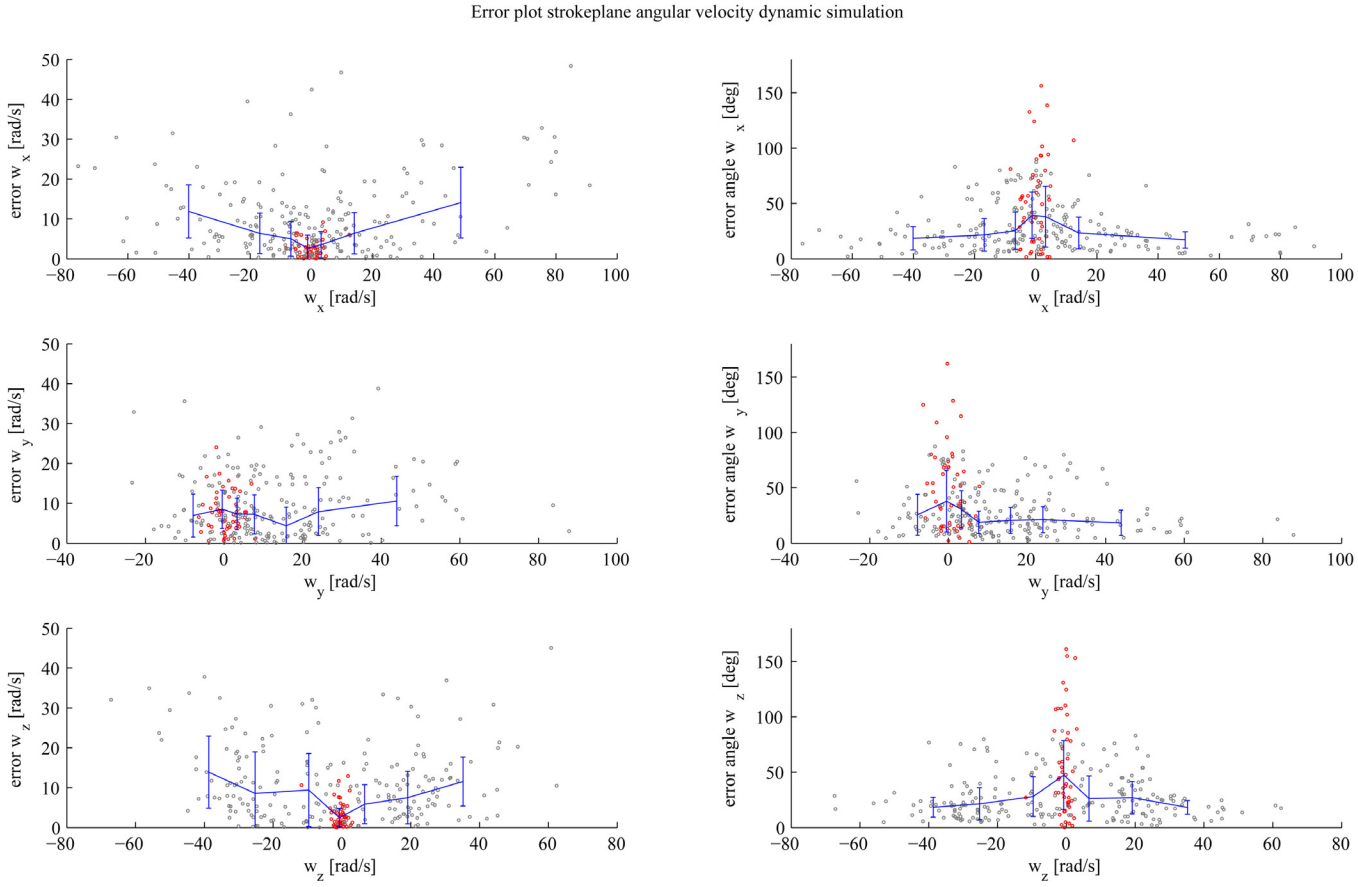

Figure 10.19: Plot of the error norm and error angle of the dynamic simulation of the body angular velocity for the three orthogonal axes of the strokeplane reference frame.

In Fig. 10.19 the error terms of the body angular velocity in the strokeplane reference frame are shown. Again the plots contain 300 simulated wingbeats which are the same wingbeats as in Fig. 10.18. Compared to the body velocity, there are more differences between the dynamic simulation and the filtered body dynamics. The error angle is almost arbitrary for steady wingbeats but the angle rapidly decreases as the magnitude of ω increases. At $\omega = 40$ $[rad/s]$ the mean error angle is for the angular velocity along all three axes lower than $20\,^{\circ}$. For negative ω_y there is not much data, which means that there are few fast pitch down maneuvers. The error magnitude of ω_y has a constant mean error magnitude around 8 $[rad/s]$. For ω_x and ω_z the mean error magnitude is increasing with ω, but the error magnitude as a percentage of ω stays generally constant. It is important to note that the Kalman filtering procedure of the body orientation gives angular velocities which have an

oscillation with the wingbeat length as period. The amplitude of this oscillation is around 5 $[rad/s]$, it is caused by the roll angle determination algorithm of the tracking software (see Fig. 3.4) and the oscillation cannot be filtered out whilst maintaining sufficient temporal resolution. The model of the angular velocity is less accurate than the velocity, with ω_z being somewhat less accurate than ω_x and ω_y. Although the errors are higher, the simulated angular velocities are still useful especially for higher angular velocities.

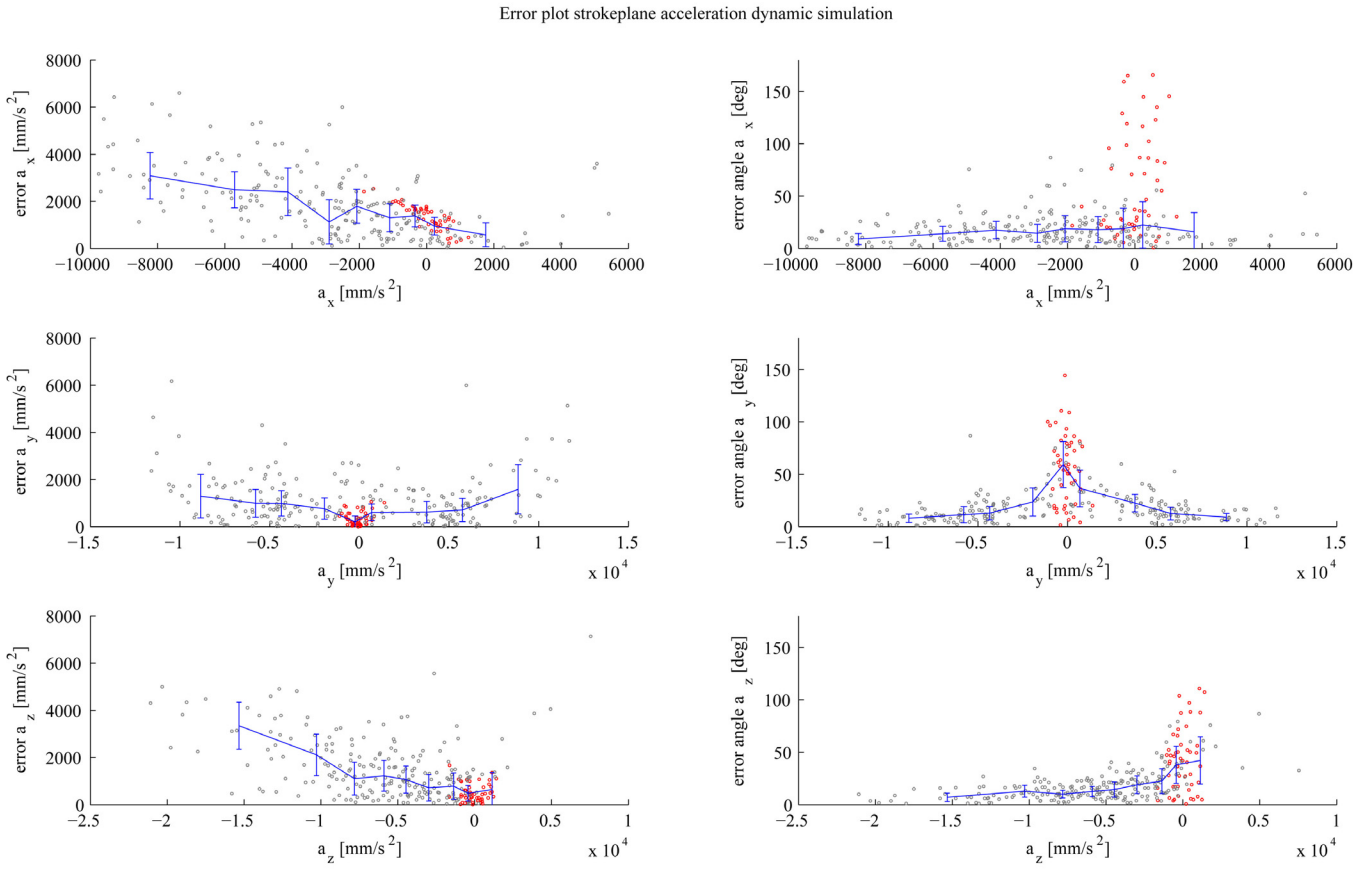

Figure 10.20: Plot of the error norm and error angle of the dynamic simulation of the body acceleration for the three orthogonal axes of the strokeplane reference frame.

Fig. 10.20 shows two different error parameters of the body velocity vector, in the strokeplane reference frame, of the dynamic simulation. The distribution of the 300 wingbeats shows that there are more wingbeats in the $a_x(-)$ direction (backward acceleration) and the $a_z(-)$ direction (upward acceleration). The distribution of wingbeats in the y direction is symmetric. The error magnitude of the steady wingbeats of a_x is rather high, the accuracy of a_x therefore increases with increasing backwards acceleration. Accelerations a_y and a_z are more accurate than a_x in error magnitude, the error angle of a_x is more accurate over the whole range of accelerations. The error angle of a_y and a_z decreases rapidly with increasing acceleration and for strong accelerations the mean error angle becomes less than $10\,^\circ$. For a_x this decrease is not so strong, and the mean error angle a_x can be seen as constantly lower than $20\,^\circ$. The

acceleration vector is prediction is accurate for strong accelerations especially considering the error angle, the relative error magnitude is predicted less well in comparison to the prediction of the velocity and angular velocity.

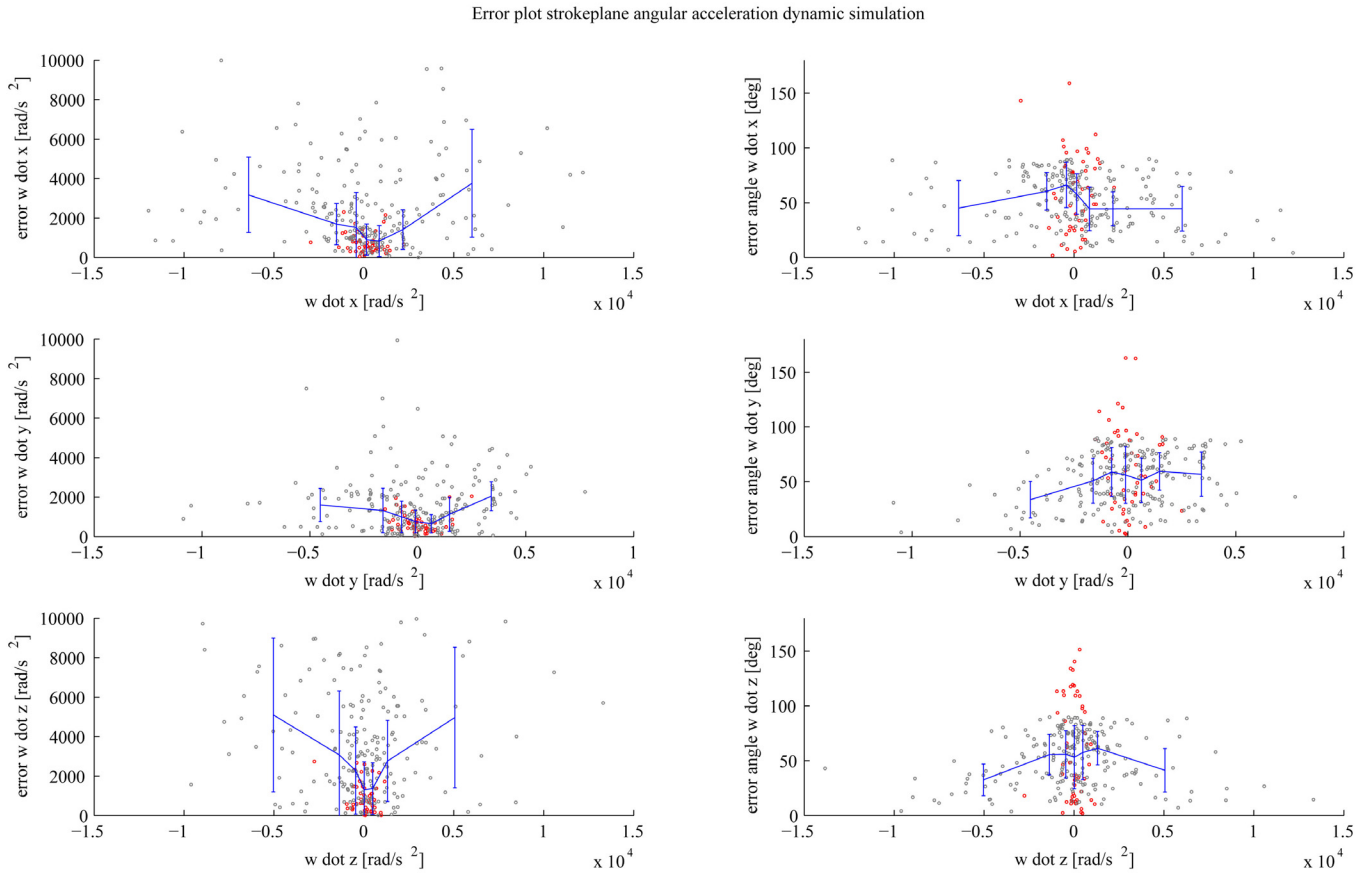

Figure 10.21: Plot of the error norm and error angle of the dynamic simulation of the body angular acceleration for the three orthogonal axes of the strokeplane reference frame.

In Fig. 10.21 the error terms of the body angular velocity in the strokeplane reference frame are shown. Looking at the error terms of $\dot{\omega}$ it becomes clear that the prediction of the angular acceleration by the dynamic simulation is the least accurate in the sequence v, ω, a and $\dot{\omega}$. The error magnitude is the worst for $\dot{\omega}_z$, followed by $\dot{\omega}_x$ and $\dot{\omega}_y$ yields the best results. This might be surprising as the quasi-steady aerodynamic model is over predicting M_y. When looking at Euler's equations of motion the source of this contradicting results can be found, the angular velocities affecting $\dot{\omega}_y$ are $\omega_x \cdot \omega_z$ whilst $\dot{\omega}_x$ is affected by $\omega_y \cdot \omega_z$ and $\dot{\omega}_z$ by $\omega_x \cdot \omega_y$. The over prediction of the pitch moment yields a stronger rotational velocity ω_y during the wingbeat which primarily affects $\dot{\omega}_x$ and $\dot{\omega}_z$. The error angle is decreasing slightly with $\dot{\omega}$ for $\dot{\omega}_x$ but the mean error angle never drops below 40 °. For $\dot{\omega}_y$ the error angle decreases with $\dot{\omega}_y(-)$ but stays constant for $\dot{\omega}_y(+)$. The error angle for $\dot{\omega}_z$ decreases the most with $\dot{\omega}$, still the mean error angle never drops below 30 °. The poor accuracy of the $\dot{\omega}$ prediction strengthens the earlier made observation that the M_y prediction of the dynamic simulation is

too strong and severely affects the magnitude and orientation of the $\dot{\omega}$ vector. One must also note that the Kalman filtering of the body orientation yields less accurate results for angular velocity than the Kalman filtering of wing orientation. The oscillations in ω will generate even stronger errors for $\dot{\omega}$, making the benchmarks results of $\dot{\omega}$ less reliable.

10.4 Aerodynamic and Inertial Damping

With the limitations of the dynamic simulation known the focus can shift to the results of the dynamic simulation for the maneuvering flight model. The main difference between the RoboFly experiments and the dynamic simulation is the incorporation of body velocities and angular velocities. If the body is rotating at a certain angular velocity its motion will be aerodynamically damped. The wing inertia can also damp the rotation of the body, the flapping wings show some similarities with a gyroscope which also resists rotation. In this thesis: damping is defined as the moment generated by a rotation around a specified axis with a specified angular velocity. The damping is positive when the generated moment opposes the rotation, the damping is negative when the damping moment strengthens the rotation. The strength of the damping moments will be computed for the average wingbeat and the different maneuver types as the aerodynamic and inertial characteristics are dependent on the wing kinematics. The combined effect of inertial and aerodynamic damping is called total damping. By using the dynamic simulation model the effects of total damping can be computed. This is done by simulating a single average or maneuvering wingbeat with a certain angular body velocity around one of the axes of the strokeplane reference frame. Besides the angular velocity for which the damping is tested, the initial conditions are set to hovering flight conditions. The initial force and moment vectors (F_0 and M_0) are defined such that the resultant force and moment vector are zero for the symmetric average wingbeat with a horizontal strokeplane. The body velocity, v_b, and body angular velocity, ω_b, are set such that the linear and angular momentum at the start of the wingbeat are zero. Subsequently the angular velocity around the strokeplane axis for which the damping is simulated will replace the body angular velocity terms required for zero angular momentum. The simulation of only the aerodynamic damping can be performed using just the quasi-steady aerodynamic model and applying a constant angular velocity around one of the strokeplane axes. The simulation of the inertial damping is performed using the dynamic simulation without the aerodynamic and gravity model. The initial conditions are the same as for the total damping simulation.

Total damping rates for ω_x			
$M_x^* \cdot 10^{-5}$	$\frac{dM_x}{d\omega_x} \cdot 10^{-8}$	$\frac{dM_y}{d\omega_x} \cdot 10^{-9}$	$\frac{dM_z}{d\omega_x} \cdot 10^{-8}$
0	-2.23	-2.78	3.50
0.715	-2.27	-4.27	3.33
1.430	-2.28	-6.07	3.17
2.145	-2.26	-7.94	2.92

Table 10.1: Total damping moment rate ($[N \cdot mm \cdot s/rad]$) for a roll rate, ω_x. The wing kinematics tested are the symmetric average wingbeat, a_{glob}, and three roll moment generating wingbeats ($M_x^* = 0.715 \cdot 10^{-5},\ 1.430 \cdot 10^{-5},\ 2.145 \cdot 10^{-5}$).

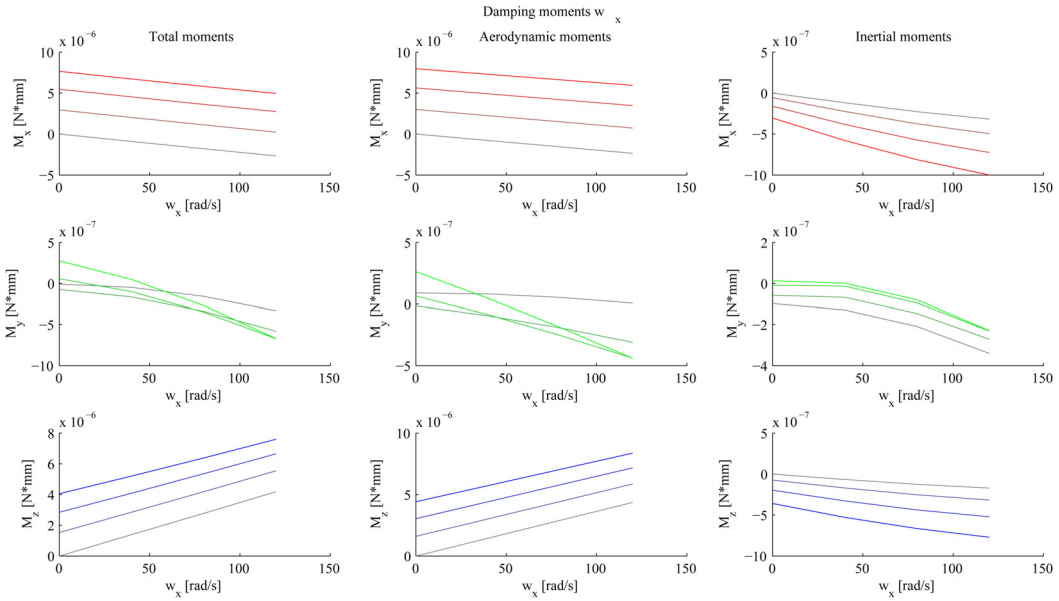

Figure 10.22: Aerodynamic and inertial damping of the average wingbeat and maneuvering wing kinematics for the roll moment (M_x) versus the angular velocity around the x-axis of the stroke-plane reference frame. In the plots a color code is used for the identification of the wing kinematics used. The grey line represents the average wingbeat and the maneuvering wing kinematics are plotted with increasing color intensity as the non-dimensional force associated to the wingbeat becomes stronger. In this plot the average wingbeat and three maneuvering wingbeats for M_x are plotted against the negative angular velocity ω_x, the non-dimensional moments associated to the maneuvering wing kinematics are: $M_x^* = 0.715 \cdot 10^{-5},\ 1.430 \cdot 10^{-5},\ 2.145 \cdot 10^{-5}$. The first column of plots show the effects of the roll rate, ω_x, on the *total or resultant moments* around the three principal axes of the strokeplane reference frame. The second column of plots show the effects of the roll rate, ω_x, on the *aerodynamic moments* around the three principal axes of the strokeplane reference frame. Finally the third column of plots shows the effects of the roll rate, ω_x, on the *inertial moments* around the three principal axes of the strokeplane reference frame.

In Fig. 10.22 the effects of aerodynamic damping and inertial damping for a roll rate, ω_x, are shown. For the simulation of the damping the average wingbeat kinematics are used in combination with the maneuvering wingbeat kinematics of M_x maneuvers. The analysis of Fig. 10.22 will start with considering the effects of damping on the moment M_x. The total damping of M_x does not vary much with different wing kinematics and the slope of the total moment curves for M_x are shown in Table 10.1. The aerodynamic damping is the strongest contributor to the total damping, although the inertial damping is not negligible. Especially for higher angular velocities the contribution of inertial damping to total damping can go up to 20%, Fig. 10.22. The total pitch moment M_y shows large variations in the M_y curves for different wing kinematics, but the main trend for M_y is the generation of a pitch down moment with increasing angular velocity. The contributions of the aerodynamic moment and inertial moment are comparable in strength. The inertial moment has more uniform curves w.r.t. ω_x than the aerodynamic moment. This might be an artifact of the poor computation of M_y by the quasi-steady aerodynamic model. The fact that a moment M_y is generated for the maneuvering wing kinematics of M_x is not surprising. The maneuvering wing kinematics M_x generate the strongest moment around the x axis but not solely, generation of forces and

Total damping rates for ω_y			
$M_y^* \cdot 10^{-5}$	$\frac{dM_x}{d\omega_y} \cdot 10^{-8}$	$\frac{dM_y}{d\omega_y} \cdot 10^{-8}$	$\frac{dM_z}{d\omega_y} \cdot 10^{-8}$
0	0	-1.11	0
0.658	0	-1.11	0
1.332	0	-1.11	0
1.997	0	-1.11	0

Table 10.2: Total damping moment rate ($[N \cdot mm \cdot s/rad]$) for a pitch rate, ω_y. The wing kinematics tested are the symmetric average wingbeat, a_{glob}, and three pitch moment generating wingbeats ($M_y^* = 0.658 \cdot 10^{-5},\ 1.332 \cdot 10^{-5},\ 1.997 \cdot 10^{-5}$).

moments around other axes is not impossible but standard. In the actual maneuvers the fruit fly never performs a roll maneuver which is solely around the x axis of the strokeplane, there will be always yaw and pitch motion as well. For the inertial moment this is also the case as the inertial moment is strongly coupled to the angular velocity. Besides a moment M_x, a strong yaw moment M_y is generated by the maneuvering wing kinematics. When the angular velocity is low, the moment M_x is stronger than M_z. However for high ω_x, M_z becomes stronger than M_x. This is mainly due to aerodynamic moments, the inertial moment produces a small yaw moment opposing the aerodynamic yaw moment.

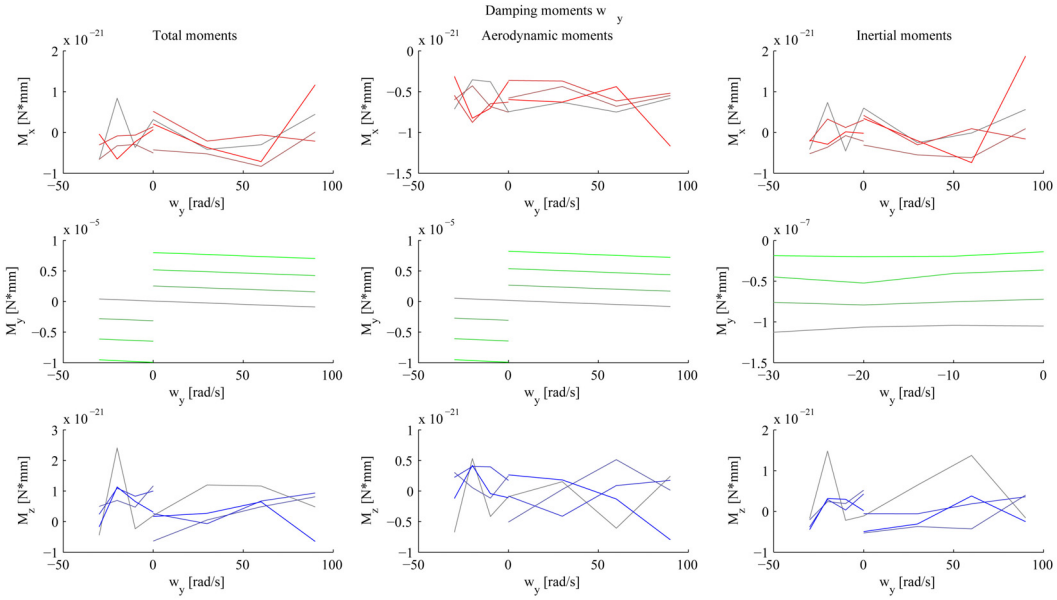

Figure 10.23: Aerodynamic and inertial damping of the average wingbeat and maneuvering wing kinematics for M_y *down* and M_y *up* versus the angular velocity along the y axis of the strokeplane reference frame. The maneuvering wingbeats for M_y *down* are plotted against the negative angular velocity ω_y and the maneuvering wingbeats for M_y *up* are plotted against the positive angular velocity ω_y, the associated maximum non-dimensional forces are increasing $M_y^* = -2.615 \cdot 10^{-5}$ and $M_y^* = 1.997 \cdot 10^{-5}$ respectively.

Fig. 10.23 shows the effects of damping for the pitch rate, ω_y, on the average wingbeat and the maneuvering wingbeats of M_y *down* and M_y *up*. As M_y *down* and M_y *up* have symmetric

Total damping rates for ω_z			
$M_z^* \cdot 10^{-5}$	$\frac{dM_x}{d\omega_z} \cdot 10^{-8}$	$\frac{dM_y}{d\omega_z} \cdot 10^{-8}$	$\frac{dM_z}{d\omega_z} \cdot 10^{-8}$
0	-2.27	0.57	-2.51
1.370	-2.43	-1.43	-2.80
2.739	-2.80	-3.71	-3.10
4.109	-3.49	-6.43	-3.50

Table 10.3: Total damping moment rate ($[N \cdot mm \cdot s/rad]$) for a yaw rate, ω_z. The wing kinematics tested are the symmetric average wingbeat, a_{glob}, and three yaw moment generating wingbeats ($M_z^* = 1.370 \cdot 10^{-5},\ 2.739 \cdot 10^{-5},\ 4.109 \cdot 10^{-5}$).

wing kinematics, there is no resultant moment around the x and z axes of the strokeplane reference frame. Compared to the damping for ω_x, the damping around the y axis is much weaker. The maneuvering wing kinematics of M_y *down* and M_y *up* do not deviate much in damping compared to the average wingbeat, the slope of the total moment curve is shown for the pitch-up angular velocities in Table 10.2. For the pitch-down angular velocites the damping rate is the same. The damping is generated by aerodynamic damping, inertial damping has hardly any influence.

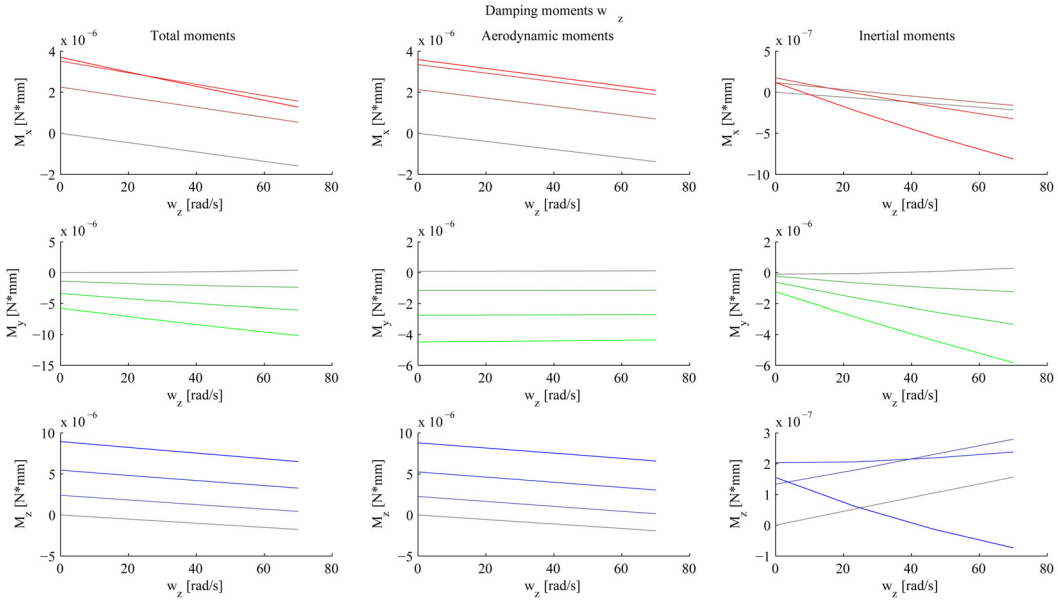

Figure 10.24: Aerodynamic and inertial damping of the average wingbeat and maneuvering wing kinematics for M_z versus the angular velocity along the z axis of the strokeplane reference frame. The maneuvering wingbeats for M_z are plotted against the positive angular velocity ω_z and the associated non-dimensional forces are increasing with a uniform step size upon a maximum of $M_z^* = 4.1088 \cdot 10^{-5}$.

In Fig. 10.24 the effects of aerodynamic damping and inertial damping for a yaw rate, ω_z, are shown. The total damping rates for the yaw motion are shown in Table 10.3. The yaw motion experiences the strongest total damping. The damping is caused by aerodynamic damping, the inertial yaw damping is negligible. Besides a moment around the z axis, also

a roll and pitch moment are created. The roll moment is about the half the strength of the yaw moment and is also mainly generated by aerodynamic moments, although inertial damping has a stronger effect here. The pitch moment is comparable in strength to the yaw moment and is generated by the combination of a strong aerodynamic pitch down moment and a strong inertial pitch down moment.

Fig. 10.22, Fig. 10.23 and Fig. 10.24, show the relations between aerodynamic and inertial effects on the maneuvering wingbeats. The dynamic simulation might be inaccurate for some results, especially when considering pitching moments. However the set-up of the simulations for aerodynamic and inertial damping is rather simple such that the amount of complicated interactions between forces, moments and body dynamics is reduced. The main goal of the dynamic simulation of damping is to show the importance of the wing inertia. The centripetal and Coriolis forces, generated by the rapidly rotating, accelerating and decellerating wings, increase with an increasing angular velocity of the fly. The rigid body of the fly itself does not experience inertial forces due to angular velocity. The inertial damping of the fly is due to the motion of the wings, which is remarkable as the virtual wing weight of both wings combined is less than 1% of the weight of the fly. In order to validate whether the results for damping in Fig. 10.22, Fig. 10.23 and Fig. 10.24 are close to nature, a more accurate dynamic simulation or force/moment measurements on actual rotating fruit flies will be necessary.

10.5 Flow Visualization

Besides the force and moment measurements of the maneuvering flight model on the RoboFly, a small number of flow visualizations experiments have been performed on the RoboFly. For these experiments a rather simple set-up for flow visualization has been built. From the analysis of the maneuvering flight model it has become clear that the downward plunge plays an important role in generating control forces and moments. The downward plunge in the maneuvering flight model is the strongest for the roll maneuver. A brief study of the downward plunge might yield some interesting results.

The flow visualization set-up uses air bubbles in the flow as flow visualization particles. The air bubbles are around the 1 mm in diameter and the ascending speed of the bubbles in the oil is less than 1 $[mm/s]$. The bubbles are illuminated by a stage light which projects a sheet of light with a thickness of 2 cm in the area of interest. The set-up is definitely not comparable with a PIV set-up, however it suffices for a qualitative analysis of the flow. The sequence of wingbeats studied consists of 13 subsequent wingbeats, the first 6 wingbeats are average wingbeats followed by one transition wingbeat and then there are 6 maneuvering wingbeats. The maneuvering wingbeats are the same and are obtained from the M_x maneuvering wing kinematics. The right wing of the RoboFly is the wing which is illuminated and a negative roll moment is taken such that the strong downward plunge is present in the right wingbeat kinematics. In this section the downward plunge during an average wingbeat and the downward plunge during a maneuvering wingbeat will be studied.

In Fig. 10.25 the downward plunge of an average wingbeat is shown. In all the figures the

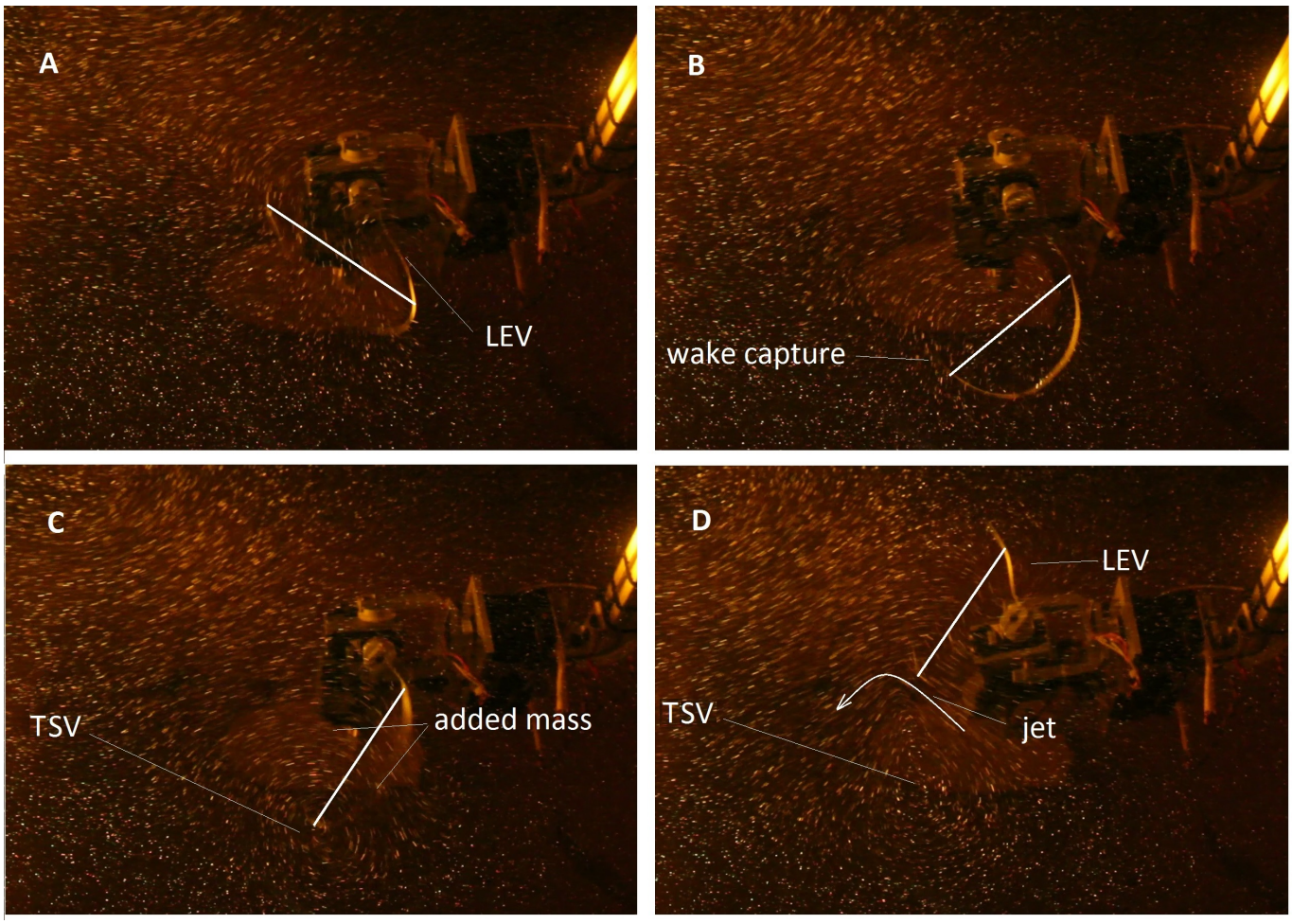

Figure 10.25: Snapshots of flow visualization average wingbeat. **A**: wing at end of the downstroke. **B**: wing at the start of the downward plunge, the wake of the downstroke in combination with the LEV of the downstroke hit the lower wing and flow around the LE and TE. **C**: wing in the middle of the downward plunge, air on the lower and upper side of the wing is transported with the wing downwards (added mass). A strong translational starting vortex (TSV) is formed at the TE. **D**: TSV is shed from the wing and the TSV in combination with the LEV on the wing create a strong jet downwards. The jet contains a considerable amount of the added mass of **C**.

cross-section of the wing which is illuminated is marked by a white line, other features as vortices and other flow effects are tagged. The illumination plane does not track a certain span wise section of the wing, however during the downward plunge the illuminated section is between the 50% and 80% of the span. One must keep in mind that the flow visualization does not correspond to a single blade element on the wing, however the span wise areas which contain strong $3D$ flow effects, as a tip vortex for example, are kept out of the image. Subfigure **A** shows the wing at the end of the downstroke, the LEV is visible on the LE of the wing and behind the wing a strong wake is visible. In **B** the wing is at the end of the rotation phase and the translational velocity of the wing is almost zero. As a consequence the wake of the wing is decelerating against the lower side of the wing, at the LE and TE

the decelerated flow is moving towards the upper side. The effect of the wake decelerating against the almost stationary wing and thereby generating an aerodynamic force is called wake capture. Subfigure **C** shows the wing during the middle of the downward plunge which started at **B**. A volume of air on the lower and upper side is moving downwards with the wing, the volume of air can be called added mass or virtual mass. At the TE of the wing a strong Translational Starting Vortex (TSV) is present, the TSV is actually a combination of a starting vortex due to the downward acceleration of the wing and the rotation of the wing during the downward plunge. The TSV is moving downwards with the wing during the plunge. In **D** the wing has ended its downward plunge and is moving roughly parallel to the strokeplane. A LEV is clearly visible on the LE and the TSV has been shed from the TE. Between the TSV and the LE a strong downward flow or jet is induced. This downward jet contains a significant part of the added mass of the downward plunge, which is now no longer attached to the wing. The virtual mass of the wing is now mainly the attached LEV, the TSV and the volume of air on the upper and lower wing of the downward plunge are no longer moving along with the wing.

The generation of a strong upward aerodynamic force during the downward plunge can be explained by the acceleration of the added mass on the wing in combination with the high drag forces on the wing due to the high angle-of-attack. If the wing would stop at the end of the downward plunge the added mass would be decelerated again and the net force due to added mass would be close to zero. At the end of the downward plunge the wing transfers its motion to a motion parallel to the strokeplane however. This results in the shedding of the TSV and a strong downward jet at the TE. The downward jet contains a significant amount of the added mass of the downward plunge which is now no longer attached to the wing. As a result the vertical force at the end of the downward plunge shows only a small dip instead of a strong downward force. The removal of added mass of the wing also helps to establish a LEV and to help the wing accelerate in horizontal direction. Less virtual mass helps means less mass which has to be accelerated with the wing which reduces the drag force in the x, y plane of the strokeplane.

The downward plunge during the M_x maneuver, Fig. 10.26, is a stronger variant of the downward plunge of the average wingbeat in Fig. 10.25. The duration of the downward plunge is longer, the wing velocity during the downward plunge is higher, the TSV has more strength and the size and velocity of the downward jet are larger. Interesting to note however is that the effect of wake capture in **A** seems to be weaker than during an average wingbeat. Subfigure **C** gives a good image of the influence of the downward jet on the wing. In **D** the wing is at the start of the next downstroke, during the upstroke the velocity of the jet has moved the TSV downward far away from the point of pronation. Therefore the induced velocity in the area of the future end of the downstroke and the future start of the upstroke is practically zero. In this way the strong wake effects of the downward plunge do not influence the next stroke.

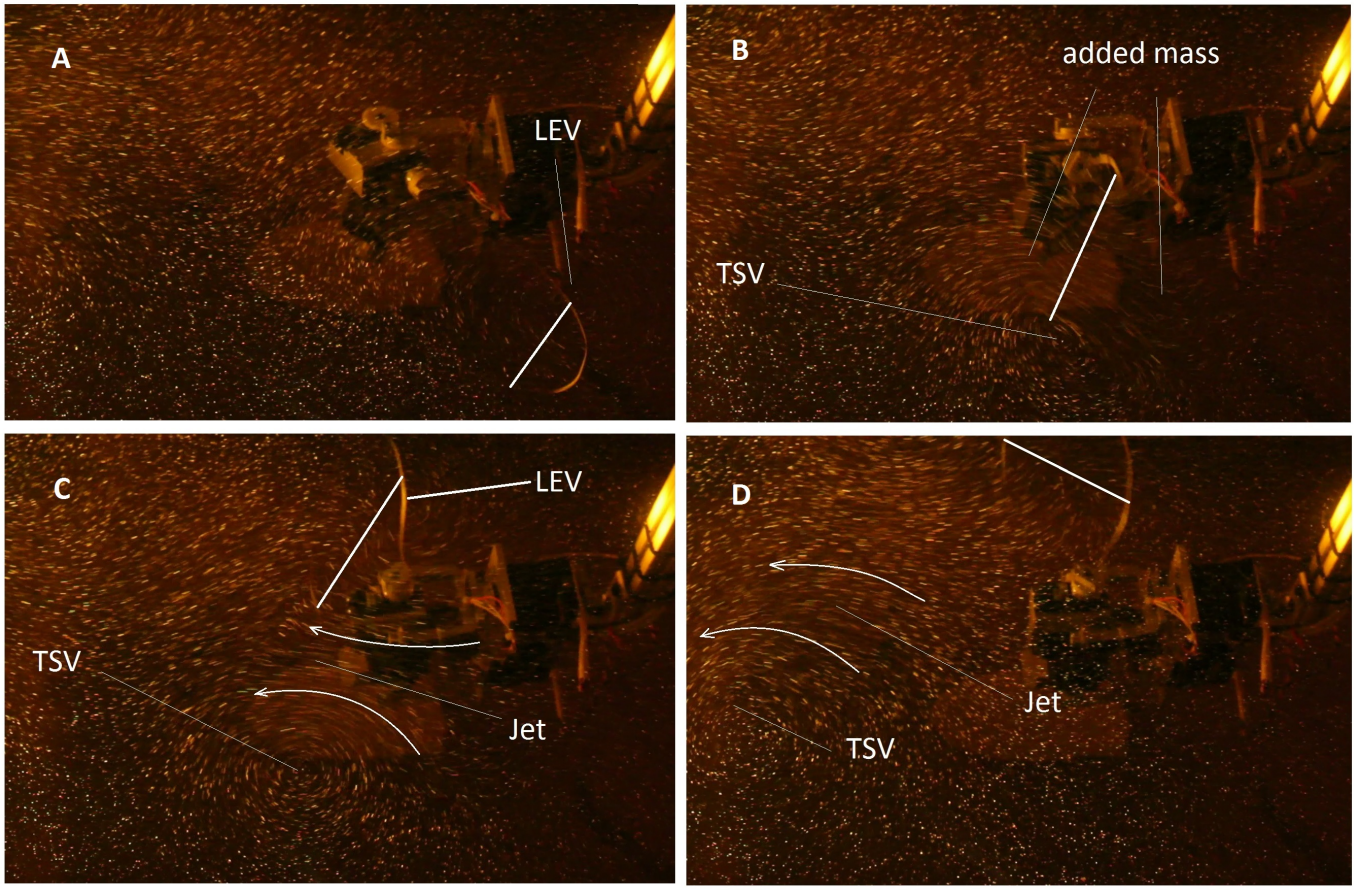

Figure 10.26: Snapshots of flow visualization M_x generating wingbeat. $\mathbf{A}$: wing at the start of the downward plunge, LEV of the downstroke is still present at the LE. $\mathbf{B}$: wing in the middle of the downward plunge, a TSV is generated at the TE and a large volume of added mass is present on the lower and upper side of the wing. $\mathbf{C}$: the end of the downward plunge, a strong TSV is shed and a LEV is attached to the wing. Between the TSV and the LEV a strong downward jet is present. $\mathbf{D}$: the TSV and the jet have moved far away from the strokeplane. The oil in the volume where the next downward plunge will take place is stationairy.

Part IV

Conclusions & Recommendations

Chapter 11

Conclusions

In the introduction of this report a main goal was formulated, which was establish and validate a model of maneuvering fruit fly flight, linking wing kinematics to body dynamics and independent of variations in body and wing shapes and dimensions between individual fruit flies.. In Chapter 8 the lay-out of two escape maneuvers were presented. Chapter 10 contains the results of the maneuvering flight model, the validation results of the maneuvering flight model and an analysis of the aerodynamic and inertial characteristics of the maneuvering flight model. The chapter will start with drawing conclusions about the escape maneuvers, the maneuvering flight model, the dynamic simulation and the aerodynamic and inertial influences on the maneuvering flight model. The conclusions of these four sections will be used to conclude whether and how well the main goal of the thesis is fulfilled.

Escape Maneuvers

Chapter 8 analyses how the fruit flies respond on the looming stimulus. In the movie sequences in which the flies perform an escape maneuver, two phases can be distinguished; steady flight and maneuvering flight. Steady flight corresponds on average to hovering flight conditions due to the low velocity of the fly, although spontaneous maneuvers in the steady flight sequence can occur. Maneuvering flight differs significantly from hovering flight marked by high accelerations and/or high angular velocities. Two stereotypical escape maneuvers have been analyzed, which are the roll maneuver and the pitch up maneuver. All the observed escape maneuvers are performed according to this procedure:

- When the looming stimulus is observed the fly rapidly rotates its strokeplane such that the aerodynamic force vector normal to the strokeplane points away from the direction of the stimulus.
- Simultaneously with the start of the maneuver to orient the strokeplane, the fly increases

its wingbeat frequency to increase the magnitude of the aerodynamic force production. It generally takes 5 wingbeats before the wingbeat frequency has reached its final value.

- Once the strokeplane is rotated away from the looming stimulus, the fly stays 1 or 2 wingbeats in this orientation accelerating away from the stimulus. In these orientations there is generally little weight support and after a few wingbeats the fly gradually changes the orientation of the strokeplane such that there is weight support and a (smaller) resultant force to accelerate away from the stimulus.

For the roll maneuver and the pitch-up maneuver it was possible to link the wing kinematics of the initiation of the maneuver, using the quasi-steady aerodynamic model, to the performed maneuver. This was possible due to the extremity of the maneuvers which made the wing kinematics deviate significantly from steady wingbeats. The variation in wing kinematics during steady and maneuvering flight prevents quantitative analysis of maneuvers using more subtle wing kinematics The deviation in wing kinematics from the steady wingbeat is not sufficient to distinguish maneuvering wing kinematics from steady wing kinematics.

Maneuvering Flight Model

The maneuvering flight model is obtained from a large scale analysis of the maneuvering wingbeat data set. The result is a polynomial description of the wingbeat deviation coefficients of 8 different maneuver types being; F_x *forward*, F_x *back*, F_y, F_z *up*, M_x, M_y *down*, M_y *up* and M_z. The maneuvers are named after the direction in which they generate a force or a moment. The average and maneuvering wingbeats are characterized by a polynomial fit. When the polynomial deviation coefficients of a certain maneuver are added to the polynomial coefficients of an average wingbeat, the maneuvering wing kinematics are formulated.

This maneuvering flight model has been validated by RoboFly experiments. The maneuvering flight model is dependent on the quasi-steady aerodynamic model, the RoboFly experiments of the average wingbeat showed that the rotational force model of the quasi-steady model was not implemented correctly. After the correction of the rotational force model, a new maneuvering flight model has been obtained. It was not possible to adjust the RoboFly experiments for the new maneuvering flight model, however this is not critical as the new maneuvering flight model does not drastically deviate in wing kinematics. The primary goal of the RoboFly experiments is to establish how well the quasi-steady aerodynamic model performs for maneuvering wing kinematics, this can be tested using both maneuvering flight models.

The performance of the quasi-steady model for the 8 different maneuver types can be summarized:

- F_x *forward*: good correspondence with RoboFly results.
- F_x *back*: good correspondence with RoboFly results.

- F_y: good correspondence with RoboFly results.
- F_z *up*: slight over prediction by quasi-steady model (up to 15%).
- M_x: good correspondence with RoboFly results.
- M_y *down*: severe over prediction of the quasi-steady model, RoboFly results are smaller by a factor 3.
- M_y *up*: severe over prediction of the quasi-steady model, RoboFly results are smaller by a factor 4.
- M_z: slight under prediction by quasi-steady model (up to 15%) for wing kinematics generating strong yaw moments.

Part of the RoboFly experiments was to determine the importance of the three different wing kinematic angles, θ, η and ϕ. A qualitative analysis of the maneuvering wing kinematics using the forces and moments of the RoboFly in combination with the RoboFly study on the importance of the wing kinematic angles gives a good overview of how the control forces are generated and which phases of the maneuvering wingbeat are used to generate these control forces. The results of this analysis correspond well to the results of Chapter 8.

The prediction of the maneuvering flight model of the generated force or moment by the maneuvering wingbeat by, means of a non-dimensional force or moment, is generally close to the force or moment computed by the quasi-steady model for the maneuvering wingbeat. When the non-dimensional force or moment is high, the prediction and actual results of the quasi-steady model diverge. This can be solved by using higher order fits on the deviation coefficients, however the current dataset of wing kinematics does not allow higher order fits. A bigger database of wingbeats in combination with a refined selection of maneuvering wingbeats could enable higher order fits.

The maneuvering flight model overestimates the pitch moment generated by M_y *down* and M_y *up*, resulting in maneuvering wing kinematics not powerful enough to generate the required pitching moment. This can be improved by improving the quasi-steady model w.r.t. the computation of the pitch moment.

Despite the just mentioned inaccuracies it can be concluded that the maneuvering flight model fullfills the requirements:

- The maneuvering flight model is independent of the variations in body and wing characteristics between the different flies in the database.
- The maneuvering flight model excludes the effects of aerodynamic and inertial damping from its analysis, which means that the maneuvering wing kinematics are based on wingbeats of all observed flight conditions.
- Finally the maneuvering flight model is very capable of extracting subtle wing motions, used for maneuvers, out of the database. Phases during the wingbeat where a good

temporal and spatial resolution of all the wing kinematic angles combined is required are captured very well by the maneuvering flight model. An example is the downward plunge for F_x *forward*, which requires an accurate description of θ, η and ϕ in time and compared to each other.

Dynamic Simulation

The RoboFly experiments can test the maneuvering wing kinematics under stationary conditions, body motion is however hard to implement in these experiments. The dynamic simulation has no limitations in simulating body motion, and therefore allows to test the performance of the aerodynamic and inertial model under all maneuvering flight conditions.

For the wingbeat averaged values of forces and moments of the dynamic simulation the gravitational force, aerodynamic force and aerodynamic moment have a dominant influence on the body motion. During the wingbeat however the forces and moments due to wing inertia determine the body motion. When the wingtip path of a simulated wingbeat forms a closed contour (periodic boundary condition), the wingbeat averaged force due to wing inertia is zero. When the body has rotational velocity there will be a wingbeat averaged resultant moment due to wing inertia, the so-called inertial damping.

The comparison of the simulated body dynamics and the body dynamics obtained from the filtered high-speed video data uses the polynomial fit of the wingbeat with a symmetry correction. The symmetry correction is necessary as the average wingbeat of many flies is not symmetric whilst the body and wing model used in the dynamic simulation is symmetric. The results for the wing kinematics with symmetry correction are satisfactory, symmetry corrected wing kinematics predict the body dynamics better than wing kinematics without symmetry correction.

The wingbeat averaged forces of the dynamic simulation yield a resultant force. This resultant force and the body acceleration vector are aligned, the simulated acceleration vector is close to the acceleration vector obtained by the filtered high-speed video data. The magnitudes of the two acceleration vectors are similar and the angle between the two vectors is generally small. The dynamic simulation predicts the body velocity and acceleration well.

This situation is different for the wingbeat averaged moments. The magnitude of the aerodynamic moment is large, generally there is a strong aerodynamic moment around the y axis. This corresponds to the overestimation of M_y by the quasi-steady model observed in the RoboFly. The angular acceleration vector of the dynamic simulation is much stronger than the angular acceleration vector of the filtered high-speed video data. The angle between the two vectors is generally large, the large variation in direction of the angular acceleration is enforced by the complicated equations of motion. Another aspect which might introduce an erroneous moment vector is the determination of the center of gravity in the dynamics simulation. The position of the center of gravity is based on the body model and not the position which creates moment equilibrium for hovering flight, which might create an erroneous

moment-arm.

A comparison of the wingbeat averaged body dynamics of 300 simulated wingbeats and the body dynamics obtained from the filtered high-speed video data shows the accuracy of the dynamic simulation of the body dynamics:

- The body velocity v is well predicted by the simulation. The error magnitude is small compared to v and increases slightly with higher velocities. The mean error angle is small and does not vary significantly with increasing velocity.
- The body acceleration a is predicted well, the error magnitude increases with increasing a however the relative error magnitude decreases with increasing a. The error angle for steady wingbeats is large, however the angle decreases rapidly with increasing a.
- The body angular velocity ω is predicted poorly for wingbeats with small ω. The error magnitude for these wingbeats is however small. The error magnitude increases rapidly with increasing ω, the relative error magnitude stays constant with increasing ω. The mean error angle is large for steady wingbeats, it decreases rapidly for maneuvering wingbeats with increasing ω. One must keep in mind that the results of the filtered high-speed video data contain an oscillation in angular velocity of 5 $[rad/s]$. The conclusion is that the angular velocity is predicted poorly by the dynamic simulation for small ω, when the magnitude of ω increases the prediction becomes better.
- The body angular acceleration $\dot{\omega}$ is predicted poorly. The error magnitude of steady wingbeat is small, however for maneuvering wingbeats there is a large scatter. The mean error angle shows a decrease with increasing $\dot{\omega}$, it never reaches acceptable values for the error angle.

Aerodynamic and Inertial Influence

From the dynamic simulation results it has become clear that the effects of wing inertia are not negligible. For studying the effects of wing inertia and the aerodynamics on the maneuvering flight model the aerodynamic and inertial damping have been simulated by the dynamic simulation.

A damping moment occurs for steady and maneuvering wing kinematics around the x, y and z axis of the strokeplane reference frame. The damping is the strongest for a yaw rotation, followed by roll rotation, the pitch rotation has the smallest damping. The damping moment for maneuvering wing kinematics is not sufficient to cancel out the generation of a resultant moment for the range of body angular velocities present in the database, a substantial counter-torque is needed to stop the rotation of a fly. The maneuvering wing kinematics of the roll and yaw maneuver generate strong moments around other axes as well. This is primarily due to aerodynamic moments, however the generation of inertial moments can play a significant role as well.

Inertial damping is significant for a rotation around the x axis of the strokeplane reference frame (up to 20%). For the pitch and yaw maneuver inertial damping is not significant, the maneuvering wing kinematics can generate moments around the other axes of the strokeplane reference frame which are comparable in strength with the aerodynamic moments around these axes.

The dynamic simulation is not reliable enough, considering body angular velocities, to rely on these results without validation experiments. The equations of motion used for the dynamic simulation are proven however, therefore it can be concluded that the aerodynamic moments, inertial moments and the body angular velocity have a strong relation. An improved version of the dynamic simulation is a good way to study the effects of aerodynamic and inertial damping.

Flow visualization experiments have been performed to study how the aerodynamic force is generated during the downward plunge. Analysis of the experiments showed how the downward plunge can generate a strong control force primarily in the z direction of the strokeplane reference frame whilst the increase in drag forces in the $x-y$ plane of the strokeplane remains small. The bulk of the force generation during the downward plunge can be explained by the acceleration of a large volume of added mass followed by shedding this volume of added mass from the wing by a means of a downward jet. The direction of this force vector can be controlled by the wing tip path during the downward plunge. The magnitude of the force vector is determined by the duration of the downward plunge.

The flow visualization experiments show that the the distribution and volume of added mass changes significantly during the downward plunge. The model for added mass (the mass of a constant volume of air around the wing incorporated in the inertial model) used in the thesis is unlikely to be accurate for the downward plunge. An improved model of the added mass effects is necessary to model both the aerodynamic and inertial forces and moments correctly. A more accurate modeling of the added mass can also improve the accuracy of the dynamic simulation.

Synopsis

The main findings and conclusions of the four sections discussing the results are summarized in this list:

- A qualitative model of how escape maneuvers are performed is established. Strong maneuvering wingbeats and their wing kinematics are identified and related to the body motion. The qualitative model is not able to analyze more subtle maneuvering wing kinematics as they are overshadowed by the variation in wing kinematics between the wingbeats.
- A maneuvering flight model has been established in which the maneuvering wing kinematics describe all translational and rotational motions around the axes of the stroke-

plane reference frame with the exception of descending flight. The maneuvering wing kinematics are built upon the quasi-steady aerodynamic model and RoboFly results show that the quasi-steady model is valid for the obtained maneuvering wing kinematics. Exception is the pitch moment, in this case the quasi-steady model overestimates the moment generation up to a factor of 4.

- The dynamic simulation is used to test the performance of the quasi-steady aerodynamic model under maneuvering flight conditions. The dynamic simulation yields good predictions for the body velocity and body acceleration, the body angular velocity and body angular acceleration are predicted poorly. This is caused by the presence of a strong aerodynamic pitch moment.

- The study on aerodynamic and inertial damping showed that there is a strong effect of body angular velocity on the aerodynamic and inertial moments. The flow visualization experiments of the downward plunge show how the force peak of the downward plunge is generated. The maneuvering flight model shows that the downward plunge is an important mechanism heavily used by some maneuver types. The role of added mass during the downward plunge asks for a more accurate model of added mass effects.

Chapter 12

Recommendations

The experimental data which was used in this thesis proved to be a rich source of information. There are several aspects of the data which have not been investigated. For the aerodynamic analysis of maneuvering fruit fly flight in this thesis, several methods have been developed. The methods could be improved by the following recommendations.

The maneuvering wing kinematics can be improved by the following improvements of the maneuvering flight model:

- Extend the database of wingbeats with more (maneuvering) wingbeats.
- Enforce more strict selection criteria on the maneuvering wingbeats.
- Use higher order fits for the trend lines of the polynomial deviation coefficients versus the non-dimensional force or moment.

During the thesis a couple of short-comings of the aerodynamic and inertial model used in the thesis were found. The quasi-steady aerodynamic model and the inertial model can be improved by:

- Defining a more accurate description of the pitch moment in the quasi-steady aerodynamic model.
- Improve the added mass model and include it in the aerodynamic and/or inertial model.

The maneuvering wing kinematics obtained by the maneuvering flight model are defined on the principal axes on the strokeplane reference frame. In the actual flight sequences the resultant force and moment generated by maneuvering wing kinematics are seldom aligned with one of the principal axes. Using multiple linear regression it could be possible to define

maneuvering wing kinematics which are based on combinations of the maneuvering wing kinematics at the principal axes. In this way maneuvering wing kinematics can be created which can generate a resultant force or moment vector in an arbitrary direction with arbitrary magnitude.

The dynamic simulation can be improved by:

- Implementing an improved quasi-steady aerodynamic model.
- Implementing an improved inertial model w.r.t. added mass effects.
- Improve the determination of the center of gravity of the fly.

Bibliography

[1] Hikaru Aono, Fuyou Liang, and Hao Liu. Near-and far-field aerodynamics in insect hovering flight: an integrated computational study. *Journal of Experimental Biology*, 211(2):239–257, 2008.

[2] Attila J Bergou, Leif Ristroph, John Guckenheimer, Itai Cohen, and Z Jane Wang. Fruit flies modulate passive wing pitching to generate in-flight turns. *Physical review letters*, 104(14):148101, 2010.

[3] James M Birch and Michael H Dickinson. The influence of wing–wake interactions on the production of aerodynamic forces in flapping flight. *Journal of Experimental Biology*, 206(13):2257–2272, 2003.

[4] Gwyneth Card and Michael Dickinson. Performance trade-offs in the flight initiation of drosophila. *Journal of Experimental Biology*, 211(3):341–353, 2008.

[5] B Cheng, SN Fry, Q Huang, and X Deng. Aerodynamic damping during rapid flight maneuvers in the fruit fly drosophila. *The Journal of Experimental Biology*, 213(4): 602–612, 2010.

[6] Bo Cheng, Steven N Fry, Qingfeng Huang, William B Dickson, Michael H Dickinson, and Xinyan Deng. Turning dynamics and passive damping in flapping flight. In *Robotics and Automation, 2009. ICRA'09. IEEE International Conference on*, pages 1889–1896. IEEE, 2009.

[7] Michael Dickinson. Insect flight. *Current Biology*, 16(9):R309, 2006.

[8] Michael H Dickinson. The initiation and control of rapid flight maneuvers in fruit flies. *Integrative and comparative biology*, 45(2):274–281, 2005.

[9] Michael H Dickinson and KARL G Gotz. Unsteady aerodynamic performance of model wings at low reynolds numbers. *Journal of Experimental Biology*, 174(1):45–64, 1993.

[10] Michael H Dickinson, Fritz-Olaf Lehmann, and Sanjay P Sane. Wing rotation and the aerodynamic basis of insect flight. *Science*, 284(5422):1954–1960, 1999.

[11] William B Dickson, Andrew D Straw, Christian Poelma, and Michael H Dickinson. An integrative model of insect flight control. In *Proceedings of the 44th AIAA Aerospace Sciences Meeting and Exhibit*, 2006.

[12] James Diebel. Representing attitude: Euler angles, unit quaternions, and rotation vectors. *Matrix*, 2006.

[13] Charles P Ellington, Coen Van Den Berg, Alexander P Willmott, and Adrian LR Thomas. Leading-edge vortices in insect flight. 1996.

[14] CP Ellington. The aerodynamics of hovering insect flight. *Philosophical Transactions of the Royal Society of London. B, Biological Sciences*, 305(1122):1–15, 1984.

[15] Ebraheem I Fontaine, Francisco Zabala, Michael H Dickinson, and Joel W Burdick. Wing and body motion during flight initiation in drosophila revealed by automated visual tracking. *Journal of Experimental Biology*, 212(9):1307–1323, 2009.

[16] Steven N Fry, Rosalyn Sayaman, and Michael H Dickinson. The aerodynamics of free-flight maneuvers in drosophila. *Science*, 300(5618):495–498, 2003.

[17] Steven N Fry, Rosalyn Sayaman, and Michael H Dickinson. The aerodynamics of hovering flight in drosophila. *Journal of Experimental Biology*, 208(12):2303–2318, 2005.

[18] Mohinder S Grewal and Angus P Andrews. *Kalman filtering: theory and practice using MATLAB*. Wiley. com, 2011.

[19] H Hamdani and M Sun. Aerodynamic forces and flow structures of an airfoil in some unsteady motions at small reynolds number. *Acta mechanica*, 145(1-4):173–187, 2000.

[20] J.C. van der Vaart J.A. Mulder, W.H.J.J. van Staveren and E. de Weerdt. *Flight Dynamics (Lecture Notes)*. TU Delft, 2007.

[21] David Lentink and Michael H Dickinson. Rotational accelerations stabilize leading edge vortices on revolving fly wings. *Journal of Experimental Biology*, 212(16):2705–2719, 2009.

[22] Leonard Meirovitch. *Methods of analytical dynamics*. DoverPublications. com, 2010.

[23] Brian J Odelson, Murali R Rajamani, and James B Rawlings. A new autocovariance least-squares method for estimating noise covariances. *Automatica*, 42(2):303–308, 2006.

[24] M Richter and M Patil. Influence of wing flexibility on the stability of flapping flight. In *AIAA Atmospheric Flight Mechanics Conference*, pages 2–5, 2010.

[25] Sanjay P Sane. The aerodynamics of insect flight. *The journal of experimental biology*, 206(23):4191–4208, 2003.

[26] Sanjay P Sane and Michael H Dickinson. The aerodynamic effects of wing rotation and a revised quasi-steady model of flapping flight. *Journal of Experimental Biology*, 205(8): 1087–1096, 2002.

[27] Josef S Török. *Analytical mechanics: With an introduction to dynamical systems*. Wiley, 2000.

[28] Marcos Vanella, Timothy Fitzgerald, Sergio Preidikman, Elias Balaras, and Balakumar Balachandran. Influence of flexibility on the aerodynamic performance of a hovering wing. *Journal of Experimental Biology*, 212(1):95–105, 2009.

[29] Robert J Wood. Liftoff of a 60mg flapping-wing mav. In *Intelligent Robots and Systems, 2007. IROS 2007. IEEE/RSJ International Conference on*, pages 1889–1894. IEEE, 2007.

[30] Xiaoping Yun and Eric R Bachmann. Design, implementation, and experimental results of a quaternion-based kalman filter for human body motion tracking. *Robotics, IEEE Transactions on*, 22(6):1216–1227, 2006.

Part V

Appendices

Appendix A

Quaternions

Quaternions, though beautifully ingenious, have been an unmixed evil to those who have touched them in any way. Lord Kelvin, 1892.

Definition Quaternion

Quaternions define an orientation by defining an axis of rotation, the so-called Euler axis, by a unit vector **e** and performing a single rotation around this reference frame θ, Fig. A.1. The quaternion is derived from the Euler formula and consists of four identities:

$$\mathbf{q} = \begin{bmatrix} q_1 \\ q_2 \\ q_3 \\ q_4 \end{bmatrix} = \begin{bmatrix} sin\left(\frac{\theta}{2}\right) e_x \\ sin\left(\frac{\theta}{2}\right) e_y \\ sin\left(\frac{\theta}{2}\right) e_z \\ cos\left(\frac{\theta}{2}\right) \end{bmatrix}.$$

The first three identities are called the vector part of the quaternion, the fourth identity is the scalar part which is a result of the derivation of a quaternion from Euler's formula. Opposite to the Euler angles, the identities of a quaternion are not indepenent which results and can be real or imaginairy.

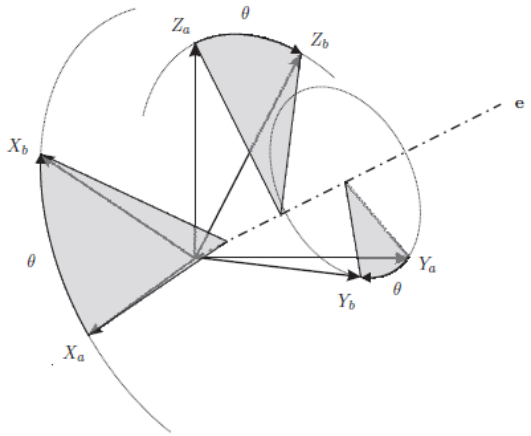

Figure A.1: Quaternion rotation of reference frame a to reference frame b, Ref. [20].

Unit Quaternion

In order to construct a rotation matrix from a quaternion, the quaternion must be a unit quaternion. Which means that the norm of the quaternion needs to be 1,

$$\|\mathbf{q}\| = \sqrt{q_1^2 + q_2^2 + q_3^2 + q_4^2} = 1,$$

In order to be sure the quaternion norm is 1 the quaternion can be normalized:

$$\mathbf{q} = \frac{\mathbf{q}}{\|\mathbf{q}\|}.$$

Quaternion Multiplication

Quaternion multiplication differs from the common vector multiplication. The multiplication is non-communicative which means that $\mathbf{q}_a \otimes \mathbf{q}_b \neq \mathbf{q}_b \otimes \mathbf{q}_a$. This is analogous to the product of two rotation matrices, as a quaternion indirectly represents a rotation matrix. The quaternion mulitplication operator is represented by the $\otimes$ symbol and can be expressed in matrix form:

$$\mathbf{q}_a \otimes \mathbf{q}_b = \begin{bmatrix} q_a(4) & q_a(3) & -q_a(2) & q_a(1) \\ -q_a(3) & q_a(4) & q_a(1) & q_a(2) \\ q_a(2) & -q_a(1) & q_a(4) & q_a(3) \\ -q_a(1) & -q_a(2) & -q_a(3) & q_a(4) \end{bmatrix} \begin{bmatrix} q_b(1) \\ q_b(2) \\ q_b(3) \\ q_b(4) \end{bmatrix}$$

Quaternion Adjoint and Inverse

The adjoint of a quaternion is defined as:

$$\bar{\mathbf{q}} = \begin{bmatrix} -q_1 \\ -q_2 \\ -q_3 \\ q_4 \end{bmatrix}.$$

The inverse is defined as:

$$\mathbf{q}^{-1} = \frac{\bar{\mathbf{q}}}{\|\mathbf{q}\|}.$$

Quaterion $\leftrightarrow$ Rotation Matrix

The relation between a quaternion and the according rotation matrix is given by:

$$R = \begin{bmatrix} q_4^2 + q_1^2 - q_2^2 - q_3^2 & 2q_1q_2 + 2q_3q_4 & 2q_1q_3 - 2q_2q_4 \\ 2q_1q_2 - 2q_3q_4 & q_4^2 - q_1^2 + q_2^2 - q_3^2 & 2q_2q_3 + 2q_1q_4 \\ 2q_1q_3 + 2q_2q_4 & 2q_2q_3 - 2q_1q_4 & q_4^2 - q_1^2 - q_2^2 + q_3^2 \end{bmatrix}.$$

It is necessary for the quaternion to have a norm of 1, otherwise the resulting matrix will not satisify all properties of a rotation matrix.

Quaterion $\leftrightarrow$ Angular Velocity

The quaternion and its derivative can be linked to the angular velocity vector. This is done by the following relation:

$$\dot{\mathbf{q}} = \frac{1}{2} \begin{bmatrix} \omega_x \\ \omega_y \\ \omega_z \\ 0 \end{bmatrix} \otimes \mathbf{q}.$$

The angular velocity vector can be obtained by:

$$\omega = 2 \begin{bmatrix} q_4 & q_3 & -q_2 & -q_1 \\ -q_3 & q_4 & q_1 & -q_2 \\ q_2 & -q_1 & q_4 & -q_3 \end{bmatrix} \dot{\mathbf{q}}.$$

In both expressions the angular velocity is defined in body-fixed coordinates.

Quaternion Update

The quaternion update from t_i to t_{i+1} is given by:

$$\mathbf{q}_{i+1} = \mathbf{q}_i \otimes \Delta\mathbf{q}.$$

The expression for $\Delta\mathbf{q}$ can be given by the following integral:

$$\Delta\mathbf{q} = \int_0^{\Delta t} \dot{\mathbf{q}} dt,$$

in which Δt is the difference between t_{i+1} and t_i. The expression can be written as a first order differential equation resulting in the following expression for the update:

$$\mathbf{q}_{i+1} = \mathbf{q}_i \otimes e^{\omega\Delta t + \frac{1}{2}\dot{\omega}\Delta t^2} = \mathbf{q}_i \otimes e^{\mathbf{v}} = \mathbf{q}_i \otimes \begin{bmatrix} sin\left(\frac{|\mathbf{v}|}{2}\right)\frac{\mathbf{v}}{|\mathbf{v}|} \\ cos\left(\frac{|\mathbf{v}|}{2}\right) \end{bmatrix},$$

the final expression of sines and cosines is obtained by applying Euler's formula. The value for $\dot{\omega}$ can be included in the vector $\mathbf{v}$ for additional accuracy, depending on how well $\dot{\omega}$ is known. Normalization of the obtained $\mathbf{q}_{i+1}$ is necessary after each update.

For the Extended Kalman Filter to work, the quaternion update needs to be linearized. The linearized quaternion update is based on Ref. [30], and is also based on the expression for the quaternion derivative. If the state vector $\mathbf{x}$ is defined as:

$$\mathbf{x} = \begin{bmatrix} \omega_x \\ \omega_y \\ \omega_z \\ q_1 \\ q_2 \\ q_3 \\ q_4 \end{bmatrix},$$

and the state vector update is given by:

$$\frac{d\mathbf{x}}{dt} = F(\mathbf{x}, t),$$

the linearization of the state vector update is given by:

$$\frac{d\mathbf{x}}{dt} = F(\mathbf{x}_0, t) + J_F(\mathbf{x}_0, t)(\mathbf{x} - \mathbf{x}_0).$$

The matrix $J_F(\mathbf{x}_0, t)$ is the Jacobian of $F(\mathbf{x}_0, t)$ and is given by:

$$J_F = \frac{1}{2}\begin{bmatrix} q_4 & -q_3 & q_2 & 0 & \omega_z & -\omega_y & \omega_x \\ q_3 & q_4 & -q_1 & -\omega_z & 0 & \omega_x & \omega_y \\ -q_2 & q_1 & q_4 & \omega_y & -\omega_x & 0 & \omega_z \\ -q_1 & -q_2 & -q_3 & -\omega_x & -\omega_y & -\omega_z & 0 \end{bmatrix}.$$

Integration of $\frac{d\mathbf{x}}{dt}$ from t_i to t_{i+1} yields to the state vector update:

$$\mathbf{x}_{i+1} = \Phi_i \mathbf{x}_i,$$

in which the state update matrix Φ_i is given by:

$$\Phi_i = \begin{bmatrix} 1 & 0 & 0 & 0 & 0 & 0 & 0 \\ 0 & 1 & 0 & 0 & 0 & 0 & 0 \\ 0 & 0 & 1 & 0 & 0 & 0 & 0 \\ q_4\frac{\Delta t}{2} & -q_3\frac{\Delta t}{2} & q_2\frac{\Delta t}{2} & 1 & \omega_z\frac{\Delta t}{2} & -\omega_y\frac{\Delta t}{2} & \omega_x\frac{\Delta t}{2} \\ q_3\frac{\Delta t}{2} & q_4\frac{\Delta t}{2} & -q_1\frac{\Delta t}{2} & -\omega_z\frac{\Delta t}{2} & 1 & \omega_x\frac{\Delta t}{2} & \omega_y\frac{\Delta t}{2} \\ -q_2\frac{\Delta t}{2} & q_1\frac{\Delta t}{2} & q_4\frac{\Delta t}{2} & \omega_y\frac{\Delta t}{2} & -\omega_x\frac{\Delta t}{2} & 1 & \omega_z\frac{\Delta t}{2} \\ -q_1\frac{\Delta t}{2} & -q_2\frac{\Delta t}{2} & -q_3\frac{\Delta t}{2} & -\omega_x\frac{\Delta t}{2} & -\omega_y\frac{\Delta t}{2} & -\omega_z\frac{\Delta t}{2} & 1 \end{bmatrix}.$$

After the state update it is necessary to normalize the updated quaternion.

Quaternion Average

It might be necessary to obtain an average orientation out of a sequence of quaternions. In this case the use of an algorithm is necessary to obtain the average quaternion. This is performed by obtaining the following matrix A:

```
for i = 1:M                                                    1
    A = q(:,i)'q(:,i) + A;
end
```

in which M is the number of quaternions to be averaged. The matrix A is scaled by the number of quaternions:

$$A = \left(\frac{1}{M}\right) A,$$

from the scaled matrix A the largest eigenvalue and corresponding eigenvector is obtained. The eigenvector is the average quaternion.

Appendix B

Wing Kinematics, Rotation Matrices, Angular Velocities and Accelerations

Wing Kinematic Angles and Derivatives

The wing kinematic angles can be obtained from the Legendre matrix X, which gives the Legendre polynomials for N points in the domain $-1 \geq x \geq 1$. Multiplication of the polynomial fit a with the matrix will generate a certain wing kinematic angle for the duration of a wingbeat. As the wingbeat is divided into two different Legendre domains for the downstroke and the upstroke, it is necessary to divide the number of points in the downstroke and in the usptroke according to the *down_up* ratio such that there is a uniform distribution of N points over the wingbeat. The start of the upstroke is the transition point between the two domains and is averaged as can be seen in Fig. 6.2. The derivatives of the wing kinematic angles can be obtained by a similar matrix as in Fig. 6.2. however now the Legendre polynomials are replaced by their derivatives. The derivatives are scaled with the *down_up* ratio in order to make sure that the different domain sizes in the wingbeats do not affect the resulting derivative of the wing kinematic angle. The scaling on the derivatives of the Legendre polynomials is:

$$P_n^k(x) = \left(\frac{t_{wb}}{t_{down}}\right)^k \cdot P_n^k(x)$$

and for the upstroke:

$$P_n^k(x) = \left(\frac{t_{wb}}{t_{up}}\right)^k \cdot P_n^k(x).$$

With the Legendre matrix defined the wing kinematic angles can be obtained:

$$\begin{aligned} \theta_L &= X_\theta \cdot a_{\theta_L}, \qquad \theta_R = -X_\theta \cdot a_{\theta_R} \\ \eta_L &= -X_\eta \cdot a_{\eta_L}, \qquad \eta_R = -X_\eta \cdot a_{\eta_R} \\ \phi_L &= -X_\phi \cdot a_{\phi_L}, \qquad \phi_R = X_\phi \cdot a_{\phi_R}. \end{aligned}$$

The negative signs are necessary to make sure that the wing kinematic angles are positively defined in the strokeplane reference frame. The first derivative of the wing kinematic angles is given by:

$$\begin{aligned}\dot{\theta}_L =& X_{\dot{\theta}} \cdot a_{\theta_L}, \qquad \dot{\theta}_R = -X_{\dot{\theta}} \cdot a_{\theta_R} \\ \dot{\eta}_L =& -X_{\dot{\eta}} \cdot a_{\eta_L}, \qquad \dot{\eta}_R = -X_{\dot{\eta}} \cdot a_{\eta_R} \\ \dot{\phi}_L =& -X_{\dot{\phi}} \cdot a_{\phi_L}, \qquad \dot{\phi}_R = X_{\dot{\phi}} \cdot a_{\phi_R}.\end{aligned}$$

The second derivative of the wing kinematic angles is given by:

$$\begin{aligned}\ddot{\theta}_L =& X_{\ddot{\theta}} \cdot a_{\theta_L}, \qquad \ddot{\theta}_R = -X_{\ddot{\theta}} \cdot a_{\theta_R} \\ \ddot{\eta}_L =& -X_{\ddot{\eta}} \cdot a_{\eta_L}, \qquad \ddot{\eta}_R = -X_{\ddot{\eta}} \cdot a_{\eta_R} \\ \ddot{\phi}_L =& -X_{\ddot{\phi}} \cdot a_{\phi_L}, \qquad \ddot{\phi}_R = X_{\ddot{\phi}} \cdot a_{\phi_R}.\end{aligned}$$

Rotation Matrix

The rotation matrices of the left and right wing reference frame are defined as:

$$\begin{aligned}R_L =& R_{180} \cdot R_{\eta_L} \cdot R_{\theta_L} \cdot R_{\phi_L} \cdot R_{strk} \\ R_R =& R_{180} \cdot R_{\eta_R} \cdot R_{\theta_R} \cdot R_{\phi_R} \cdot R_{strk},\end{aligned}$$

with the following rotation matrices:

$$R_{\theta_L} = \begin{bmatrix} 1 & 0 & 0 \\ 0 & cos(\theta_L) & sin(\theta_L) \\ 0 & -sin(\theta_L) & cos(\theta_L) \end{bmatrix}, \qquad R_{\theta_R} = \begin{bmatrix} 1 & 0 & 0 \\ 0 & cos(\theta_R) & sin(\theta_R) \\ 0 & -sin(\theta_R) & cos(\theta_R) \end{bmatrix},$$

$$R_{\eta_L} = \begin{bmatrix} cos(\eta_L) & 0 & -sin(\eta_L) \\ 0 & 1 & 0 \\ sin(\eta_L) & 0 & cos(\eta_L) \end{bmatrix}, \qquad R_{\eta_R} = \begin{bmatrix} cos(\eta_R) & 0 & -sin(\eta_R) \\ 0 & 1 & 0 \\ sin(\eta_R) & 0 & cos(\eta_R) \end{bmatrix},$$

$$R_{\phi_L} = \begin{bmatrix} cos(\phi_L) & sin(\phi_L) & 0 \\ -sin(\phi_L) & cos(\phi_L) & 0 \\ 0 & 0 & 1 \end{bmatrix}, \qquad R_{\phi_R} = \begin{bmatrix} cos(\phi_R) & sin(\phi_R) & 0 \\ -sin(\phi_R) & cos(\phi_R) & 0 \\ 0 & 0 & 1 \end{bmatrix},$$

$$R_{180} = \begin{bmatrix} 1 & 0 & 0 \\ 0 & -1 & 0 \\ 0 & 0 & 1 \end{bmatrix}, \qquad R_{strk} = \begin{bmatrix} cos(\beta_{strk}) & 0 & -sin(\beta_{strk}) \\ 0 & 1 & 0 \\ sin(\beta_{strk}) & 0 & cos(\beta_{strk}) \end{bmatrix}.$$

Angular Velocity

The angular velocity in the wing frame of reference can be obtained by transferring the Euler angle rates, or wing kinematic angle rates, to the wing reference frame. For the left wing this

is performed by the following operation:

$$\omega_L = R_{180} \cdot R_{\eta_L} \cdot R_{\theta_L} \cdot \begin{bmatrix} 0 \\ 0 \\ \dot{\phi}_L \end{bmatrix} + R_{180} \cdot R_{\eta_L} \cdot \begin{bmatrix} \dot{\theta}_L \\ 0 \\ 0 \end{bmatrix} + R_{180} \cdot \begin{bmatrix} 0 \\ \dot{\eta}_L \\ 0 \end{bmatrix}.$$

And for the angular velocity vector of the right wing:

$$\omega_R = R_{180} \cdot R_{\eta_R} \cdot R_{\theta_R} \cdot \begin{bmatrix} 0 \\ 0 \\ \dot{\phi}_R \end{bmatrix} + R_{180} \cdot R_{\eta_R} \cdot \begin{bmatrix} \dot{\theta}_R \\ 0 \\ 0 \end{bmatrix} + R_{180} \cdot \begin{bmatrix} 0 \\ \dot{\eta}_R \\ 0 \end{bmatrix}.$$

Angular Acceleration

The angular acceleration can be obtained by differentiating the expressions for ω_L and ω_R. The left wing angular acceleration is:

$$\begin{aligned} \dot{\omega}_L =& R_{180} \cdot R_{\dot{\eta}_L} \cdot R_{\theta_L} \cdot \begin{bmatrix} 0 \\ 0 \\ \dot{\phi}_L \end{bmatrix} + R_{180} \cdot R_{\eta_L} \cdot R_{\dot{\theta}_L} \cdot \begin{bmatrix} 0 \\ 0 \\ \dot{\phi}_L \end{bmatrix} + R_{180} \cdot R_{\eta_L} \cdot R_{\theta_L} \cdot \begin{bmatrix} 0 \\ 0 \\ \ddot{\phi}_L \end{bmatrix} \\ &+ R_{180} \cdot R_{\dot{\eta}_L} \cdot \begin{bmatrix} \dot{\theta}_L \\ 0 \\ 0 \end{bmatrix} + R_{180} \cdot R_{\eta_L} \cdot \begin{bmatrix} \ddot{\theta}_L \\ 0 \\ 0 \end{bmatrix} + R_{180} \cdot \begin{bmatrix} 0 \\ \ddot{\eta}_L \\ 0 \end{bmatrix}. \end{aligned}$$

The right wing angular acceleration is:

$$\begin{aligned} \dot{\omega}_R =& R_{180} \cdot R_{\dot{\eta}_R} \cdot R_{\theta_R} \cdot \begin{bmatrix} 0 \\ 0 \\ \dot{\phi}_R \end{bmatrix} + R_{180} \cdot R_{\eta_R} \cdot R_{\dot{\theta}_R} \cdot \begin{bmatrix} 0 \\ 0 \\ \dot{\phi}_R \end{bmatrix} + R_{180} \cdot R_{\eta_R} \cdot R_{\theta_R} \cdot \begin{bmatrix} 0 \\ 0 \\ \ddot{\phi}_R \end{bmatrix} \\ &+ R_{180} \cdot R_{\dot{\eta}_R} \cdot \begin{bmatrix} \dot{\theta}_R \\ 0 \\ 0 \end{bmatrix} + R_{180} \cdot R_{\eta_R} \cdot \begin{bmatrix} \ddot{\theta}_R \\ 0 \\ 0 \end{bmatrix} + R_{180} \cdot \begin{bmatrix} 0 \\ \ddot{\eta}_R \\ 0 \end{bmatrix}. \end{aligned}$$

The derivatives of the rotation matrices used to obtain the angular velocities are:

$$R_{\dot{\theta}_L} = \begin{bmatrix} 0 & 0 & 0 \\ 0 & -\dot{\theta}_L sin(\theta_L) & \dot{\theta}_L cos(\theta_L) \\ 0 & -\dot{\theta}_L cos(\theta_L) & -\dot{\theta}_L sin(\theta_L) \end{bmatrix}, \qquad R_{\dot{\theta}_R} = \begin{bmatrix} 0 & 0 & 0 \\ 0 & -\dot{\theta}_R sin(\theta_R) & \dot{\theta}_R cos(\theta_R) \\ 0 & -\dot{\theta}_R cos(\theta_R) & -\dot{\theta}_R sin(\theta_R) \end{bmatrix},$$

$$R_{\dot{\eta}_L} = \begin{bmatrix} -\dot{\eta}_L sin(\eta_L) & 0 & -\dot{\eta}_L cos(\eta_L) \\ 0 & 0 & 0 \\ \dot{\eta}_L cos(\eta_L) & 0 & -\dot{\eta}_L sin(\eta_L) \end{bmatrix}, \qquad R_{\dot{\eta}_R} = \begin{bmatrix} -\dot{\eta}_R sin(\eta_R) & 0 & -\dot{\eta}_R cos(\eta_R) \\ 0 & 0 & 0 \\ \dot{\eta}_R cos(\eta_R) & 0 & -\dot{\eta}_R sin(\eta_R) \end{bmatrix}.$$

Appendix C

Steady and Maneuvering Wingbeats

Steady Wingbeats

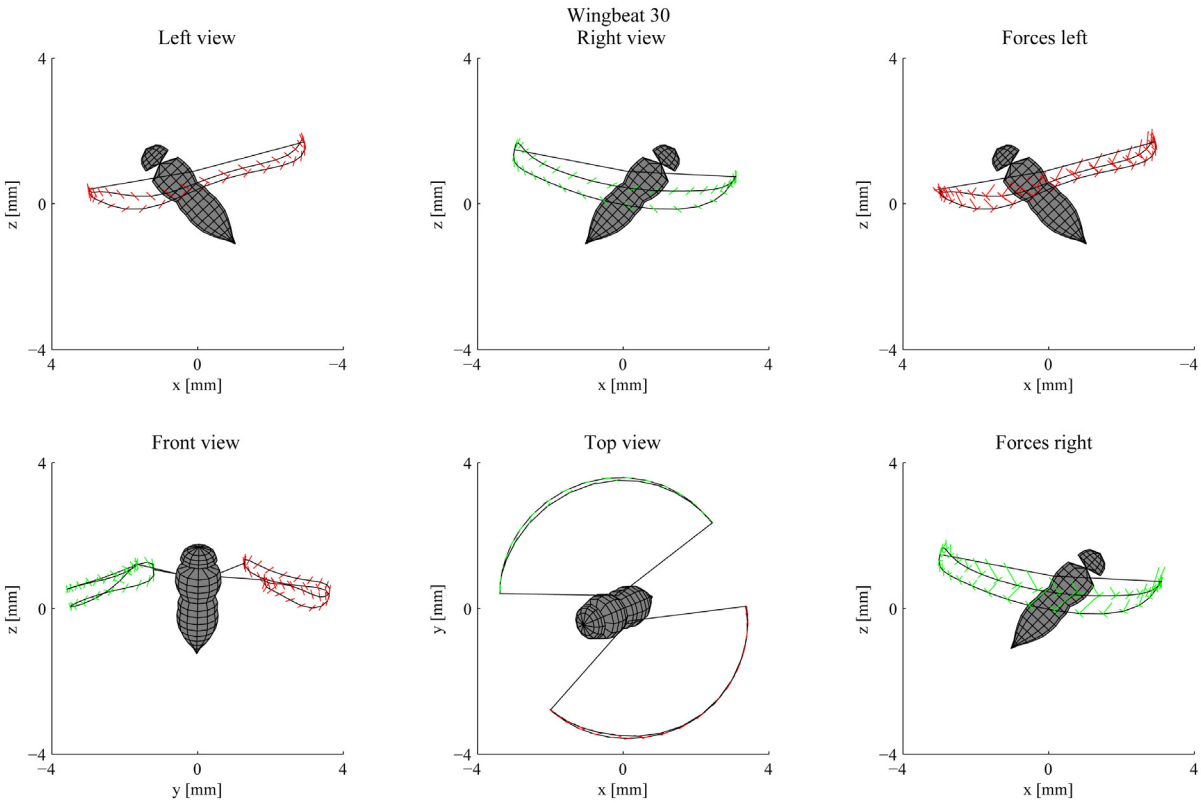

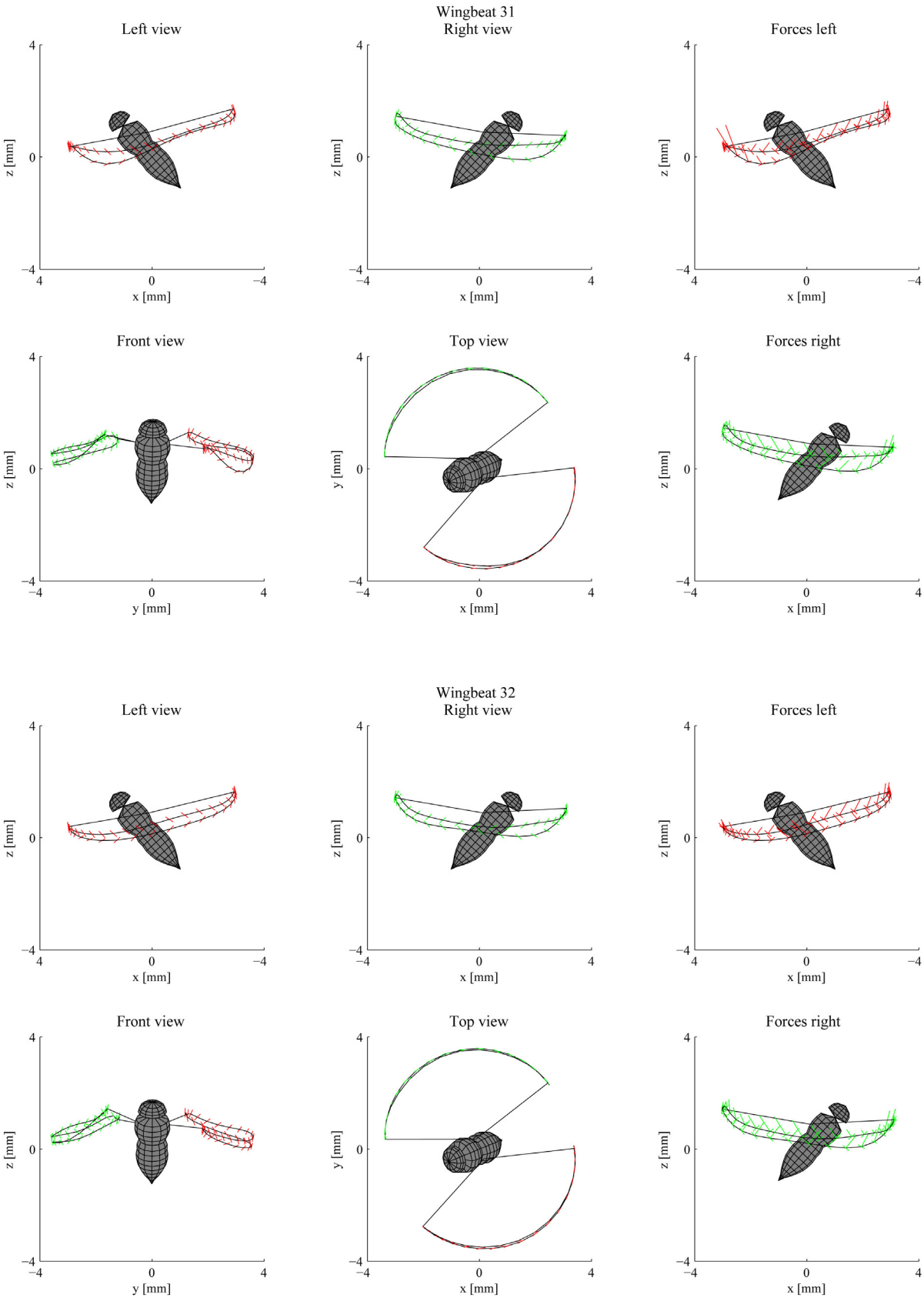
Left view
Wingbeat 31
Right view
Forces left
Front view
Top view
Forces right
Left view
Wingbeat 32
Right view
Forces left
Front view
Top view
Forces right
z [mm]
y [mm]
x [mm]
4
0
−4

Roll Maneuver

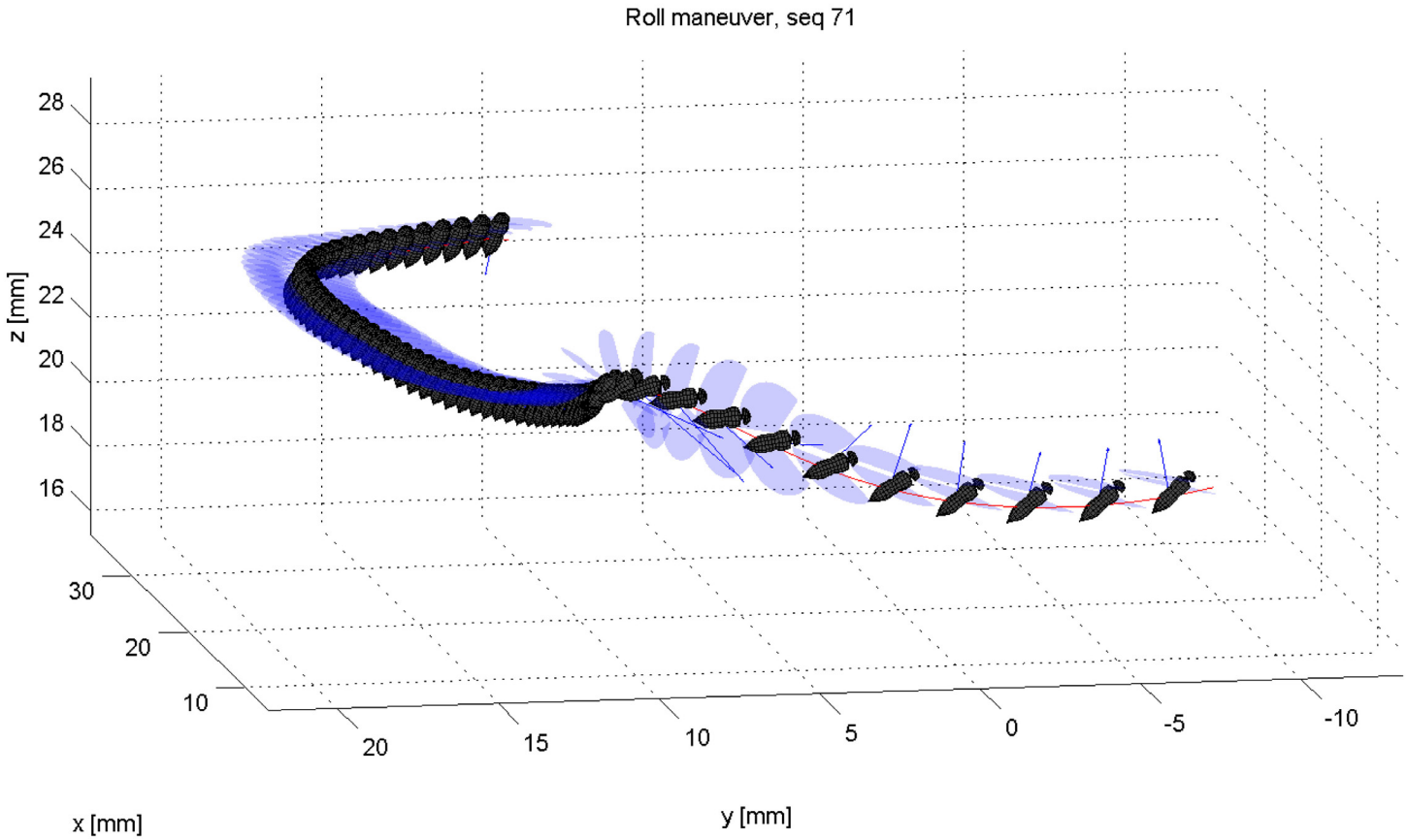

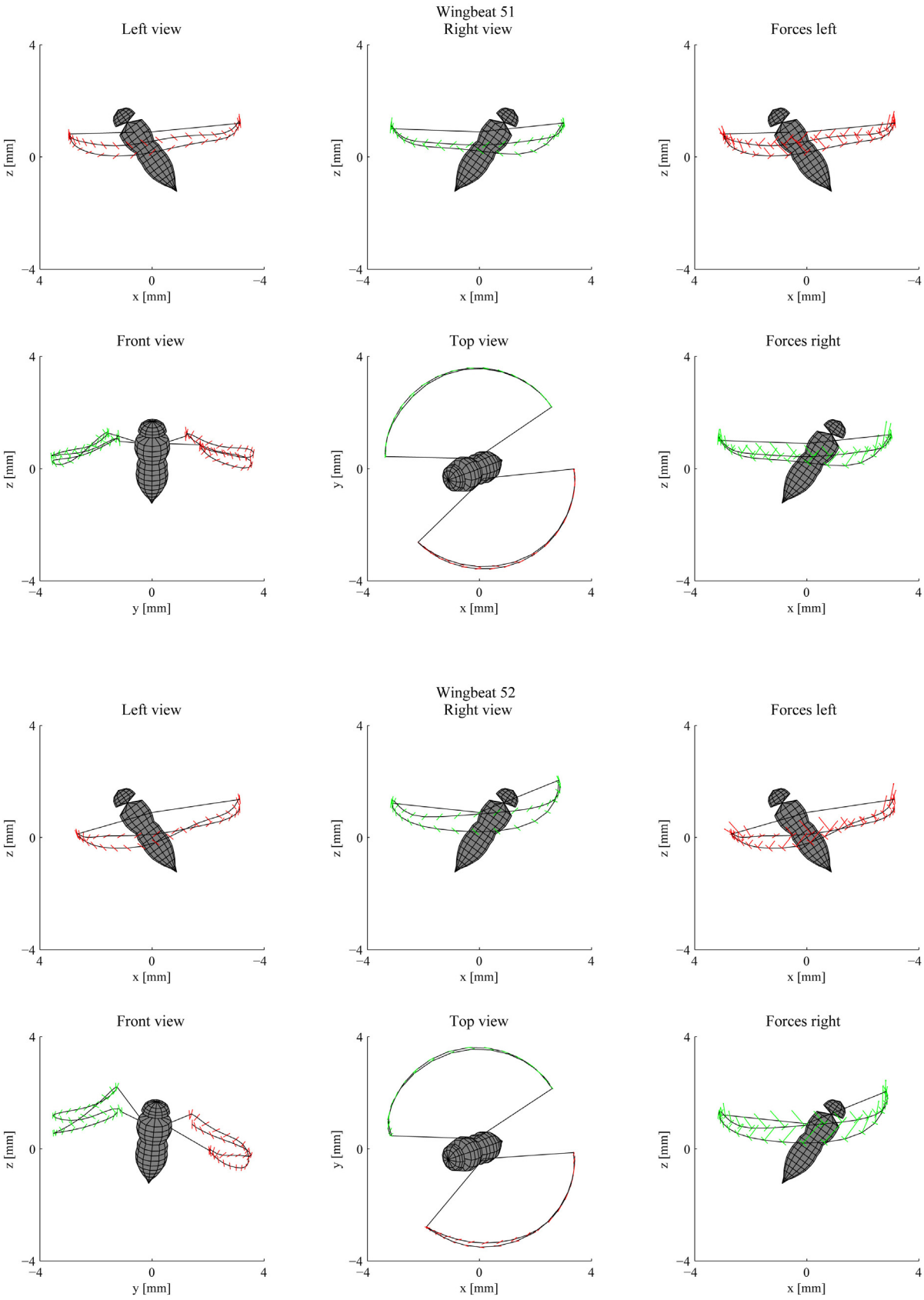
Wingbeat 51
Left view
Right view
Forces left
Front view
Top view
Forces right
Wingbeat 52
Left view
Right view
Forces left
Front view
Top view
Forces right
z [mm]
y [mm]
x [mm]
4
0
−4

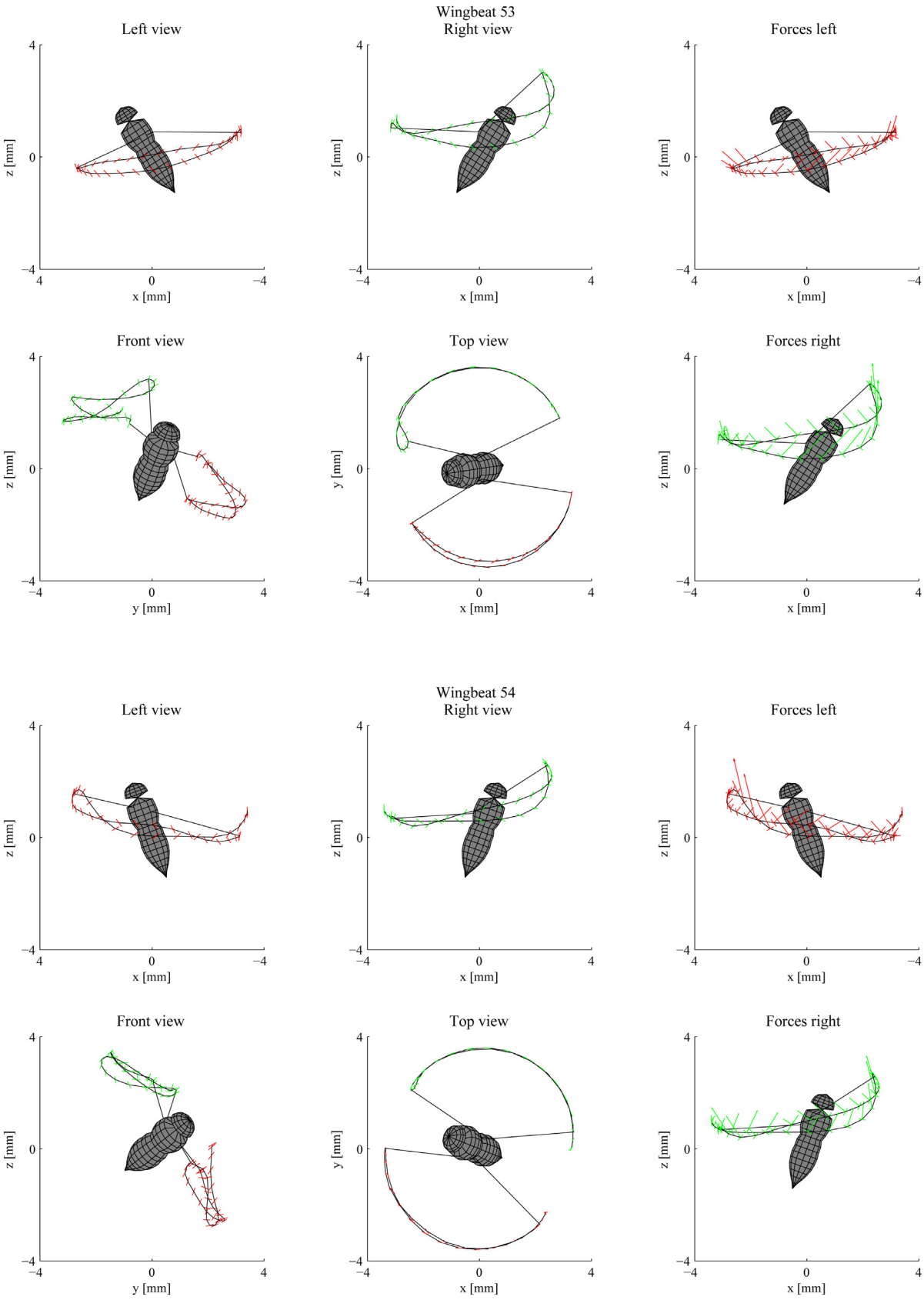
Left view
Wingbeat 53
Right view
Forces left
Front view
Top view
Forces right
Left view
Wingbeat 54
Right view
Forces left
Front view
Top view
Forces right
z [mm]
y [mm]
x [mm]
4
0
−4

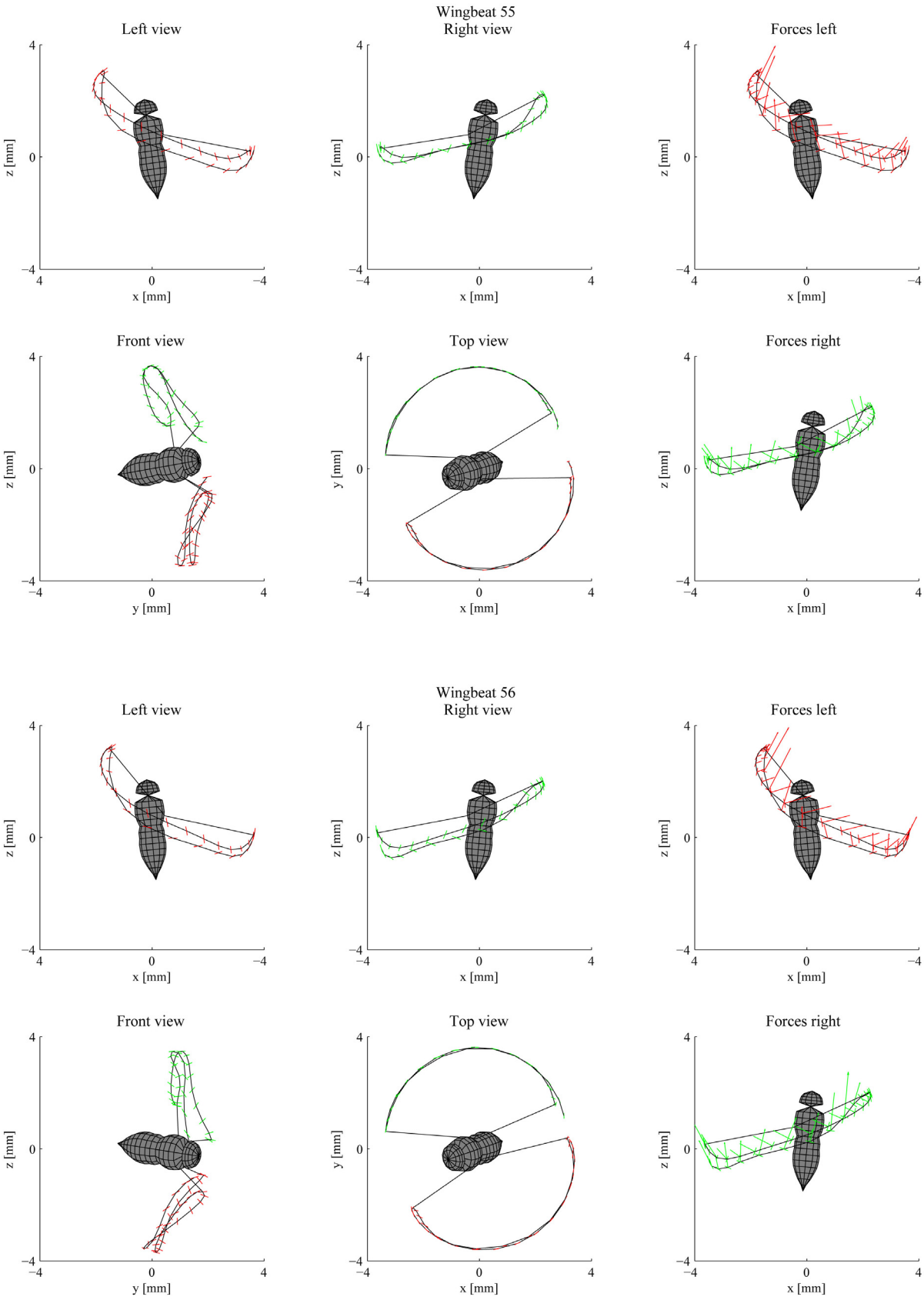
Wingbeat 55
Left view
Right view
Forces left
Front view
Top view
Forces right
Wingbeat 56
Left view
Right view
Forces left
Front view
Top view
Forces right
x [mm]
y [mm]
z [mm]

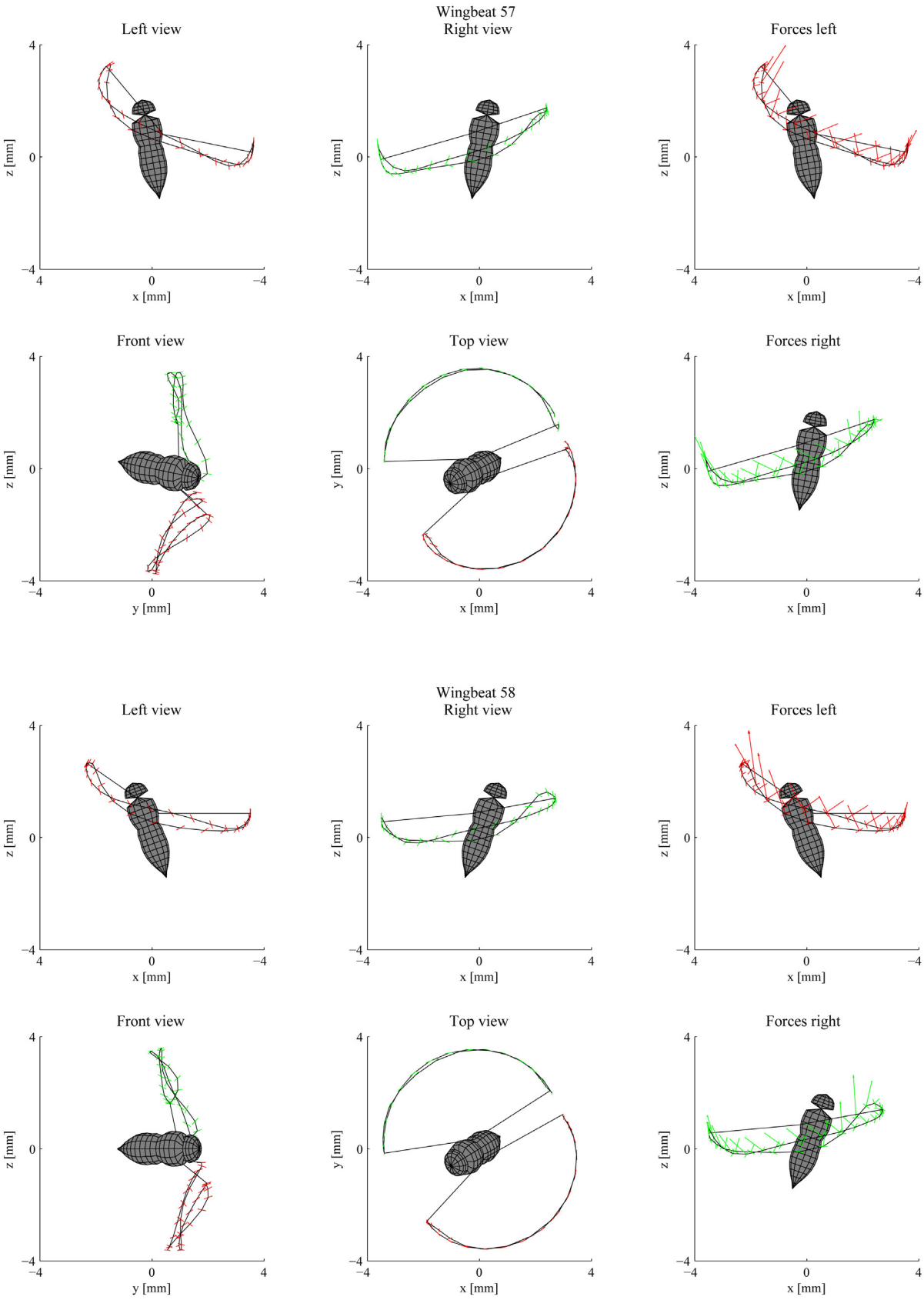
Left view
Wingbeat 57
Right view
Forces left
Front view
Top view
Forces right
Left view
Wingbeat 58
Right view
Forces left
Front view
Top view
Forces right
z [mm]
y [mm]
x [mm]
4
0
−4

Pitch-up Maneuver

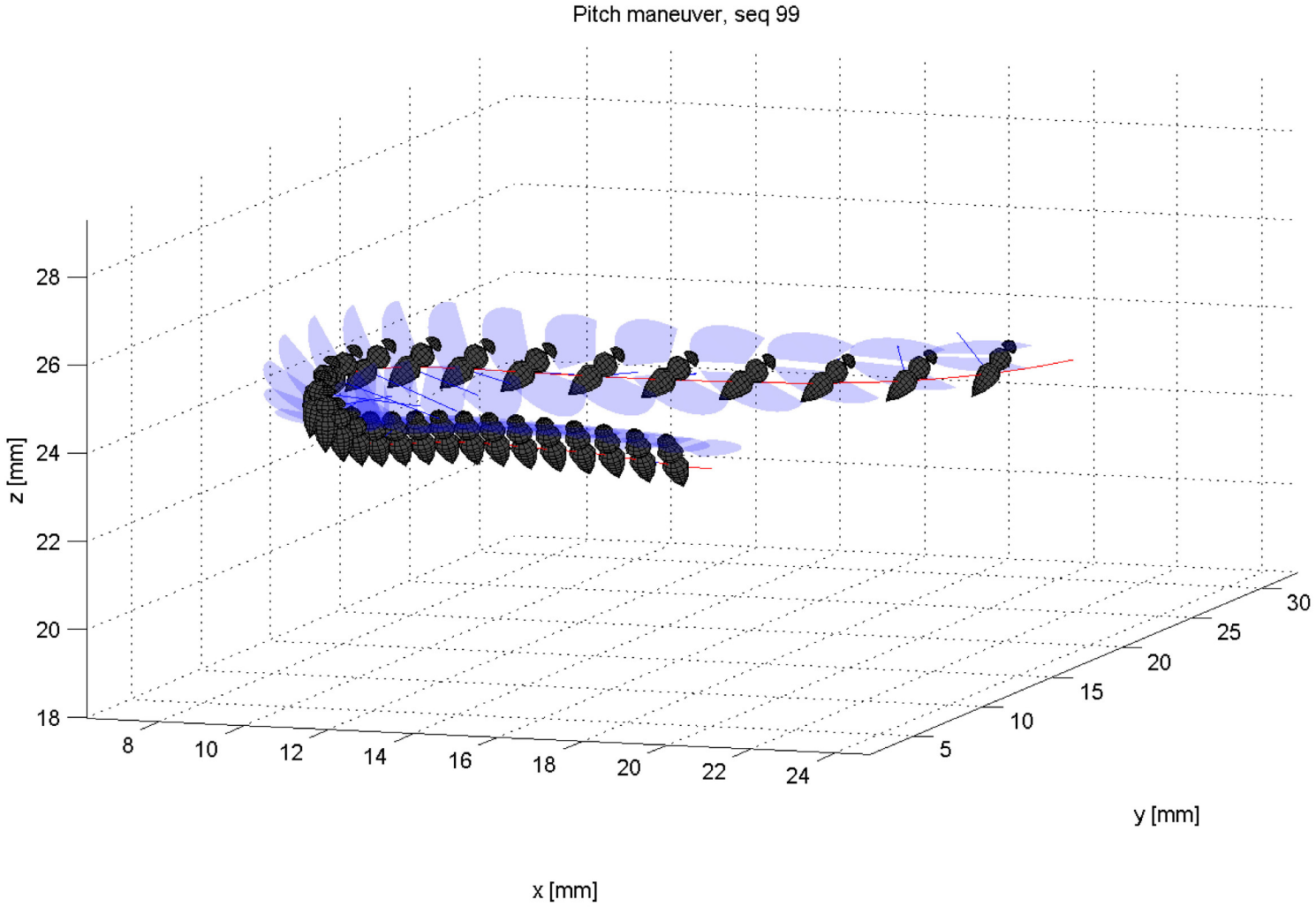

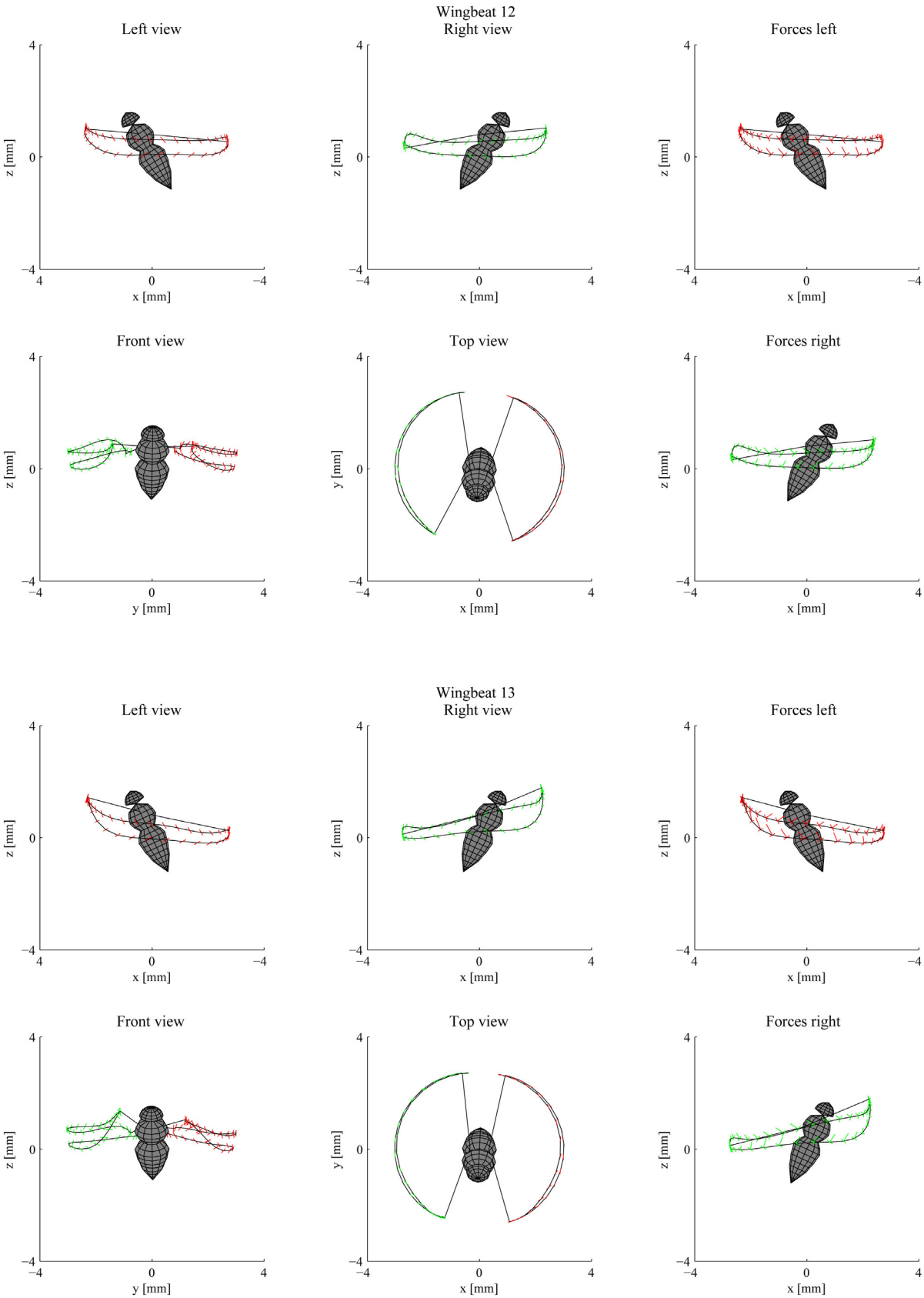
Left view
Wingbeat 12
Right view
Forces left
Front view
Top view
Forces right
Left view
Wingbeat 13
Right view
Forces left
Front view
Top view
Forces right
z [mm]
y [mm]
x [mm]
4
0
−4

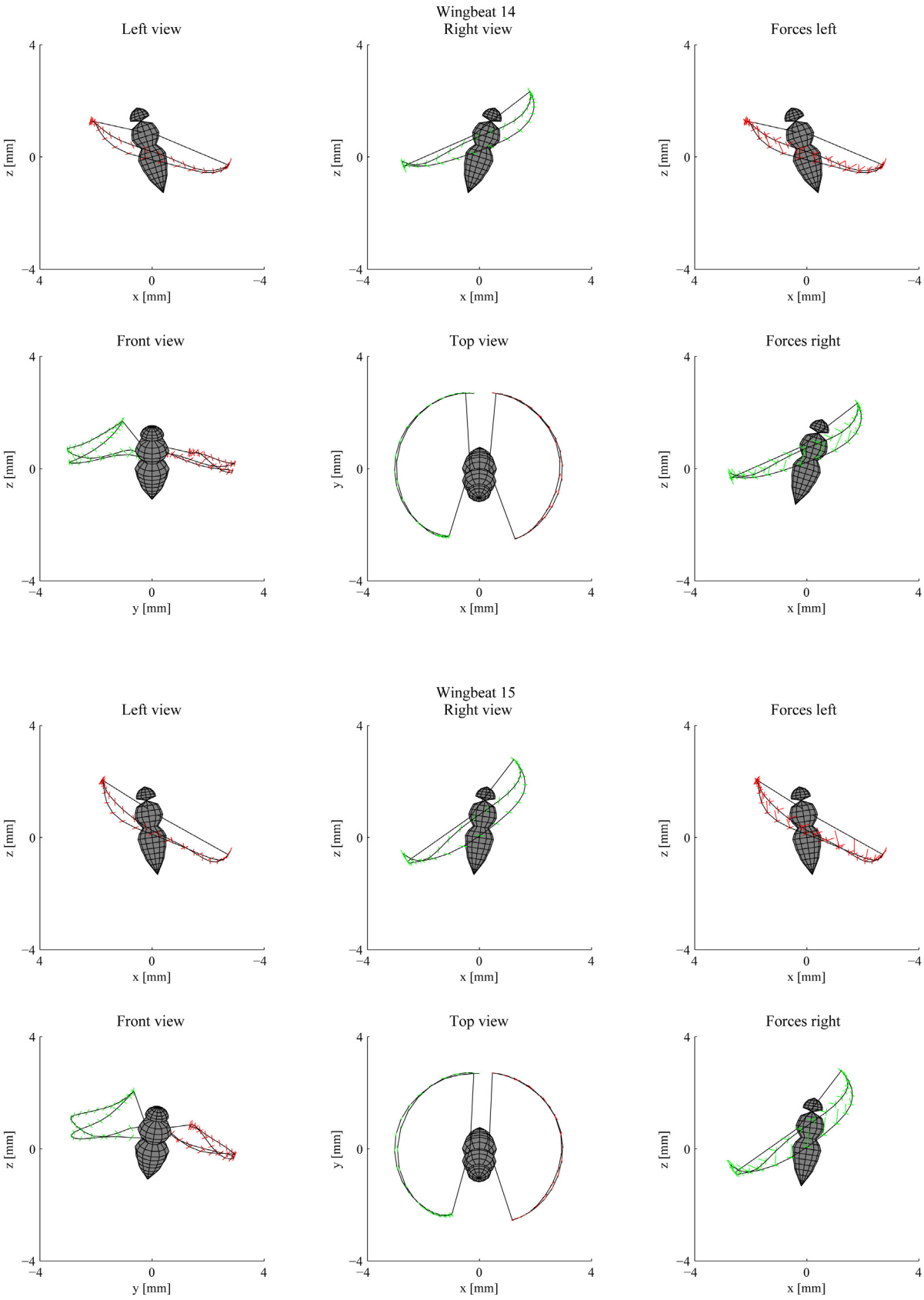
Left view
Wingbeat 14
Right view
Forces left
Front view
Top view
Forces right
Left view
Wingbeat 15
Right view
Forces left
Front view
Top view
Forces right
z [mm]
y [mm]
x [mm]
4
0
−4

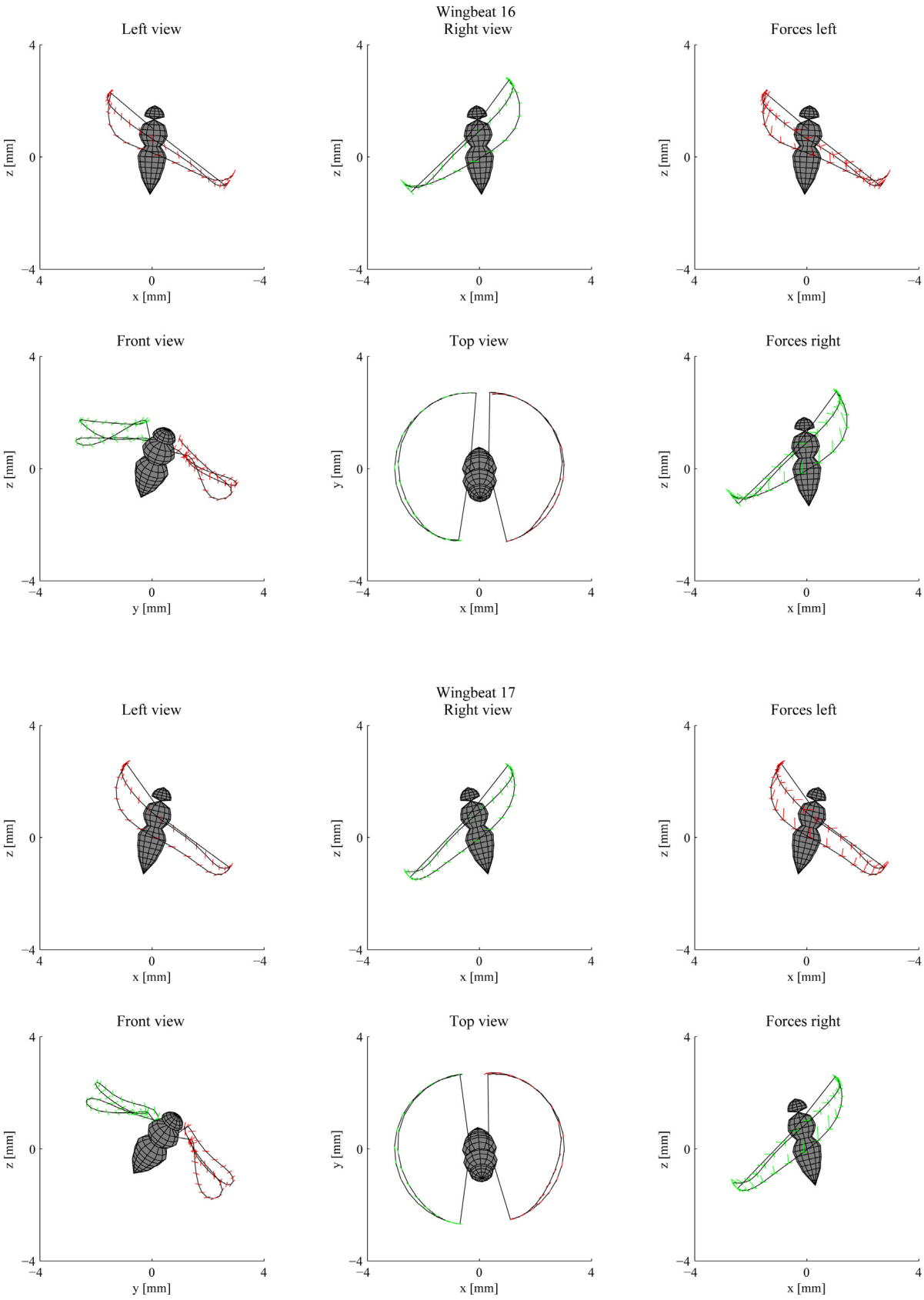
Left view
Wingbeat 16
Right view
Forces left
Front view
Top view
Forces right
Left view
Wingbeat 17
Right view
Forces left
Front view
Top view
Forces right
z [mm]
y [mm]
x [mm]
4
0
−4

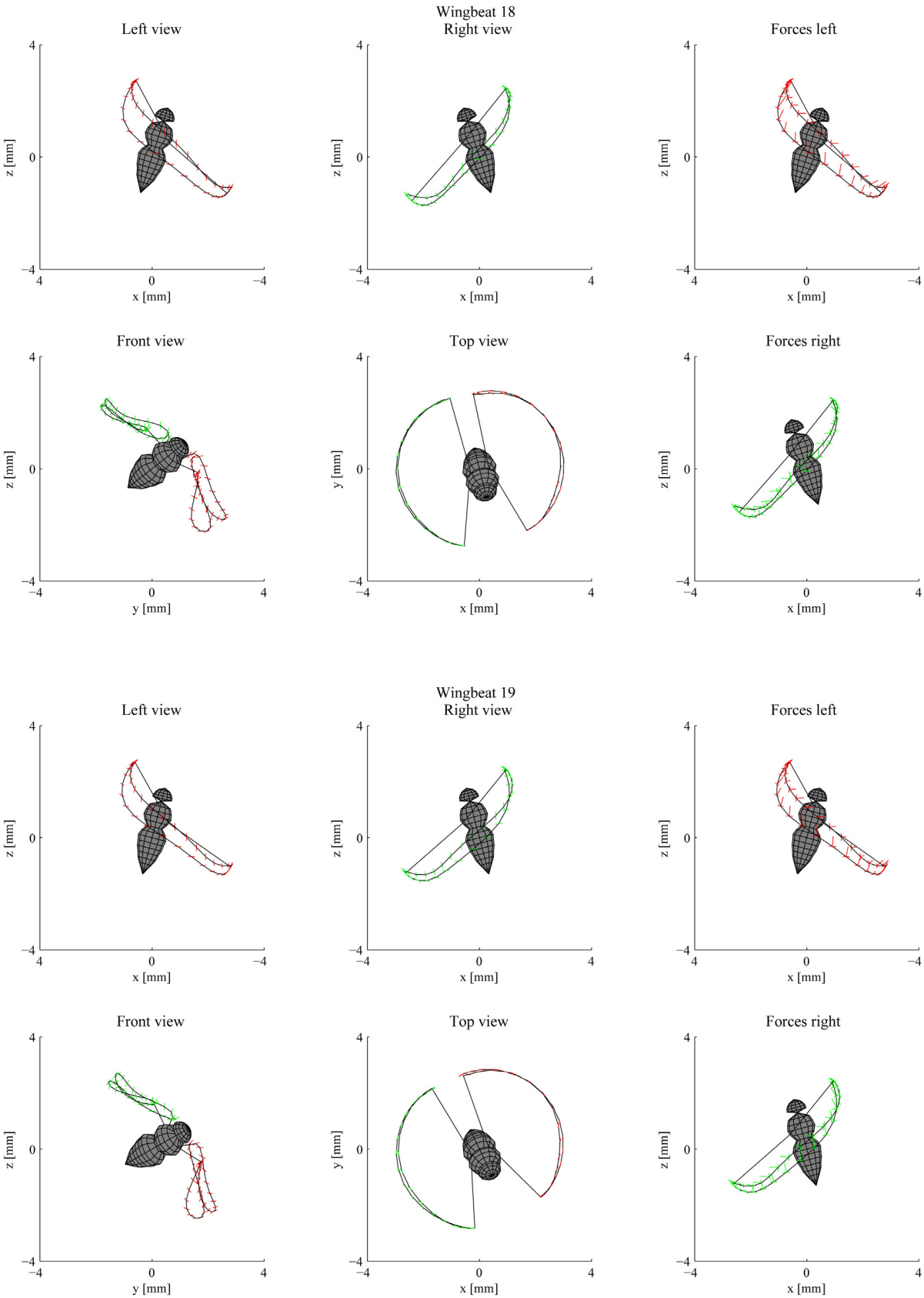
Left view
Wingbeat 18
Right view
Forces left
Front view
Top view
Forces right
Left view
Wingbeat 19
Right view
Forces left
Front view
Top view
Forces right
z [mm]
y [mm]
x [mm]
4
0
−4

Appendix D

Maneuvering Flight Model Chapter 9

Polynomial fit global wingbeat						
	a_{θ_L}	a_{η_L}	a_{ϕ_L}	a_{θ_R}	a_{η_R}	a_{ϕ_R}
downstroke	-0.0684	2.2054	0.0306	-0.0684	2.2054	0.0306
	-0.0007	-0.1824	-1.3703	-0.0007	-0.1824	-1.3703
	0.1161	-0.4300	0.1446	0.1161	-0.4300	0.1446
	-0.0165	0.2174	0.2227	-0.0165	0.2174	0.2227
	-0.0448	-0.2517	-0.0398	-0.0448	-0.2517	-0.0398
	0.0257	0.1047	0.0081	0.0257	0.1047	0.0081
	-0.0250	-0.0031	-0.0066	-0.0250	-0.0031	-0.0066
	0.0055	-0.1395	-0.0039	0.0055	-0.1395	-0.0039
	0.0140	0.1241	0.0044	0.0140	0.1241	0.0044
	-0.0099	-0.0030	0.0006	-0.0099	-0.0030	0.0006
	-0.0010	-0.0677	-0.0007	-0.0010	-0.0677	-0.0007
	0.0023	0.0346		0.0023	0.0346	
	-0.0003	0.0010		-0.0003	0.0010	
		-0.0091			-0.0091	
		0.0045			0.0045	
upstroke	-0.1557	0.7948	0.0803	-0.1557	0.7948	0.0803
	-0.0122	0.1528	1.3977	-0.0122	0.1528	1.3977
	0.2022	0.6026	0.0664	0.2022	0.6026	0.0664
	-0.0230	-0.2684	-0.2687	-0.0230	-0.2684	-0.2687
	-0.0560	0.3870	-0.0014	-0.0560	0.3870	-0.0014
	0.0493	0.0122	0.0123	0.0493	0.0122	0.0123
	-0.0179	-0.2598	-0.0192	-0.0179	-0.2598	-0.0192
	-0.0285	0.1622	0.0019	-0.0285	0.1622	0.0019
	0.0283	0.0440	0.0072	0.0283	0.0440	0.0072
	0.0096	-0.1076	-0.0004	0.0096	-0.1076	-0.0004
	-0.0119	0.0356	-0.0010	-0.0119	0.0356	-0.0010
	-0.0015	0.0285		-0.0015	0.0285	
	0.0017	-0.0295		0.0017	-0.0295	
		-0.0024			-0.0024	
		0.0068			0.0068	
$down\_up = 0.5384$						
$f = 189.0\,[Hz]$						

F_x *back*			
	$b_\theta \cdot 10^3$	$b_\eta \cdot 10^3$	$b_\phi \cdot 10^3$
downstroke	1.3324	3.2300	-3.9696
	-1.8643	-6.5474	3.9450
	-2.5546	1.5831	1.6867
	-0.8802	-1.5614	-2.1217
	0.4717	-1.4237	0.4717
	-0.0098	5.2924	0.1570
	-0.2619	-2.2272	0.1128
	0.6807	-1.2203	-0.0537
	-0.1930	2.8678	-0.1384
	-0.4220	-1.4400	0.0242
	0.2289	-1.1443	0.0192
	0.0801	1.0952	
	-0.0480	-0.2545	
		-0.2313	
		0.1821	
upstroke	-0.4088	2.5809	-0.0957
	3.9225	2.0858	-1.1526
	-1.6414	-2.3201	-1.6806
	-2.1008	3.0027	-0.4781
	1.0489	2.3021	0.3536
	0.8531	-0.9765	-0.6116
	-0.2340	-0.0634	-0.6226
	-0.3828	0.9531	0.3409
	0.3902	0.9794	0.2628
	0.1524	-0.5005	-0.0494
	-0.2134	-0.5534	-0.0350
	-0.0290	0.0201	
	0.0340	-0.2422	
		-0.0280	
		0.1299	
$N = 204$			
F_x range: $\left[0 : -0.4015 \cdot 10^{-4}\right]$, factor: 1.2.			

F_x *forward*			
	$b_\theta \cdot 10^3$	$b_\eta \cdot 10^4$	$b_\phi \cdot 10^3$
downstroke	2.8114	0.2345	-0.0713
	-1.4540	0.2039	-4.6221
	0.9668	0.0839	-1.2497
	0.0857	-0.2163	-0.7416
	0.2750	0.2924	0.5874
	0.8157	0.0442	0.7554
	-0.2697	-0.3023	0.1004
	0.0193	0.3038	-0.0444
	0.1026	0.0029	-0.2939
	-0.2955	-0.1615	-0.1069
	0.0761	0.1515	0.0705
	0.0812	0.0212	
	-0.0429	-0.0675	
		0.0024	
		0.0091	
upstroke	2.6552	0.9086	-3.4705
	-0.1148	-1.0813	5.3694
	2.4101	0.0596	3.5372
	1.2472	0.8733	-0.7212
	-1.1799	-1.0892	-1.1287
	-0.4079	0.3879	0.1456
	0.4139	0.4938	0.3566
	-0.1201	-0.5863	-0.1522
	-0.8098	0.1653	-0.1904
	0.1906	0.2526	0.0279
	0.5368	-0.1801	0.0392
	-0.0473	-0.0456	
	-0.1074	0.0523	
		0.0017	
		-0.0057	
$N = 70$			
F_x range: $[0 : 0.5038 \cdot 10^{-4}]$, factor: 1.2.			

F_y						
	$b_{\theta_L} \cdot 10^3$	$b_{\eta_L} \cdot 10^4$	$b_{\phi_L} \cdot 10^3$	$b_{\theta_R} \cdot 10^3$	$b_{\eta_R} \cdot 10^4$	$b_{\phi_R} \cdot 10^3$
downstroke	4.9278	-0.3946	-2.9959	-0.8743	0.1761	-0.4535
	2.3382	5.3481	-4.7375	-0.7664	-2.0064	-3.1196
	0.6185	-4.2875	1.3929	1.3885	1.5501	-1.4586
	-0.9451	0.0651	1.1563	0.8357	1.3083	0.5201
	-0.2226	0.5222	-0.3030	0.0686	-0.3774	0.6682
	0.1060	-2.7489	-0.2768	0.2331	-0.0944	-0.6530
	-0.3683	2.9585	0.2902	0.3437	0.7790	0.1246
	-0.0008	0.6240	0.1699	-0.1599	0.0893	0.3876
	0.5150	-2.8870	-0.1294	0.0234	-0.8578	-0.0413
	-0.0962	2.1752	-0.0305	-0.0284	0.1777	-0.0668
	-0.3672	0.2210	0.0115	-0.1971	0.2582	-0.0082
	0.0358	-1.6192		0.0229	-0.1554	
	0.0846	008491		0.0510	0.3206	
		0.3450			0.0325	
		-0.2693			-0.1488	
upstroke	3.7652	1.3222	-3.3119	-0.0185	0.7151	-1.5277
	-1.0950	-7.4742	3.8018	-1.6687	0.9352	4.0803
	1.5352	-3.0132	2.9704	1.8791	4.2122	1.2284
	-0.3230	2.4679	0.1885	1.9605	-3.0451	-1.4493
	-0.5323	-3.7349	-1.4586	-1.2116	-3.6800	-0.9497
	0.1896	3.5225	-0.2926	-0.0886	4.9368	0.4657
	0.9479	1.3058	-0.0718	0.4955	-0.6039	-0.0710
	-0.4476	-4.1112	-0.0151	-0.6401	-3.0003	-0.1989
	-0.6611	1.7016	0.1673	-0.5447	2.3960	0.1877
	0.2949	1.5713	0.0059	0.3632	0.9870	0.0339
	0.1321	-1.1577	-0.0290	0.2360	-2.3266	-0.0365
	-0.0568	-0.1226		-0.0634	-0.1779	
	0.0007	0.3513		-0.0319	1.2444	
		-0.0429			0.0127	
		-0.0627			-0.2574	
$N = 455$						
F_y range: $[0 : 0.4685 \cdot 10^{-4}]$, factor: 1.2.						

F_z up			
	$b_\theta \cdot 10^3$	$b_\eta \cdot 10^3$	$b_\phi \cdot 10^3$
downstroke	-1.5852	0.3999	-0.0377
	0.0685	-1.5645	4.6358
	-1.0078	1.5811	0.1732
	-0.1722	-0.0314 8	-0.7640
	0.1261	-0.3195	-0.1353
	-0.3280	0.6142	0.0660
	0.4264	-0.4042	0.0967
	-0.0768	0.1258	-0.1082
	-0.3002	0.1114	-0.0338
	0.1397	-0.3685	0.0254
	0.1345	0.1096	0.0006
	-0.0312	0.2006	
	-0.0267	-0.2021	
		-0.0414	
		0.0705	
upstroke	-1.3224	0.3120	1.2065
	1.3572	1.3259	-4.4444
	-1.0308	0.2556	-1.9316
	-1.1163	-0.5808	0.6615
	0.1917	1.2343	1.0771
	0.1845	-0.2069	-0.1614
	-0.1742	-0.7548	-0.3334
	-0.0200	1.0511	0.1085
	0.1128	0.3989	0.0538
	-0.0110	-0.6620	-0.0192
	-0.0045	0.0510	-0.0032
	0.0055	0.1447	
	-0.0056	-0.2175	
		-0.0067	
		0.0672	
$N = 414$			
F_z range: $\left[0 : -0.6561 \cdot 10^{-4}\right]$, factor: 0.6667.			

M_x						
	$b_{\theta_L} \cdot 10^3$	$b_{\eta_L} \cdot 10^3$	$b_{\phi_L} \cdot 10^3$	$b_{\theta_R} \cdot 10^4$	$b_{\eta_R} \cdot 10^4$	$b_{\phi_R} \cdot 10^3$
downstroke	6.6967	1.5666	-4.1451	-1.2402	0.0236	5.2561
	8.0965	3.7092	2.3542	-0.9224	0.3368	9.8972
	-0.6708	2.8077	1.1913	-0.3598	0.1032	-3.5588
	0.0554	-0.7898	-0.5790	0.2610	0.3764	-2.5166
	0.2207	-2.1320	-0.6396	0.0435	0.4993	1.3520
	-0.7130	-0.7005	0.3921	0.0019	-0.1389	0.0544
	0.0108	1.3898	0.2883	0.0981	0.2416	0.0095
	-0.2335	1.3210	-0.0861	-0.0832	-0.0137	0.1547
	0.0576	-2.3401	-0.0757	-0.0143	-0.3027	-0.1766
	0.1884	1.1072	-0.0043	-0.0280	0.2184	-0.0398
	-0.1028	0.6304	0.0067	-0.0263	0.0320	0.0396
	-0.0390	-1.1015		-0.0013	-0.1466	
	0.0267	-0.0621		0.0089	0.1043	
		0.2146			0.0288	
		0.0673			-0.0400	
upstroke	4.6372	2.2277	-3.8272	-0.9491	0.7007	2.3554
	-7.1470	-5.7806	-2.3773	0.8283	-1.1.294	-0.8419
	2.0330	-1.8474	0.9169	-0.7684	1.1051	0.0983
	-0.4478	0.1947	-0.3511	0.0773	-0.0931	-0.0032
	-0.3521	-0.8978	-0.5628	0.1436	-1.4870	-0.0494
	-0.4781	1.7529	0.9790	-0.2872	1.1287	0.0944
	-0.0277	2.0363	0.0905	0.1759	0.2945	-0.0069
	1.1391	-0.1199	-0.3756	0.1015	-0.8239	-0.0391
	-0.0830	0.5902	0.0127	-0.1104	0.2482	0.0090
	-0.4963	0.7637	0.0481	-0.0006	0.3225	0.0057
	0.0392	0.8221	-0.0042	0.0172	-0.3956	-0.0012
	0.0752	-0.7289		-0.0032	-0.0728	
	-0.0031	-1.3806		-0.0010	0.2507	
		0.1579			0.0066	
		0.3772			-0.0552	
$N = 330$						
M_x range: $[0 : 0.2067 \cdot 10^{-4}]$, factor: 1.0667.						

M_y *down*			
	$b_\theta \cdot 10^3$	$b_\eta \cdot 10^4$	$b_\phi \cdot 10^3$
downstroke	1.0255	0.2125	-4.5477
	4.2663	-0.2463	-1.5166
	-2.6608	-0.0175	-1.5166
	-1.1299	-0.3315	0.2777
	1.1177	-0.0340	-0.0625
	-1.3107	0.2086	-0.4297
	-0.0388	-0.0792	0.9538
	1.1248	0.0202	-0.0012
	-0.6843	0.1138	-0.3030
	-0.4065	-0.0880	0.0275
	0.4985	-0.0624	0.0217
	0.0533	0.0560	
	-0.1018	-0.0814	
		-0.0126	
		0.0406	
upstroke	-2.3018	-0.3989	-7.7541
	-0.6141	0.3840	3.1790
	2.2209	-0.2623	2.0766
	-3.1433	0.3184	-1.4168
	-0.4755	1.0427	0.0320
	1.2798	-0.7430	-0.4014
	-1.1386	-0.2856	-0.8682
	-0.0313	0.7061	0.3348
	1.2457	-0.0692	0.4492
	-0.1097	-0.3421	-0.0533
	-0.4492	0.2013	-0.0687
	0.0215	0.0755	
	0.0545	-0.1842	
		-0.0052	
		0.0488	
$N = 59$			
M_y range: $[0 : -0.2655 \cdot 10^{-4}]$, factor: 1.2.			

M_y *up*			
	$b_\theta \cdot 10^3$	$b_\eta \cdot 10^4$	$b_\phi \cdot 10^3$
downstroke	1.3258	0.2498	-4.8078
	1.6792	0.3316	-0.7687
	-1.3781	0.1114	-3.2651
	2.4034	0.1487	0.1102
	0.6776	0.1245	1.3749
	-1.3018	0.0592	-0.1372
	-0.0075	0.2294	0.5645
	-0.1678	-0.0686	-0.0870
	0.5309	-0.1008	-0.3592
	-0.0037	0.0910	0.0266
	-0.2985	-0.0930	0.0404
	0.0430	-0.0661	
	0.0381	0.1279	
		0.0166	
		-0.0388	
upstroke	0.9836	0.6806	-8.8237
	-2.2945	-0.6614	2.6437
	1.5771	0.6502	4.8718
	0.0324	-0.4059	-2.4496
	-2.3347	-0.8308	-2.8685
	-0.2735	1.1102	0.7143
	1.1537	-0.0420	0.1786
	-0.5362	-0.7288	-0.0453
	-0.8582	0.3552	0.2352
	0.5312	0.1687	-0.0070
	0.4481	-0.3682	-0.0458
	-0.1116	0.0236	
	-0.0814	0.2104	
		-0.0125	
		-0.0452	
$N = 139$			
M_y range: $[0 : 0.2691 \cdot 10^{-4}]$, factor: 1.2.			

M_z						
	$b_{\theta_L} \cdot 10^3$	$b_{\eta_L} \cdot 10^3$	$b_{\phi_L} \cdot 10^3$	$b_{\theta_R} \cdot 10^3$	$b_{\eta_R} \cdot 10^4$	$b_{\phi_R} \cdot 10^3$
downstroke	4.5419	2.4520	-2.4101	-1.2953	0.0509	0.9483
	1.7454	0.2743	-3.4991	-4.3421	0.2703	-1.8756
	0.0853	0.1673	0.2342	0.5938	0.0518	-0.5873
	-0.1566	-0.0221	0.2254	1.2095	-0.0042	-1.5498
	0.6207	-0.2189	-0.2075	0.3558	0.0909	1.0093
	-0.0015	0.5387	0.1846	0.6272	0.0477	0.2894
	-0.8024	-0.2895	0.3743	-0.3481	0.0698	-0.4102
	0.2572	1.8691	-0.0588	0.0493	0.0120	0.5055
	0.0650	-0.6106	-0.0922	-0.0449	-0.0965	-0.1701
	-0.2370	-0.4932	0.0068	-0.1751	0.0399	-0.1364
	0.1184	0.5981	-0.0054	0.1864	0.0426	0.0632
	0.0568	-0.1958		0.0356	-0.0501	
	-0.0307	0.1194		-0.0591	0.0393	
		0.0590			0.0142	
		-0.0935			-0.0204	
upstroke	3.2634	7.9562	-3.9005	-0.1536	0.0291	-2.2538
	-2.8960	-9.6121	4.2187	1.1850	-0.5311	2.8257
	1.5154	-2.4945	3.5021	-0.1947	1.0618	4.0092
	1.9796	6.5820	-1.3264	1.9692	-0.2378	-0.5220
	-0.5394	-7.5476	-1.9353	-0.8395	-1.1913	-0.9975
	-0.9486	3.9942	0.3027	-0.9229	1.0100	1.0556
	0.7253	3.7854	0.0662	1.3541	0.3318	0.2574
	0.1305	-5.0807	-0.0590	0.5329	0.8496	-0.7142
	-0.5098	1.6319	0.2027	-1.2578	0.0772	-0.2089
	0.1011	2.9919	0.0052	-0.1935	0.3250	0.1218
	0.1671	-1.6962	-0.0419	0.5824	-0.1753	0.0468
	-0.0309	-1.0652		0.0248	-0.0447	
	-0.0237	0.5781		-0.1022	0.1247	
		0.1598			-0.0017	
		-0.0891			-0.0296	
$N = 422$						
M_z range: $[0 : 0.4233 \cdot 10^{-4}]$, factor 1.2.						

Appendix E

Maneuvering Flight Model Chapter 10

Polynomial fit global wingbeat						
	a_{θ_L}	a_{η_L}	a_{ϕ_L}	a_{θ_R}	a_{η_R}	a_{ϕ_R}
downstroke	-0.0684	2.2054	0.0306	-0.0684	2.2054	0.0306
	-0.0007	-0.1824	-1.3703	-0.0007	-0.1824	-1.3703
	0.1161	-0.4300	0.1446	0.1161	-0.4300	0.1446
	-0.0165	0.2174	0.2227	-0.0165	0.2174	0.2227
	-0.0448	-0.2517	-0.0398	-0.0448	-0.2517	-0.0398
	0.0257	0.1047	0.0081	0.0257	0.1047	0.0081
	-0.0250	-0.0031	-0.0066	-0.0250	-0.0031	-0.0066
	0.0055	-0.1395	-0.0039	0.0055	-0.1395	-0.0039
	0.0140	0.1241	0.0044	0.0140	0.1241	0.0044
	-0.0099	-0.0030	0.0006	-0.0099	-0.0030	0.0006
	-0.0010	-0.0677	-0.0007	-0.0010	-0.0677	-0.0007
	0.0023	0.0346		0.0023	0.0346	
	-0.0003	0.0010		-0.0003	0.0010	
		-0.0091			-0.0091	
		0.0045			0.0045	
upstroke	-0.1557	0.7948	0.0803	-0.1557	0.7948	0.0803
	-0.0122	0.1528	1.3977	-0.0122	0.1528	1.3977
	0.2022	0.6026	0.0664	0.2022	0.6026	0.0664
	-0.0230	-0.2684	-0.2687	-0.0230	-0.2684	-0.2687
	-0.0560	0.3870	-0.0014	-0.0560	0.3870	-0.0014
	0.0493	0.0122	0.0123	0.0493	0.0122	0.0123
	-0.0179	-0.2598	-0.0192	-0.0179	-0.2598	-0.0192
	-0.0285	0.1622	0.0019	-0.0285	0.1622	0.0019
	0.0283	0.0440	0.0072	0.0283	0.0440	0.0072
	0.0096	-0.1076	-0.0004	0.0096	-0.1076	-0.0004
	-0.0119	0.0356	-0.0010	-0.0119	0.0356	-0.0010
	-0.0015	0.0285		-0.0015	0.0285	
	0.0017	-0.0295		0.0017	-0.0295	
		-0.0024			-0.0024	
		0.0068			0.0068	
$down\_up = 0.5384$						
$f = 189.0\,[Hz]$						

F_x *back*			
	$b_\theta \cdot 10^3$	$b_\eta \cdot 10^3$	$b_\phi \cdot 10^3$
downstroke	-0.2405	6.0593	-2.1297
	-1.0992	-3.7905	3.1794
	-1.0758	1.8982	-0.5957
	-0.3870	-4.3611	-2.3833
	1.4899	-1.5724	0.5992
	-0.3600	6.2406	0.5732
	-0.5603	-5.1382	-0.3244
	0.7174	0.1463	-0.1070
	-0.5176	4.8061	0.1236
	-0.3540	-3.7528	0.0170
	0.4513	-0.3733	-0.0232
	0.0597	1.9256	
	-0.0895	-1.3429	
		-0.2931	
		0.4555	
upstroke	0.06801	1.5067	-2.7057
	2.2483	6.4482	-0.8484
	-1.6652	-1.2068	0.5569
	-1.3161	-2.8217	-0.1711
	0.4886	7.9617	-0.0653
	0.7806	-1.2187	-0.4234
	-0.4152	-5.7938	-0.2569
	-0.3997	3.2454	0.1887
	0.6143	3.1279	0.1449
	0.1306	-2.8405	-0.0252
	-0.2865	-0.3652	-0.0241
	-0.0207	1.2987	
	0.0414	-0.6784	
		-0.2265	
		0.2403	
$N = 197$			
F_x range: $\left[0 : -0.4522 \cdot 10^{-4}\right]$, factor: 1.2.			

F_x *forward*			
	$b_\theta \cdot 10^3$	$b_\eta \cdot 10^3$	$b_\phi \cdot 10^3$
downstroke	0.6934	3.65	-1.8128
	-2.2923	-0.5222	-3.0097
	0.8353	6.4109	-0.6826
	0.3268	-4.1805	-2.1659
	1.7031	0.4154	1.0542
	-0.0230	2.9081	0.7863
	-0.7248	-4.7336	-0.2312
	1.0419	0.3677	0.1329
	-0.0066	2.4684	-0.0637
	-0.7145	-1.5736	-0.0566
	0.1985	0.1334	0.0073
	0.1373	0.8253	
	-0.0770	-0.0164	
		-0.1248	
		-0.0835	
upstroke	1.0430	9.2616	-5.2331
	0.8450	-0.2243	5.8309
	2.7252	4.1573	5.6057
	0.9737	1.0957	-1.9132
	-0.5084	-8.2066	-2.0140
	-0.5685	5.9363	0.6949
	-0.2290	2.4493	-0.3279
	0.3314	-6.6321	-0.3593
	-1.0764	2.2688	0.3067
	-0.0484	2.2800	0.0596
	0.8390	-2.9507	-0.0482
	-0.0094	-0.0954	
	-0.1716	1.5904	
		-0.0601	
		-0.3236	
$N = 77$			
F_x range: $\left[0 : 0.2894 \cdot 10^{-4}\right]$, factor: 1.2.			

F_y						
	$b_{\theta_L} \cdot 10^3$	$b_{\eta_L} \cdot 10^4$	$b_{\phi_L} \cdot 10^3$	$b_{\theta_R} \cdot 10^3$	$b_{\eta_R} \cdot 10^4$	$b_{\phi_R} \cdot 10^3$
downstroke	7.9952	0.0701	-3.5036	-0.8625	0.0734	0.6053
	1.3428	0.8248	-7.9491	-2.6987	-0.0144	-6.6948
	1.1617	-0.3359	0.9973	2.4932	-0.0129	-2.9584
	0.3374	-0.1163	1.3407	0.9937	0.1047	1.2703
	0.1429	0.1043	-0.0938	-0.5716	0.1385	1.2490
	0.4141	-0.0348	-0.3439	0.9112	-0.1020	-0.4181
	-0.6366	0.1454	0.6666	0.1399	0.1192	-0.2694
	0.1904	0.1042	0.3602	-0.4736	0.1050	0.4142
	0.7488	-0.2492	-0.4925	0.4777	-0.1764	0.2315
	-0.4197	0.1396	-0.0744	-0.0736	0.0935	-0.0917
	-0.7792	0.0501	0.0844	-0.5163	0.0437	-0.0707
	0.1126	-0.1383		0.0542	-0.1211	
	0.2214	0.1065		0.1257	0.0409	
		0.0313			0.0320	
		-0.0407			-0.0154	
upstroke	7.2337	0.6286	-6.2322	0.1308	0.2014	-2.9545
	-3.1635	-1.4950	7.2303	-0.3435	-0.1282	6.3858
	1.5113	-0.3671	6.3978	2.0321	0.8050	3.5269
	1.5922	0.4391	-0.4088	2.7261	-0.4378	-1.3725
	-1.1032	-0.8274	-2.7266	-1.4085	-1.0573	-1.9683
	-0.4646	0.6533	-0.0265	-1.1635	0.9470	0.9112
	1.9989	0.3404	0.1496	1.1661	-0.0030	-0.1351
	-0.1358	-0.6320	-0.1665	-0.2002	-0.6759	-0.4821
	-0.5688	0.2216	0.0768	-0.8247	0.4357	0.4013
	0.2606	0.2848	0.0381	0.3458	0.2041	0.0779
	-0.3502	-0.2424	-0.0069	0.1950	-0.2017	-0.0830
	-0.0664	-0.0657		-0.0779	0.0036	
	0.1324	0.1241		-0.0048	0.0330	
		0.0048			-0.0106	
		-0.0274			-0.0020	
$N = 455$						
F_y range: $\left[0 : 0.4019 \cdot 10^{-4}\right]$, factor: 1.2.						

F_z up			
	$b_\theta \cdot 10^3$	$b_\eta \cdot 10^3$	$b_\phi \cdot 10^3$
downstroke	-2.1202	-0.0567	0.5689
	0.5080	-0.1782	5.1156
	-0.6628	1.5196	0.2333
	-0.3816	0.7748	-0.7104
	0.0318	-0.1929	-0.2902
	-0.1272	0.1950	0.0066
	0.3602	0.5162	0.1743
	-0.1130	-0.2551	-0.0958
	-0.2316	-0.3896	-0.0580
	0.0821	0.3718	0.0240
	0.0998	-0.1087	0.0096
	-0.0115	-0.1446	
	-0.0201	0.0919	
		0.0122	
		-0.0030	
upstroke	-1.6395	0.6861	1.7633
	0.8944	-1.8221	-5.0524
	-1.0808	1.7872	-2.0203
	-0.9119	-0.1606	0.7710
	0.1726	-1.3324	1.2204
	0.0857	1.7205	-0.1396
	0.0300	-0.5266	-0.3816
	-0.0768	-0.3313	0.0991
	-0.0693	1.2539	0.0591
	0.0636	-0.2737	-0.0181
	0.0573	-0.4634	-0.0030
	-0.0119	0.0963	
	-0.0132	-0.0751	
		-0.0050	
		0.0471	
$N = 405$			
F_z range: $[0 : -0.7772 \cdot 10^{-4}]$, factor: 0.9333.			

M_x						
	$b_{\theta_L} \cdot 10^3$	$b_{\eta_L} \cdot 10^3$	$b_{\phi_L} \cdot 10^3$	$b_{\theta_R} \cdot 10^4$	$b_{\eta_R} \cdot 10^4$	$b_{\phi_R} \cdot 10^4$
downstroke	7.5812	0.8961	-2.9325	-1.3593	0.0923	0.7724
	8.2126	4.1933	2.1738	-1.1008	0.7912	1.0689
	-2.0923	2.1249	0.8884	-0.1240	0.0471	-0.6142
	0.6183	-2.6068	-0.6730	0.3296	0.3305	-0.3036
	1.0122	-0.3360	-0.9652	-0.0774	0.5379	0.2775
	-0.3804	-1.9469	0.0530	0.0042	-0.2314	0.0004
	0.1793	1.3200	0.6609	0.1577	0.3153	-0.0181
	-1.0582	2.5144	0.1519	-0.1009	0.0125	0.0239
	0.4423	-4.6738	-0.2489	0.0187	-0.4528	-0.0178
	0.4502	1.5623	-0.0488	0.0367	0.3108	-0.0056
	-0.4118	1.8529	0.0359	-0.0660	0.1305	0.0034
	-0.0506	-2.0247		-0.0025	-0.2444	
	0.0808	0.5143		0.0177	0.0999	
		0.4815			0.0552	
		-0.2811			-0.0470	
upstroke	6.4497	1.6417	-3.5244	-0.8904	0.5743	0.3534
	-7.6591	-1.8508	-1.4480	0.9236	-1.5963	-0.8419
	1.0794	-3.2097	1.6058	-0.7473	1.6707	0.0983
	0.3588	-0.3758	-1.1663	0.1208	-0.0017	-0.0032
	-0.3434	1.5924	-0.8532	0.1254	-1.9528	-0.0494
	-1.2636	-1.2537	1.4506	-0.3056	1.3284	0.0944
	-0.3909	2.7208	0.2636	0.2046	0.3946	-0.0069
	0.9404	1.1892	-0.5720	0.0939	-1.1329	-0.0391
	-0.1756	-1.3488	-0.0621	-0.1624	0.1684	0.0090
	-0.1744	0.5259	0.0788	0.0053	0.4422	0.0057
	0.2126	-0.4037	0.0090	0.0393	-0.2999	-0.0012
	0.0062	-0.4737		-0.0042	-0.0598	
	-0.0401	0.5864		-0.0017	0.2220	
		0.0658			-0.0042	
		-0.1616			-0.0542	
$N = 330$						
M_x range: $[0 : 0.2002 \cdot 10^{-4}]$, factor: 0.9333.						

M_y *down*			
	$b_\theta \cdot 10^3$	$b_\eta \cdot 10^4$	$b_\phi \cdot 10^3$
downstroke	0.5520	-0.0568	-8.9884
	4.8614	-0.6594	3.1877
	-3.1347	0.2607	1.9454
	-2.5828	-0.3219	-1.1885
	2.7562	-0.0719	-0.3595
	-0.1975	0.1912	0.0937
	-1.5360	-0.1697	0.2796
	1.3667	0.0692	-0.2333
	-0.5332	0.3053	-0.0409
	-0.7576	-0.2067	0.0672
	0.5953	-0.0939	-0.0132
	0.1278	0.1493	
	-0.1120	-0.1031	
		-0.0340	
		0.0440	
upstroke	-2.8738	-0.2496	-6.2379
	-1.8273	1.0406	-1.0590
	1.2965	-0.4687	-0.8436
	-2.1248	-0.1013	-0.5470
	0.2857	1.4812	0.4270
	1.3564	-0.5476	-0.7279
	-0.9593	-0.0692	-0.8831
	-0.1957	0.8271	0.4845
	1.4458	-0.0692	0.4264
	-0.0298	-0.5519	-0.0775
	-0.7246	0.2201	-0.0658
	0.0031	0.1615	
	-0.1433		
		-0.0163	
		0.0342	
$N = 81$			
M_y range: $\left[0 : -0.2790 \cdot 10^{-4}\right]$, factor: 1.0667.			

M_y *up*			
	$b_\theta \cdot 10^3$	$b_\eta \cdot 10^4$	$b_\phi \cdot 10^3$
downstroke	2.5966	-0.5729	-4.7007
	3.7826	-0.0046	-3.1893
	-2.4605	-0.6880	-2.5360
	-0.1541	-0.1065	1.8081
	0.8245	-0.0824	1.2498
	-0.0303	-0.6630	-0.1978
	0.3301	0.2819	0.0327
	-0.2599	0.3809	-0.2547
	-0.2489	-0.1712	-0.1174
	0.1117	0.0544	0.0655
	-0.0341	0.0142	0.0075
	-0.0107	-0.0955	
	0.0253	-0.0059	
		0.0184	
		0.0057	
upstroke	-0.0601	-0.3200	-8.7338
	-4.7756	0.6228	2.5174
	0.8137	-1.8002	4.3491
	2.0809	0.5346	-0.8459
	0.9238	0.6165	-1.5920
	-0.9644	-1.2724	-0.0810
	-0.9018	0.7885	-0.3714
	0.1952	0.4763	0.2226
	0.3356	-0.6687	0.3398
	0.0386	0.2124	-0.0450
	-0.0956	0.1881	-0.0558
	-0.0140	0.1969	
	-0.0262		
		0.0390	
		0.0033	
$N = 117$			
M_y range: $\left[0 : 0.2397 \cdot 10^{-4}\right]$, factor: 1.2.			

M_z						
	$b_{\theta_L} \cdot 10^3$	$b_{\eta_L} \cdot 10^3$	$b_{\phi_L} \cdot 10^3$	$b_{\theta_R} \cdot 10^4$	$b_{\eta_R} \cdot 10^4$	$b_{\phi_R} \cdot 10^4$
downstroke	3.3271	2.7580	-0.3407	3.3616	-0.0665	1.0282
	-0.5697	0.2347	-3.7857	-5.5204	5.3761	-4.6581
	1.5256	-0.0200	-3.4419	1.3812	-1.7660	0.1539
	0.7966	-3.5960	0.5982	1.2167	-0.3249	-2.5421
	0.8729	0.2101	1.0707	0.3942	-0.6098	2.2896
	0.0921	0.6463	0.1113	0.6055	1.7989	1.0302
	-0.4567	-1.5451	-0.1042	-0.4317	1.2340	-1.9117
	-0.2609	2.3319	-0.3503	0.4518	-0.5480	0.7362
	0.1832	-0.0116	0.4226	-0.2575	-0.8429	0.0934
	-0.0500	-1.4684	0.0891	-0.4514	-0.1701	-0.2251
	0.0063	1.9364	-0.1420	0.2869	1.1183	0.0810
	0.0458	-0.0201		0.0865	-0.0706	
	-0.0277	-0.8313		-0.0740	-0.3204	
		0.1162			0.0678	
		0.0647			-0.0208	
upstroke	5.0044	9.3332	-4.4311	2.6619	0.7388	-2.8732
	-1.4338	0.5849	5.2883	2.6379	-9.0345	4.3967
	1.2466	-3.6980	4.6758	2.6170	3.9139	4.9051
	2.9191	3.0691	-1.8475	1.6457	-0.6757	1.0540
	-0.4586	-5.4186	-3.0268	-0.8664	-9.6554	-0.4453
	-1.8024	-0.7194	-0.4888	-1.4720	9.1103	1.1429
	-0.0027	2.5053	-0.3769	1.0543	4.2894	0.7060
	-0.0023	-3.2506	0.4660	1.1677	-8.3913	-1.1397
	-0.8506	-0.1465	0.7862	-1.3668	0.2543	-0.7002
	0.3484	2.7423	-0.0806	-0.4195	3.2785	0.2048
	0.6130	-0.3337	-0.1626	0.6806	-1.7640	0.1420
	-0.0829	-0.7092		0.0513	-0.3760	
	-0.1215	0.4568		-0.1198	1.2184	
		0.0383			-0.0405	
		-0.1390			-0.2695	
$N = 422$						
M_z range: $[0 : 0.3835 \cdot 10^{-4}]$, factor: 0.9333.						